THE UNIVERSITY *of* EDINBURGH

Exploring the structure and function of key enzymes involved in microbial sphingolipid biosynthesis

Peijun Tang

A Thesis Submitted for the Degree of Doctor of Philosophy

The University of Edinburgh

2020

Lay summary

Sphingolipids (SLs) are essential small molecules found in the membrane walls of every human cell and are made from common building blocks such as amino acids and fatty acids. Research has shown that SLs are structural components and potent signal molecules that are involved in cell-to-cell communication, growth regulation and cell death in complex species. The biosynthesis of SLs in mammals, yeast and plants has been well-examined through studying the enzymes that make these molecules, detailed chemical analysis and understanding the genes/genetics involved. Moreover, mammalian SL biosynthesis has been suggested to be associated with many diseases, such as Alzheimer's disease, sensory neuropathies, cancer and skin disorders, all due to unbalanced SL regulation within cells. Recent research has identified that SLs also exist in many bacteria that co-exist or are symbiotic with human hosts. These bacteria are found throughout the body such as the gut and oral cavity.

SL biosynthetic enzymes and SLs are related to cell growth and survival ability in the bacteria. The human bacteria have an impact on host metabolism and the human immune system and have been linked to human diseases, including diabetes, obesity, allergies, autism, cancer and inflammatory. Furthermore, many novel bioactive SL species (for example, *iso*-branched SLs) have also been found in those human bacteria and a hypotheticed pathway is defined that requires a suite of essential enzymes that catalyse the conversion of those SL intermediates.

In this work, three different types of enzymes, serine palmitoyltransferase (SPT), *iso*-branched amino acid transferase (IlvE) and 3-ketosphingosine reductase (3-KDS), all involved in the essential steps of SL biosynthesis, will be examined to provide kinetic, mechanistic and structural information for SL biosynthetic pathways in the human microbiota.

Abstract

Sphingolipids (SLs) are a diverse class of lipid molecules derived from the amino acid L-serine and long chain fatty acids (e.g. carbon chain lengths C14-C26). When combined together these building blocks form a so-called “sphingoid”, also known as a long-chain base (LCB). Decades of research into these enigmatic molecules has revealed that SLs are essential components of eukaryotic cell membranes and control many critical cellular functions. The SL biosynthetic pathway begins in all organisms with the Claisen-like, decarboxylative condensation of L-Ser and long-chain fatty acid acyl-CoA thioester (CoASH) substrates (most commonly C16/palmitoyl) to form the intermediate 3-ketodihydrosphingosine (3-KDS). This first key irreversible reaction is catalysed by the pyridoxal 5’-phosphate (PLP)-dependent serine palmitoyltransferase (SPT). The 3-KDS product is then reduced by a NAD(P)H-dependent enzyme (KDS reductase, KDSR) to generate dihydrosphingosine (DHS). Acylation of this molecule with a long-chain fatty acid by a ceramide synthase (CerS) leads to the formation of ceramide (Cer). Downstream, phosphorylation with a phosphate group can occur on the serine-derived head group and lead to the formation of sphingosine-1-phosphate (S-1-P). The balance between Cer and S-1-P concentrations has been proposed to control the cell survival rate in the host system. Alternatively, sugars such as glucose can be added to give the family of glycosphingolipids (GSLs).

In contrast to higher order species, research into SL biosynthesis in bacteria has lagged much further behind. However recent studies have revealed a number of important microbes that produce a range of SLs and Cers. Interestingly, SLs from the human microbiota including those from *Bacteroides fragilis*, a Gram-negative commensal bacterium from the human gut, and from the oral pathogen *Porphyromonas gingivalis* have recently been shown to play an essential role in host/microbe communication. Of note is that these bacterial SLs and Cers display many similar structural features to their mammalian homologues. However, there appears to be “chemical signatures” distinct to those of bacterial origin. For example, *B. fragilis* SLs have *iso*-Me branched acyl chains which are also similar to those found in the round-worm *Caenorhabditis elegans*. This suggests a PLP-dependent branched-chain amino acid transferase (BCAT/IlvE) transfers *iso*-Me chains from amino acid precursors such as L-Leu to branched-chain keto acids. To fully understand the role of bacterial SLs and their metabolism detailed investigations of the enzymes, pathways and metabolism are required.

In this thesis, studies of different types of the three key enzymes (SPT, IlvE/BCAT and KDSR) involved in the core microbial SL biosynthetic pathway have been presented. Firstly, both recombinant *B. fragilis* SPT (BfSPT, encoded by gene BF2461) and *P. gingivalis* (PgSPT, gene PG1780) were expressed in *E. coli*, purified and studied with protein UV-vis spectrometry, enzyme kinetics, inhibition assays, mass spectrometry and protein crystallization screening. 3-KDS products were detected derived from a range of straight-chain CoA substrates (C14-C18) and amino acids (Gly, L-Ala and L-Ser) produced by BfSPT and PgSPT. Mutagenesis of a conserved loop (PAVAP) in SPT homologues was found to be associated with the catalytic efficiency of PgSPT. Also the presence of a Val353 residue in BfSPT was shown to be essential to allow the enzyme to interact with the C16-CoA substrate. Moreover, data suggested that the position (N- or C- terminus) of the 6His-affinity tag used to purify SPT influenced substrate inhibition by C16-CoA. A hypothetical 3D structural model of the PgSPT PLP:L-Ser external aldimine complex was built in order to explore the active site and residues involved in substrate binding and catalysis. In collaboration with Prof. Mary-Ellen Davey (Florida), the role on SL biosynthesis in *P. gingivalis* was also explored and found that SLs impact on the way this pathogen interacts with human cells.

Secondly, a branched acid transaminase *P. gingivalis* IlvE (PgIlvE, gene PG1290) was expressed, purified and studied using UV-vis spectrometry to investigate substrate binding and enzyme activity. A multi-enzyme coupled assay for PgIlvE was developed in both the ‘forward’ and ‘reverse’ direction, studied with inhibitors such as L- and D- cycloserine (LCS/DCS), as well as x-ray crystallography. In collaboration with Dr. Jon Marles-Wright (University of Newcastle) the crystal structures of four different forms of PgIlvE; the PLP-bound, internal aldimine form, LCS ring-opened ring-closed form and the PMP form, were obtained. Two residues (F56 and Y188) were identified which played a role in substrate binding and activity.

In the final chapter, recombinant KDSR from the yeast *Saccharomyces cerevisiae* (ScKDSR) was isolated from *E. coli*. Kinetic parameters for a soluble, truncated form of the enzyme were determined using the substrates KDS and NADPH. The product C18 DHS derived from C18 KDS was detected with MALDI-ToF-MS. Recent studies of human KDSR revealed that patients with point mutations in this enzyme suffered from skin disorders (erythrokeratoderma). To investigate the impact of these mutations, a series of ScKDSR mutant mimics (G176S, Y180F and G263E) were prepared. To date there has been no crystal structure of a KDSR determined but

it is a member of the short-chain dehydrogenases/reductases (SDR) superfamily. A homology model of the 3D structure of ScKDSR with three possible NADPH docking positions were constructed, and residues involved in substrate binding and catalysis were suggested.

The results in this thesis shed light on the key enzymes involved in the core biosynthetic pathway of microbial SLs and lay down a blueprint for future studies.

Acknowledgements

Firstly, I would like to thank my supervisor Prof. Dominic Compopiano for giving me the opportunity to work in his group. He has been an outstanding supervisor for the patient support, instructive advice and useful suggestions on my project even when the novel project is not working for at least six months at the beginning of PhD. Without his consistent and illuminating instruction and persevering patience, this thesis could not have reached its present form.

Secondly, I would like to send my substantial gratitude to Dr. Mary Ellen Davey (University of Florida) who provides the *Porphyromonas gingivalis* genes for my project. I am grateful to Dr. Julia Richardson (School of Biological Sciences) and Dr. Jon Marles-Wright (Newcastle University) for the help in crystal trails and showing me the exciting area of research in the crystallography. I would also like to thank Dr. Logan Mackay and Dr. Faye Cruickshank for the help and suggestions on MS analysis in SIRCAMS. My thanks also go to Dr. Amanda Jarvis and Dr. Richard Brewster for all the help and the support for me and my summer student in the organic synthesis.

Thirdly, I would like to give my thanks to all the members that have been in the Lab 229 during my PhD and without them, I would not be able to achieve anything. So today I would say thank you for the following people in no particular order. Thank you to Dr. Pete Harrison for maintaining the lab together and helping me to get starting with my project at the beginning. Thank you to Dr. Van Kelly for MS advice especially for the KDS determination. Thank you to Dr. Joanna Simpson for the kindness to help me run and analyse most of the samples and teachings for the knowledge of MS. Thanks to Dr. Annabel Serpico for lots of joys in the lab and helping me with lots of problems in molecular biology. Thank you to Dr. Piera Marchetti for being helpful and kind all the time and supporting me when I am down. Thanks to Alexis and Silvia for being friends and colleagues at the same time to be accompanied by my PhD. Thank Alexis for all the fun, energy and joys that bring in this group and thank Silvia for good management for the lab and those amazing Italian cuisines. Thank you to Ben for showing me the hard-working attitude to the research and science and all the ‘sarcastic jokes’ in the office. Thank Catherine for the help on organic chemistry mechanisms and experimental skills in the chemistry lab. Thank you to Shona for kindness to do proof-reading of my thesis and all the language problems that I encountered. Thanks to Michael for the support and suggestions on structural modelling and analysis. I would also like to thank Zenam, Rhona and Alice for keeping

a friendly and comfortable atmosphere in the office and lab and hope them have a great time in the group for their rest of PhD journey.

Fourthly, I would like to thank my one and only project summer student, Eric, for being an amazing student all the time, and hope we would give your data published and you could successfully be a physical doctor in future. And I am looking forward to keeping contact in future.

Fifthly, I want to thank all my friends that I encountered and accompanied during my PhD study. Thanks to Jingyin and Xinchi in the same programme for being supportive and positive to me, and all the delicious meals and time that we had when we wanted to release our stress. Thanks to all the gaming pals and all the happy chats we had online that made me laugh for these years. Especially for Senyu for always being a motivational and supportive friend through my undergraduates to postgraduates, and I hope he would successfully finish his PhD in next year and our friendship could last forever. Also thank you to Yanan for enduring all my complaints from my projects and life and I am excepting to hang out together one day to have all the amazing foods that you mentioned in your hometown. Thanks to Eva for the house hosting and party with Silvia and those delicious food. Many thanks to Innis and Pinar for being excellent friends for the whole time, and all of your leads to enjoyable time and remarkable experience in Edinburgh.

Last but not least, I would give my sincere gratitude to my mum and dad who always believe me for the financial and mental support. Without their spurring, I would not be able to presume my dreams and take risks to do everything I loved. I would also like to thank for Edinburgh Global Research Scholarship from University of Edinburgh, who give me a chance to study in this amazing place.

Declaration

I, PEIJUN TANG, declare that this thesis has been completed by myself. Except where otherwise acknowledged and stated by reference, it is a record of my work, and that is has not been accepted in partial or complete fulfilment of a degree or professional qualification.

PEIJUN TANG

University of Edinburgh

2020

Abbreviations

1-methoxy-PMS	1-Methoxy phenazine methosulfate
2xYT	2xYeast extract tryptone
4MBH	4-methylbenzyl hydrazine
ACN	Acetonitrile
α-KG	α-ketoglutaric acid
α-KIC	α-ketoisocaproic acid
ALAS	5-Aminolevulinate synthase
AT	Aminotransferase
ATP	Adenosine triphosphate
B.fragilis	*Bacteroides fragilis*
BCAA	Branched-chain amino acids
BCAT	Branched-chain amino acids transferase
BfSPT	*Bacteroides fragilis* SPT
BHA	O-benzylhydroxylamine
Bis-Tris	2,2-Bis(hydroxymethyl)-2,2′,2″-nitrilotriethanol
C16-CoA	Palmitoyl-CoA
CASTp	Computed atlas of surface topography of protein
Cer	Ceramides
Cer1P	Ceramide-1-phosphate
CERK	Ceramide kinase
CGT	Ceramide galactosyltransferase
CHAPS	3-((3-Cholamidopropyl) dimethylammonio)-1-propanesulfonate
CHCA	Apha-cyano-4-hydroxycinnamic acid
CHES	n-Cyclohexyl-2-aminoethanesulforic acid
CO_2	Carbon dioxide
CoA, SCoA, CoASH	Coenzyme A
CRDs	Cysteine-rich domains
CS	Cycloserine
DCS	D-cycloserine
DDM	n-Dodecyl-β-D-maltoside
DES	Dihydroceramide desaturase
DHCer	Dihydroceramide
DHCerS	Dihydroceramide synthase
DHS	Dihydroxysphingosine
DHSL	Dihydro-sphingolipids
DM	n-Decyl-β-D-Maltopyranoside
DSS	Dextran sulfate sodium
DTT	Dithiothreitol
E.coli	Escherichia coli
ERG240	4-methyl-5-oxohexanoic acid
ESI	Electrospray ionization
FA	Formic acid
FT-ICR	Fourier-transform ion cyclotron resonance

FVT-1	Follicular lymphoma variant translocation-1
GalCer	Galactosylceramide
GC	Glucosylceramide
GCS	Glucosylceramide synthase
GDH	Glutamate dehydrogenase
GIPCs	Glycosyl inositolphosphoceramides
GlcCer	Glucosylceramide
GSL	Glycosphingolipid
GSLs	Glycosphingolipids
HEPES	(4-(2-hydroxyethyl)-1-piperazineethanesulfonic acid)
HEX	Hexadecenal
HSAN1	Hereditary sensory and autonomic neuropathy type 1
HSN1	Hereditary sensory neuropathy type 1
IC50	Half maximal inhibitory concentration
iNKT	Natural killer T
INT	Iodonitrotetrazolium
IPTG	Isopropyl β-D-1-thiogalactopyranoside
KDH	α-Ketoglutarate dehydrogenase
3-KDS	3-ketodihydrosphingosine
KDSR	3-ketodihydrosphingosine reductase
K_i	Inhibition constant
k_{inact}	The rate constant of enzyme inactivation
LB	Lysogeny broth
LC	Liquid chromatography
LCB	Long chain base
LCS	L-cycloserine
L-Glu	L-glutamic acid
LPS	Lipopolysaccharide
L-Ser	L-serine
L-Val	L-valine
MALDI-TOF-MS	Matrix-assisted laser desorption/ionization-time-of-flight-mass spectroscopy
MES	2-(N-Morpholino)ethanesulfonic acid
MS	Mass spectrometry
MS/MS	Tandom mass spectrometry
MTT	Thiazolyl blue tetrazolium bromide
NaCl	Sodium chloride
NADH	Nicotinamide adenine dinucleotide
NADPH	Nicotinamide adenine dinucleotide phosphate
NF-κB	Nuclear factor kappa-light-chain-enhancer of activated B cells
NKT	Natural killer T
NP-40	Nonyl phenoxypolyethoxylethanol-40
OG	Octyl-beta-glucopyranoside
OGH	Oxoglutarate dehydrogenase
PCR	Polymerase chain reaction

PEA	Phosphoethanolamine
PgSPT	*Porphyromonas gingivalis W83* SPT
PHCer	Phytoceramide
PHS	Phytosphingosine
PLP	Pyridoxal 5'-phophate
PMP	Pyridoxamine 5'-phosphate
PMS	Phenazine methosulfate
PSL	Phyto-sphingolipids
S-1-P	Sphingosine-1-phosphate
S1PL	Sphingosine-1-phosphate lyase
SDR	Short chain dehydrogenases/reductases
SDS	Sodium dodecyl sulfate
SEC	Size exclusion chromatography
SK	Sphingosine kinases
SLs	Sphingolipids
SM	Sphingomyelin
SMA	Spinal muscular atrophy
SMS	Sphingomyelin synthase
SOC	Super optimal broth
SpSPT	*Sphingomonas paucimobilis* SPT
SPT	Serine palmitoyltransferase
SwSPT	*Sphingomonas wittichii RW1* SPT
TDM	n-Tetradecyl-β-D-maltoside
TEV	Tobacco Etch Virus
TFA	Trifluoroacetic acid
TLR4	Toll-like receptor 4
Tris	Tris(hydroxymethyl)aminomethane
UV-vis	Ultraviolet-visible
XTT	2, 3-Bis-(2-methoxy-4-nitro-5-sulfopenyl)-2H-tetrazolium-5-carboxanile

Table of Contents

Chapter 1 Introduction

1.1 Sphingolipids

Sphingolipids (SLs) were first characterized by Johann Ludwig Wilhelm Thudichum near the end of the 19th century. In 1874, Thudichum, a German physician and biochemist, isolated numerous substances of the brain by fractional crystallization of ethanolic extracts including sphingomyelin (SM), sulphatides and cerebrosides – these were all reported in his treatise 'The Chemistry of the Brain' [1, 2]. In the 20th century, the biochemistry giant Prof. Herbert E. Carter identified the chemical structure and synthesis of sphingosine, based on his interest in the amino acid threonine [3-6]. Further study led Carter to identify more structures of the SLs family and the discovery of the branched-chain sphingolipid from the parasite *Crithidia fasciculata* and the mammalian kidney [7-13]. The common structural feature of SLs is the sphingosine (*2S,3R,4E*-2-aminooctadec-4-ene) backbone, also known as the long-chain base (LCB) or sphingoid base in mammals, represented in red in Figure 1.1.1 [14]. The long-chain fatty acid is linked to the sphingoid base through an amide bond, which gives rise to the ceramide (Cer) family of lipids – the fundamental molecules in SL biosynthesis [15]. Further modification on the C1 head group with phosphate, sugar, and phosphocholine groups leads to different constructs including SMs, glucosylceramides (GCs), glycosphingolipids (GSLs), and over 1000 structurally specific SLs [14, 16].

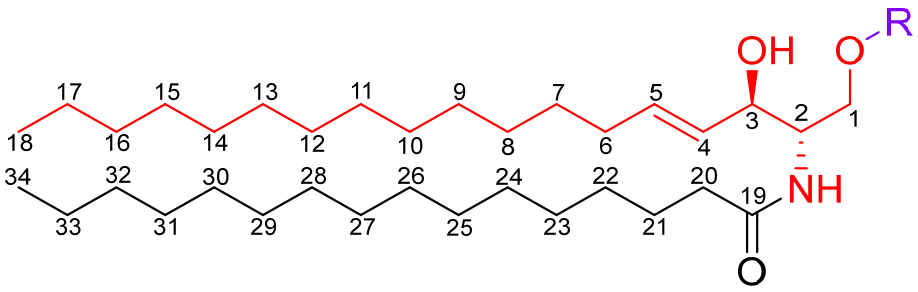

Figure.1.1.1 The basic sphingolipid/ceramide structure. The sphingoid base is coloured red, the acyl chain attached to the amide part is black, and the variable head group is purple, R=H, C16 ceramide.

Even with research spanning over 100 years, the mysterious role of the SL family is still being investigated. SLs were discovered to be essential molecules in cell compartments involved in the regulation of cell growth, differentiation senescence, and apoptosis [17, 18]. Cers (also named as N-acylsphingosines) are acylated on the amino group of sphingoid bases with C14 to C36 fatty acids [19]. As central intermediates of the SLs family, the bioactive Cers control a plethora of cellular

processes such as signal transduction and cell death [20-22]. Ceramides are thought to diffuse through the membrane bilayer and interact directly with specific lipid-binding domains known as cysteine-rich domains (CRDs), also known as cathepsin D, in order to increase cellular response and stress signaling [23-25]. In medicinal applications, C2-Cer has an anti-proliferative effect on lung cancer cells and other age-related diseases [26, 27].

SMs are derivatives from the C16 Cer through replacement of a phosphocholine group on the C1 head group. In the mammalian system, SMs mostly exist in the Golgi apparatus and have a close relationship with Cers in the propagation of inflammatory signaling [28, 29]. In most conditions, over-production of C16 Cer is considered to be responsible for programmed cell death and pharmacological inhibition of SM hydrolysis. It reduces the toll-like receptor 4 (TLR4) association with lipid rafts in order to lessen the progress of steatohepatitis and hepatic reactive oxygen species generation [30-33]. According to recent pathophysiologic studies, the breakdown of SMs would impact the T-cell activation and function on tissue homing, cell differentiation and effector function [34]. On the other hand, hindering SM synthesis would decrease the lipopolysaccharide (LPS) response and nuclear factor kappa-light-chain-enhancer of activated B cells (NF-κB) by macrophages, which acts against Inflammatory Bowel Disease – dextran sulfate sodium (DSS)-induced colitis and artery disease [35-37].

GSLs are a further metabolic lipid family derived from Cers found in the plasma membranes of organisms from bacteria to humans. The glycans of GSLs range with up to more than 20 sugar residues within 11 different monosaccharide types (Figure 1.1.3) [38]. Essentially, the expression and organization of their specific enzymes controls the elongation of glycans in GSLs. The different GSL glycans have been shown to interact with different receptors located in the plasma membranes to modulate their activity [39, 40]. The initial characterized GSLs are galactosylceramides (GalCer), which are the simplest, and one of the most abundant monosaccharides in the mammalian brain. The dysfunction of GalCer leads to an unusual and dreadful disorder of the nervous system – Krabbe's disease in humans [41]. The sugar residue epimer of GalCer and glucosylceramide (GlcCer) is also associated with the cause of Gaucher's disease, an inherited disorder that disturbs the human organ and tissue function [40, 42]. There is also a growing link between mammals and microbes. Research has shown that GSLs from the bacteria *Sphingomonas wittichii* could activate human and murine Natural Killer T (NKT) cells and stimulate the mammalian immune response. Those GSLs extracted from the bacteria *Sphingomonas paucimobilis* could also activate production of chemokines in various cells [43, 44].

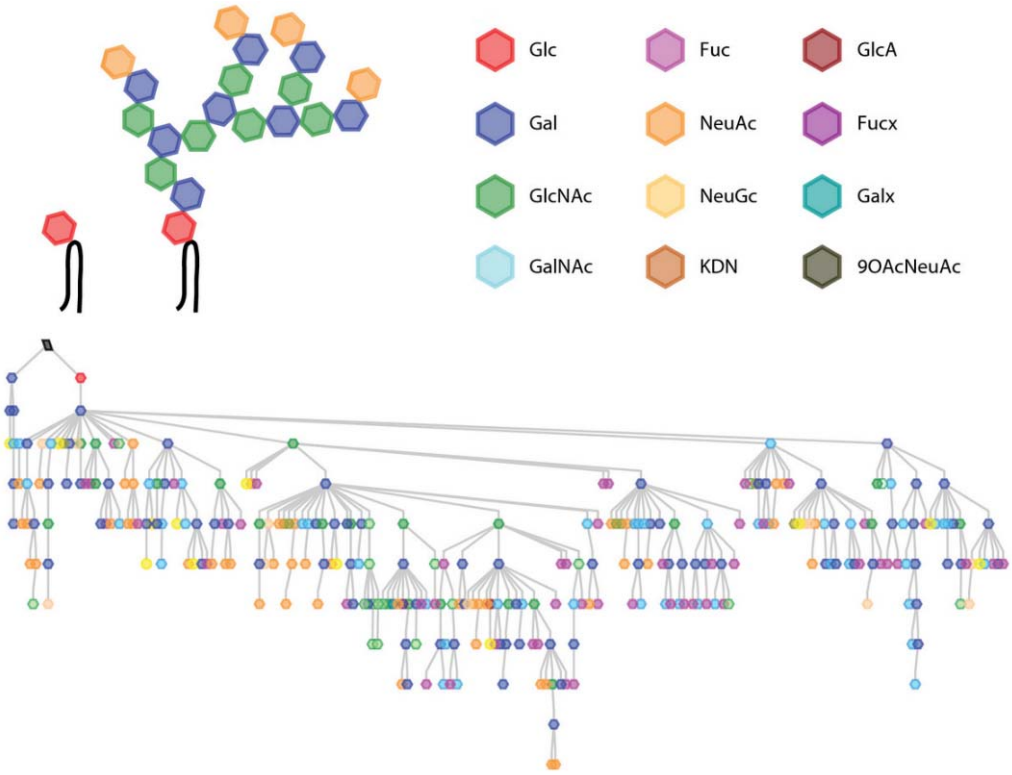

Figure 1.1.2 GSLs complexity of sugar residues involved in the structure and hierarchical tree of GSL chain elongation (taken from Angelo *et al.*'s paper [38]).

1.2 The *de novo* sphingolipid biosynthetic and catabolic pathway

The *de novo* SL biosynthetic pathway (Figure 1.2.1) provides an essential blueprint or map of the abundance, diversity, and network relationship of SLs among cell types and tissues in mammals [45]. It is interesting that SLs in this pathway cause opposite cell behavior such as growth arrest (Cer and sphingosine) or growth stimulation (sphingosine-1-phosphate, S-1-P) [46]. Recent studies have shown that the neurodegenerative disorder Huntington's disease is caused by a defective pathway [47]. This biosynthetic pathway can be split into three main sections: the biosynthesis of sphingoid bases (LCBs), Cers, and complex SLs.

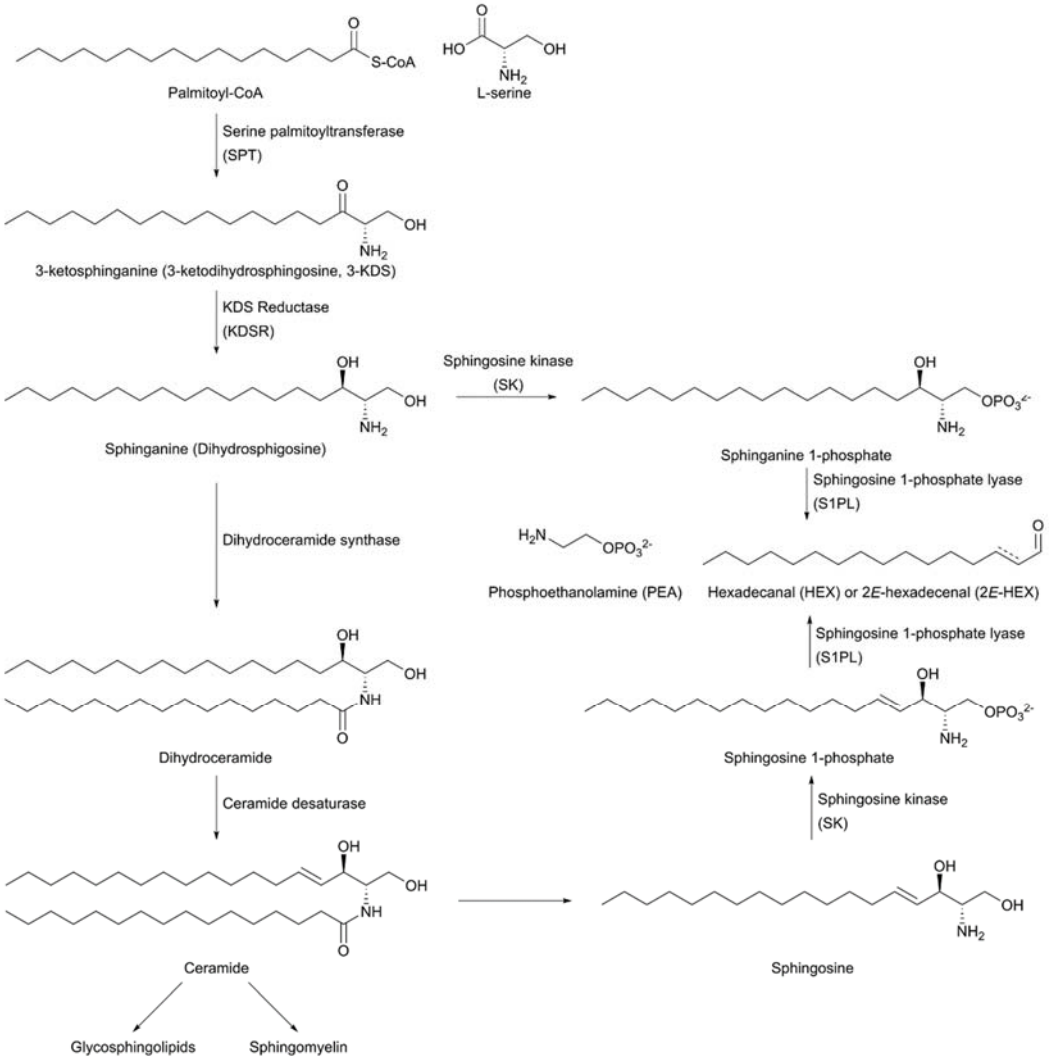

Figure 1.2.1 General overview of the *de novo* SL biosynthetic and metabolic pathway in the mammalian system (taken from Harrison *et al.*'s review paper [45]).

In the first step, the initial reaction is the decarboxylative Claisen-like condensation of an amino acid with the long-chain fatty acid acyl-CoA thioester substrates. Usually, the building blocks are L-serine (L-Ser) and palmitoyl-CoA (C16-CoA) to form the intermediate 3-ketodihydrosphingosine (3-KDS) and the reaction is catalyzed by the the pyridoxal 5'-phosphate (PLP) dependent enzyme serine palmitoyltransferase (SPT) [48]. This is followed by the nicotinamide adenine dinucleotide phosphate (NADPH) dependent, stereospecific reduction of the 3-KDS ketone into a hydroxyl group by the 3-KDS reductase (KDSR) to give DHS, which to date, has only been characterised within mammals, yeast and fungi [49].

Moving onto the biosynthesis of Cers; the direct product of KDSR, dihydrosphingosine (DHS), is rapidly converted to dihydroceramide (DHCer) by acylation with a long-chain fatty acid catalysed by a (dihydro)ceramide synthase (CerS). In mammals, six unique CerS isozymes have been identified; different CerSs display distinct functions and acyl-chain specificity e.g. both CerS5 and CerS6 prefer the C16-KDS substrate forming C16-Cers derivatives [49, 50]. This is followed by a dehydration reaction on the C4 position of the DHS backbone, catalyzed by a dihydroceramide desaturase (DES) producing an oxidised ceramide with a carbon-carbon double bond. As the enzyme reaction requires NADPH and oxygen, the cellular redox balance may cooperatively influence the DES activity. Therefore, the attention on redox-sensitive DES inhibitors has risen for the potential treatment of cancer, diabetes, reperfusion injury and other diseases [51].

The early steps of the SL and Cers pathways occur in the endoplasmic reticulum (ER), but after this the ceramide intermediate is transported from the ER to the Golgi either through vesicular transport or through a ceramide transfer protein (CERT) (Figure 1.2.2) [52]. Several enzymes, such as glucosylceramide synthase (GCS), ceramide galactosyltransferase (CGT) and SM synthase (SMS) then execute the formation of complex downstream SLs and Cers. A small amount of the acyl chain Cers that contain more than 12 carbons can be phosphorylated to ceramide-1-phosphate (Cer1P) by ceramide kinase (CERK) [53]. Those products, Cer1P, SM, and GSLs, are thought to stay in the plasma membrane and become significant contributors to the hydrophobic barrier of many cells.

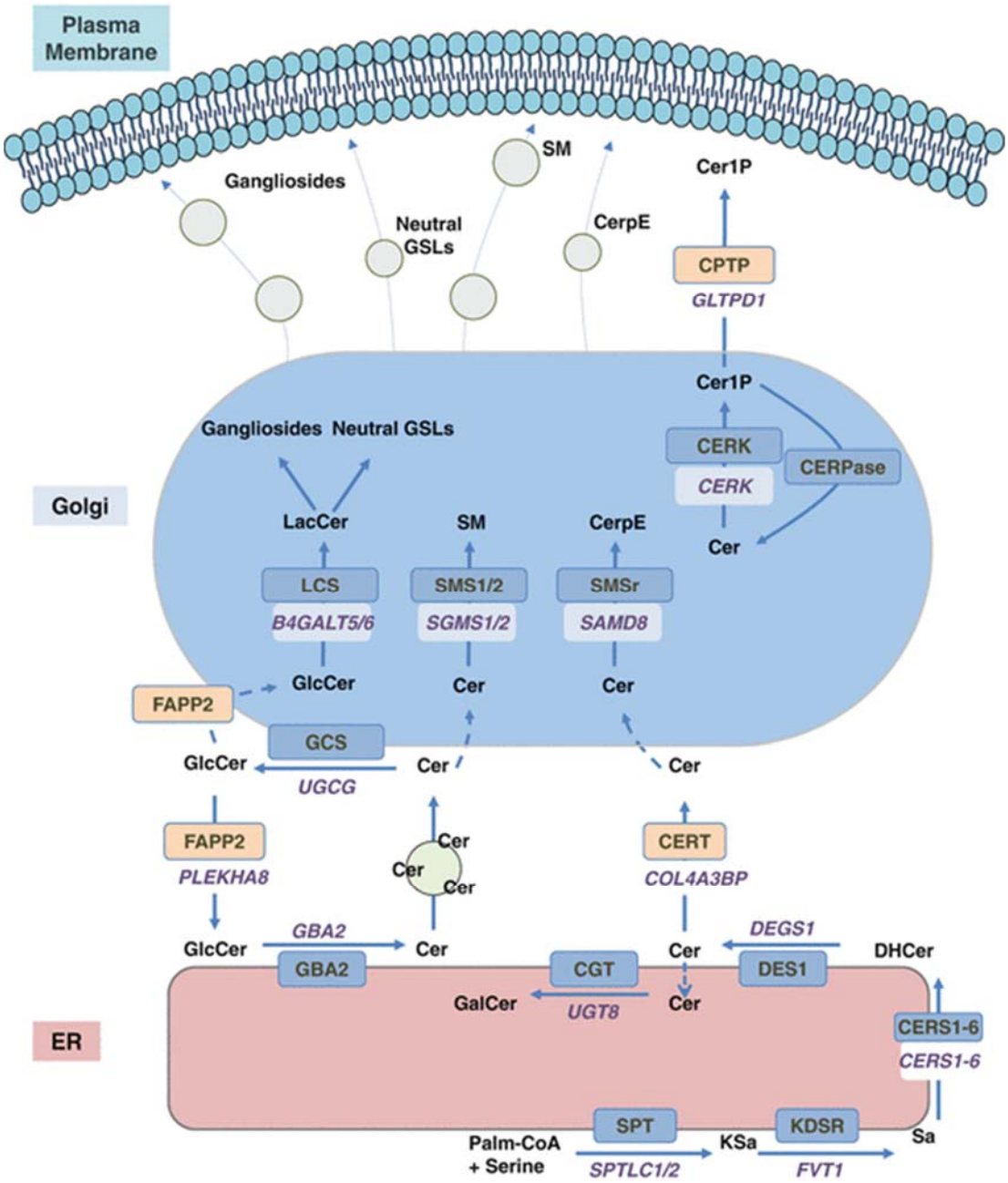

Figure 1.2.2 Subcellular compartmentalization of SLs biosynthesis. For each enzymatic reaction or transport event, the names of the corresponding protein (in boxes) and genes are indicated. (taken from Colacio *et al.*'s book [52])

Only a few SL precursors are required to produce hundreds of complex SLs. Most SLs break down into Cer, sphingosine and S-1-P. This occurs through a number of steps. Firstly, the pH-dependent ceramidases catabolize the ceramide species into the sphingosine species resulting in the lipid storage disease in humans known as Farber disease [54, 55]. Then, two membrane-associated sphingosine kinases (SKs, SKI and SKII) use adenosine triphosphate (ATP) to phosphorylate the sphingosine species to give S-1-P, which prevent inflammation [56]. In the last step of SL metabolism, the S-1-P is broken down irreversibly by another PLP-dependent

sphingosine-1-phosphate lyase (S1PL) exclusively in the ER to generate phosphoethanolamine (PEA) and hexadecenal (HEX) or 2E-hexadecenal (2E-HEX) [57, 58]. Research suggests that S1PL is critical for normal lipid homeostasis and that the regulation of SPL is related to atopic dermatitis and Alzheimer's disease. Therefore, S1PL seems to be a target of physiological progress and pharmacological modulation of human disease [18, 57, 59]. It is worth noting that the SL biosynthetic pathway is effectively book-ended by two PLP-dependent enzymes; SPT at the beginning and S1PL at the end.

The yeast, *Saccharomyces cerevisiae*, displays numerous conserved genes and SL metabolites when compared to mammals and plants. Therefore, it has proved to be the most straightforward and useful eukaryotic model system for SL research due to the excellent tools and resources which have generated detailed yeast genomics, proteomics and metabolomics databases [60]. In fact many of the mammalian genes, such as the six mammalian CerSs, were discovered based on their homology to their yeast counterparts (Lag1p and Lac1p) [61, 62]. It is highly likely that the discoveries of SL biosynthesis, regulation, and function in yeast may also apply to mammals, including humans.

As in the mammalian SL pathway, the yeast SL biosynthesis starts with the same enzymes (SPT and KDSR) in the ER to form LCBs of different carbon chain length. After LCB synthesis, the pathway (Figure 1.2.3) divides into two different arms – the dihydro-(non-hydroxylated) branch and the phyto-(hydroxylated) branch, producing dihydrosphingolipids (DHSLs) or phytosphingolipids (PSLs) [63]. The essential enzyme balancing the SL levels between the two branches is the C4-hydroxylase (Sur2) [64]. Sur2 hydroxylates DHS at the C4 position to form 4-OH dihydrosphingosine, which is also known as phytosphingosine (PHS) [64]. In the individual pathway, the critical intermediate DHS and PHS are transformed into more complex SLs using the same enzymes, such as CerS, SK, GCS and other enzymes. Over 90% of SLs in the yeast system are originally from phytoceramide (PHCer) and those PSLs can regulate the diffusion barrier in the ER, as well as the aging and stress response in the cell process [63, 65, 66]. Interestingly in recent research, the PHSs are metabolized to odd-numbered FAs rather than even-numbered FAs, suggesting that the clearance and deregulation of those metabolites may be essential for the maintenance of cellular PSL levels in the cells [67].

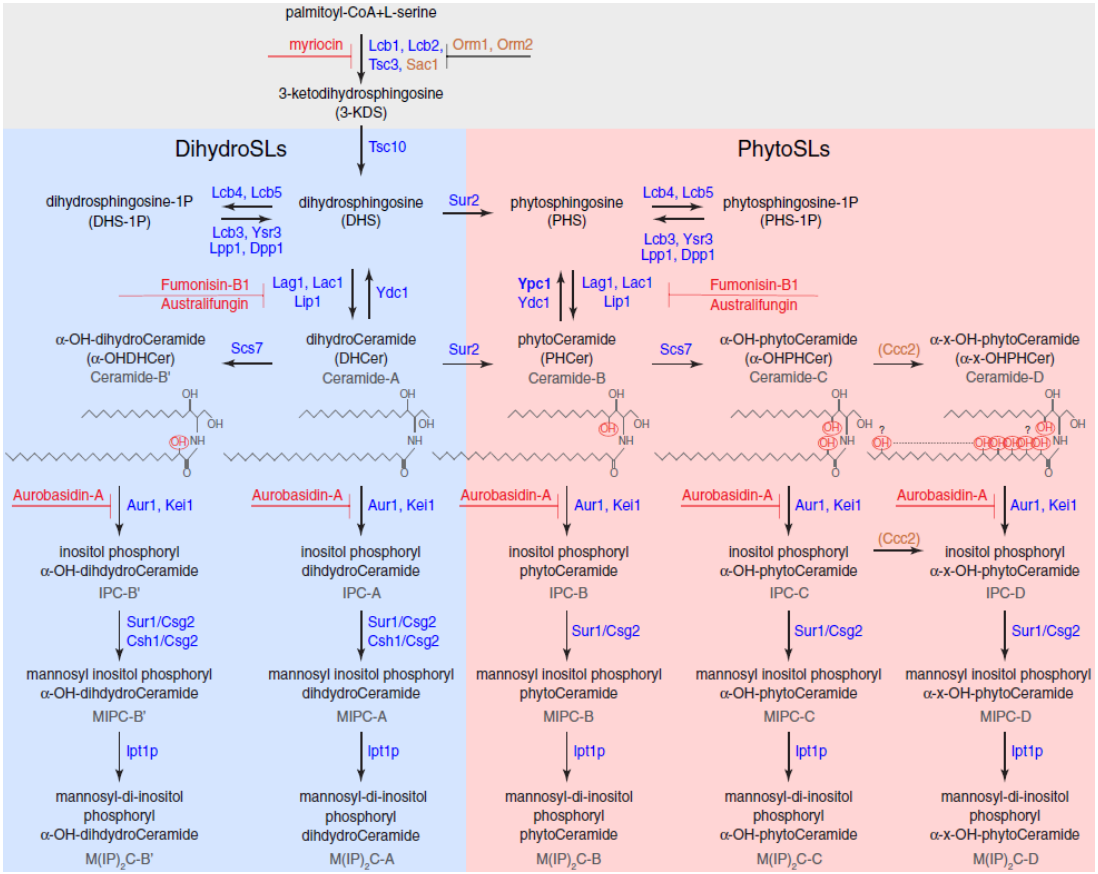

Figure 1.2.3 The SL pathway in the yeast system. The lipids are in black; the enzymes are in blue, regulators in brown, and inhibitors in red. The dihydro branch pathway is in the blue background, and the phyto-branch pathway is in the red background (taken from Megyeri *et al.*'s paper [63]).

The chemical inventory of SLs is very diverse, nearly 10% of lipids exist in higher plants and novel plant SLs are still being investigated [68]. The SL classes in plant tissues appear to differ in a species and a tissue-dependent manner, in which the ruling classes are Cers, GlcCers, glycosyl inositolphosphoceramides (GIPCs) and free LCBs [69]. Compared to the mammalian SLs, the SMs or phosphorylceramides have not been discovered in plants. However, PSLs and IPCs, which are dominant in the yeast system do exist [70, 71]. The unique Δ^8-unsaturated LCBs are only broadly found in plants, not in the animals nor the yeast *S. cerevisiae*. This lipid species may impact the subcellular location of the other SLs and relate to the freezing tolerance of plants [72, 73].

The SL biosynthetic pathway in the plant kingdom begins with the same LCB synthetic pathway as illustrated in mammals. The LCB modification then happens either through C4 hydroxylation or C4/C8 desaturation on an 18 carbon atom chain moiety to generate essential SL intermediates [71]. The enzyme Δ^4-desaturase found in pollen alters the specific C16 acyl chain SLs in order to provide structural information for the relative ceramide synthase. The Δ^8-desaturase in plants catalyses

formation of both *cis* and *trans* isomers of LCBs in a distinct ratio and contributes to the formation of GlcCers [74]. In the next step, three different ceramide synthases (LOH1-3), which require fatty acid chains 16 – 26 carbons long forming the Cers that are associated with sterols in the membrane microdomains. LOH2 preferably acts on the C16 dihydroxy LCB that would impair growth and result in the dwarf plant, whereas LOH1 and LOH3 are more likely to react with the trihydroxy 20~26 LCBs that increase the cell division to produce larger plants in *Arabidosis* [75-77]. Meanwhile, it has been proven that Cer and hydroxyCer levels play a vital role in the biotic or abiotic stress response of plants in different environmental changes [78]. In the end, complicated SLs such as GlcCer and GIPCs are synthesized by GCS, at least three functional IPC synthases and several sugar transferases [79]. Plants defective in these enzymes would become dis-functional in cell proliferation and differentiation and would not be able to grow callus tissue or transmit pollen [80, 81]. Additionally, phosphorylated SLs, such as phytosphingosine-1-phosphate, have been suggested to associate with cold tolerance and stomata sensitivity in the plant [82, 83].

In contrast to studies on mammals, plants, yeast and fungi, there are surprisingly relatively few detailed studies on SLs in bacteria, however this area is gaining in interest. The chemical structure of sphingoid bases in SLs is different for bacteria and eukaryotes. As mentioned earlier, it is mostly even-chained, linear sphingoid backbones that exist in mammals. However, the bacteria usually contain odd-chained, methylated or hydroxylated SLs. There are over 100 bacterial phyla that have been proposed to produce SLs, including the majority of the Bacteroidetes phylum, Chlorobi phylum, along with Alpha-Proteobacteria such as *Novosphingobium* and *Sphingomonas* and Delta-Proteobacteria [84, 85]. Interestingly, the occurrence of SLs in bacteria is mainly limited to anaerobes. The glycosphingolipids (GSLs) were first isolated and characterized from the Gram-negative bacterium *Sphingomonas paucimobilis* in 1991, bringing attention to SLs in bacterial systems. However, Bacteroidetes, which are dominant in the mammalian gut, are the most commonly known to produce SLs in recent research [86]. Within the Bacteroidetes phylum, the three main genera containing SLs are the Gram-negative anaerobic *Bacteroides*, *Porphyromonas,* and *Prevotella*. The SLs in the *Bacteroides* species occupy approximately 40 – 70% of the total lipids and share a striking taxonomic feature [87]. Additionally, there are also noteable changes in the head groups of SLs. For instance, the incorporation of phosphorylethanolamine groups instead of human sphingomyelins, the phosphorylglycerol glycans instead of the phosphoinositol glycans and sulfonyl group instead of the hydroxyl group (Figure 1.2.4) [45, 85, 88, 89].

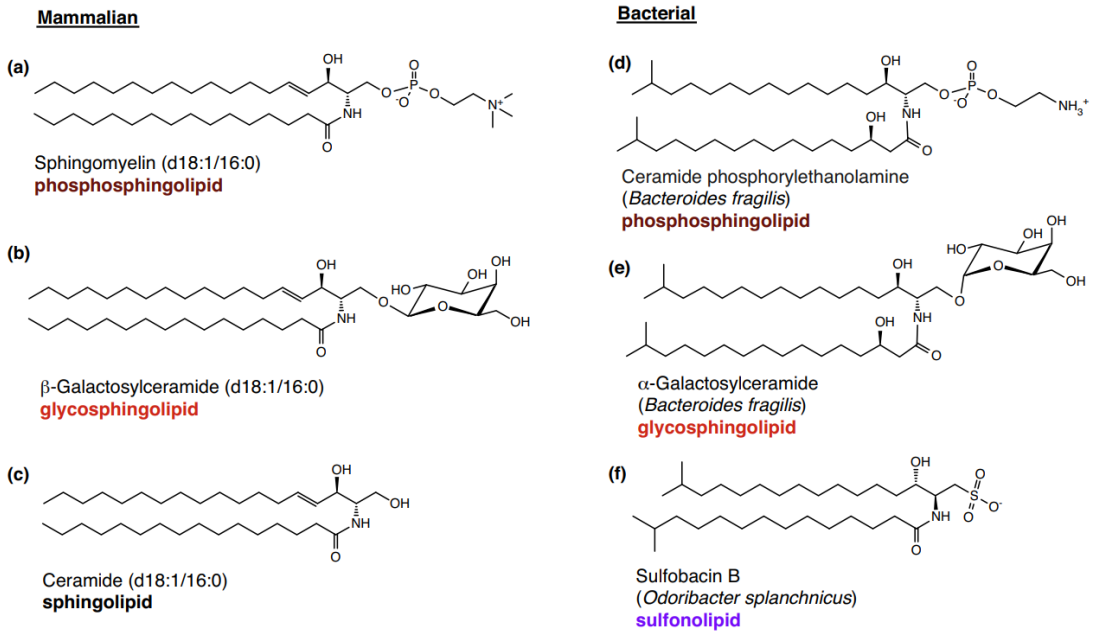

Figure 1.2.4 Structural comparisons of select mammalian and bacterial sphingolipids. (inspired by Heaver *et al.*'s paper [85]).

There is growing evidence to suggest that SLs from the human microbiome (*Bacteroides*, *Porphyromonas*, *etc.*) regulate a delicate balance between the host and the microbes in order to prevent virulence of a pathogen or maintain the bacterium if it is defined as a symbiotic species with beneficial properties. It has been suggested that the human body hosts >10-100 trillion symbiotic microbes, which is ten times as many as actual human cells, therefore the "power" of these microbes should not be underestimated [90]. Evidence is growing that dysbiosis in the microbiome is related to numerous diseases, such as type 1 and 2 diabetes, allergies, asthma, autism, cancer, and inflammatory bowel disease [91]. Furthermore, the relationship between the host and microbial SLs explains the signs and symptoms of the immune system. In bacterial systems, GSLs, often involved in signaling receptors, and Cers frequently support the lipid rafts resulting in the phagocytosis and eventually lysis of bacteria [92, 93]. To be specific, the exceptional *Bacteroides fragilis* (*B.fragilis*) in the human gut and α-GalCer are capable of modifying the homeostasis of natural killer T (iNKT) cells by supporting the endogenous lipid antigen milieu, especially in the mouse and human cells [94, 95].

Moreover, the deletion of SL biosynthesis in *Bacteroides* has recently been shown to lead to intestinal inflammation and damage to the host immunity [96]. This is in contrast to *Porphyromonas gingivalis*, which is dependent on SL production for its virulence to survive in the human mouth and also causes gingival/gum disease [97]. It appears that bacteria produce SLs to improve their ability to survive environmental stress/attack. However, the host can indirectly absorb a small amount of SLs from

these microbes to maintain health. Overall SLs, either from microbes or the host itself, have the ability to trigger biological behaviours and responses that may initiate damage, advance the pathological process, or inhibit the damage from each other to prevent disease [98]. The exact molecular details of this host/microbe balancing act are currently unclear but it certainly appears to rely on a complex series of interactions.

Unfortunately, lots of questions still remain about the biological and chemical roles of SLs in the bacterial system due to many of the genes responsible for SL biosynthesis still being unidentified [87, 99]. Luckily, based on the conserved gene sequences from eukaryotes, several bacterial SPTs have been biochemically and structurally characterized in the genera of *Sphingomonas*, *Bacteroides*, *Porphyromonas* and so on. It is assumed that the SPT-catalysed, decarboxylative Claisen-like condensation is still involved in the initial step of bacterial SL biosynthesis. Also, the terminal enzyme, S1PL, in the sphingolipid metabolic pathway has been identified in several bacterial species, such as *Burkholderia pseudomallei*, *Symbiobacterium thermophilum* and *Legionella pneumophila* [45]. This small number of S1PL-metabolising bacterial enzymes suggests other novel mechanisms may be involved. However, the other enzymes in the bacterial SL metabolic pathway are still unknown or have proved to be too difficult to isolate and characterise using current research methods.

Interestingly, the bacterial SLs appear to have unique chemical fingerprints such as an odd-chain LCB with an *iso*-Me group. Moreover, those particular *iso*- and *anteiso*-branched SLs are generated from the species that make up part of the human microbiome, instead of the host itself. It has been showed that with the lack of straight-chained SLs in *S. cerevisiae*, the *iso*-branched SLs would not support the growth of mutant cells and was toxic to wild type yeast cells by complementation experiments [100]. The branched-chain sphingoid base, 19-methyl-C20-phytosphingosine, firstly appeared in *Crithidia fasciculate*, a species of parasitic excavates discovered by Carter and co-workers [12]. Since the presence of the *iso*-branched SLs has been confirmed for five human bacterial genera including *Bacteroides*, *Porphyromonas*, *Prevotella*, *Tannerella* and *Parabacteroides* [89, 101, 102]. *Prevotella melaninogenica* mainly forms *iso*-C19 sphingoid bases where as *Bacteroides thetaiotaomicron* predominantly produce *iso*-C17 sphingoid bases [103, 104]. As shown in Figure 1.2.4 above, *B.fragilis* SLs are composed of *iso*-branched sphingoid bases as well [94]. It has been found that there are also *iso*-branched SLs and fatty acids in the *Caenorhabditis elegans* (*C. elegans*), a free-living and transparent roundworm found in soil environments [105]. These SLs influence the postembryonic development, which limits developmental rates of the organisms but elongates the lifespan.

Supplementing the *iso*-branched SL-deficient *C. elegans* with the straight-chained SLs would also disturb the metabolism of the worm [100, 106]. These findings provide evidence that the chemical differences between these straight-chained and *iso*-branched SLs are critical for the cells in the pathological mechanism of the species.

Recently, by using labellled isotopes of carbon and nitrogen in the three *iso*-branched amino acids (L-Leu, L-Ile and L-Val) the incorporation of these precursors into *C. elegans* SLs has been monitored. Only the labeled isotope of L-Leu was converted into the relevant branched-chain acyl-CoA and finally into *iso*-C17-sphinganine and *iso*-C17-deoxysphinganine. This research shows that L-Leu may be involved in the biosynthetic route of producing branched-chain SLs in the worm [100]. Furthermore, a possible SL metabolic pathway has been suggested (Figure 1.2.5) and a branched-chain amino acid transaminase (IlvE or BCAT) may catalyse those branched-chain amino acids (BCAA) into individually branched-chain acyl-CoA substrates. After fatty acid chain elongation, one of the vital substrates of the SPT reaction, isomyristol-CoA, is generated. This leads to the hypothesis that are similar pathway is in operation in *iso*-Me branched SL-producing microbes, which is one of the targets of this thesis.

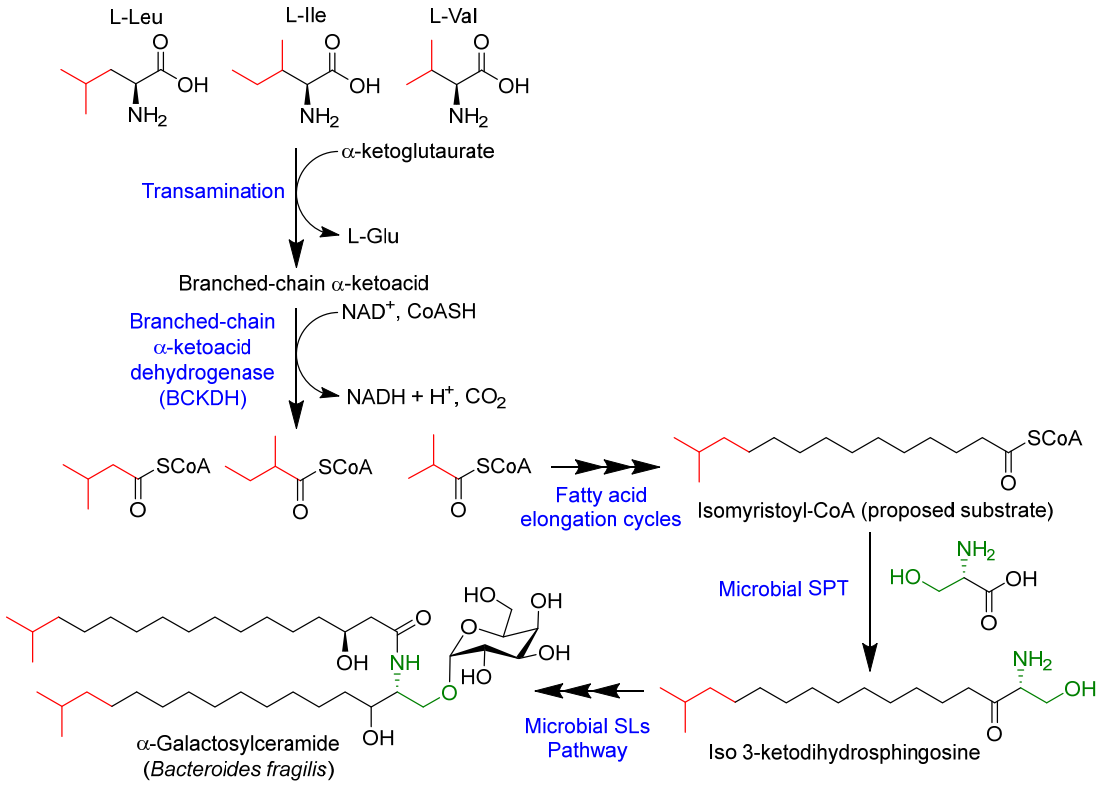

Figure 1.2.5 A proposed route to the formation of *iso*-branched SLs in the microbiome.

1.3 Pyridoxal 5'-phosphate (PLP) dependent enzymes

Pyridoxal 5'-phosphate (PLP) plays a vital role in SL biosynthesis as it is an essential cofactor in the activation of the SPT, IlvE and S1PL reactions as illustrated above. It is also one of the metabolically active forms of vitamin B_6 identified in the early 1940s by the Hungarian physician Paul Gyorgy (Figure.1.4.1) [107]. In biochemistry, PLP had been shown to catalyse more than 160 distinct enzymatic reactions that regulate primary cellular metabolism and higher organism progress. According to the Enzyme Commission, these PLP-dependent enzymes can be classified into five catalogs, which are oxidoreductases, transferases, hydrolases, lyases and isomerases [108].

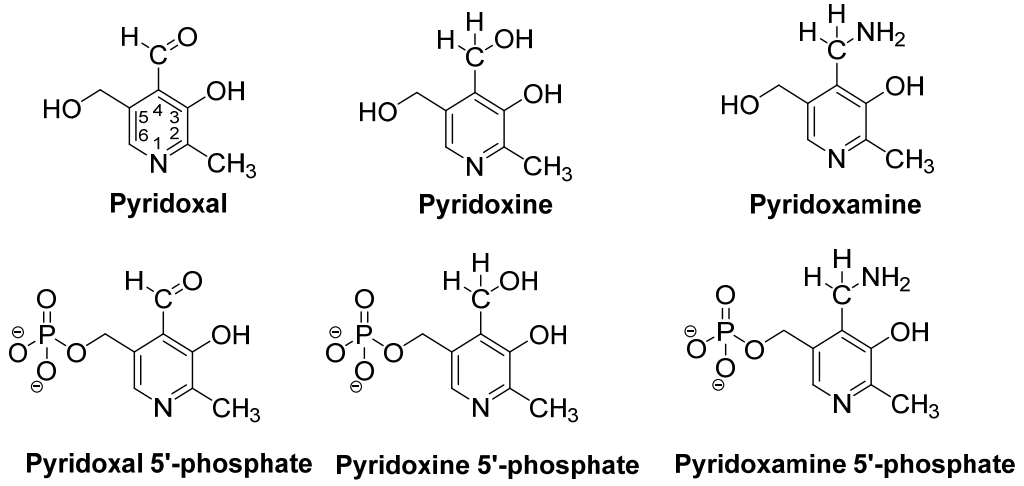

Figure.1.3.1 The natural derivatives of vitamin B6.

The mechanism of PLP-dependent enzymes has been studied over the last 60 years. The catalytic cycle starts and ends with the same PLP cofactor form (the internal aldimine), which is derived from transamination and heterolytic cleavage to maintain the carbanionic intermediates (Figure 1.3.2). The internal aldimine structure consists of an imine linkage between the amino group of a lysine residue from the enzyme and the aldehyde carbon of free PLP. Then, within the interaction of amino acids (L-Ser as an example in Figure 1.3.2) or other similar amino-containing compounds, a *geminal* diamine intermediate is formed which finally leads to the PLP:external aldimine allowing substrate binding and product release [109, 110]. Additionally, the proton in the external aldimine can transfer (or is shared) between oxygen in the pyridine ring and imine nitrogen forming two tautomeric isoforms – enolimine and ketoenamine separately. This transformation shows specific maximal absorbance values at 335 nm for enolimine and 425 nm for ketoenamine when analysed by ultraviolet-visible (UV-vis) spectroscopy [111].

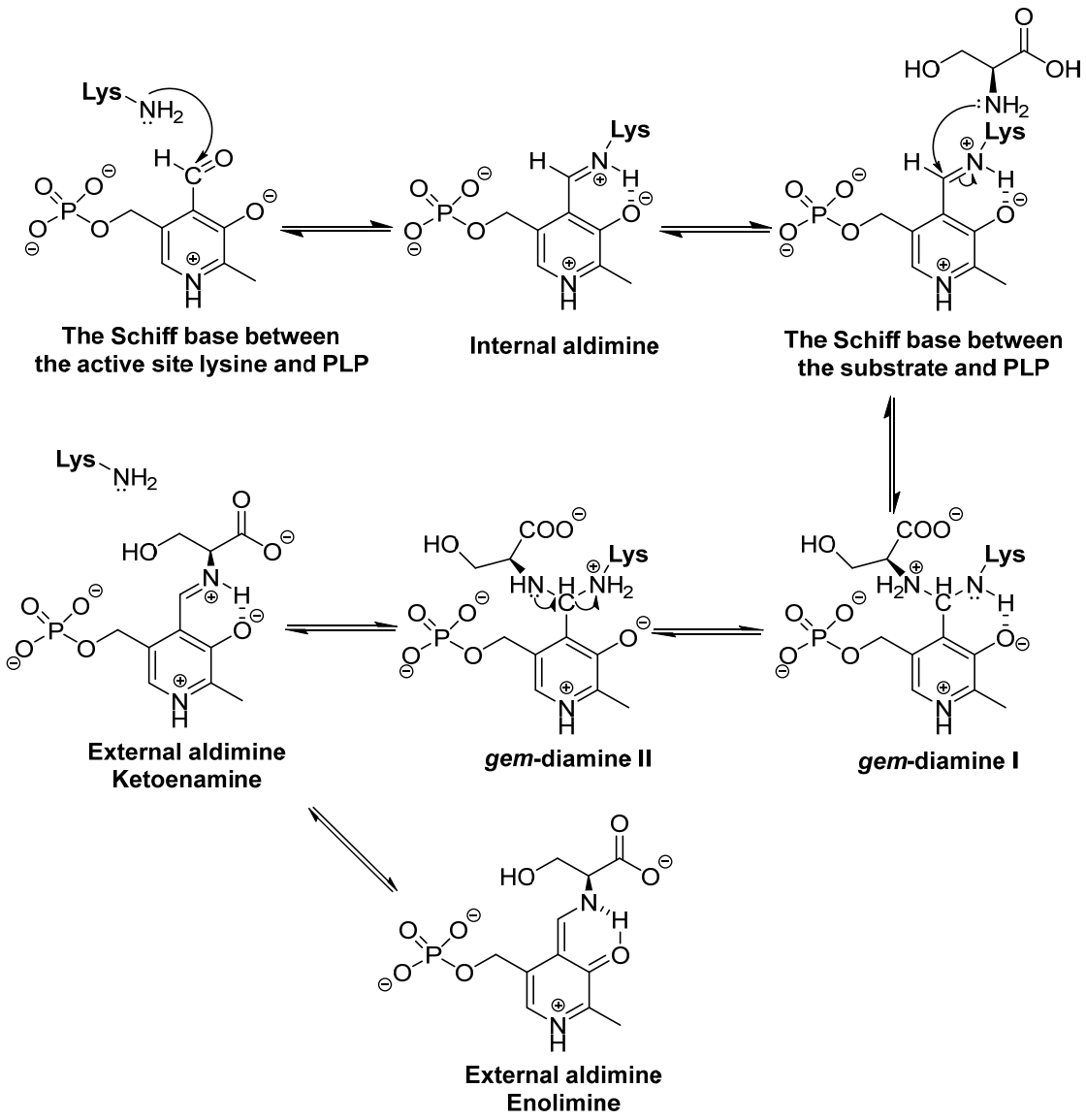

Figure 1.3.2 The reversible reaction between PLP and L-Ser from internal aldimine to external aldimine. (taken from Salvo, M. L. *et al.*'s paper [110]).

The PLP:external aldimine is the crucial intermediate for all the PLP-dependent enzymes during the catalysis of various reactions. Meanwhile, the efficiency of the PLP enzymatic reaction is predominately dependent on the heteroaromatic pyridine ring. The electrophilicity of the C4 of the external aldimine is enhanced because of the protonated pyridinium nitrogen, the resonance and hydrogen bonding of the hydroxyl group, leading to an 'electron sink.' Therefore, the protonated imine nitrogen can withdraw electrons from α-carbon of the substrate. The π-conjugation of the pyridine ring delocalizes and stabilizes the net negative charge of external aldimine. Due to the electronic delocalization energy, the stereo-chemical rearrangement of σ bonds is activated by a π system, forming the Dunathan intermediate (Figure 1.3.3). The imine nitrogen cleaves the bond in order to control

the reaction specificity. It promotes the bond-breaking process of the perpendicular bond of the pyridine ring. As a consequence, the heterolytic cleavage happens and the Cα hybridization changes generate the resonance-stabilized quinonoid intermediate [112]. However, the quinonoid intermediate has not always been observed by UV-vis spectroscopy in many the PLP-dependent reactions suggesting that they maybe extremely short lived or transient [113].

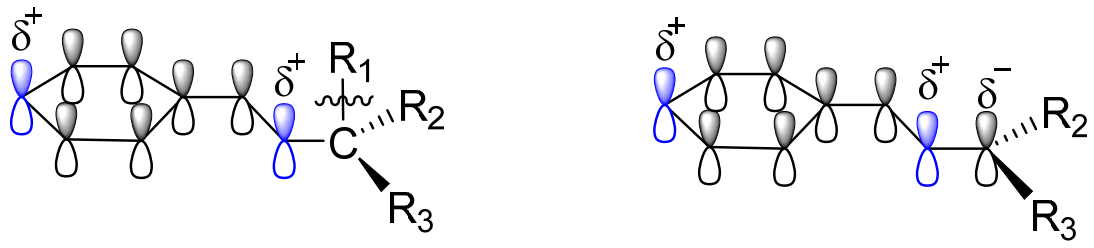

Figure 1.3.3 The schematic representation of Dunathan intermediate (**Left**) and quinonoid intermediate (**Right**). (taken from Salvo, M. L. *et al.*'s paper [110]).

PLP-dependent enzymes can catalyse a wide range of enzymatic reactions including transamination, elimination, decarboxylation, and racemization. With many x-ray structures of PLP enzymes in the Protein Data Bank (PDB) it has been able to sub-classify PLP-dependent enzyme 3D-folds and split them into five original fold-types (I to V) by Grishin *et al.* and two novel fold-types (VI and VII) (Figure 1.3.4) [114, 115]. Fold type I enzymes are the aspartate aminotransferase (AT) family. These are homodimers or homotetramers with each subunit composed of a small domain, a vast domain and a PLP molecule. The active site of fold type I enzymes lies at the interface between these subunits [116]. Fold type II enzymes are the tryptophan synthase β-family with all active site residues provided by one subunit. Most of the fold type II enzymes are dimers, tetramers or oligomers and under allosteric control during the binding [117]. Alanine racemase and the eukaryotic ornithine decarboxylase family are the fold type III enzymes. Each monomer of fold type III enzymes contains α/β barrel and β-strand domains within the PLP cofactor in a gap of those two domains. As there is only one PLP molecule bound at the interface of the enzymes, most of these enzymes are homodimers [118]. The BCAT family and D-Ala AT family are members of the fold type IV enzymes. Similar to fold type I or II enzymes, fold type IV function as homodimers or homohexamers with two domains in each subunit. However, the PLP cofactor of the fold type IV enzymes undergoes *re*-face hydrogen transfer rather than *si*-face hydrogen transfer in the chemical mechanism [119]. Fold type V enzymes are the glycogen phosphorylase family and use the phosphate group of PLP to catalyze the reaction differently to the others. The two forms of glycogen phosphorylase (α and

β) generate the tetramer or dimer individually in the quaternary level and transform between the two by phosphorylase kinase and phosphorylase phosphatase. There are three distinctive domains (C-terminal domain, N-terminal domain and glycogen-binding domain) in fold type V enzymes [120, 121].

The two novel fold types VI and VII include the lysine 5,6 aminomutase family and lysine 2,3 aminomutase family respectively [115]. The quaternary structure of fold type VI enzymes is a $\alpha_2\beta_2$ tetramer, in which the PLP and adenosylcobalamin (coenzyme B_{12}) bind a triosephosphate domain in the a subunit and the β subunit in the N-terminal and Rossmann domain [122]. Moreover, the cofactor adenosylcobalamin binds away from the active site to avoid radical generation. The lysine 2,3 aminomutase is a homotetramer containing a dimer of domain-swapped dimers. Each subunit is composed of three domains including an N-terminal domain, central globular domain and a C-terminal domain. Apart from for the fold type VI enzymes, the [4Fe-4S] cluster, S-adenosyl-L-methionine and PLP cofactors in the subunit are surrounded by a channel formed by a six β/α fold [123].

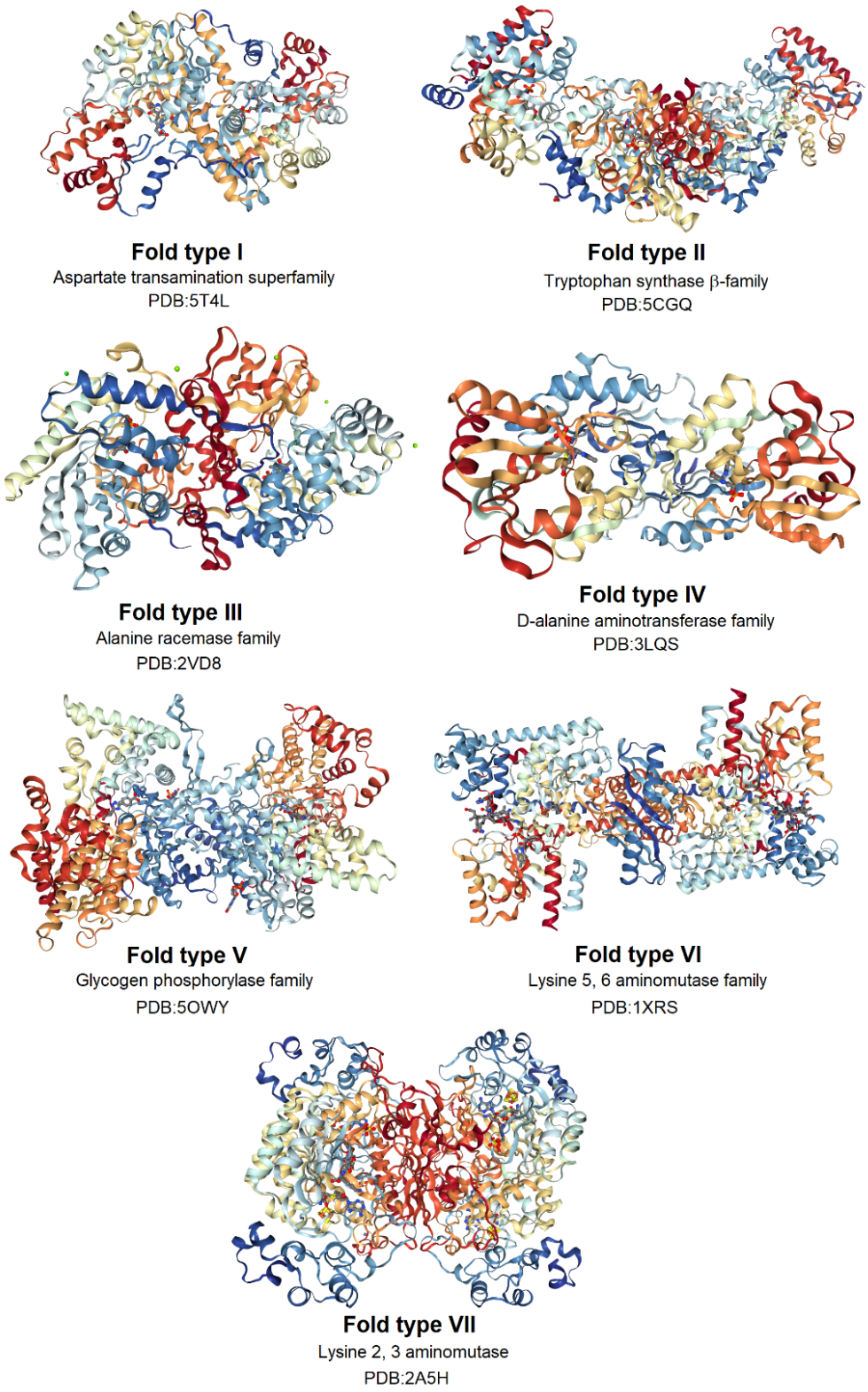

Figure 1.3.4 Structural examples of PLP-dependent enzyme fold types. (taken from PDB database website). Fold-type I example from *Bacillus subsidies* (PDB:5T4L) [124]; Fold-type II example from *Salmonella typhimurium* (PDB:5CGQ) [125]; Fold-type III example from *Bacillus anthracis* (PDB:2VD8) [126]; Fold-type IV example from *Bacillus sp. strain YM-1* (PDB:3LQS) [127]; Fold-type V example from *Oryctolagus cuniculus* (PDB:5OWY) [128]; Fold-type VI example from *Acetoanaerobium sticklandii* (PDB:1XRS) [121]; Fold-type VII example from *Clostridium subterminale* (PDB:2A5H) [129].

1.3.1 Serine palmitoyltransferase (SPT)

In all organisms studied to date SPT catalyses the first step of the *de novo* sphingolipid biosynthesis – the Claisen-like condensation of the amino acid (mainly L-Ser) with long-chain thioester (palmitoyl-CoA, C16-CoA) to form the product 3-KDS (Figure 1.3.5) [48]. SPT is commonly localised to the ER in mammals, yeast and plants; in contrast, the enzyme has been found in the cytoplasm of the bacteria [130].

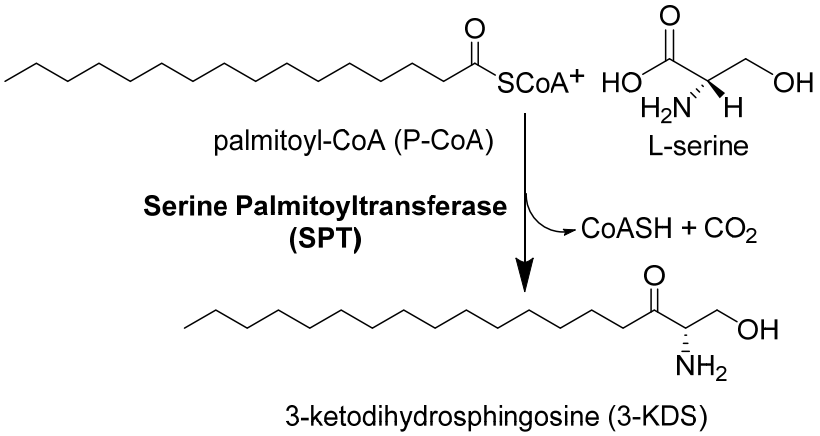

Figure 1.3.5 The decarboxylative condensation reaction of palmitoyl-CoA with L-Ser catalysed by SPT.

In the 1970s, Snell's group and Stoffel's group identified and isolated the first SPT from yeast *Hansenula ciferrii*, which has now merged into the species *Pichia anomala*. Using C14-labeled L-Ser, SPT activity was successfully monitored by determining the production of carbon dioxide (CO_2) [131, 132]. After a few decades, the yeast *S. cerevisiae* SPT was found as a complex of membrane-associated heterodimeric catalytic subunits named LCB1 and LCB2 which display 51% similarity between each other [133, 134]. Additionally, LCB1 expression is crucial to maintain the expression and stability of LCB2 and together they support an active SPT complex in mammalian cells [135]. Apart from these two catalytic subunits, several regulatory subunits, such as Tsc3p, Orm 1/2 and Sac1, are proven to affect the higher order SPT activity in different ways [136-138]. Dunn's group discovered a small 80-amino acid protein (Tsc3p) in yeast which was associated with SPT and increased the reaction activity >10 fold. Moreover, the Tsc3p-deficient mutant lost growth ability at elevated temperatures [136]. On the other hand, Orm 1 and Orm 2 found by Weissman's group and Chang's group respectively was also linked to the SPT complex and can somehow negatively regulate the activity of the SPT complex [137, 139, 140]. Recently, it was suggested that the first transmembrane domain of LCB1 is necessary for Orm

subunit binding to the SPT complex to regulate oligomerization, activity and localization [141]. In the last subunit, a phosphatidylinositol phosphatase (Sac1) copurified from the SPOTS complex (SPT, Orm 1/2, Tsc3p and Sac1) also modulates SPT activity and affects the phosphorylation in the SL pathway [138].

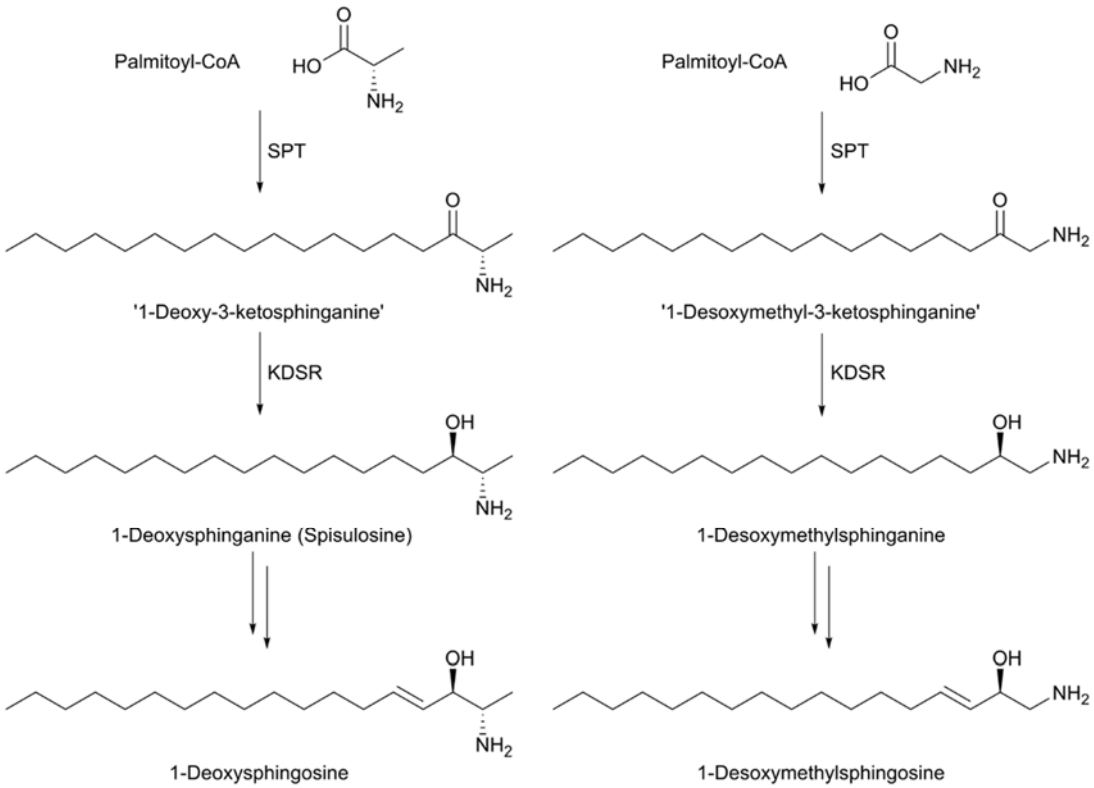

Figure 1.3.6 Schematic of deoxysphingolipids pathway from substrate L-Ala (**Left**) and glycine (**Right**) (taken from Harrison *et al.*'s paper [45]).

Once the yeast SPT genes had been discovered, Braun and Kanfer's group discovered the first mammalian SPT in microsomal fractions of rat and mouse brains and also provided kinetic analysis, substrate specificity and the pH influence of the enzyme. Based on the homologues of yeast LCB1 and LCB2, the corresponding genes, SPT1 and SPT2, were found in humans [133, 142, 143]. Meanwhile, the human SPT1/2 complex showed a strong preference for L-Ser and narrow acyl-CoA substrate scope within the C15-C17 carbon acyl chain [144]. Biochemical and gene expression analysis of different tissues (e.g. in placenta) identified another subunit – named SPT3 that showed 68% homology to SPT2 [145]. The sequencing of the human genome and the ability to complement yeast SL biosynthesis with human SPT subunits led to the discovery of new mammalian subunits. Inspired from finding Tsc3p, two equivalent proteins (ssSPTa and ssSPTb) in human cells were identified by Dunn and colleagues, which were about 71 and 76 amino acids long respectively and shared a conserved

hydrophobic central domain. The co-expression of either of the ssSPT enzymes in the presence of human SPT can increase SPT activity over 100-fold [146]. These small subunits have been found to alter the SPT substrate specificity and control the acyl-CoA preference, even for C14 or C20 carbon chain length [147, 148]. Pathology study proposed that the rare disease hereditary sensory and autonomic neuropathy type 1 (HSAN1) is related to mutations in the SPT genes, leading patients with distal sensory loss and venous leg ulcers. The direct link of the HSAN1 disease with human SPT hypothesizes that a specific class of deoxysphingolipids is generated from the substrate of glycine and L-Ala through SLs pathway (Figure 1.3.6) [149-152].

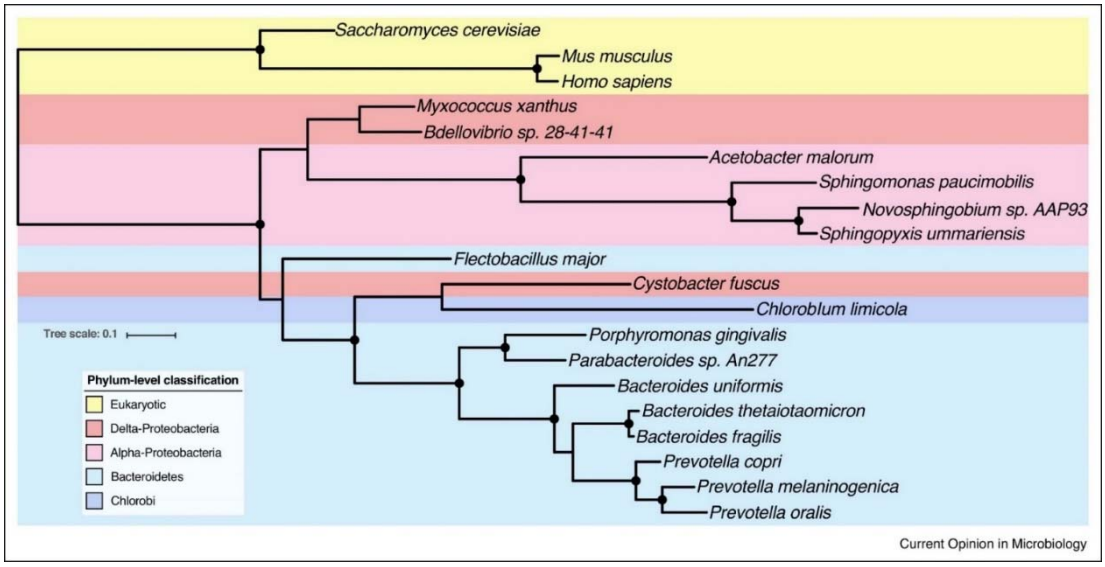

Figure 1.3.7 The phylogenetic tree of the SPT gene and homologs encoded by eukaryotes and bacteria. (taken from Heaver *et al*'s paper [85]).

The SPTs were not only encoded by higher order cells, Heaver *et al.* found out lots of bacteria were also able to generate SPTs to produce SLs and they suggested a lateral transfer event happened in nature (Figure 1.3.7) [85]. As well as the multi-subunit, membrane-bound eukaryotic SPTs, a homodimeric and soluble SPT was isolated from the Gram-negative bacterium *S. paucimobilis* by Ikushiro's group in 2001. The SpSPT displayed high sequence similarity to mammalian SPT1 and SPT2, but without membrane-associated domains [153]. After that, bacterial SPTs were also found in *Sphingomonas wittichii*, *Sphingomonas multivorum*, *Sphingomonas spiritivorum* and *Bdellovibrio stolpii* [71, 154]. Additionally, bacterial SPTs have brought attention to the phylum of *Bacteroides*, since SLs play an important role between host and microbiomes [155]. The gene BF2461 in *B.fragilis* has been suggested as putative SPT, with 35% sequence identity to SpSPT, the gene generates SL-deficient organisms [94, 156]. The gene BF2461 has also been previously characterized and

confirmed as an SPT in the Campopiano group. Thus one of the main aims of this PhD thesis is to explore the enzyme through further mutagenesis and to study the difference with other SPT isoforms. Recently, in a similar manner, a putative gene product (PG1780) in the chromosome of the *P.gingivalis* strain W83 was suggested by Davey's group as an SPT. The deletion of this gene from the strain leads to weakening of the cell surface properties and bacterial survival ability [97, 157]. Therefore, the other aim of this project is to examine this putative SPT.

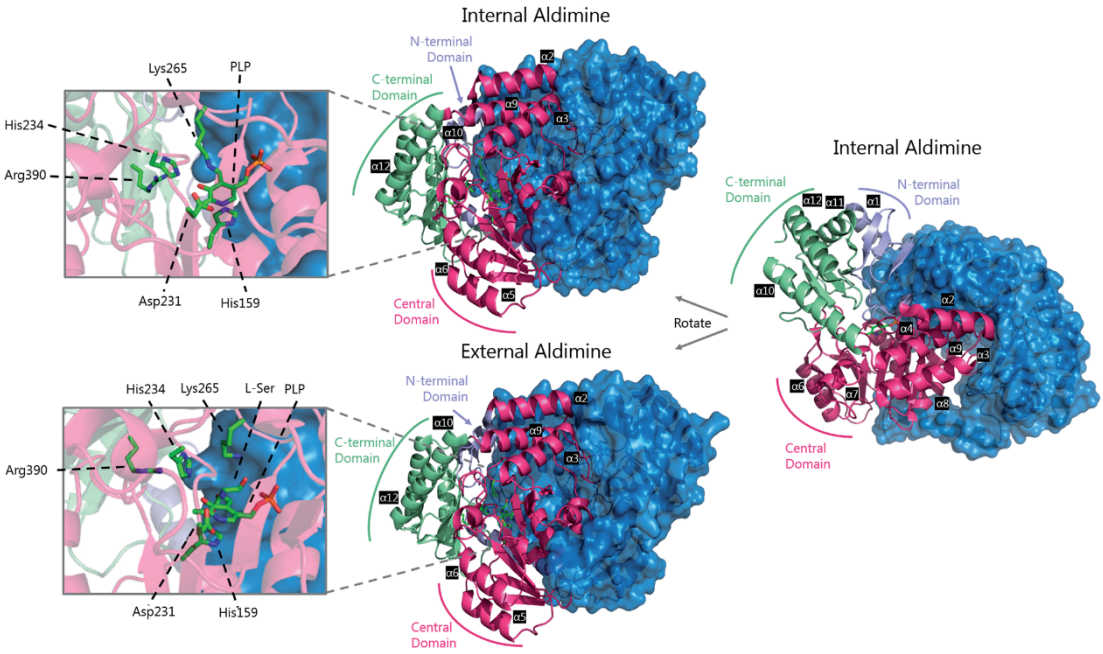

Figure 1.3.8 The first crystal structure of bacterial SPT homodimer in the internal aldimine (PDB:2JG2) and the external aldimine (PDB:2W8J) forms. The active sites and key residues are highlighted in left, one monomer is highlighted as ribbon form and the other is shown as surface (taken from Harrison *et al.*'s paper [45, 158, 159]).

The first published crystal structure (PDB: 2JG2) of bacterial SPT was from *S. paucimobilis* and was determined by Yard *et al.* – a collaboration of the Campopiano group with Prof. Jim Naismith's group in 2007 (Figure 1.3.8). It is a PLP-bound homodimer, with each monomer consisting of an N-terminal domain, a central catalytic domain and a C-terminal domain. The PLP cofactor is attached to the active site lysine 265, which is referred to as the internal aldimine [158]. Followed by the previous work, the crystal structure of PLP: L-Ser SPT complex (PDB: 2W8J), also known as external aldimine forms of the enzyme, was characterised by Raman et al. in 2009 [159]. Furthermore, the other protein structures of bacterial SPT from *S. wittichii* (PDB: 2X8U) and *S. multivorium* (PDB: 3A2B) have been determined and published [160, 161]. The internal aldimine and external aldimine forms of SPT support an excellent prospect about the link between the PLP cofactor and active residues in the enzyme.

For example, histidine 159 provides a π-stacking interaction with the PLP pyridine ring in the internal aldimine. This residue also supports L-Ser by forming a hydrogen bond with the carboxylate of the L-Ser during the formation of the external aldimine [162, 163]. Meanwhile, the arginine 378 residue performs a conformational switch into L-Ser binding in order to interact with the carboxylate group [159, 161]. Arginine 390 has been confirmed to stabilise the reactions transition state and aid the decarboxylation [160, 164]. Overall, these findings provide effective models for studying the SPT mechanism.

In the early 1960s, a proposed catalytic mechanism of the reaction was initially proposed using other established PLP-dependent enzymes and their models with cofactors [109]. As mentioned in Section 1.3, the external aldimine is a crucial intermediate for all PLP-dependent enzymes during the catalysis of various reactions. Ikushiro's group utilized elegant NMR experiments to observe the movement of the α-carbon in L-Ser during the reaction process, which observed deprotonation occurring before decarboxylation [165]. Because of the delocalization of negative charge, the stereo-chemical rearrangement of the σ bonds is activated by a π system forming a Dunathan intermediate [166]. Consequently, the heterolytic cleavage on αC-H bond of the amino acid takes place and the resonance-stabilized quinonoid intermediate is generated. The C16-CoA is presumed to react with the quinonoid through a Claisen-like condensation to produce a β-keto acid external aldimine intermediate. After that, the decarboxylation and deprotonation occur either through the non-quinonoid mechanism or the quinonoid mechanism and proceeds to generate the external aldimine product. Finally, the active site lysine regenerates the internal aldimine and releases 3-KDS through transaldimination [167]. The involvement of C16-CoA in the course of the reaction was proposed by using the analogue S-(2-oxoheptadecyl)-CoA. This mimic can reduce the rate of breaking the thioester bond and unleashing free CoA under physiological conditions, leading to both substrates remaining bound to the enzyme[165]. This detailed reaction mechanism for SPT has now been accepted (Figure 1.3.9). Recently, the Campopiano and Dunn groups showed that SpSPT displays a clear kinetic isotope effect (KIE) with [2,3,3-D] L-Ser compared to the human SPT isoform. This suggests there may still be subtle kinetic differences between different species and each isoform binds each substrate in a slightly different way – not surprising due to the nature of the regulatory subunits found in complex with the eukaryotic complex [168].

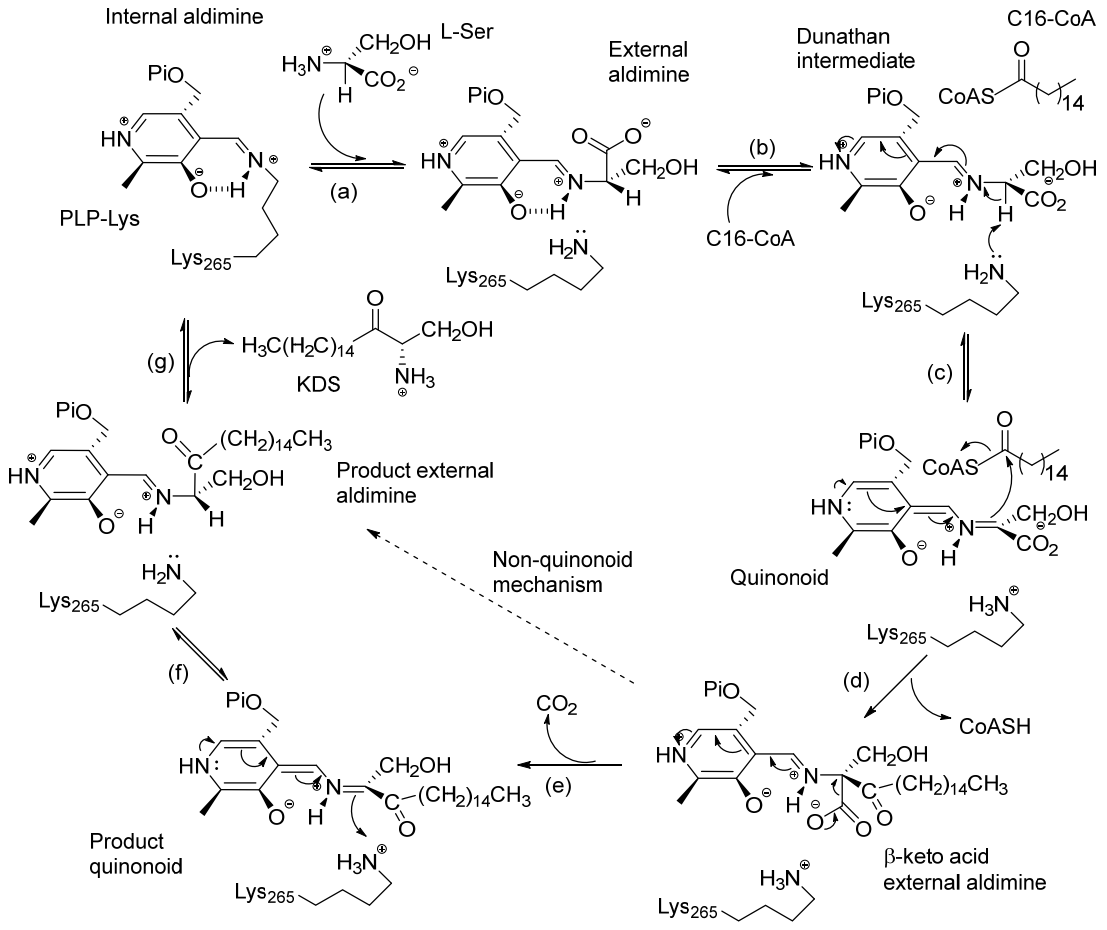

Figure 1.3.9 Proposed catalytic mechanism of SPT (based on Raman et al. [159]).

Based on the enzyme reaction mechanism, several natural product inhibitors (Figure 1.3.10) of SPT have been probed up to date for the role of SLs *in vivo* or *in vitro* [137]. For instance, sphingofungin B from *Aspergillus fumigatus* showed specific inhibition of SPT through a radiolabelled substrate assay, for which the half-maximal inhibitory concentration (IC_{50}) is 20 nM [169]. Myriocin shares a similar core structure to sphingofungin B and is the best-known SPT inhibitor. It was first found in two different fungi and isolated from *Myriococcum albomyces* by Kluepfel's group in the 1970s [170, 171]. However, the mechanism of inhibition was unknown until 2013, when it was solved by Wadsworth et al. They observed a novel stable PLP adduct (PLP-myriocin aldimine) by mass spectrometry and obtained structural data (PDB:4BMK). Myriocin would start with the retro-aldol type reaction to cleave the C2-C3 bond to produce C18 aldehyde. Finally, the active site lysine 265 interacts with the aldehyde to form a second irreversible inhibitory complex and cause the enzyme to inactivate [172].

As a PLP-dependent enzyme, some molecules which inhibit the PLP cofactor also have inhibitory effects on SPT enzymes. L- and D-cycloserine (LCS and DCS) were reported as inhibitors by Lowther et al. in 2010. It is suggested that SPT would react with both enantiomers of cycloserine (CS) to form pyridoxamine

monophosphate (PMP) and an amino aldehyde product. This irreversible inhibition of SPT involves ring-opening, decarboxylation and amide bond hydrolysis. A published crystal structure of SpSPT (PDB: 2XBN) with CS provides a clear perspective about the inhibitory mechanism of the enzyme [173]. Other inhibitors like L-penicillamine and β-chloro-alanine also display the same inhibition and form different PLP inhibitor complexes (Figure 1.3.10). Medlock's study showed that the concentration of β-chloro-alanine required for the inhibition of SPT was much lower than the one required for inhibiting other PLP-dependent enzymes [174]. Moreover, L-penicillamine was transformed into a thiazolidine complex in the active site to render PLP inactive, which was elucidated by Lowther et al. [175].

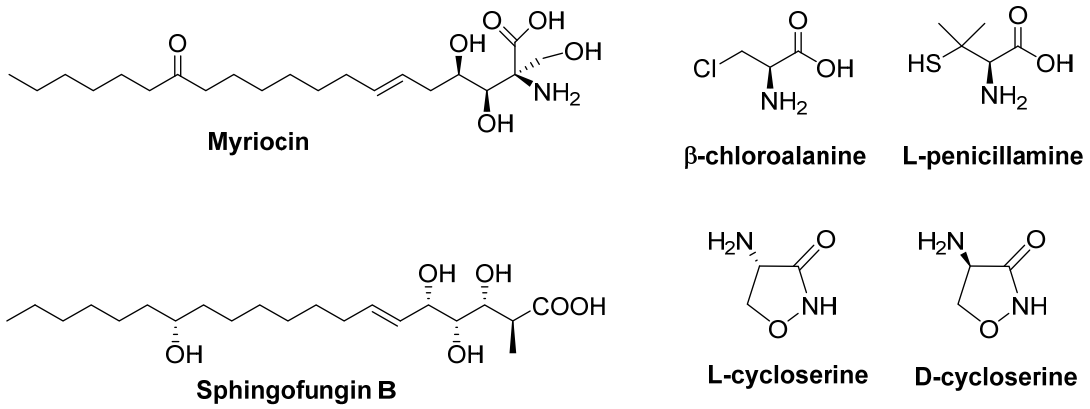

Figure 1.3.10 Structures of the various known inhibitors of SPT.

1.3.2 Iso-branched chain aminotransferase (IlvE or BCAT)

The branched-chain amino acids (BCAAs), such as natural leucine, isoleucine, and valine, are essential and are related to numerous diseases and disorders in the human system [176]. Research has shown there are eight enzymes required for the biosynthesis of these three BCAAs in nature. The *iso*-branched chain aminotransferase (IlvE or BCAT) catalyses the final step of BCAA biosynthesis [177]. IlvE or BCAT transfer the amino group from the *iso*-branched chain amino acids into keto-acids forming new amino acids. The catalytic mechanism is similar to common aminotransferases (ATs) and is split into two half-reactions with PLP cofactor recycling between the internal aldimine and PMP forms (Figure 1.3.11) [178].

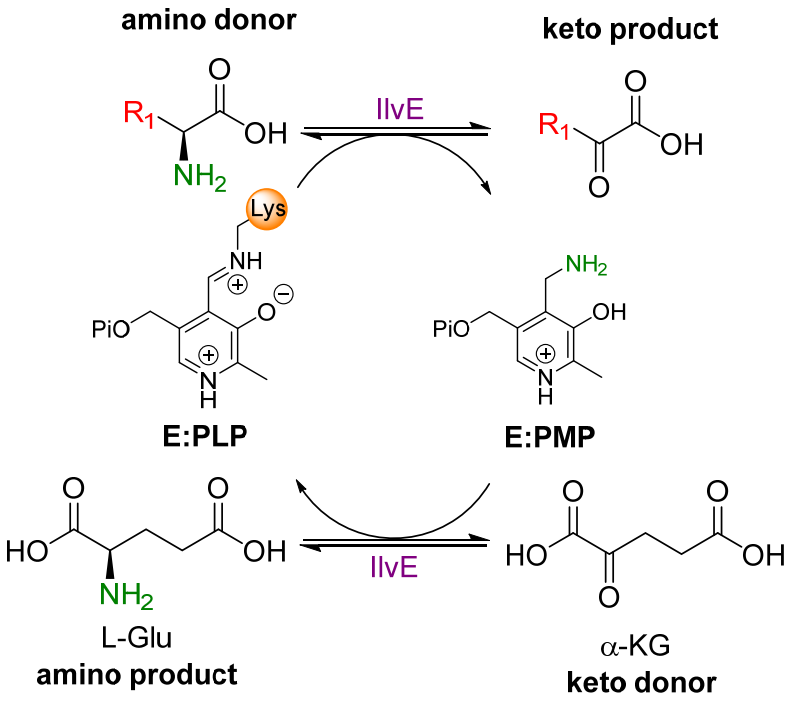

Figure 1.3.11 Schematic diagram of the IlvE reaction. R1 represents a branched chain amino acid (BCAA) such as L-Leu, L-Ile or L-Val.

The first mammalian BCAT enzyme appeared in 1966 when Ichihara and Koyama isolated the enzyme named 2-oxoglutarate AT from a hog heart [179]. In the same year, Taylor and co-workers successfully purified leucine transaminase from pig heart muscle [180]. Until the 1990s, Hutson's group reported that there are two BCATs in the mammalian system – cytosolic BCAT1 (BCATc) and mitochondrial BCAT2 (BCATm) [181]. These enzymes have a specific order of substrate preference. From most active to weakest are isoleucine, leucine, valine, and glutamic acid [182]. The BCAT2 usually distributes in the kidney, colon, skeletal muscle and liver; however, the

BCAT1 only expresses in the brain [183]. BCAT1 and BCAT2 share 58% similarity in sequence homology and are both homodimers, with the monomer comprising a small and large domain, where the active site close to the interface [184, 185]. Nevertheless, BCAT1 showed double the catalytic ability compared to BCAT2 under the same substrate conditions [182]. In physiology, studies showed that BCAT2 tended to form a metabolon protein complex with the branched-chain α-keto acid dehydrogenase (BCKD) in order to channel substrates or products through the body [186]. Alzheimer's disease has been reported to have a relationship with increased levels of BCAT2 in the frontal and temporal lobe [187]. Deletion of BCAT2 results in an impressive increase in BCAAs which is not used for energy consumption and can reduce the growth speed of lymphoma cancers in mammals [188]. On the other hand, BCAT1 has been reported to affect T cell receptors as well as the mammalian target of rapamycin (mTOR) signaling and eventually promoting cell proliferation [189].

In bacteria, two aminotransferases were initially discovered in *Escherichia coli* in 1953. One of them showed higher activity with BCAA substrates, named as transaminase B. The other enzyme had a preference for aromatic amino acids [190]. After that, more and more bacterial BCATs were discovered in *Pseudomonas aeruginosa*, *Mycobacterium tuberculosis*, *Lactococcus lactis*, *Helicobacter pylori* and so on [191-194]. Meanwhile, the unique name of IlvE was assigned to the genes from bacterial BCATs [195]. The deficiency or upregulation of IlvE would cause the changes in BCAA levels in the cell. The same as in the human system, IlvE undoubtedly influences BCKD production for generating different acyl-CoAs, which affects not only protein synthesis but also protection against host defenses. For instance, studies showed an impaired *Staphylococcus aureus* strain, a bacterium causing pneumonia (lung infection) in humans, lost adherence to host cells and infection was debilitated *in vivo* [196-198].

The x-ray crystal structure of human BCAT2 has been solved in several forms, such as the PLP internal aldimine form (PDB: 1EKF, 1EKP), the ketimine form with bound isoleucine (PDB: 1KT8) and the PMP form (PDB: 1KTA) [184, 185]. In the PLP form, the active site Lys202 uses a Schiff-base linkage to the cofactor. Also, mainly hydrophobic residues surround the substrate-binding pocket for controlling substrate specificity [184, 185, 199]. The hypothesis suggests that these thiol groups formed a redox-linkage with BCAT proteins. Meanwhile, Cys315 in the BCAT2 was proven to be key for the orientation of the substrate in the active site, while the other three residues of this motif stabilized the carboxylate binding site [200]. However, human BCAT1 has only been successfully co-crystallized with different inhibitors [201, 202]. The PLP active site and substrate-binding pocket of BCAT1 showed similar structural alignment with

BCAT2. Tyr193 has been found to facilitate a strong interaction with inhibitor molecules [202].

The *holo* form of the bacterial IlvE crystal structure from *E. coli* was determined in 1997 with a resolution of 2.5 Å (PDB: 1A3G). The structure displayed a unique homotrimer [203]. After that, crystal structures of IlvEs have been solved in other bacterial species such as *Mycolicibacterium smegmatis* (PDB: 3JZ6), *Mycobacterium tuberculosis* (PDB: 3HT5), and so on [195, 204, 205]. However, the quaternary structures of IlvE are different in different species. For example, *M. tuberculosis* IlvE (Figure 1.3.12) presents as a homodimer with two domains connected by an interdomain loop. The Cys196 residue is absent from other orthologues and appears only in the *M. tuberculosis* IlvE structure. The proximity and position between cysteine in each monomer suggests the formation of a disulfide bond; however, the electron density does not agree with the bond formation [204]. Comparison between IlvE *holo*-form and IlvE substrate complex indicated the direction of PLP rotation and the existence of a hydrogen bond between the imine nitrogen and the phenol group of PLP. This is due to a change in the torsion angle (C3-C4-C4'-N) during the transition from the internal aldimine to the external aldimine [206].

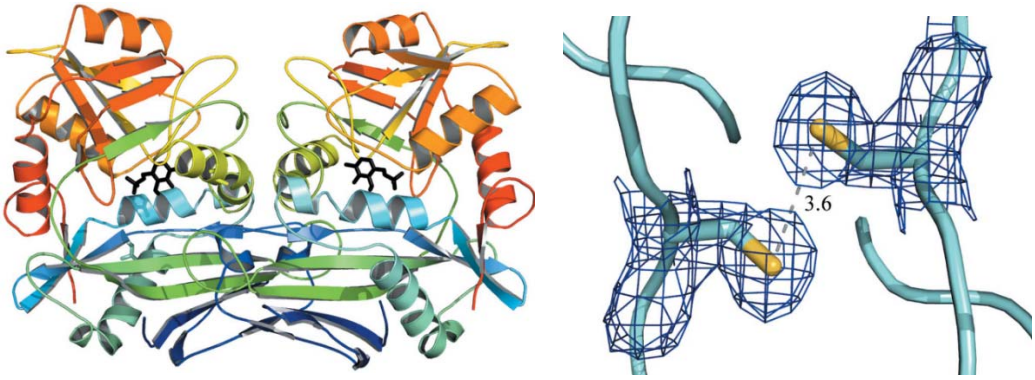

Figure 1.3.12 The crystal structure of MtIlvE homodimer coloured like a rainbow (**Left**), and cysteine residues reside at the interface with no disulfide formation (**Right**) (taken from Blanchard et al. paper [204]).

As a classic PLP-dependent AT, the IlvE performs a two-step mechanism, which is also known as ping-pong reaction. In the first ping half-reaction, the internal aldimine reacts with the donor amino acid, generating the external aldimine and culminating the PMP form of the enzyme as suggested by Blanchard's group. Then, in the second pong half-reaction, the amine group in the PMP form of the enzyme is transferred to a different α-keto acid to form the new amino acid. The internal aldimine of enzyme is regenerated and the catalytic cycle is completed [178, 207]. Studies proposed that the deprotonation of the external aldimine or ketimine hydrolysis is the

rate-limiting step of the transaminase reaction [208, 209]. Interestingly, a unique 1,3-prototropic shift mechanism is found in the *M.tuberculosis* IlvE, where the protonation of C4' of the PLP happens at the same time as α-C-H bond cleavage from L-glutamic acid (L-Glu) (Figure 1.3.13) [178, 210].

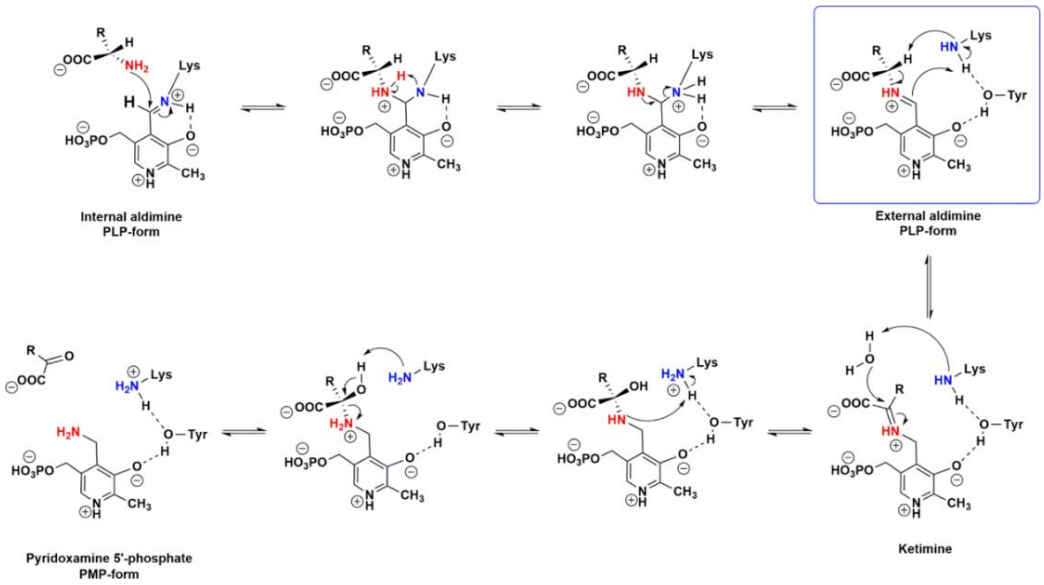

Figure 1.3.13 Proposed catalytic mechanism of IlvE with a single transition state in ping reaction (taken from Blanchard et al. paper) [178].

The BCAT or IlvE has been studied as a drug target for several years since it is crucial in BCAA and BCKA biosynthesis in the human system [211]. For example, gabapentin is a selective inhibitor for BCAT1 but not BCAT2. As described before, the crystal structure of the BCAT1-gabapentin complex was determined (PDB: 2COI and 2COJ) to understand the inhibitory mechanism by affecting the binding [202]. Recently, a novel leucine analogue inhibitor (ERG240) was reported to inhibit the BCAT1 leading to a series of inflammatory diseases [212]. However, it is suggested that the BCAT1 inhibitors may not be deadly to the host and that BCAT2 can actually repair the BCAA biosynthesis since the depletion of BCAT1 in mice has no apparent implication [213]. For bacteria, researches have shown that O-benzylhydroxylamine and LCS and DCS have different inhibitory effects on both *M. tuberculosis* IlvE and *M. smegmatis* IlvE. Furthermore, the protein structure of the enzyme with O-benzylhydroxylamine and DCS has already been published (Table 3.1.1) [205, 214]. Both kinetic and structural analysis of these cases illustrated a distinctive aspect of the proposed inhibitory mechanism, which was a stable PLP-inhibitor adduct forming during reaction [214]. Since the IlvE has a possible involvement in the *iso*-branched SL biosynthesis as stated in section 1.2, one of the aims of this project is to isolate the gene encoding IlvE from the *P. gingivalis* strain, then characterize the enzyme and study the chemical and biological role in the bacterial system.

1.4 3-Ketodihydrosphingosine reductase (KDSR)

In the second step of the SLs biosynthetic pathway, the 3-KDS derived from the SPT reaction was reduced by KDSR to generate DHS (Figure 1.4.1). In 1998, the first KDSR (Tsc10p) was identified in the yeast bacterium *S. cerevisiae* through a temperature/calcium sensitivity screen assay [215]. After six years, the first human KDSR and mouse KDSR were found by Igarashi and Kihara. Named follicular lymphoma variant translocation-1 (FVT-1), this KDSR had a 41% sequence similarity with Tsc10p [216]. Therefore, through gene-based analysis other microbial strains such as *Aspergillus fumigatus* and *Candida albicans* were also shown to encode KDSR enzymes [217, 218]. The immunoprecipitation experiments illustrated both FVT-1 and Tsc10p were multimeric enzymes, obtaining different transmembrane regions in the ER membrane. However, the membrane domain of Tsc10p has been proven not to affect the enzyme activity [219]. In addition, KDSR was reported as a member of the short-chain dehydrogenases/reductases (SDR) family and catalyzes the NADPH dependent reduction [45, 219]. Fornarotto et al. also proposed a homology model of KDSR from *A. fumigatus* dependent on one of the SDR enzymes. The homology model showed that the active site is close to the C-terminus of the enzyme, which is close to the membrane. Meanwhile, most of the 3-KDS substrates are in the solvent, not in the binding site. This suggests that *in vivo* the hydrophobic substrates stay within the membrane to easily interact with downstream SL enzymes [217].

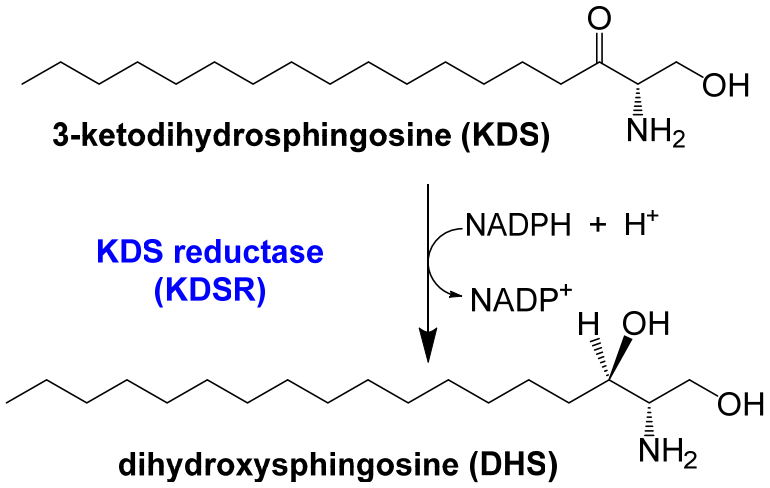

Figure 1.4.1 The NADPH-dependent, KDSR-cataysed reduction of 3-KDS.

Recently, some diseases have been found to be related to mutations in the KDSR gene. For example, the neurodegenerative disease spinal muscular atrophy (SMA) which results in the loss of motor neurons was caused by a missense G-to-A mutation

altering Ala 175 to Thr in the KDSR enzyme. Interestingly, both FVT-1 and FVT-1 A175T mutants complement the growth of the yeast *S. cerevisiae* Tsc10pΔ knockout strain [220]. Patients with the new genetic determinants inherit skin mendelian disorders and have been investigated as exon skipping in the KDSR gene [221, 222]. This recessive mendelian disorder leads to thick red scaly skin on the face, hands and feet [223, 224].

Additionally, Park et al. reported that a mutation in zebrafish also causes hepatomegaly to steatosis, finally a hepatic injury phenotype. SL analysis between the control and mutants suggested KDSR mutant I105R increased the accumulation of SLs and activated the SL salvage pathway (Figure 1.4.2) [220]. However, without a crystal structure of the human KDSR, it is hard to explain the changes in the catalytic mechanisms by mutagenesis. These mutations raise interests as to whether the same impact happens for the yeast KDSR. One of the aims of the project is to characterize the yeast KDSR and understand its catalytic mechanism.

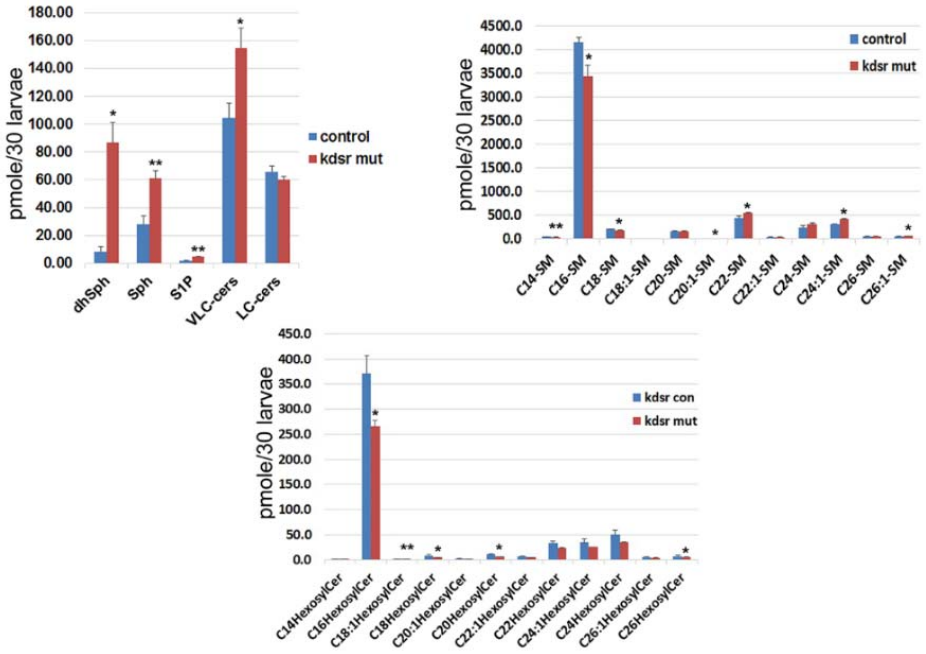

Figure 1.4.2 The comparison of SLs concentration in zebrafish between control and KDSR I105R mutant (taken from Park et al. paper [220]).

1.5 Aims

The aims of this thesis:

Chapter 2:

(1) To express, purify and characterise recombinant forms of *B. fragilis* SPT (BfSPT) and *P. gingivalis* SPT (PgSPT).

(2) To study the inhibition of PgSPT by L- and D-cycloserine (LCS/DCS).

(3) To generate SPT mutants to understand the effect of the C16-CoA substrate.

(4) To understand how the position of the 6His affinity tag influences SPT activity.

(5) To determine the crystal structure of bacterial SPT homologues.

Chapter 3:

(1) To express, purify and characterise recombinant transaminase *P. gingivalis* IlvE (PgIlvE).

(2) To study the inhibition of PgIlvE by inhibitors such as LCS and DCS.

(3) To determine the crystal structure of PgIlvE to understand residues involved in substrate binding and the catalytic mechanism

(4) To generate site directed mutants that may affect the enzyme activity.

Chapter 4:

(1) To express, purify and characterise a soluble *S. cerevisiae* KDSR (ScKDSR) isolated from *E. coli* host.

(2) To observe enzyme activity of ScKDSR mutants based on the human KDSR mutants from the skin pathologic patient.

(3) To determine the crystal structure of ScKDSR or build a hypothetic model using homologues from the SDR superfamily.

Chapter 2 Serine palmitoyltransferase (SPT)

2.1 Expression, purification, and characterization of *B. fragilis* SPT (BfSPT)

The *Bacteroidetes*, one of the dominant microbial species in the human gut, are a source of bacterial SLs that has evolved a complicated relationship with our host systems (immunity, metabolism *etc.*). Johnson *et al.* recently showed that bacterial SLs are linked with mammalian SL pathways by introducing *B. thetaiotaomicron* into mice. This resulted in the reduction of *de novo* SLs production and the increase of liver ceramides (Cers) [225]. Brown *et al.* provided evidence for intestinal inflammation and alternation of Cer levels caused by the deficiency of bacterial SLs through the deletion of the SPT in *B. thetaiotaomicron* [96]. In 2011, Wieland Brown et al. discovered three unique *iso*-branched SLs that simulate mammalian iNKT cells. They also proposed a putative SPT (BF2461) homologue from the *B. fragilis* found in the human gut which showed high homology to other well-characterised bacterial SPTs studied in the Campopiano group and proposed that this SPT catalysed the first step in the SL biosynthetic pathway [94]. The gene BF2461 had previously been studied and confirmed as BfSPT by group members Edward Bower and Bohdan Mykhaylyk in preliminary studies [226, 227].

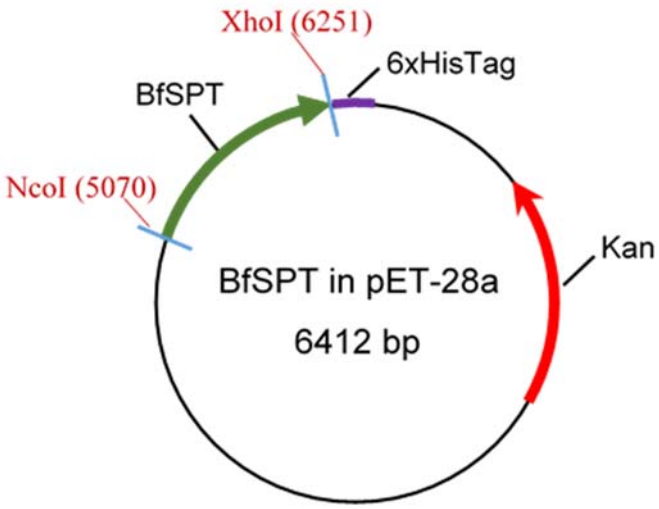

Figure 2.1.1 Plasmid map of *B.fragilis* SPT in pET-28a

In order to obtain a better understanding of the SPT mechanism and biochemistry, the initial work of my PhD was a re-investigation on BfSPT. The gene had been cloned into a C-terminal His_6-tag pET-28a (Figure 2.1.1). The protein was expressed in BL21 (DE3) for 4~5 hours at 30 °C after induction with 0.1 mM IPTG. The purification methods consisted of HisTrap HP (1 ml column) with buffer A and B

(buffer details in Section 6.1), followed by a HiLoad 16/60 Superdex 200 prep grade column with buffer C or D for further clean-up (Figure 2.1.2). Typical yields of recombinant, pure BfSPT were ~ 9.0 mg per litre of *E. coli* culture.

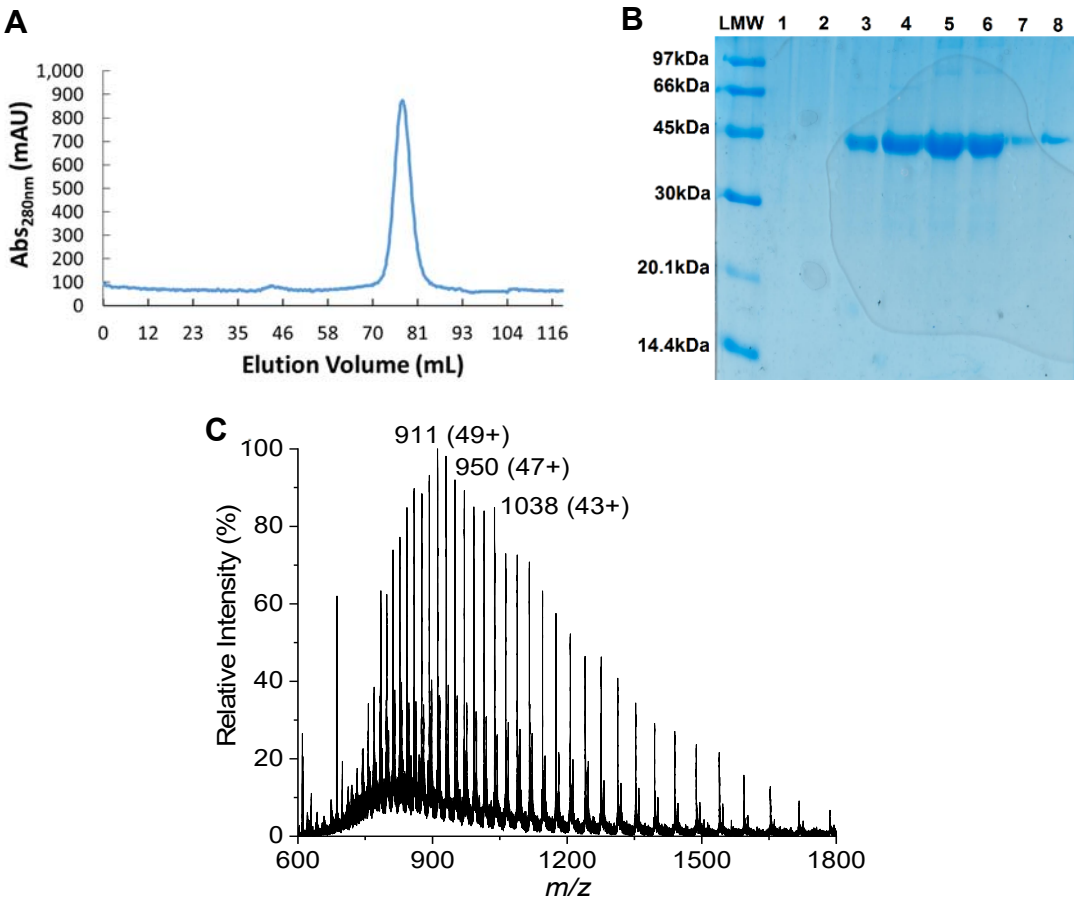

Figure 2.1.2 BfSPT purification and analysis. (A) Chromatogram from SEC column. (B) 15% SDS-PAGE gel after SEC. LMW: Low molecular weight marker, Lane 1-8: elution fractions from 68-91 mL. (C)

The positive ion mass spectrum of recombinant BfSPT (10 μM) with a deconvoluted mass of 44614.14 ± 1.37 Da.

The protein purity was confirmed by SDS-PAGE analysis and LC-ESI-MS. A denatured mass of 44614.14 ± 1.37 Da was measured (Figure 2.1.2), which matched the theoretical mass with the loss of the initial methionine (44614.30 Da) calculated from the recombinant protein sequence using ExPaSy ProtParam tool website (https://web.expasy.org/compute_pi/). It is common that the initial methionine is lost during post-translational modification, and that gluconoylation of the histidine tag of the protein during *E.coli* expression would also cause an additional peak (+178 Da) to appear in the mass spectrum [228, 229].

In addition, the elution peak from SEC column was around 76 mL corresponding to a mass of ~90 kDa calculated from a calibration curve (Appendix 7.1). This also predicted that the protein was a homodimer which is similar to other

bacterial SPT isoforms that had been published in the past such as SpSPT and SwSPT.[111, 158, 161, 230].

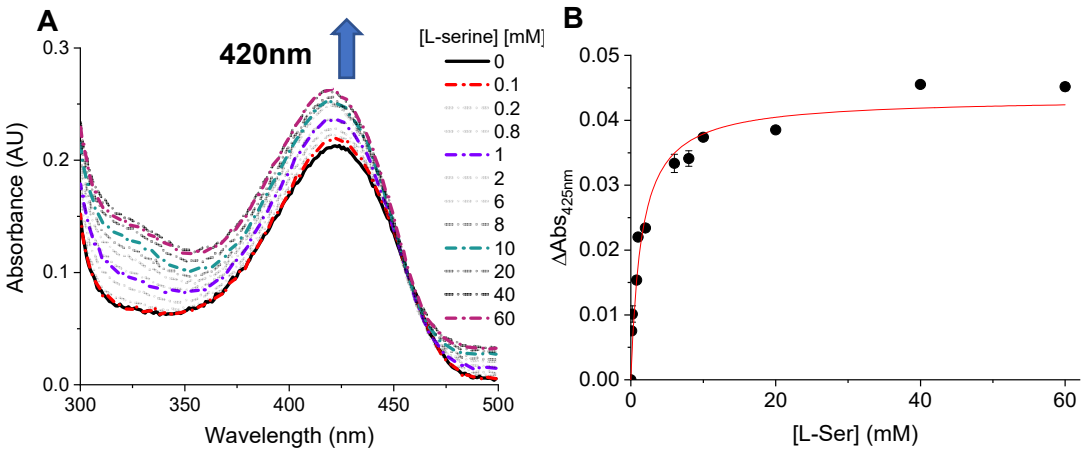

Figure 2.1.3 Monitoring and characterization of BfSPT binding with L-Ser. (A) UV-vis spectrum of BfSPT. (B) The determination of dissociation constant (K_d). The assay contained 20 μM BfSPT and variable concentrations of L-Ser (0-60 mM). The data were plotted as mean readings ±2-SD error bars.

The binding of ligands such as L-Ser to PLP-dependent enzymes can be monitored by UV-vis spectroscopy with maxima wavelengths of ~330-335 nm and ~415-425 nm, respectively for SpSPT. This represents the equilibrium between the enolimine and ketoenamine forms or the PLP-bound (internal aldimine) and PLP:L-serine (external aldimine) forms of PLP enzymes [159]. In contrast to other SPTs, for BfSPT (Figure 2.1.3), there was no obvious peak around 335 nm, and only an increasing absorbance at 420 nm with binding different concentration of the substrate, which meant the PLP cofactor only remained as ketoenamine form in this enzyme. Meanwhile, an estimated K_d value could be determined by the difference in absorbance at 425 nm against a range of L-Ser concentrations (0.1 - 60 mM), which was measured as 1.45 ± 0.22 mM, and these findings agreed with the previously reported value of 1.48 mM (Mykhaylyk) and 1.34 mM (Bower). Compared to SpSPT (1.1 mM) and SwSPT (0.8 mM), BfSPT was still characterised with the ligand bound [159, 160].

As with other SPTs described in the introduction, BfSPT activity was measured using the coupled DTNB assay to obtain the kinetic parameters for both L-Ser and C16-CoA substrates (Figure 2.1.4). However, substrate inhibition was found with high concentrations of C16-CoA with the reaction rate decreasing when a concentration above 80 μM was used and significant inhibition occurring when it was over 400 μM. By using substrate inhibition analysis (the high substrate inhibition from Origin), an estimated inhibition constant (K_i) could be calculated as 165.74 ± 72.58 μM. It is noted that the 3-KDS product could still be detected by MALDI-ToF-MS analysis during the

inhibition stages, so the enzyme was still active but incredibly slow to produce 3-KDS. This phenomenon was also observed in the previous study [227], with the straight-chain acyl-CoA substrate (C16-CoA) causing reaction inhibition – C17-CoA and C15-CoA also showed similar patterns. The reason behind acyl-CoA substrate inhibition will be discussed more in a later section 2.6 with another human microbial SPT (PgSPT).

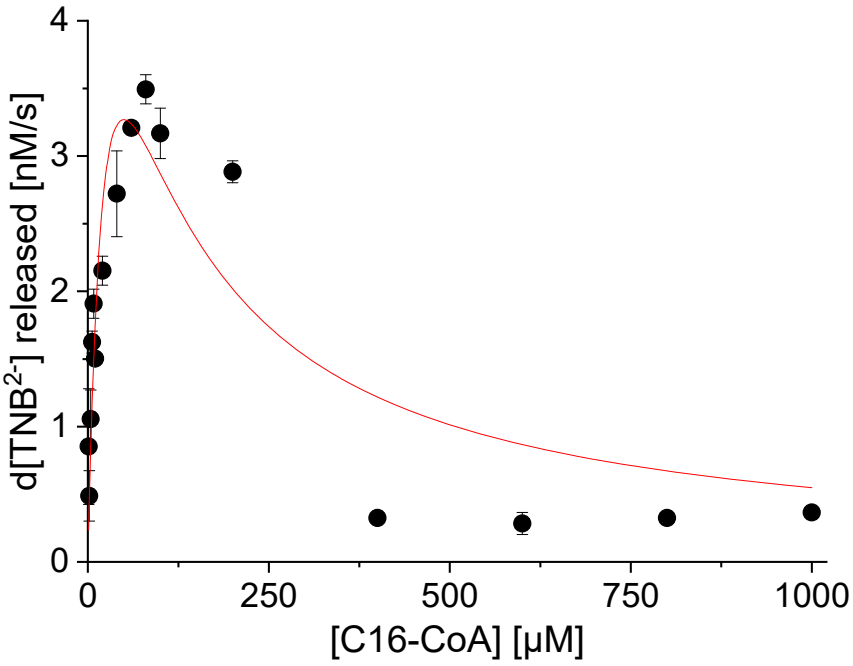

Figure 2.1.4 Substrate inhibition analysis of BfSPT reactions for substrates C16-CoA. Each assay contained 0.1 μM BfSPT, 20 mM L-Ser and variable con centration of C16-CoA (0-1.0 mM). The data were plotted as mean readings ±2-SD error bars.

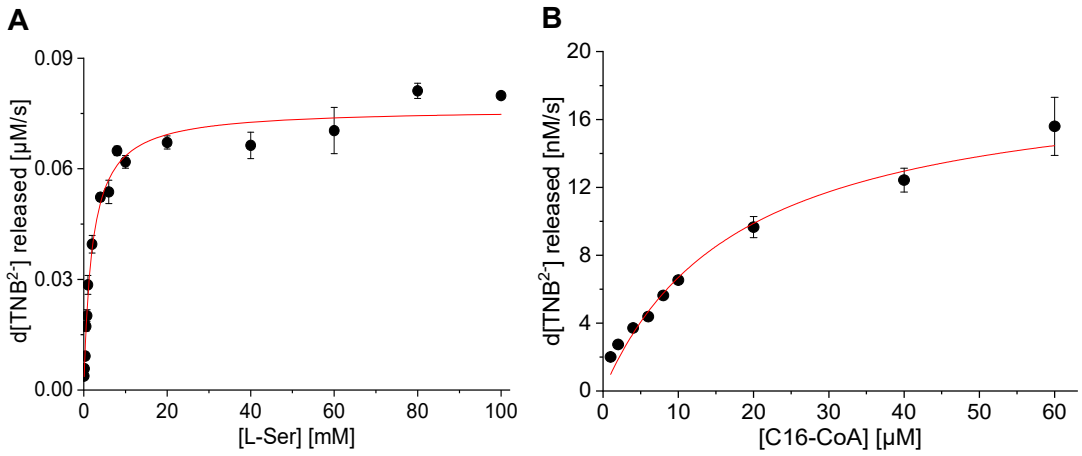

Figure 2.1.5. Kinetic analysis of BfSPT reactions for optimized substrate L-Ser (A) and C16-CoA (B). Each assay contained 0.35 μM BfSPT, variable concentration of L-Ser or C16-CoA. All data were plotted as mean readings ±2-SD error bars.

Assay conditions for substrate L-Ser and C16-CoA were optimized by increasing the BfSPT concentration from 100 nM to 350 nM and lowering the concentration of the substrate, in order to gain kinetic parameters for BfSPT WT (Figure 2.1.5). This allowed measurements for both substrates; for L-Ser, the K_M value was 2.02 ± 0.17 mM, V_{max} value was 0.08 ± 0.01 μM/s, k_{cat} value was 0.22 ± 0.01 s^{-1} and k_{cat}/K_M value was 0.11 $mM^{-1}s^{-1}$. There is no large difference in substrate affinity (K_M) compared to *S. paucimobilis* SPT (SpSPT) and *S. witichii* SPT (SwSPT), which were 1.40 mM and 0.78 mM respectively. However, the turnover number (k_{cat}) is more than 5 times slower than for SpSPT (1.15 s^{-1}) and almost 1.5 times faster than SwSPT (0.15 s^{-1}) [159, 160]. For substrate C16-CoA, the K_M value was 18.15 ± 2.26 μM, V_{max} value was 18.84 ± 1.06 nM/s, k_{cat} value was 0.05 ± 0.01 s^{-1} and k_{cat}/K_M value was 2.98 $mM^{-1}s^{-1}$. Compared to the substrate affinity with SpSPT (35.4 μM) and SwSPT (23.4 μM), BfSPT showed a higher affinity with P-CoA than L-Ser. Considering the low turnover number, the catalytic efficiency (k_{cat}/K_M) is approximately 10 times lower than SpSPT (32.47 $mM^{-1}s^{-1}$), but nearly the same as SwSPT (2.94 $mM^{-1}s^{-1}$). There has been a discussion as to whether k_{cat}/K_M is a useful comparator to compare two enzymes [231]. More details of these data will be discussed along with the analysis of the *P. gingivalis* (PgSPT) in a later section 2.5 and 2.6.

2.2 Exploring the mutant BfSPT V353R

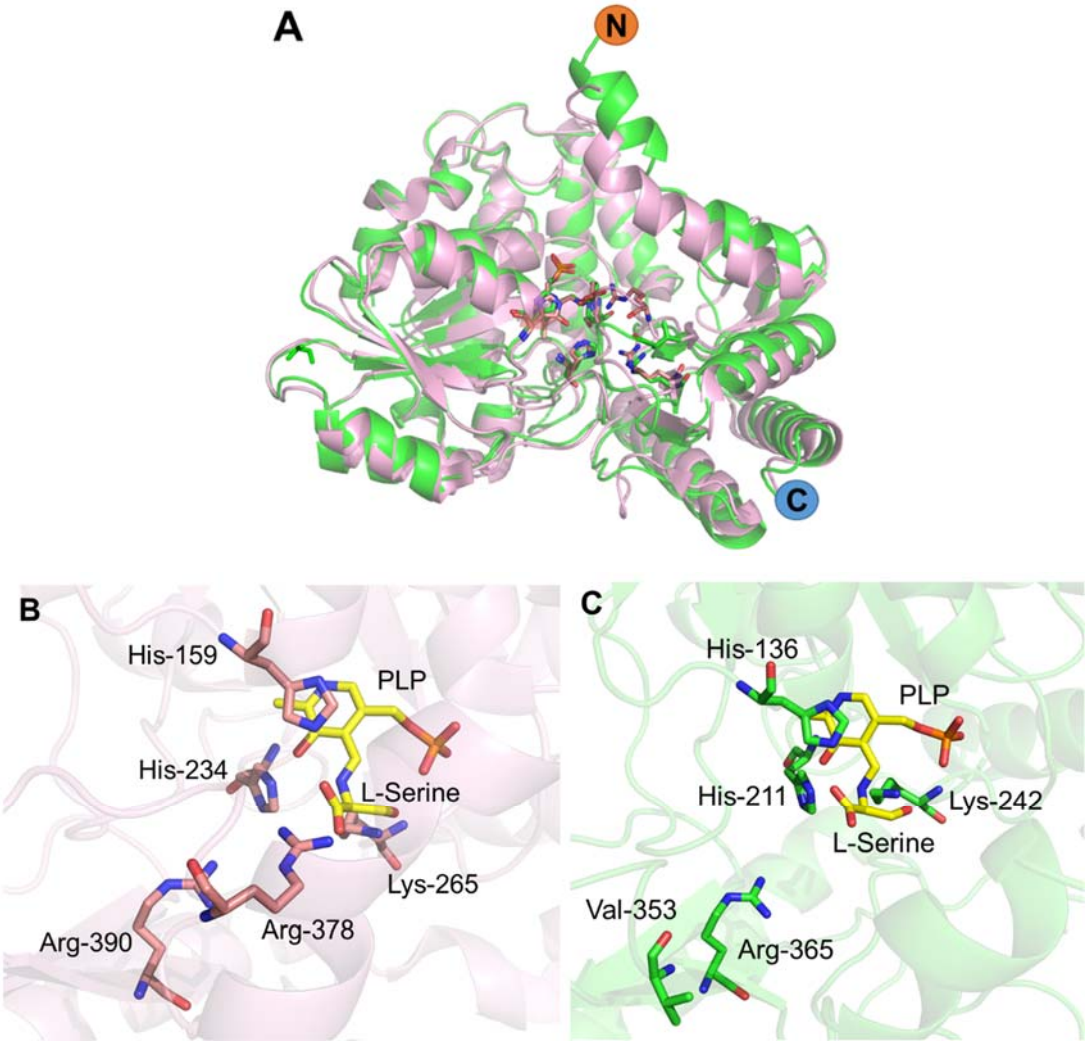

Figure 2.2.1 Comparison of PLP: L-Ser external aldimine SPT structures and relevant residues. (A) Structural overlay of SpSPT and BfSPT. (B) The SpSPT:PLP: L-Ser complex (PDB: 2W8J) [159]. (C) The BfSPT: PLP: L-ser complex, PDB:unpublished.

The x-ray structures of BfSPT with both PLP and other bound ligands are currently undergoing final refinement (Mykhaylyk, Naismith and Campopiano), but a working structure is used for comparison. By analysing the structures and residues around the PLP: L-Ser external aldimine (Figure 2.2.1), Arg378 in SpSPT appears to flip inside to interact with the PLP: L-Ser ligand. It has been discussed by Raman et al [159] that, during the binding process, that the conformation and position of Arg378 are altered to retain the hydrogen-bonds with the conserved His159 and also bind the carboxylate group of L-Ser. It is suggested that this residue plays an important, but not essential, role by affecting the stabilization of an intermediate of both substrates. Rather than an Arg residue at the position, there is a Val residue (V353) near to the PLP: L-Ser external aldimine in the BfSPT structure, so it is time to explore the impact on the catalytic activity and substrate binding by replacing the Val with Arg (V353R).

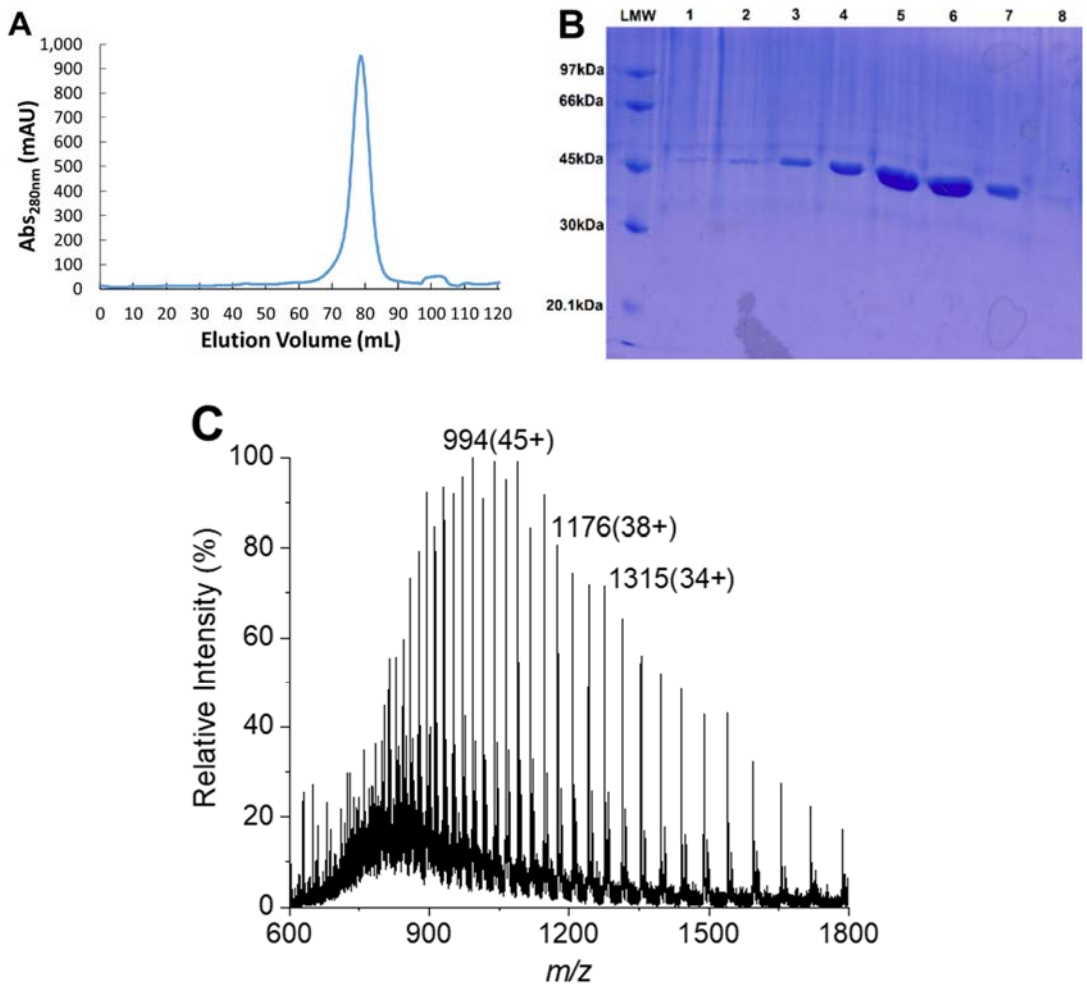

Figure 2.2.2 BfSPT V353R purification and analysis. (A) Chromatogram from SES column. (B) 12% SDS-PAGE gel after SEC. LMW: Low molecular weight marker, Lane 1-8: elution fractions from 68-89 mL. (C) The +ve ion mass spectrum of recombinant BfSPT (10 μM) with a deconvoluted mass of 44664.88 ± 1.81 Da.

The mutant BfSPT V353R was successfully cloned by PCR and confirmed by commercial DNA sequencing. The soluble mutant enzyme was well-expressed and isolated by using the same buffers and purification method as BfSPT WT (Figure 2.2.2), which showed similar data compared to the WT enzyme. The pure protein was analysed by LC-ESI-MS, with a mass of 44664.88 ± 1.81 Da, which was slightly lower than the theoretical mass minus the initial methionine (44671.35 Da). To ensure the correct protein was obtained, it was also subjected to FT-ICR-MS/MS analysis of the tryptic digest, as well as confirmation of the protein sequence using the Protein Prospector online tool.

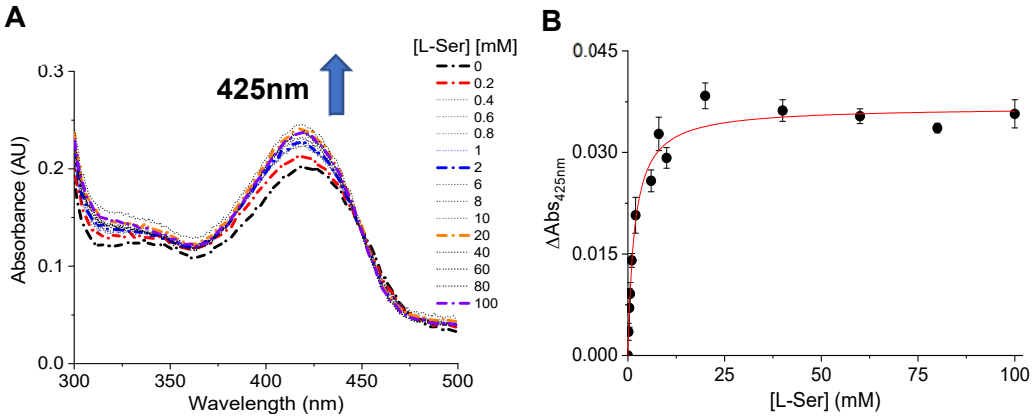

Figure 2.2.3 Monitoring and characterization of BfSPT V353R binding with L-Ser. (A) Absorption UV-vis spectrum of BfSPT V353R. (B) The determination of dissociation constant (K_d). The assay contained 20 μM BfSPT and variable concentrations of L-Ser (0-100 mM). The data were plotted as mean readings ±2-SD error bars.

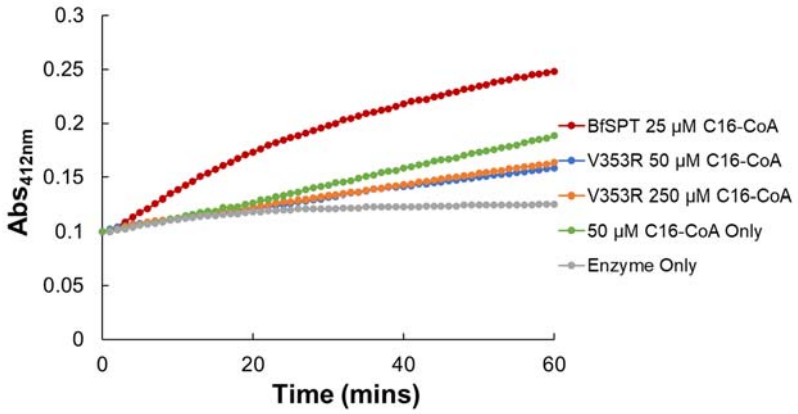

Figure 2.2.4 Enzyme assays of BfSPT WT, BfSPT V353R and negative controls. The BfSPT WT and V353R assay contained 20 mM L-Ser and different concentrations of C16-CoA and enzyme as labelled.

The enzyme was analysed by UV spectroscopy to examine the binding of PLP-L-Ser, and a K_d value of 1.70 ± 0.23 mM for BfSPT V353R was obtained (Figure 2.2.3). Compared to the WT enzyme (K_d =1.45 mM), there was no significant difference in the dissociation of the L-Ser from the PLP-bound complex, where one might have predicted the introduction of the Arg residue in place of Val would lead to tighter binding. Surprisingly (Figure 2.2.4), when the mutant was first tested through the enzyme assay with positive and negative controls, then MALDI-ToF-MS to examine the 3-KDS products, it seemed that the mutant could not catalyse the reaction normally and no relevant products were determined from MS. Since L-Ser binding appeared to be unaffected by this mutation this observation suggested that the Val at position 353 was essential to control the second, C-C bond-forming catalytic step of the reaction mechanism i.e. when C16-CoA binds to the PLP: L-Ser external aldimine form and leads to the formation of the reactive carbanion (Fig. 1.3.8).

2.3 Cloning, expression, purification and characterization of *P. gingivalis* C-terminal pETHis$_{10}$SPT

An *et al.* suggested SLs were able to form SL-dependent membrane microdomains, like eukaryotic lipid rafts, to support long-term survival in *B. fragilis* [156]. As mentioned in the introduction, the group of Prof. Mary Davey (University of Florida) discovered a similar phenomenon that SLs were essential to the existence of surface polysaccharides in oral bacterial *P. gingivalis* [97]. Recently, they also found out the synthesis of SLs controlled the inflammatory response and homeostasis with the host [232]. They suggested a potential SPT homologue (PG1780, UniProt code: Q7MTZ6) as the PgSPT in the *P. gingivalis W83* strain [97]. As discussed in the introduction, all the bacterial SPTs belong to AONS catalogues, and the average amino acid sequence similarity is ~30% to 35% depending on different functions. The sequence analysis of PgSPT is carried out with other bacterial SPT isoforms (Table 2.3.1 and Figure 2.3.1). The PgSPT showed high sequence homology, with the conservation of key active sites residues involved in PLP binding and catalysis (Table 2.3.2). Furthermore, the PgSPT shared the highest amino acid sequence identity (76%) with the *B. fragilis* BfSPT found by both Wieland Brown *et al* and An *et al*. The data in this section were summaried and published in a paper (F.G. Rocha, **P. Tang**, et al., *Journal of Dental Research*, 2020, 99, 568-576) [232]

Table 2.3.1 Percentage sequence of identity and similarity of SPT isoforms.

SPT (% Identity/ % Similarity)	***S. paucimobilis***	***S. wittichii***	***S. multivorum***	***B. fragilis***	***P. gingivalis***
S. paucimobilis	100/100	75/86	38/60	35/58	34/56
S. wittichii	75/86	100/100	36/59	39/61	37/58
S. multivorum	38/60	36/59	100/100	58/79	59/77
B. fragilis	35/58	39/61	58/79	100/100	76/89
P. gingivalis	34/56	37/58	59/77	76/89	100/100

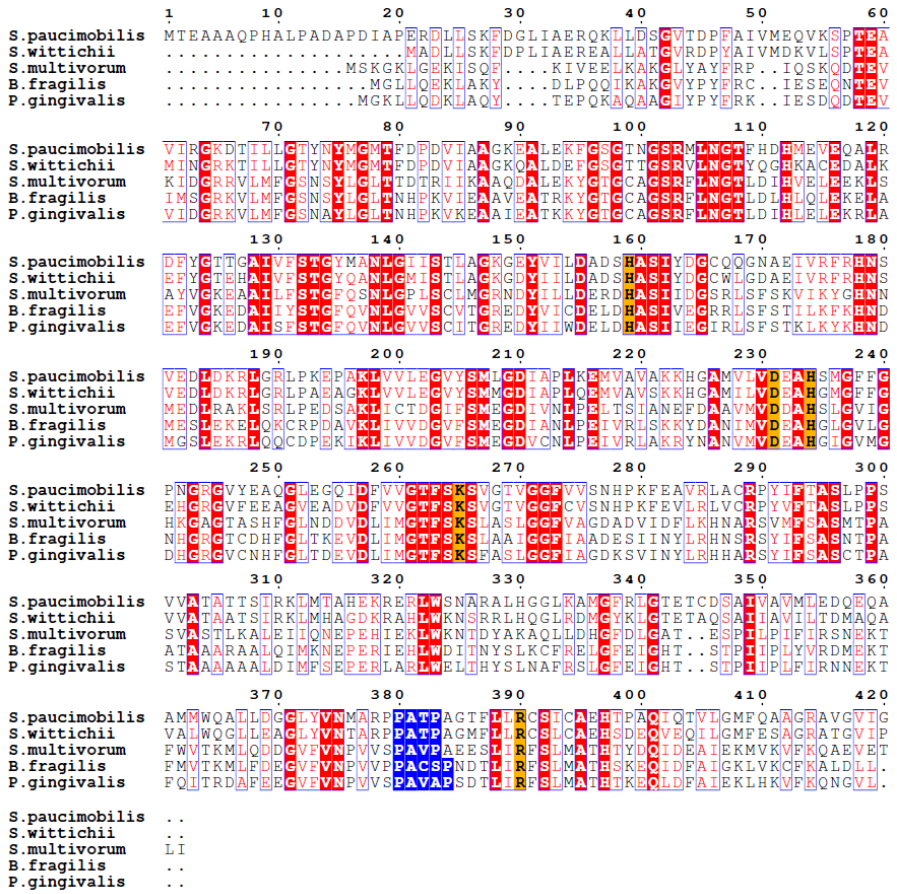

Figure 2.3.1 A sequence alignment of five main bacterial SPTs numbered according to SpSPT. (Conserved residues are highlighted red, the key functional residues are in yellow, PACSP loop is highlighted blue. Uniprot codes are: *S. paucimobilis*: Q93UV0, *S. wittichi*: A5VD79, *B. fragilis*, BF2461, *S. multivorum*: A7BFV6, *P. gingivalis*: Q7MTZ6.).

Table 2.3.2. Potential roles of conserved residues [151, 158, 159, 162, 165]

Residue in SpSPT)	Proposed role
His159	Stacks with pyridinium ring of PLP
Asp231	Polar contact with protonated nitrogen of the PLP ring
His234	Hydrogen bond with pyridinium ring
Lys265	Forms internal aldimine with PLP
Arg378	Involved in binding L-Ser and quinonoid formation
Arg390	Involved in binding L-Ser and quinonoid formation

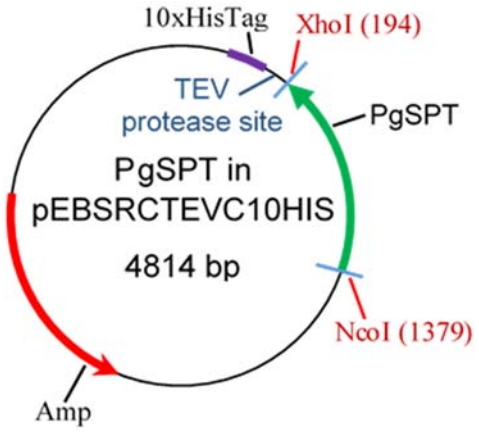

Figure 2.3.2 Plasmid map of *P. gingivalis* SPT in pEBSRCTEVC10HIS

The PgSPT gene was cloned into a pEBSRCTEVC10HIS expression plasmid modified from the pET-23 plasmid (Figure 2.3.2), which was a C-terminal 10xhistidine tag expression plasmid to isolate the PgSPT. After the gene sequence was confirmed by DNA sequencing, the soluble protein was well-expressed in BL21 (DE3) cell for 4~5 hours at 30°C after being induced with 0.1 mM IPTG. The protein was successfully isolated by HisTrap HP 1 ml column with buffer A and B for activity analysis or buffer E and F for crystallography trails. Then the protein was loaded on a calibrated Superdex 200 SEC for further purification with buffer C or H and the typical protein yields were ~ 6.0 mg/L of *E. coli* culture.

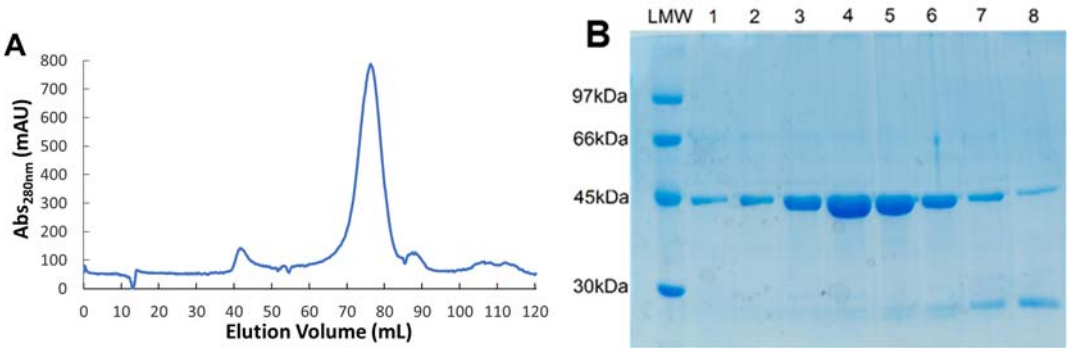

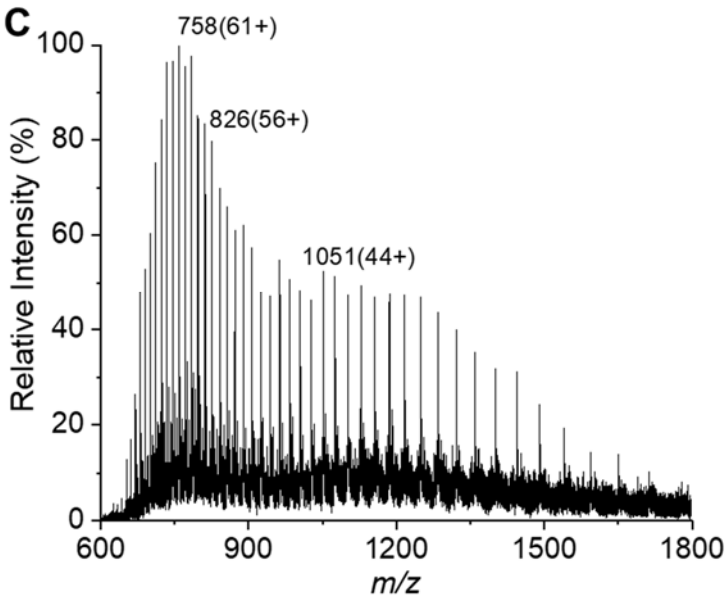

Figure 2.3.3 C'PgSPT purification and analysis. (A) Chromatogram from SES column. (B) 12% SDS-PAGE gel after SEC. LMW: Low molecular weight marker, Lane 1-8: elution fractions from 65-87 mL. (C) The +ve ion mass spectrum of recombinant C'PgSPT (10 μM) with a deconvoluted mass of 46199.18 ± 1.15 Da.

The protein was eluted at 76 mL, as shown on the S200 SEC chromatogram (Figure 2.3.3), which was the same as BfSPT, suggesting C'PgSPT also formed a homo-dimer in solution. The purity of C'PgSPT was confirmed by both SDS-PAGE and LC-ESI-MS analysis obtaining a mass of 46199.18 ± 1.15 Da, which was the same theoretical mass with the loss of initial methionine (46199.62 Da) (Figure 2.3.3). The purified PgSPT was then studied using substrate binding and enzyme assay analysis.

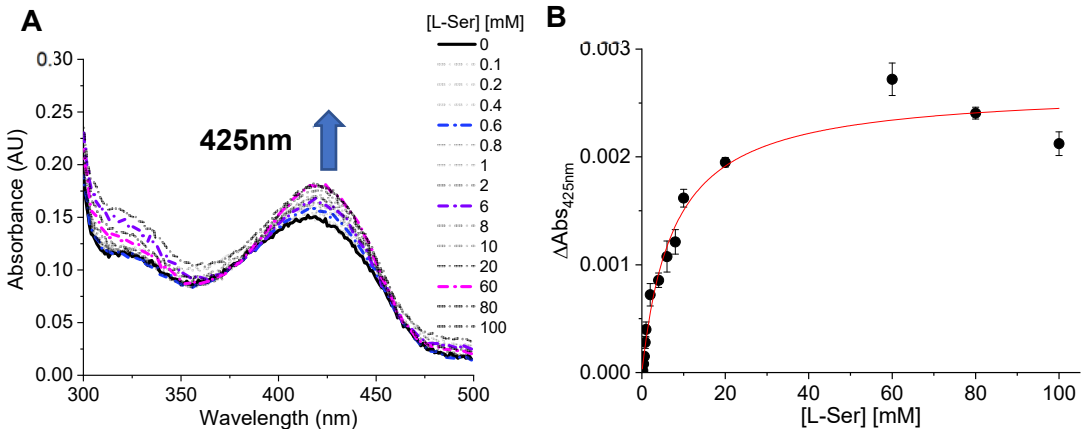

Figure 2.3.4 Monitoring and characterization of C'PgSPT binding with L-Ser. (A) UV-vis spectrum of purified C'PgSPT. (B) The determination of dissociation rate constant. The assay contained 20 μM C'PgSPT and variable concentration of L-Ser. The data were plotted as mean readings ±2-SD error bars.

Table 2.3.3 The dissociation constants for bacterial SPTs in different species [151, 159, 160, 230, 232].

Species	K_d^{Ser} (mM)
S. paucimobilis [151]	1.10 ± 0.10
S. multivorum [230]	0.47 ± 0.10
S. wittichii [159]	0.80 ± 0.10
S. spiritivorum [230]	1.20 ± 0.03
B. stolpii [230]	2.55 ± 0.12
B. fragilis	1.45 ± 0.22
P. gingivalis [232]	5.46 ± 0.60

[151] Beattie's paper; [230] Ikushiro's paper; [159] Raman's paper; [232] Rocha's paper

The purified C'PgSPT was firstly analysed by UV-vis spectrometry with an increasing concentration of the substrate L-Ser for ligand-binding. A similar pattern for BfSPT, showing only ketoenamine forms at 420 nm (Figure 2.3.4) was observed. The dissociation constant (K_d) was determined as 5.46 ± 0.60 mM. Compared to other bacterial SPT isoforms (Table 2.3.3), C'PgSPT showed the weakest L-Ser binding, which was almost 5 times and 11 times weaker than the SpSPT and SwSPT respectively and ~4 times weaker than the BfSPT. However, it was noted that during the experiment, C'PgSPT seemed to precipitate when it was exposed to room temperature for over 4 hours without the addition of PLP. As each scan had to be equilibrated for 20~25 minutes for substrate binding before measurement, the instability of C'PgSPT could influence the measurements taken and the K_d value determined. The reason for protein precipitation is still under investigation.

The C'PgSPT activity was then tested with different pH values from 6.0 to 8.0 using the DTNB assay before characterizing the kinetic parameters. These pH values were chosen since the distribution of oral mucosal pH values ranges from 6.5~7.5 [233]. The study (Figure 2.3.5) showed C'PgSPT had the best activity at 7.0 and still obtained 90% activity at 7.5 (assumed 100% activity at pH 7.0). For pH 6.0 and 8.0, only 56% and 60% activity remained. In further enzyme kinetic studies, all enzyme assays were carried out at pH 7.0.

After optimising the assay conditions, the kinetic parameters of C'PgSPT were successfully obtained (Figure 2.3.4). For L-Ser, the K_M value was 0.52 ± 0.06 mM, the V_{max} value was 0.04 ± 0.01 μM/s, the k_{cat} value was 37.9 ± 0.6 × 10^{-3} s^{-1} and the k_{cat}/K_M value was 72.9 $M^{-1}s^{-1}$. For C16-CoA, the K_M value was 84.0 ± 8.71 μM, the V_{max} value was 0.05 ± 0.01 μM/s, the k_{cat} value was 49.1 ± 1.46 × 10^{-3} s^{-1} and the k_{cat}/K_M value was 584.5 $M^{-1}s^{-1}$.

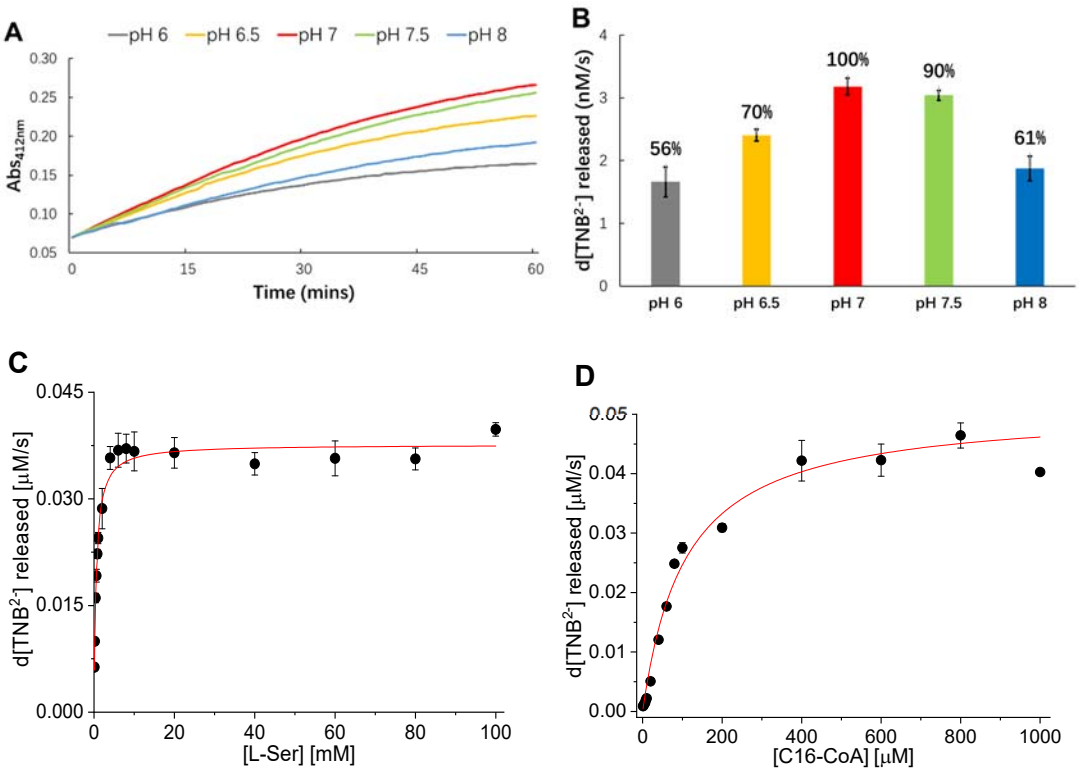

Figure 2.3.5 pH dependence and kinetic analysis of recombinant C'PgSPT by DTNB coupled assay. (A) The absorbance against time in different pH. (B) Comparison of initial rate in different pH. Each assay contained 0.1 μM enzyme. (C-D) Kinetic analysis for substrate L-serine and C16-CoA. Each assay contained 1 μM enzyme and variable concentration of L-Ser or C16-CoA. All data were plotted as mean readings ±2-SD error bars.

Table 2.3.4 Kinetic parameters for bacterial SPTs in different species [151, 159, 160, 230, 232]

SPT species	$k_{cat} \times 10^{-3}$ (s^{-1})	K_M^{Ser} (mM)	k_{cat}/K_M^{Ser} ($M^{-1}s^{-1}$)	$K_M^{C16\_CoA}$ (μM)	$k_{cat}/K_M^{C16\_CoA}$ ($M^{-1}s^{-1}$)
S.paucimobilis[151]	1150.0 ± 30.0	1.40 ± 0.10	821.4	35.4 ± 2.0	32,468
S.multivorum[230]	120.0 ± 10.0	4.80 ± 0.60	25.0	100 ± 10.0	1,200
S.wittichii[159]	68.7 ± 1.5	0.78 ± 0.10	88.1	23.4 ± 4.5	2,936
S.spiritivorum[230]	150.0 ± 10.0	5.00 ± 0.80	30.0	390 ± 40.0	385
B.stolpii[230]	30.0 ± 2.0	3.70 ± 0.40	8.1	ND	ND
B.fragilis	218.0 ± 4.0	2.02 ± 0.17	108.0	18.2 ± 2.3	2975
P.gingivalis[232]	43.5 ± 1.03	0.52 ± 0.06	72.9	84.0 ± 8.7	584

[151] Beattie's paper; [230] Ikushiro's paper; [159] Raman's paper; [232] Rocha's paper; ND, not determined

Compared to the other SPT isoforms (Table 2.3.4) [151, 159, 160, 230], PgSPT had the highest affinity for L-Ser, which was approximately 10 times higher than SsSPT and SmSPT, but had a smaller affinity with C16-CoA. The reaction speed of PgSPT was possibly limited by association with C16-CoA, as shown by observing the K_M values and $k_{cat}/K_M^{C16\_CoA}$ values of C16-CoA. To date, SpSPT is still the SPT isozyme that displays the highest catalytic activity with both substrates — L-Ser and C16-CoA.

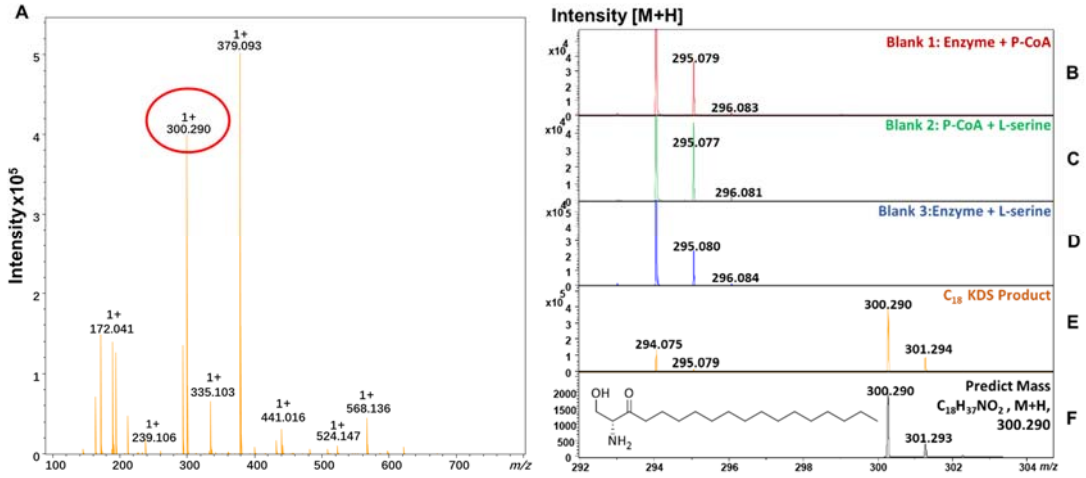

Figure 2.3.6 MALDI-ToF-MS analysis of C'PgSPT reaction product 3-KDS formed from L-Ser and C16-CoA. (A) Observation of the product 3-KDS at *m/z* = 300 amu. (B-D) negative controls (E) Full assay of C'PgSPT reaction (F) Theoretical mass. Each assay contained with 1 μM enzyme, 0.2 mM DTNB and 20 mM L-Ser or 250 μM C16-CoA was added dependent on samples. The data were analysed on the positive mode in triplicates.

The 3-KDS products produced by the SPT reaction could be successfully detected by MALDI-ToF-MS analysis (Figure 2.3.6), a C18 3-KDS product ion was shown as the main peak with an *m/z* = 300.290 and the relevant isotope peaks, which matched the theoretical mass [M+H]. A series of controls verified that only in the presence of both substrates and the enzyme, the 3-KDS was formed.

Recent studies showed that human SPT had been reported to be able to use L-Ala as well as forming deoxy-sphingolipids that caused the HSAN1 as described in the Introduction 1.3.1. Meanwhile, the *Bacteroides* SPT had also been found to act with a similar "promiscuous" catalytic activity with L-Ala and Gly in cells [96, 234, 235]. Thus, 3-KDS product screening proceeded for PgSPT and BfSPT with a variable range of amino acid substrates (Gly/L-Ala/L-Ser) and straight-chained acyl CoA substrates (C14-C18 CoAs) using the MALDI-ToF-MS method (Table 2.3.5). The data agreed with those studies that bacterial SPTs were able to catalyse the reaction with a wide range of amino acid and acyl-CoA substrates.

Table 2.3.5 Screening of 3-KDS products catalysed by PgSPT, BfSPT and BtSPT through MALDI-ToF-MS.

CoAs	Amino acids	KDSs	MW	PgSPT	BfSPT
C14-CoA	Gly	C15H31NO	243.247	✓	✓
	L-Ala	C16H33NO	256.263	✓	✓
	L-Ser	C16H33NO2	272.258	✓	✓
C15-CoA	Gly	C16H33NO	256.263	✓	✓
	L-Ala	C17H35NO	270.279	✓	✓
	L-Ser	C17H35NO2	286.274	✓	✓
C16-CoA	Gly	C17H35NO	270.279	✗	✗
	L-Ala	C18H37NO	284.294	✗	✓
	L-Ser	C18H37NO2	300.289	✓	✓
C17-CoA	Gly	C18H37NO	284.294	✓	✓
	L-Ala	C19H39NO	298.310	✗	✓
	L-Ser	C19H39NO2	314.305	✓	✓
C18-CoA	Gly	C19H39NO	298.310	✗	✗
	L-Ala	C20H41NO	312.326	✓	✓
	L-Ser	C20H41NO2	328.321	✓	✓

The study from Wieland Brown *et al.* [94] had suggested *iso*-branched SLs exist in *B. fragilis*. *Iso*-branched C17 3-KDS was detected through a PgSPT reaction with L-Ser and a small sample of *iso*-branched C15 CoA provided by Prof. Teresa Dunn's group (Uniformed Services University). It assumed that bacterial SPT could also produce *iso*-branched 3-KDS products. Unfortunately, there was commercially available *iso*-branched C15 CoA substrates to obtain kinetic data.

2.4 Inhibition studies with L- and D-cycloserine (LCS and DCS)

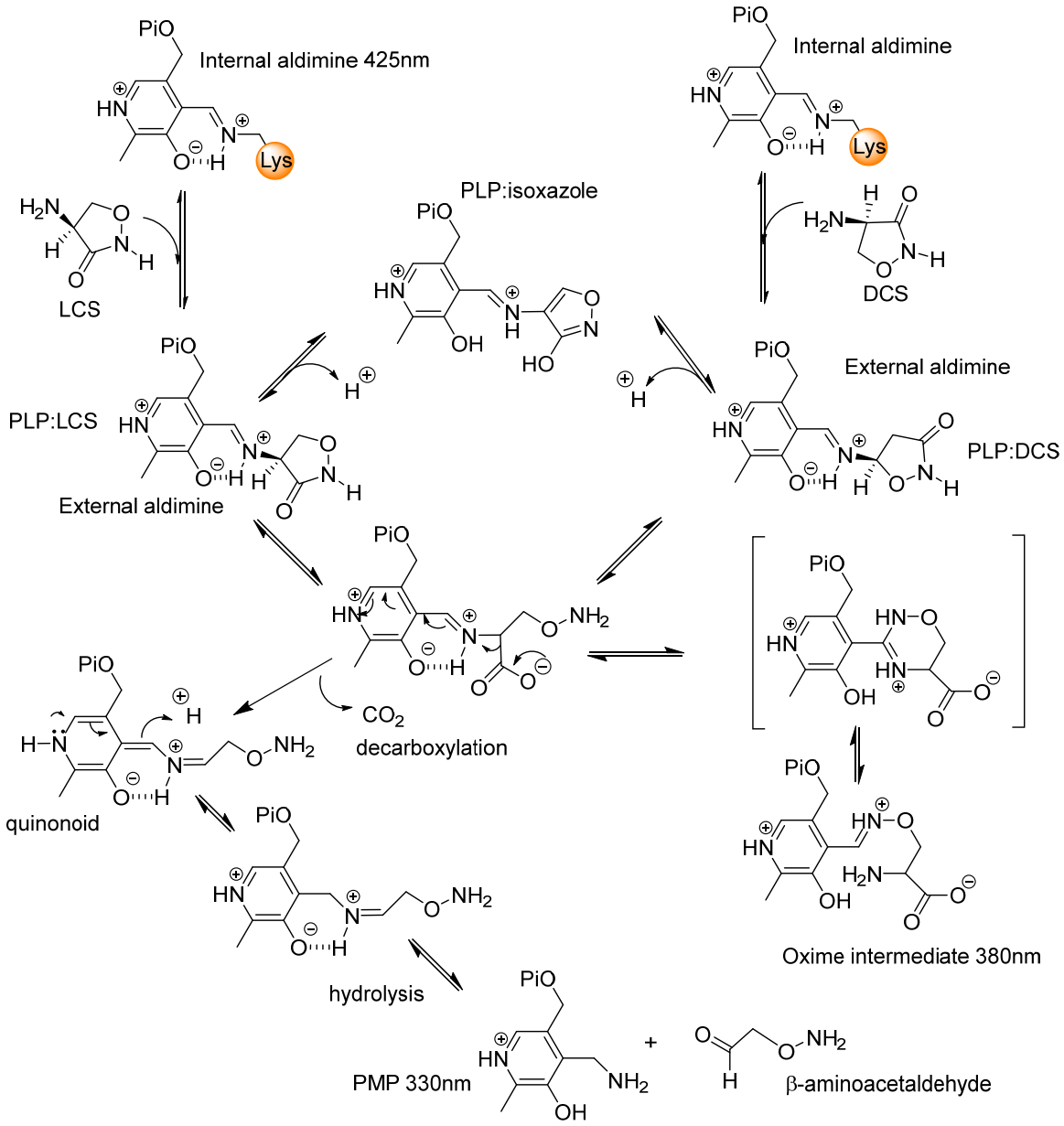

Figure 2.4.1 Proposed mechanisms of SPT inactivation by LCS and DCS inspired by studies by Lowther *et al.* and Ikushiro *et al* [173, 236].

Cycloserine (both enantiomers LCS and DCS) is a cyclic amino acid mimic which inhibits many PLP-dependent enzymes by forming an external PLP-bound isoxazole by removal of the C-α proton. However, as reported in Lowther's paper, a proposed novel decarboxylative mechanism of CS inhibition of SpSPT is shown in Figure 2.4.1 [173]. A key finding was the identification of a LCS-derived β-aminoacetaldehyde product by MS and x-ray crystallography. This suggested that SpSPT initially forms complexes of 3-hydroxyisoxazole-PMP adducts, with both LCS and DCS. The CS ring is hydrolysed and opened to form a PLP:carboxylated intermediate. This undergoes

decarboxylation (as the β-keto acid intermediate would do) in a normal SPT reaction, to give an imine. This is further hydrolysed to PMP and the β-aminoaldehyde product was observed. Alternatively, Ikushiro proposed the external aldimine of CS is opened to the transient accumulation of the oxime form of PLP [173, 236]. Lowther also noted that LCS is ~14 times more effective than DCS at inhibiting SpSPT. So, since different SPTs display different kinetic characteristics with respect to their L-Ser and acyl-CoA substrates, it was decided to examine the interaction of C'PgSPT with these interesting inhibitors.

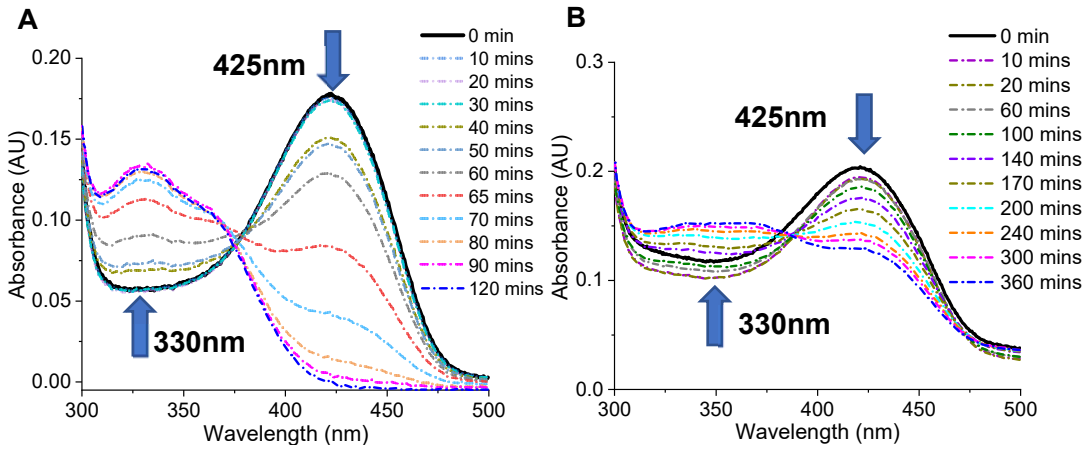

Figure 2.4.2 Absorption spectra of C'PgSPT upon the addition of (A) LCS and (B) DCS overtime period. Each assay contained 20 μM PgSPT with 0.5 mM LCS or DCS.

Analysis of the UV-vis spectrum of C'PgSPT incubated with both enantiomers of CS (Figure 2.4.2) confirms CS binds to the enzyme to form the external aldimine of the inhibitors. With LCS, the peak at 425 nm decreased with time and the 330 nm peak increased (0-120 mins). The 330 nm peak has been proposed as the PMP form. In contrast, the changes in the PLP absorbance of PgSPT incubated with DCS were different compared to LCS and they took place over 360 mins. The increased peak ranged from 320 nm to 390 nm suggesting a number of PLP-derived species were present. Moreover, it took ~2 hours for LCS to equilibrate but ~6 hours for the DCS to progress to the same extent.

$$A = A_0 e^{-k_{obs}t} \quad (1)$$

$$k_{obs} = \frac{k_{inact}[Inhibitor]}{K_i + [Inhibitor]} \quad (2)$$

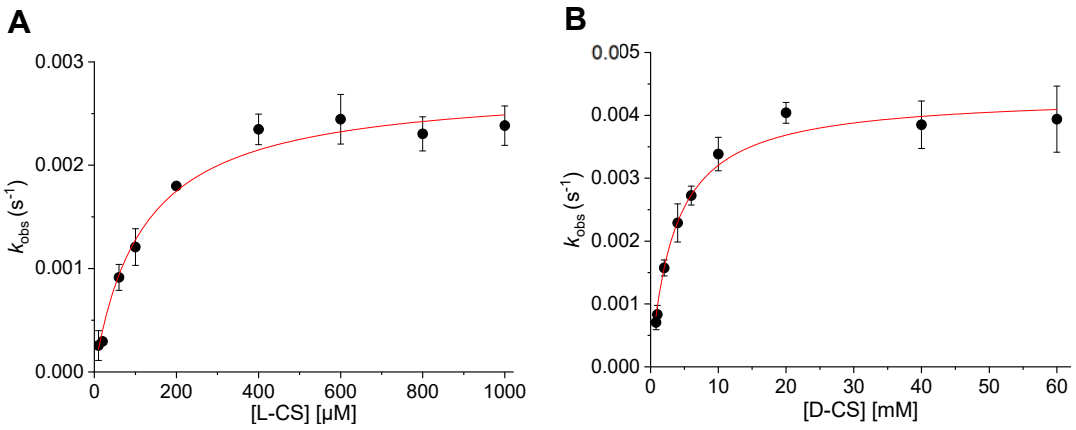

Figure 2.4.3 Irreversible inhibition analysis of C'PgSPT by (A) LCS and (B) DCS by DTNB assay. Each assay contained 0.5 μM enzyme, 20 mM L-serine, 250 μM P-CoA, and variable concentration of LCS or DCS. All data were plotted as mean readings ±2-SD error bars.

CS was reported as an irreversible inhibitor to SpSPT by Lowther *et al.* due to the weak formation of enzyme CS complex, which decomposed into PMP and β-aminoaldehyde adducts [173]. Therefore, the inhibition potency was analysed using equation (2), instead of the Kitz-Wilson plot for an irreversible inhibitor, illustrated in Figure 2.4.3 [237, 238]. This analysis was applied to any irreversible inhibitors that use the data of the proportion of enzyme activity/control that belongs to nonlinear regression. Both LCS and DCS showed inhibition of the enzyme to some extent. The maximum potential enzyme inactivation rate (k_{inact}) and the inhibition potency (K_i) of both inhibitors could be successfully estimated. For LCS, the k_{inact} value was 0.002 ± 0.001 s^{-1}, the K_i value was 117.79 ± 13.23 μM and the k_{inact}/K_i value was 22.92 ± 6.04 $M^{-1}s^{-1}$. For DCS, the k_{inact} value was 0.004 ± 0.001 s^{-1}, the K_i value was 3.52 ± 0.36 mM and the k_{inact}/K_i value was 1.22 ± 0.28 $M^{-1}s^{-1}$. In biochemical assays, the k_{inact}/K_i is used to describe the efficiency of covalent bond formation between enzyme and inhibitors, which is an essential kinetic parameter to identify the covalent inhibitors [239]. Comparing the kinetic data of both CS enantiomers, LCS was found to be ~20-fold more effective at inactivating C'PgSPT than DCS, whereas the LCS inhibitor potency was shown as ~30-fold stronger than the DCS inhibitor potency. This agreed with the evidence shown by UV-vis spectroscopy and the data obtained for SpSPT in Lowther's paper, with a k_{inact}/K_i value of LCS was 0.83 ± 0.50 $M^{-1}s^{-1}$ and k_{inact}/K_i value of DCS was 0.06 ± 0.01 $M^{-1}s^{-1}$ [173]. It would be interesting to further explore the PgSPT:CS inhibitor complexes by MS and crystallography to try to trap these proposed intermediates.

2.5 Exploring the PAVAP loop of C'PgSPT by site-directed mutagenesis

Since the AOS family of enzymes share a common mechanism with similar amino acid and acyl-CoA (or ACP) thioester substrates, a goal has been to understand the origin of the substrate specificity and explore how the complex, multi-step catalytic mechanism is controlled [111]. It appears a key step is also release of the oxoamine product in each enzyme. A highly conserved motif was identified by sequence analysis of a number of SPTs and then, once the x-ray structure of the first SpSPT had been determined by Yard et al in the Campopiano/Naismith groups, a structural and mechanistic role for this stretch of amino acids could be assigned. Within the sequence 379-PPATPAGTFLLR-390 of SpSPT is a "PPATP" loop that was shown to undergo conformational change during the catalytic cycle [158, 159]. It has been proposed that the Thr382 residue plays a similar role to the Thr352 residue in the dynamic "350-PPTVP-354" motif found in the crystal structure of the related AOS enzyme *E. coli* AONS whose structure was determined with the PLP:AON external aldimine bound [240]. The –OH from the side-chain of Thr352 is hydrogen-bonded to the carboxylate of AON in this product bound form. It is thought that dynamic nature of the loop could play a role in substrate binding and product release.

In recent research on the related AONS enzyme 5-aminolevulinate synthase (ALAS), Lendrihas *et al.* found a conserved loop increased the catalytic efficiency for the two substrates (L-Ala and succinyl-CoA) and controlled ALA product production and release [241]. By studying the loop variants with a clever mutagenesis and high throughput assay, they found out that both basicity and hydrophilicity of the enzyme were increased, which presumably stabilized the loop in the closed conformation. Having observed acyl-CoA substrate inhibition with some SPT isoforms it was a goal to explore any possible link between this conserved loop and ligand binding and product release. Interestingly, there was no substrate inhibition observed with C16-CoA in C'PgSPT in contrast to BfSPT. Based on the sequence alignment (Figure 2.3.1), we highlighted the similar loops (PAXXP or PAXP) across the bacterial SPTs. In PgSPT there is a "356-PAVAP-360" loop, therefore several loop mutants, V358C, V358A, A359S and double mutant (DM, V358C A359S) of C'PgSPT would be prepared and studied. Each enzyme was expressed and purified in a similar manner to the wild-type C'PgSPT.

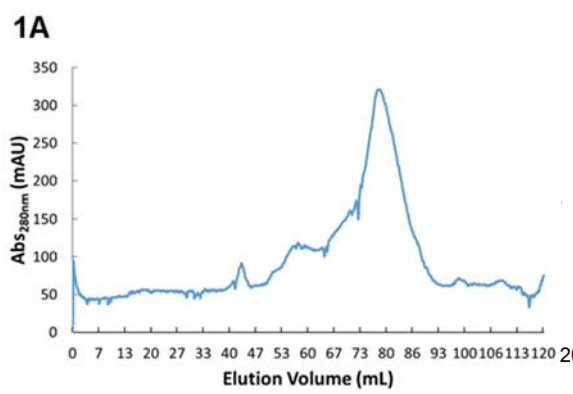
1A
Abs280nm (mAU)
350
300
250
200
150
100
50
0
0 7 13 20 27 33 40 47 53 60 67 73 80 86 93 100 106 113 120
Elution Volume (mL)

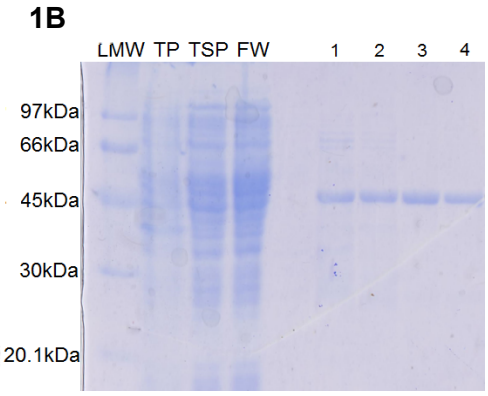
1B
LMW TP TSP FW 1 2 3 4
97kDa
66kDa
45kDa
30kDa
20.1kDa

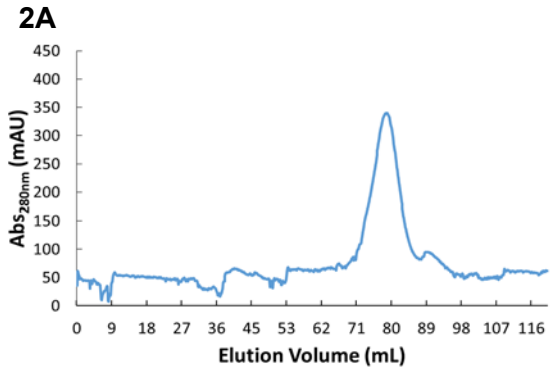
2A
Abs280nm (mAU)
450
400
350
300
250
200
150
100
50
0
0 9 18 27 36 45 53 62 71 80 89 98 107 116
Elution Volume (mL)

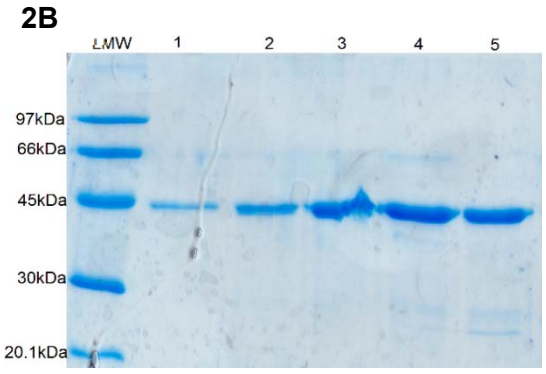
2B
LMW 1 2 3 4 5
97kDa
66kDa
45kDa
30kDa
20.1kDa

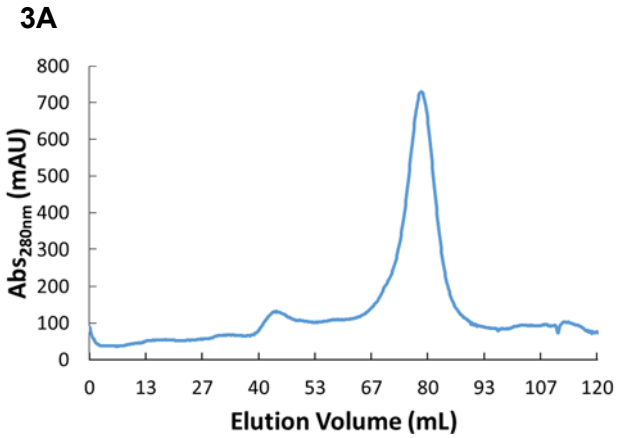
3A
Abs280nm (mAU)
800
700
600
500
400
300
200
100
0
0 13 27 40 53 67 80 93 107 120
Elution Volume (mL)

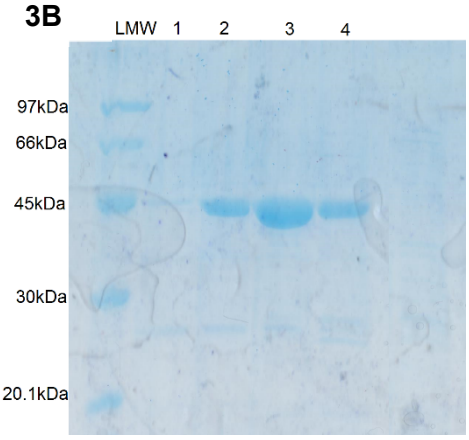
3B
LMW 1 2 3 4
97kDa
66kDa
45kDa
30kDa
20.1kDa

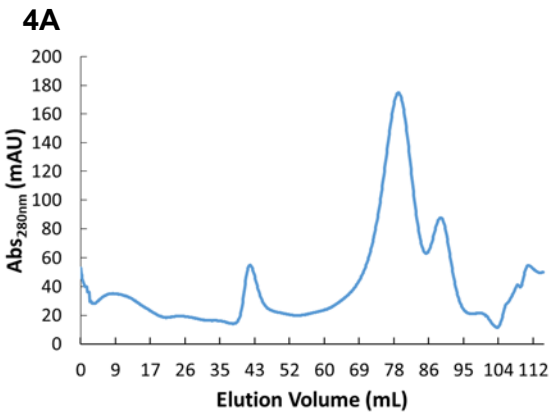
4A
Abs280nm (mAU)
200
180
160
140
120
100
80
60
40
20
0
0 9 17 26 35 43 52 60 69 78 86 95 104 112
Elution Volume (mL)

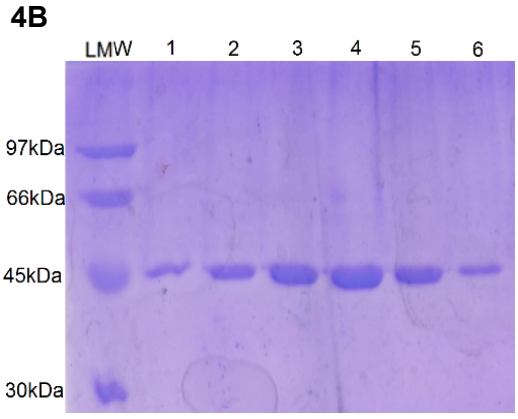
4B
LMW 1 2 3 4 5 6
97kDa
66kDa
45kDa
30kDa

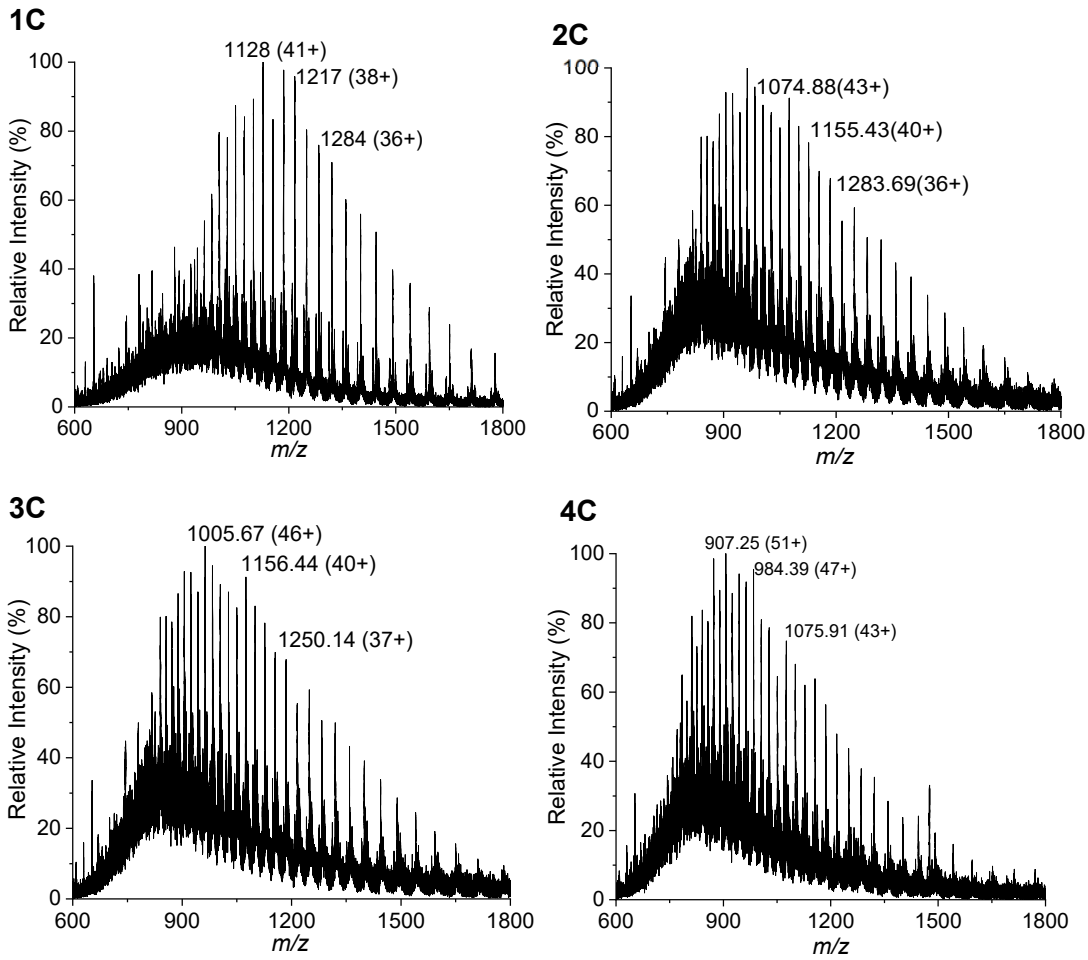

Figure 2.5.1 C'PgSPT V358C (1), V358A (2), A359S (3) and DM (4) purification and analysis. (A) Chromatogram from SES column. (B) 12% SDS-PAGE gel after SEC. LMW: Low molecular weight marker, Lane 1-8: elution fractions from main peak. (C) The mass spectrum of recombinant C'PgSPT V358C (1) with a mass of 46205.66 ± 2.85 Da, V358A (2) with a mass of 46171.06 ± 0.60 Da, A359S (3) with a mass of 46216.09 ± 1.63 Da and DM (4) with a mass of 46219.24 ± 5.74 Da. All the enzyme concentrations were 10 μM.

To further explore the function of the loop, several mutants (V385C, V358A, A359S and DM) of C'PgSPT were engineered successfully and confirmed by DNA sequencing. As shown in Figure 2.5.1, all the mutants were well expressed using the same protocol as C'PgSPT WT. This consisted of isolation using HisTrap with same buffer system and elution occurred at a similar volume ~78 mL in a calibrated SEC column. Following the purification, the integrity of all the proteins was confirmed by LC-ESI-MS, giving 46205.66 ± 2.85 Da for mutant V358C matching the theoretical mass with loss of initial methionine (46203.62 Da); 46171.06 ± 0.60 Da for mutant V358A as same as theoretical mass minus methionine (46171.56 Da); 46216.09 ± 1.63 Da for mutant A359S equalling to the theoretical mass without methionine (46215.61 Da); 46219.24 ± 5.74 Da for DM as similar to the theoretical mass missing methionine (46219.62 Da).

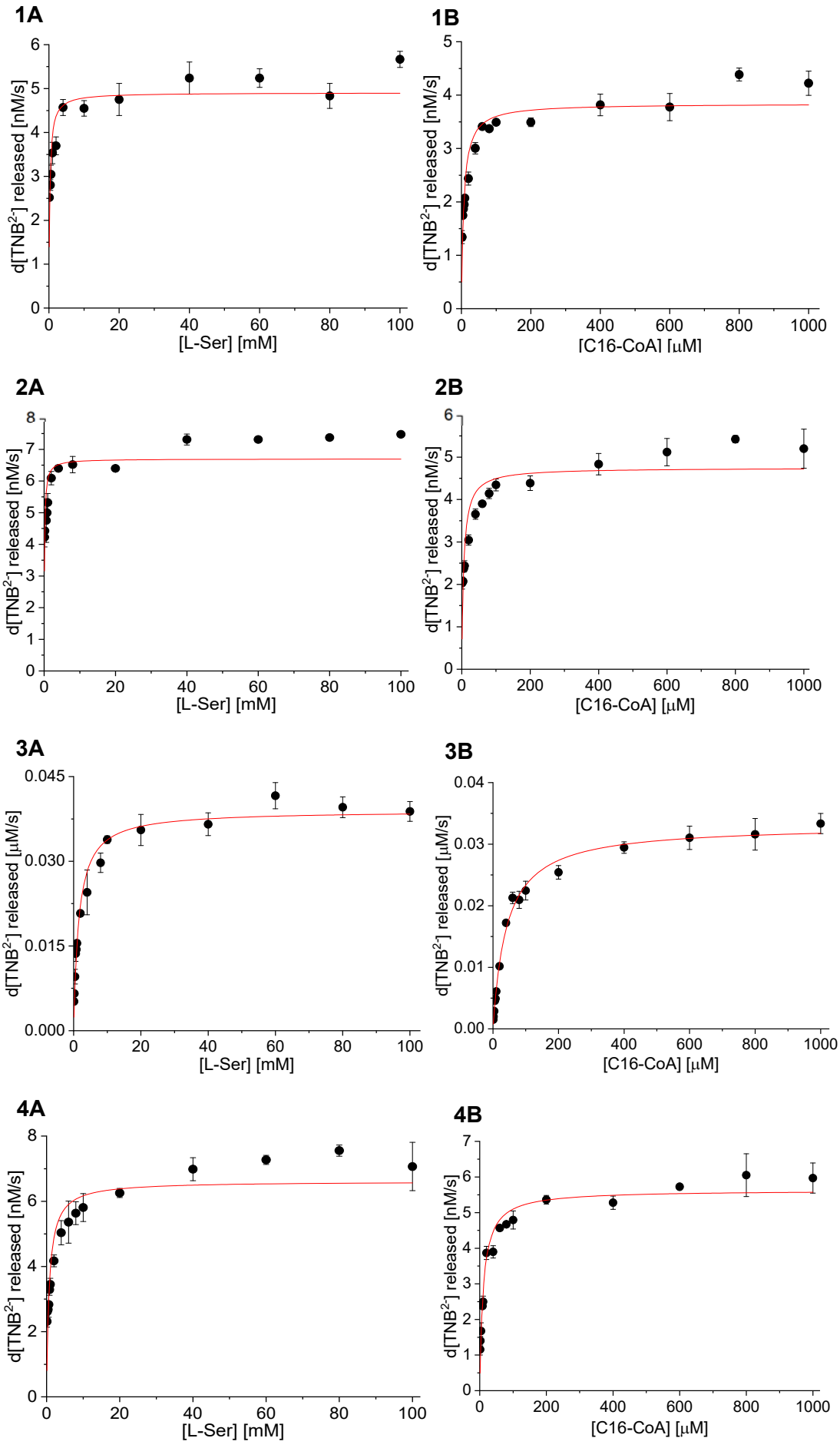
1A
d[TNB2-] released [nM/s]
[L-Ser] [mM]
1B
d[TNB2-] released [nM/s]
[C16-CoA] [µM]
2A
d[TNB2-] released [nM/s]
[L-Ser] [mM]
2B
d[TNB2-] released [nM/s]
[C16-CoA] [µM]
3A
d[TNB2-] released [µM/s]
[L-Ser] [mM]
3B
d[TNB2-] released [µM/s]
[C16-CoA] [µM]
4A
d[TNB2-] released [nM/s]
[L-Ser] [mM]
4B
d[TNB2-] released [nM/s]
[C16-CoA] [µM]

Figure 2.5.2 Kinetic analysis of C'PgSPT mutants for substrate L-Ser (A) and C16-CoA (B) by DTNB coupled assay. (1) V358C (2) V358A (3) A359S (4) DM. Each assay contained with 0.5 - 1 μM enzyme and the variable concentration of L-Ser or C16-CoA. All data were plotted as mean readings ±2-SD error bars.

After the proteins had been confirmed, a kinetic analysis carried out on each C'PgSPT mutants with both substrate L-Ser and C16-CoA (Figure 2.5.2). No substrate inhibition was observed with high concentrations of C16-CoA in all the C'PgSPT mutants. Firstly, for mutant V358C, investigating the kinetic parameters of L-Ser, the K_M value was 0.25 ± 0.05 mM, the V_{max} value was 4.91 ± 0.15 nM/s, the k_{cat} value was 4.91 ± 0.14 × 10^{-3} s^{-1} and the k_{cat}/K_M value was 19.47 $M^{-1}s^{-1}$. For C16-CoA, the K_M value was 6.70 ± 0.80 μM, the V_{max} value was 3.84 ± 0.08 nM/s, the k_{cat} value was 3.84 ± 0.08 × 10^{-3} s^{-1} and the k_{cat}/K_M value was 0.573 $mM^{-1}s^{-1}$.

Secondly, mutant V358A showed similar activity with both substrates as mutant V358C. For L-Ser, the K_M value was 0.11 ± 0.02 mM, the V_{max} value was 6.70 ± 0.15 nM/s, the k_{cat} value was 6.70 ± 0.16 × 10^{-3} s^{-1} and the k_{cat}/K_M value was 59.80 ± 8.72 $M^{-1}s^{-1}$. For C16-CoA, the K_M value was 5.65 ± 1.02 μM, the V_{max} value was 4.74 ± 0.14 nM/s, the k_{cat} value was 4.74 ± 0.14 × 10^{-3} s^{-1} and the k_{cat}/K_M value was 0.840 $mM^{-1}s^{-1}$.

Thirdly, for mutant A359S, the mutation still had an impact on the reaction activity and substrate affinity, observed via kinetics. For L-Ser, the K_M value was 1.48 ± 0.14 mM, the V_{max} value was 0.04 ± 0.01 μM/s, the k_{cat} value was 78.76 ± 1.35 × 10^{-3} s^{-1} and the k_{cat}/K_M value was 53.3 ± 9.75 $M^{-1}s^{-1}$. For C16-CoA, the K_M value was 39.48 ± 2.00 μM, the V_{max} value was 0.03 ± 0.01 nM/s, the k_{cat} value was 65.50 ± 0.80 × 10^{-3} s^{-1} and the k_{cat}/K_M value was 0.166 $mM^{-1}s^{-1}$.

Finally, the kinetic parameters of DM were determined as, for L-Ser, the K_M value was 0.72 ± 0.09 mM, the V_{max} value was 6.61 ± 0.18 nM/s, the k_{cat} value was 6.61 ± 0.18 × 10^{-3} s^{-1} and the k_{cat}/K_M value was 9.16 $M^{-1}s^{-1}$. For C16-CoA, the K_M value was 10.41 ± 0.90 μM, the V_{max} value was 5.63 ± 0.10 nM/s, the k_{cat} value was 5.63 ± 0.10 × 10^{-3} s^{-1} and the k_{cat}/K_M value was 0.540 $mM^{-1}s^{-1}$.

Table 2.5.1 Kinetic parameters for PgSPT WT and different mutants.

Enzyme	$k_{cat} \times 10^{-3}$ (s^{-1})	K_M^{Ser} (mM)	k_{cat}/K_M^{Ser} ($M^{-1}s^{-1}$)	K_M^{PCoA} (μM)	k_{cat}/K_M^{PCoA} ($M^{-1}s^{-1}$)
WT	43.5 ± 1.03	0.52 ± 0.06	72.9	84.0 ± 8.7	584
V358C	4.38 ± 0.11	0.25 ± 0.05	19.47	6.70 ± 0.80	573
V358A	5.72 ± 0.15	0.11 ± 0.02	59.80	5.65 ± 1.02	840
A359S	72.13 ± 1.08	1.48 ± 0.14	53.29	39.48 ± 2.00	1659
DM	6.12 ± 0.14	0.72 ± 0.09	9.159	10.41 ± 0.90	541

As shown in Table 2.5.1, the affinity of mutant V358C and V358A for both substrates was significantly higher, with the values 2~5-fold smaller than the K_M^{Ser} value of C'PgSPT WT and 12~15-fold times smaller than the K_M^{PCoA} value of C'PgSPT WT. On the contrary, the reaction turnover rate was dramatically decreased were ~9-fold weaker than the WT enzyme. Therefore, it is assumed that Val358 could be an important residue but may be not essential residue. However, compared to the WT enzyme, mutant A359S showed a smaller affinity with L-Ser but a higher affinity with C16-CoA. Moreover, the reaction turnover rate was twice as fast than the WT enzyme. Finally, the DM showed a higher affinity with L-Ser but a smaller affinity with C16-CoA, and the reaction turnover rate was ~7-fold weaker than the WT enzyme. Additionally, the catalytic efficiency (k_{cat}/K_M) for both substrates were the worst compared to the WT enzymes and mutant, suggesting the DM had the worst catalytic ability.

Table 2.5.2 The conserved noncatalytic loop residue in SPT isoforms.

Enzyme	Conserved loop residues
SpSPT	PATP
SwSPT	PATP
SmSPT	PAVP
BfSPT	PACSP
PgSPT	PAVAP

By analysing all k_{cat}/K_M values, it agreed with Lendrihas *et al.*'s paper [241] that both basicity and hydrophilicity of the enzyme could affect KDS release or production. Since increasing the hydrophilicity and acidity in site 358 would decrease the SPT catalytic ability, however, the changes in site 359 would increase the enzyme catalytic ability. And the undiscovered allosteric regulation could happen in the conserved loop residues (Table 2.5.2). Unfortunately, because of the high dissociation constant obtained from the WT enzyme and fragile enzyme stability without excess PLP, there was no data collected about PLP-L-Ser binding for those mutants.

2.6 The activity of SPT is influenced by the histidine affinity tag

It has been several years since people use polyhistidine affinity tags began to be used for better expression and more straightforward protein purification process. However, their potential effects on the activity and structure of the protein have been overlooked sometimes. Recent studies suggested that not only substrate specificity but also enzyme properties including structure and thermal stability had been affected by the histidine position [242, 243]. Esen *et al.* found out the C-terminal his-tagged formate dehydrogenase from *Chaetomium thermophilum* had higher catalytic efficiency, turnover number and specific activity for both substrates than N-terminal his-tagged enzyme, which C-terminus is a suitable region for tag engineering [244]. Majorek *et al.* discovered that the histidine tag could be a weak competitive inhibitor of peptide substrate for N-acetyltransferase from *Pseudomonas aeruginosa* [245]. Furthermore, Meng *et al.* showed that, in a PLP-dependent 4-aminobutyrate-2-oxoglutarate transaminase, the His-tag in both positions decreased the catalytic activity to different extents but did not influence the enantioselectivity. This phenomenon also appeared in other type I or type IV transaminase, such as *E. coli* IlvE, *etc.* [246, 247]. Thus, the N-terminal His-tag, no-tag and cleaved His-tag SPT were cloned and studied individually to understand their effects on the catalytic ability.

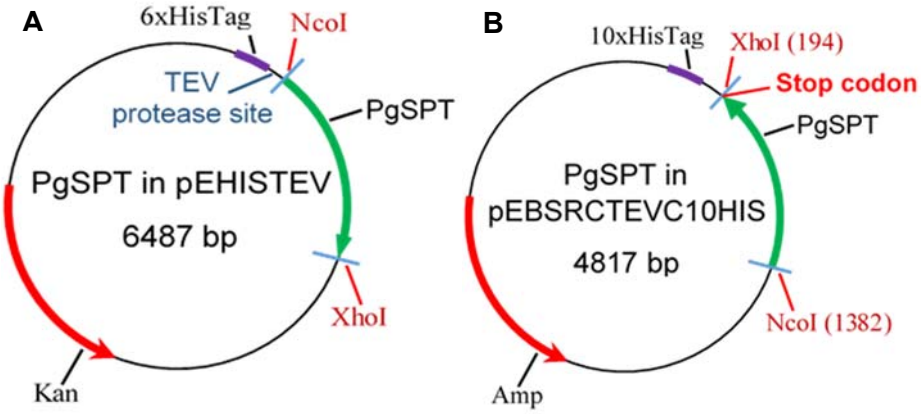

Figure 2.6.1 Plasmid map of PgSPT in N-terminal His-tag pETHISTEV (A) and no tag PgSPT in pEBSRCTEVC10HIS (B).

The PgSPT was also cloned into a N-terminal 6 x histidine expression plasmid for the crystallography trails as there had been trouble with crystallizing C'PgSPT with a 10-histidine tail in the end of the sequence. Furthermore, no tag PgSPT was designed in pEBSRCTEVC10HIS (University of St. Andrews) by putting the stop codon in the C-terminal of sequence (Figure 2.6.1).

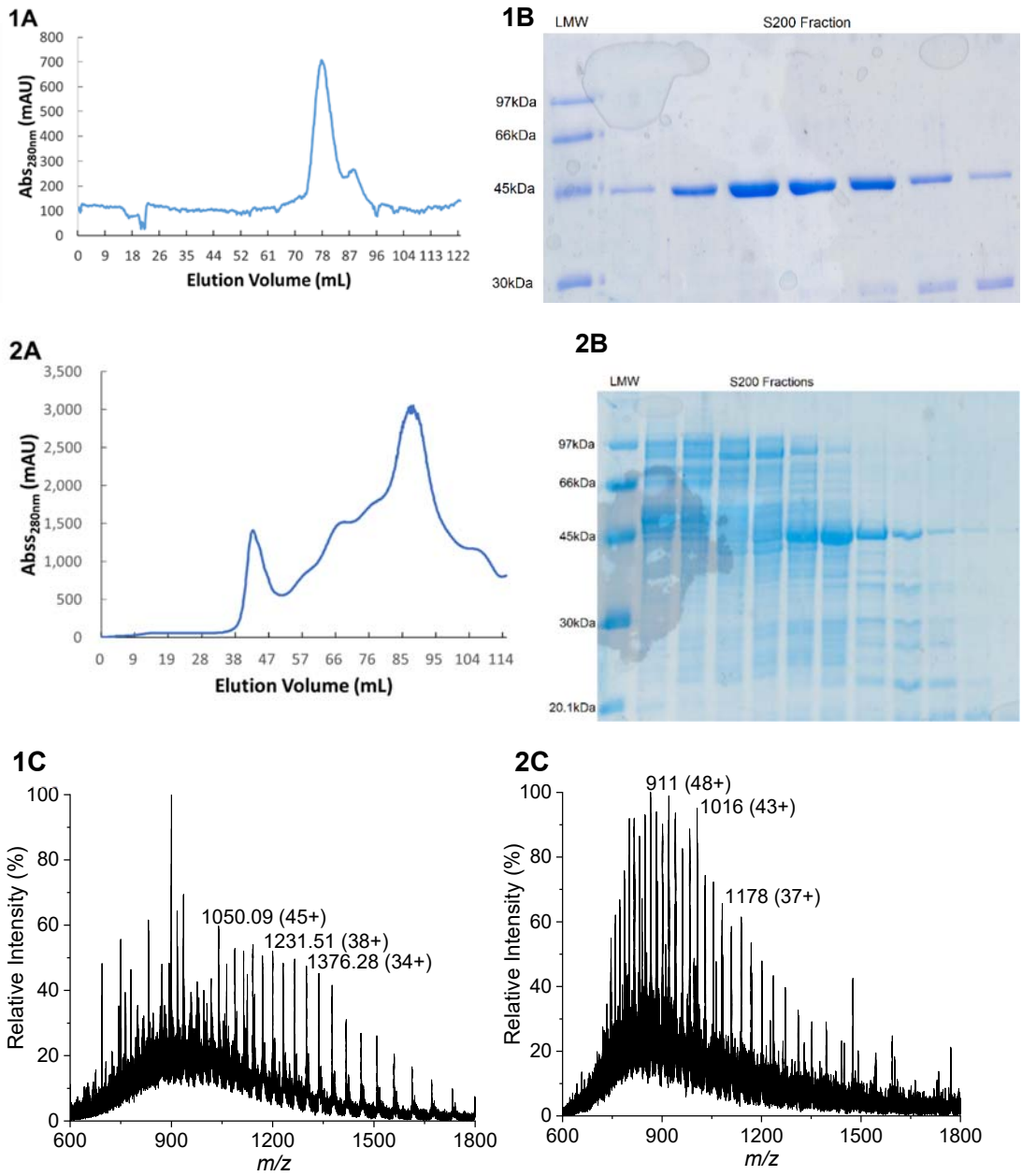

Figure 2.6.2 N'PgSPT (1) and no tag SPT (2) purification and analysis. (A) Chromatogram from SES column. (B) 12% SDS-PAGE gel after SEC. LMW: Low molecular weight marker, S200 fractions: elution fractions from the main peak. (C) The mass spectrum of recombinant N'PgSPT (1) with a mass of 46758.76 ± 0.71 Da; no tag SPT (2) with a mass of 43659.02 ± 5.67 Da. All the enzyme concentrations were 10 μM.

The N-terminal SPT (N'PgSPT) was expressed using the same conditions in *E.coli* BL21 (DE3) cells for 4~5 hours at 30°C after induction with 0.1 mM IPTG. The protein was purified using the same columns and buffer as C'PgSPT, and elution occurred at a similar volume of around 78 mL in the SEC column (Figure 2.6.2), suggesting a dimeric enzyme. The LC-ESI-MS obtained a mass at 46758.76 ± 0.71 Da, which was similar to theoretical mass without the initial methionine (46759.24 Da) calculated from protein sequence by using ExPaSy ProtParam tool website. Further

investigation was carried out to comprehend the influence of the tag on the SPT protein. However, the no tag PgSPT was expressed at 16°C overnight after 0.1 mM IPTG induction and purified using HiTrap Q 1 ml anion exchange chromatography column with buffer 0 and 1 considering the theoretical pI of the protein was 6.14. Unfortunately, the anion exchange chromatography did not separate the protein as well as HisTrap purification. Therefore, there were still impurities present in the extract after the first purification step in the main peak between 76-104 mL (Figure 3.6.6). From the SDS-PAGE analysis, there was still a strong band at ~45 kDa, which was the main no tag PgSPT, and other bands was considered as *E.coli* background proteins, which were negligible. The no tag PgSPT was also analysed by LC-ESI-MS analysis providing the protein mass of 43659.02 ± 5.67 Da, which was close to theoretical mass without the initial methionine of the no tag PgSPT (43662.94 Da).

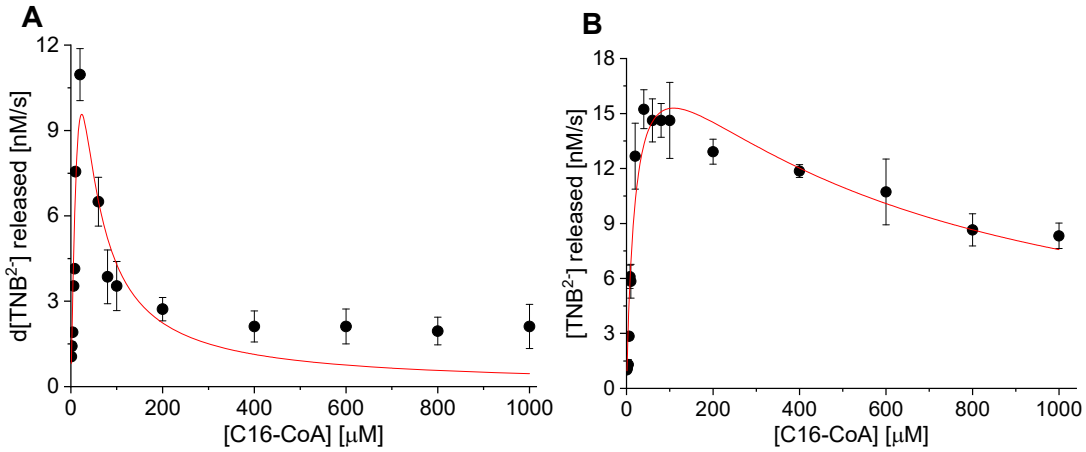

Figure 2.6.3 Substrate inhibition analysis of N'PgSPT (A) and no tag PgSPT (B) reactions for substrates C16-CoA. Each assay contained 0.5 μM enzyme, 20 mM L-Ser and variable concentration of C16-CoA. The data were plotted as mean readings ±2-SD error bars.

The purified enzyme was tested using the DTNB coupled assay to examine whether the activity had been influenced by the position of the his-tag. As shown in Figure 2.6.3, the C16-CoA substrate inhibition appeared in both N'PgSPT and no tag PgSPT, which was similar to BfSPT as discussed in section 2.1. Through substrate inhibition analysis of N'PgSPT, the estimated K_i for C16-CoA was measured as 41.42 ± 6.69 μM. Moreover, the K_M value was calculated as 20.20 ± 5.89 μM, the V_{max} value was 19.07 ± 2.87 nM/s, the k_{cat} value was 0.038 ± 0.006 s^{-1} and the k_{cat}/K_M value was 1.88 ± 1.02 $mM^{-1}s^{-1}$. For the no tag PgSPT version, the estimated K_i for C16-CoA was measured as 561.97 ± 96.32 μM. Additionally, the K_M value was measured as 21.01 ± 3.42 μM, the V_{max} value was 21.21 ± 1.40 nM/s, the k_{cat} value was 0.042 ± 0.003 s^{-1} and the k_{cat}/K_M value was 2.02 ± 0.41 $mM^{-1}s^{-1}$.

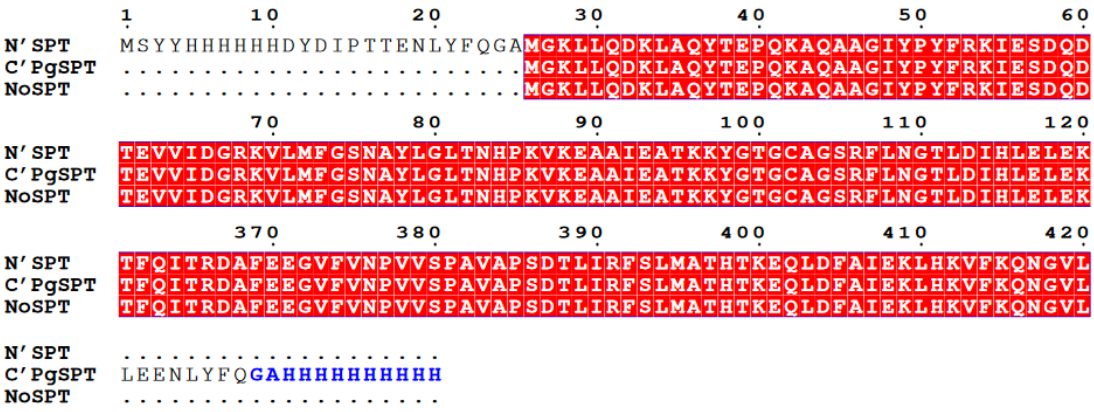

Figure 2.6.4 Sequence alignment between N'PgSPT, C'PgSPT and no tag PgSPT. The residues in blue can be cleaved by TEV protease.

Further investigation of C'PgSPT, the polyhistidine-tag could be cleaved by TEV protease, a 27kDa cysteine protease encoded by the Tobacco Etch Virus (TEV) (Figure 2.6.4) [248]. Therefore, it would be interesting to observe the enzymatic behaviour of tag-cleaved PgSPT with the substrate C16-CoA.

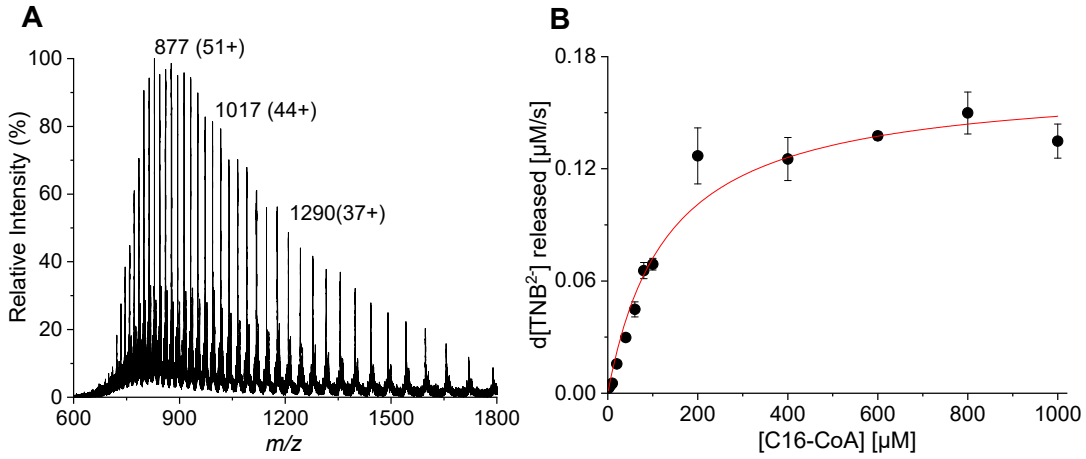

Figure 2.6.5 Characterization of tag-cleaved PgSPT. (A) The mass spectrum of recombinant tag-cleaved PgSPT with a mass of 44699.84 ± 0.61 Da. (B) Kinetic analysis of tag-cleaved PgSPT for substrate C16-CoA by DTNB coupled assay. Each assay contained with 0.5 μM enzyme, 20 mM L-Ser and variable concentration of C16-CoA. All data were plotted as mean readings ±2-SD error bars.

The tag-cleaved PgSPT was expressed and purified with HisTrap column firstly as same as C'PgSPT. The eluted protein was then dialysis with TEV protease for at least 2 hours before loading onto a HisTrap column to collect the flow-through protein. Finally, the tag-cleaved PgSPT was purified by SEC column. The tag-cleaved PgSPT was confirmed by LC-ESI-MS analysis (Figure 2.6.5) showing a mass of 44699.84 ± 0.61 Da, which corresponded to the theoretical mass without initial methionine

(44700.07 Da) calculated from recombinant protein sequence by using ExPaSy ProtParam tool website.

The pure tag-cleaved PgSPT was tested with the substrate C16-CoA by DTNB coupled assay (Figure 2.6.5). Surprisingly, the C16-CoA substrate inhibition did not appear in tag-cleaved PgSPT. The K_M value was measured as 132.0 ± 14.47 μM, the V_{max} value was 167.6 ± 6.02 nM/s, the k_{cat} value was 0.34 ± 0.01 s^{-1} and the k_{cat}/K_M value was 2.54 ± 0.42 $mM^{-1}s^{-1}$.

Table 2.6.1 Comparison of enzymatic activity with PgSPT in different tag form.

Enzyme	$k^{cat} \times 10^{-3}$ (s^{-1})	$K_M^{C16\_CoA}$ (μM)	$k^{cat}/K_M^{C16\_CoA}$ ($M^{-1}s^{-1}$)	$K_i^{C16\_CoA}$ (μM)
C'PgSPT	43.5 ± 1.03	84.0 ± 8.7	584	None
Tag-cleaved PgSPT	335.2 ± 10.0	132.0 ± 14.47	2539	None
N'PgSPT	38.0 ± 6.0	20.20 ± 5.89	1881	41.42 ± 6.69
No Tag PgSPT	42.4 ± 3.0	21.01 ± 3.42	2018	561.97 ± 96.32

In a summary table Table 2.6.1, the N'PgSPT had approximately a 4-fold higher affinity with the C16-CoA substrate than the C'PgSPT version. Surprisingly, the catalytic efficiency was nearly triple stronger than the WT enzyme because of the tight substrate affinity. As the no tag PgSPT, the substrate affinity for substrate C16-CoA was similar to N'PgSPT; however, the turnover number and catalytic efficiency were both higher. Meanwhile, the substrate inhibition was smaller compared to the N'PgSPT. For tag-cleaved PgSPT, the substrate affinity for substrate C16-CoA was ~1.5-fold smaller than the C'PgSPT, but the turnover number and catalytic efficiency was ~5-fold higher. Therefore, it was assumed that the histidine tag position did have an ability on PgSPT to affect the enzymatic activity, efficiency and specificity and caused the substrate inhibition.

2.7 Crystallography study of C-terminal pETHis$_{10}$ PgSPT

A crystal structure of C'PgSPT would give a good understanding of enzymatic activity as discussed above and possibly show the C16-CoA binding with the enzyme. Different concentration of PgSPT (7 mg/ml ~ 10 mg/ml) were screened with commercial precipitants in PEG/Ion, JCSC-plus, Midas and Structure Screen 1+2 using sitting drop vapour diffusion method into 96 well plates setting by the Art Robbins Gryphon nano-litre pipetting robot machine. Unfortunately, the crystals from all the possible conditions were sharp and overlapped even with optimization plate trails (Figure 2.7.1 A), which was poor quality for X-ray diffraction analysis in the next step. Since the crystallisation of C'PgSPT was difficult to be achieved, the tag-cleaved PgSPT version was also prepared for screening trials. Theoretically, without the flexibility of the histidine tag, the enzyme would form crystals much more easily [249]. As shown in Figure 2.7.1 B, the TEV cleaved PgSPT crystallized with a square shape morphology. Unfortunately, until the end of the PhD, the optimized PgSPT structure had not been successfully obtained. Therefore, a possible model is designed and will be discussed later.

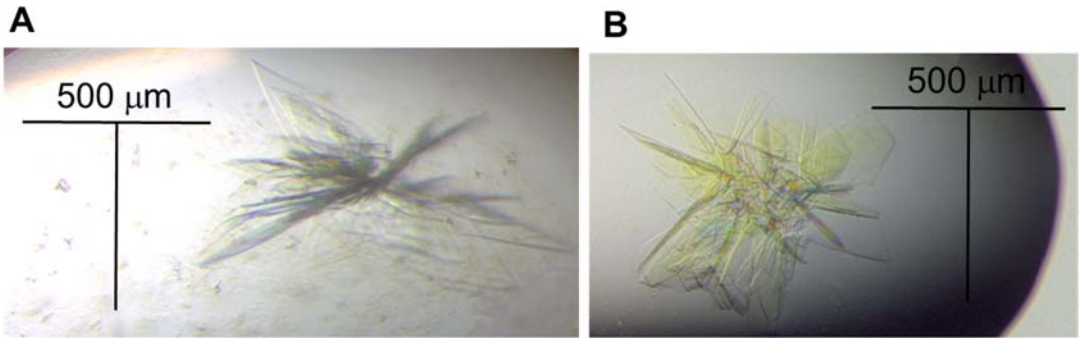

Figure 2.7.1 Crystal morphology of C'PgSPT WT (A) from JCSG+ A5 and tag-cleaved PgSPT from Midas A11 optimization plates. Precipitation condition: (A) 0.2 M magnesium formate dihydrate, 20% w/v polyethylene glycol (PEG) 3350, 8.6 mg/mL C'PgSPT; (B) 35% w/v pentaerythritol ethoxylate (15/4 EO/OH); 0.2 M calcium chloride; 0.1 M HEPES-NaOH; pH 6.5, 9.3 mg/mL tag-cleaved PgSPT.

A hypothetical homology model of PgSPT (Figure 2.7.2) is constructed based on the SmSPT (PDB:3a2b) by using Swiss-Model online software [161, 250-254]. The structure contains two monomeric chains composing a homodimer and the external aldimine (PLP:L-Ser) in the active site. The residue coverage of a monomeric chain is from 4 – 390. The interaction between PLP: L-Ser and conversed residues of SPT isoforms is shown as Figure 2.7.2 (B). The essential His137 residue holds a pi

stacking with the external aldimine. Asp209 and His212 form a hydrogen bond with the pyridinium ring. Since the L-Ser is attached to PLP via aldimine linkage, the catalytic Lys243 is detached from the PLP. Furthermore, one of the O from the carboxylic group of L-Ser make a polar contact to His212 and the hydroxyl group of L-Ser forms a polar contact with the phosphate group of PLP. the OH group of Thr240 had a polar contact with phosphate group to stabilise the PLP. Additionally, there is no direct contact with the conversed Arg366 suggesting this residue possibly plays a role in the enzyme.

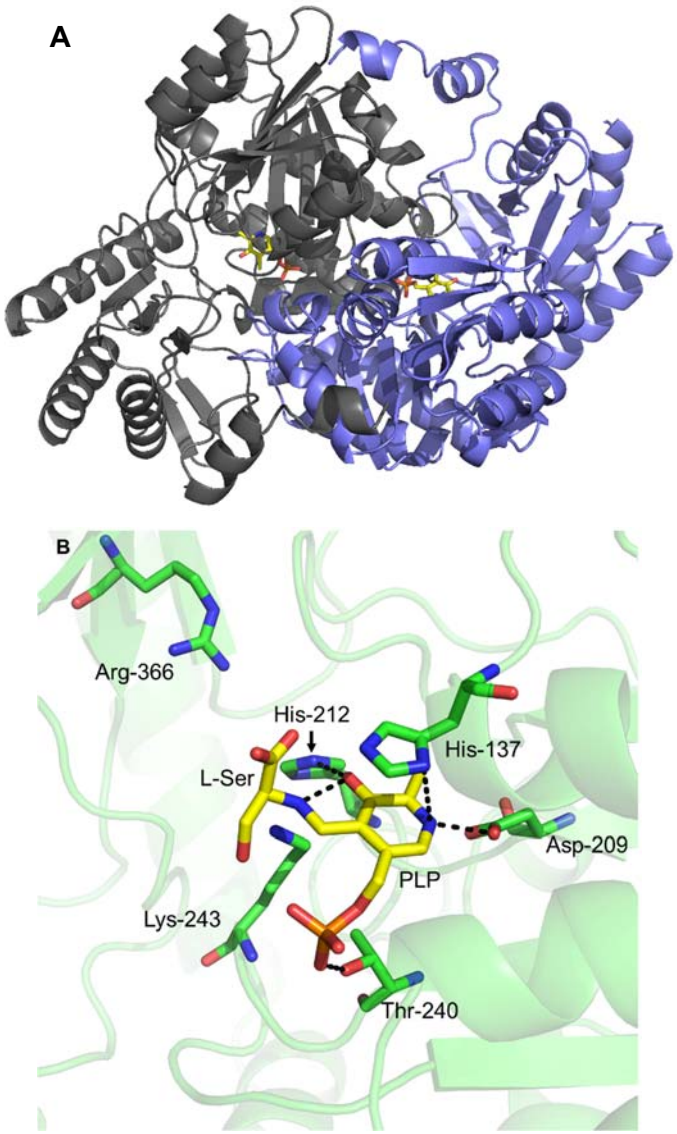

Figure 2.7.2 The homology structure model of PgSPT (A) The biological SPT dimer, the protein is shown as a cartoon with one subunit coloured blue and white. The PLP is modelled as external aldimine with L-Ser. (B) Detailed information of the external aldimine PLP:L-Ser interacted with conserved residues.

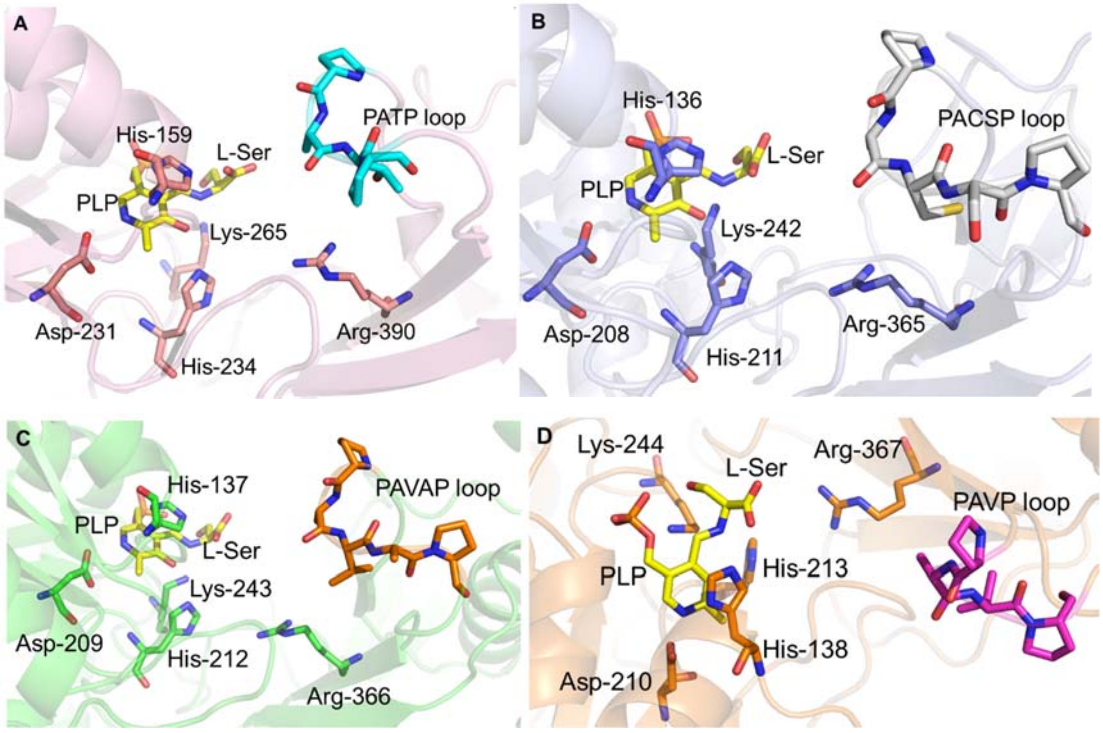

Figure 2.7.3 Comparison of the flexible loop between SPT structures. (A) SpSPT, PDB: 2W8J [159]. (B) BfSPT, PDB:unpublished. (C) PgSPT, hypothetical model. (D) SmSPT, PDB:3a2b [161].

As shown in Figure 2.7.3, the flexible loop (PAXXP or PAXP) is conserved in the other SPTs and the enzyme activity has already discussed in Section 2.5. Comparing these SPTs, it is known that the loop may influence the selection of the second substrate, due to the loop has no direct contact with the PLP:L-Ser form. And the PACSP or PAVAP (in BfSPT and PgSPT) seems to be more flexible for the second substrate compared to PATP and PAVP (in SpSPT and SmSPT), leading to the high substrate affinity but low reaction rate for the enzyme, as shown in PgSPT mutants' kinetic data. Meanwhile, the enzyme may control the substrate tighter over the reaction flux. However, the evidence for the function of the conserved loop is still investigated, a crystal structure of SPT in its quinonoid form or product external aldimine would be an excellent target to study.

Chapter 3 Iso-branched chain amino transferase (IlvE)

3.1 Analysis of IlvE/BCAT enzymes

As discussed in the introduction 1.3.2, the PLP-dependent transaminase IlvE/BCAT is a vital enzyme that is involved in branched chain fatty acid synthesis. Our hypothesis is that an IlvE is involved in the formation of the *iso*-Me branch of SLs from bacteria found in the microbiome (e.g. Bacteroides) and in the pathogen *P. gingivalis*. This suggests that branched-chain amino acids are precursors of bacterial SLs. We did genetic analysis to study the evolutionary history of the IlvE/BCAT homologs (Figure 3.1.1). Interestingly, in some specific cases, the putative *H. sapiens* IlvE is closer to the proteobacteria homolog rather than the eukaryotic version, and in the same phylum of *Deinococcus-Thermus*, *D. radiodurans* IlvE has the same ancestry with the *Bacteroides* IlvE, but *T. thermophilus* has the same ancestry with the proteobacteria IlvE. For most cases, the compatibility of the IlvE gene phylogeny displayed a high degree of conservation and similar inheritance to that shown by SPT phylogeny analysis. Furthermore, there are numerous crystal structures of IlvE isoforms in the PDB (Table 3.1.1). One interesting isoform has been studied most is the BCAT2 from *H. sapiens*, which is 29% identical to PgIlvE. By 2020, approximately 28 protein crystal structures have been published in various different crystal forms with the PLP cofactor bound and, in some cases, with bound substrates or inhibitors [185, 200, 202, 255-258]. Of interest, no structures had been published of an IlvE isolated from an organism from the human microbiome system, with the most similar being the IlvE crystal structure from *Deinococcus radiodurans* (48% similar to PgIlvE) [259]. Thus, our aim was to characterise the structure, mechanism and inhibition of PgIlvE, and begin to understand the details of the role of PgIlvE in microbial SL biosynthesis. To achieve this we began by cloning the putative PgIlvE gene identified by our bioinfomratic analysis and expressing the recombinant PgIlvE in *E. coli* using standard methods.

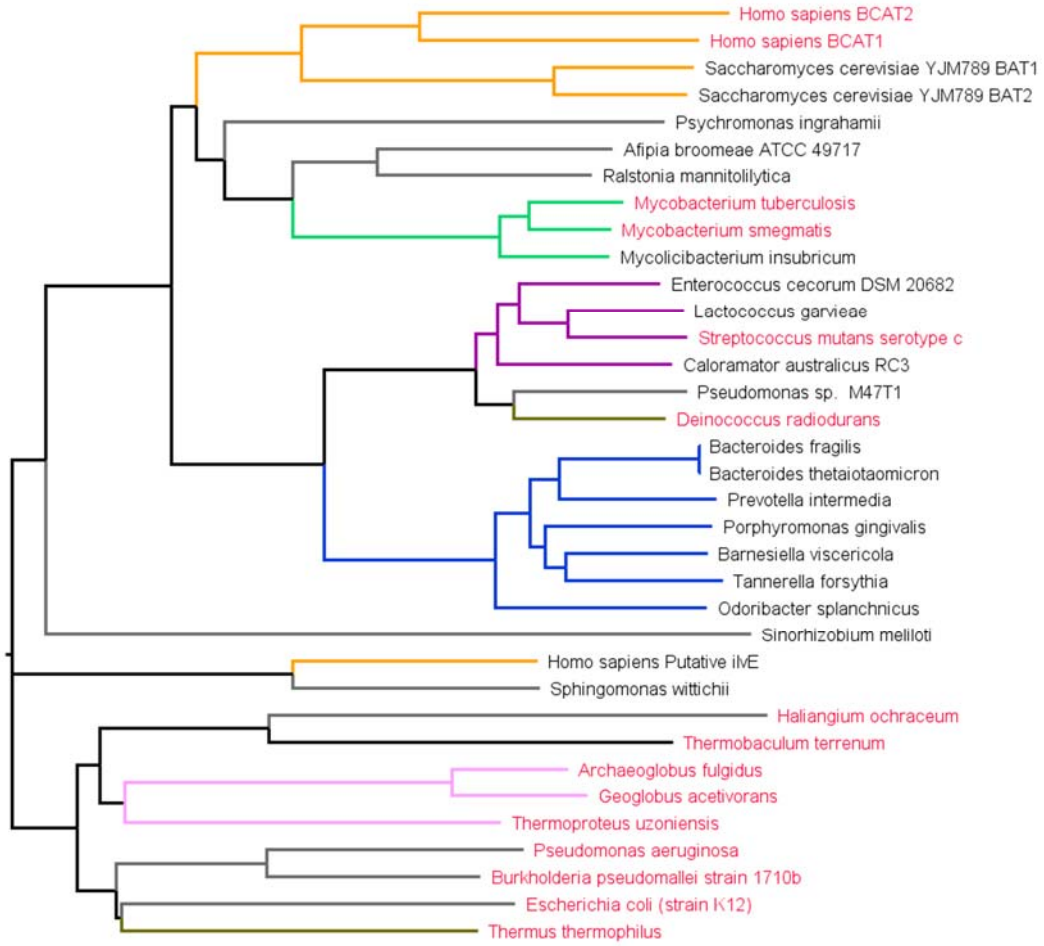

Figure 3.1.1 The phylogenetic tree of IlvE/BCAT genes. Phylum Classification: Grey line: *Proteobacteria*; Orange line: *Eukaryotic*; Green line: *Actinobacteria*; Purple line: *Firmicutes*; Blue line: *Bacteroides*; Pink line: *Archaea*; Dark yellow line: *Deinococcus-Thermus*. The species obtained pdb structure were painted in red.

Table 3.1.1 Structural information on IlvE/BCATs.

Species	Uniprot Code	PDB Code	Identity to PgIlvE	Similarity to PgIlvE
D. radiodurans	Q9RTX5	3UYY; 3UZB; 3UZO	48%	65%
S. mutans serotype c	Q8DTW7	4DQN	47%	64%
M. smegmatis	A0R066	3JZ6; 3DTF; 3DTG	39%	57%
M. tuberculosis	P9WQ75	3HT5; 5U3F	37%	53%
H. sapiens (BCAT1)	P54687	2ABJ; 2COG; 2COI; 2COJ	33%	50%
H. sapiens (BCAT2)	O15382	1EKF; 1EKP; 1EKV; 1KT8; 1KTA; 2A1H; 2HDK; 2HG8; 2HGW; 2HGX; 2HHF; 5BWR; 5BWT;5BWU; 5BWV; 5BWW;5BWX; 5CR5; 5HNE; 5I5S; 5I5T; 5I5U; 5I5V; 5I5W; 5I5X; 5I5Y; 5I60; 5MPR	29%	47%
E. coli	P0AB80	1A3G; 1I1K; 1I1L; 1I1M; 1IYD; 1IYE	28%	47%
T. terrenum	D1CCW1	6GKP; 6GKR	28%	45%
T. thermophilus	Q5SM19	1WRV; 2EIY; 2EJ0; 2EJ2; 2EJ3	29%	45%
A. fulgidus	O29329	5MQZ; 5MR0	27%	45%
G. acetivorans	A0A0A7GJ30	5CM0; 5E25	27%	45%
T. uzoniensis	F2L0W0	5CE8	27%	45%
B. pseudomallei	Q3JVJ9	3U0G	26%	44%
P. aeruginosa	O86428	6NST	26%	43%
H. ochraceum	D0LR31	6H65	24%	43%

3.2 Cloning, expression, purification of *P. gingvalis* IlvE (PgIlvE)

The IlvE gene (PG1290, Uniprot Code: Q7MV21) was firstly cloned into a pGEM-T Easy plasmid with NdeI and BamHI restriction sites, then was cut and re-cloned into a pET-28a with N-terminal 6xHis-tag with the same restriction enzymes (Figure 3.2.1).

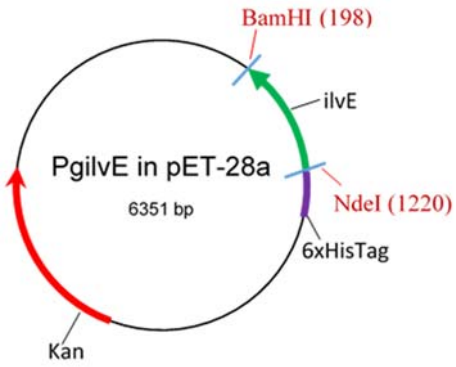

Figure 3.2.1 Plasmid map of *P.gingvalis* IlvE

After confirming the gene sequence, the protein was successfully expressed in *E. coli* BL21 (DE3) at 16 °C overnight after induction with 0.1 mM IPTG. The PgIlvE was purified by HisTrap column using buffer Q and R for protein essay or buffer S and T for crystallography trails. A further purification step using an S200 SEC was used with buffer U or V depending on the purpose (kinetic/crystals) and the pure PgIlvE was eluted around ~69mL (Figure 3.2.2). According to the calibration curve, the quaternary structure of IlvE was a dimer. The protein was confirmed by SDS-PAGE analysis and LC-ESI-MS showing a denatured mass of 39852.70 ± 1.04 Da, which matched the theoretical mass without the initial methionine (39853.49 Da) calculated from protein sequence by using ExPaSy ProtParam tool website.

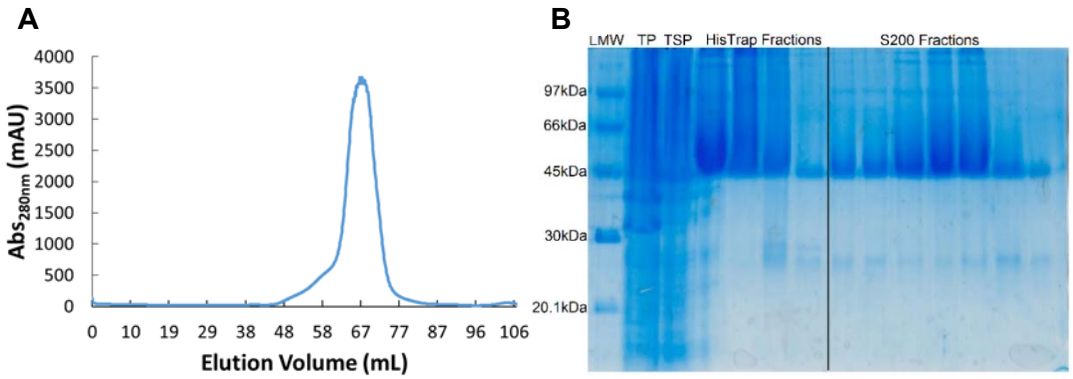

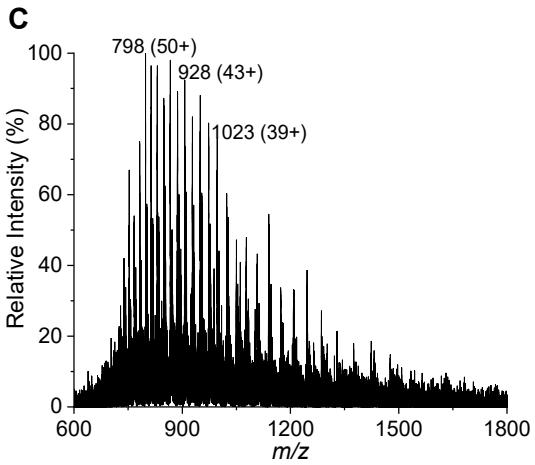

Figure 3.2.2 PgIlvE purification and analysis. (A) Chromatogram from SES column. (B) 12% SDS-PAGE gel after SEC. LMW: Low molecular weight marker, TP: total protein, TSP: total soluble protein, Lane 1-8: elution fractions from 65-87 mL. (C) The mass spectrum of recombinant PgIlvE (10 μM) with a mass of 39852.70 ± 1.04 Da.

3.3 Spectroscopic analysis of PgIlvE

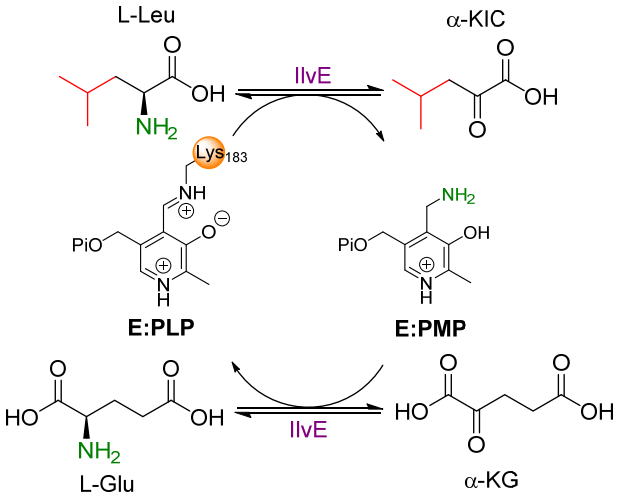

Figure 3.3.1 Schematic diagram of the IlvE reaction. L-Leu is shown as one of the *iso*-branched amino donors, α-KG as amino acceptor, α-KIC as keto product and L-Glu as amino product.

It is known that PgIlvE plays a crucial role at catalysing the metabolism of *iso*-branched amino acids using a PLP cofactor and the reversible reaction that the enzyme catalyses can be followed by UV-vis spectroscopy both in the forward (L-Leu to α-ketoisocaproic acid (α-KIC)) and reverse (L-Glu to α-ketoglutaric acid (α-KG)) directions (Figure 3.3.1) [210]. The purified PgIlvE WT displayed two forms, the enolimine (410 nm) and ketoenamine (330 nm), when bound as an internal aldimine/Schiff base. When the amino donor, L-Leu or L-Glu, was added to the enzyme, the peak around 410 nm decreased and the peak around 330 nm increased, suggesting that the PLP-bound cofactor has been converted into the PMP form and, at the same time, the first keto product was released. When the amino acceptor, α-KG or α-KIC, was added to the incubation, peaks corresponding to the PLP (410 nm) and the PMP (330 nm) forms of the PgIlvE, returned to as they were before suggesting the formation of the PLP-bound *holo*-form of the enzyme. These spectral changes are consistent with those observed for other BCAT enzymes and confirm the PgIlvE as an active enzyme.

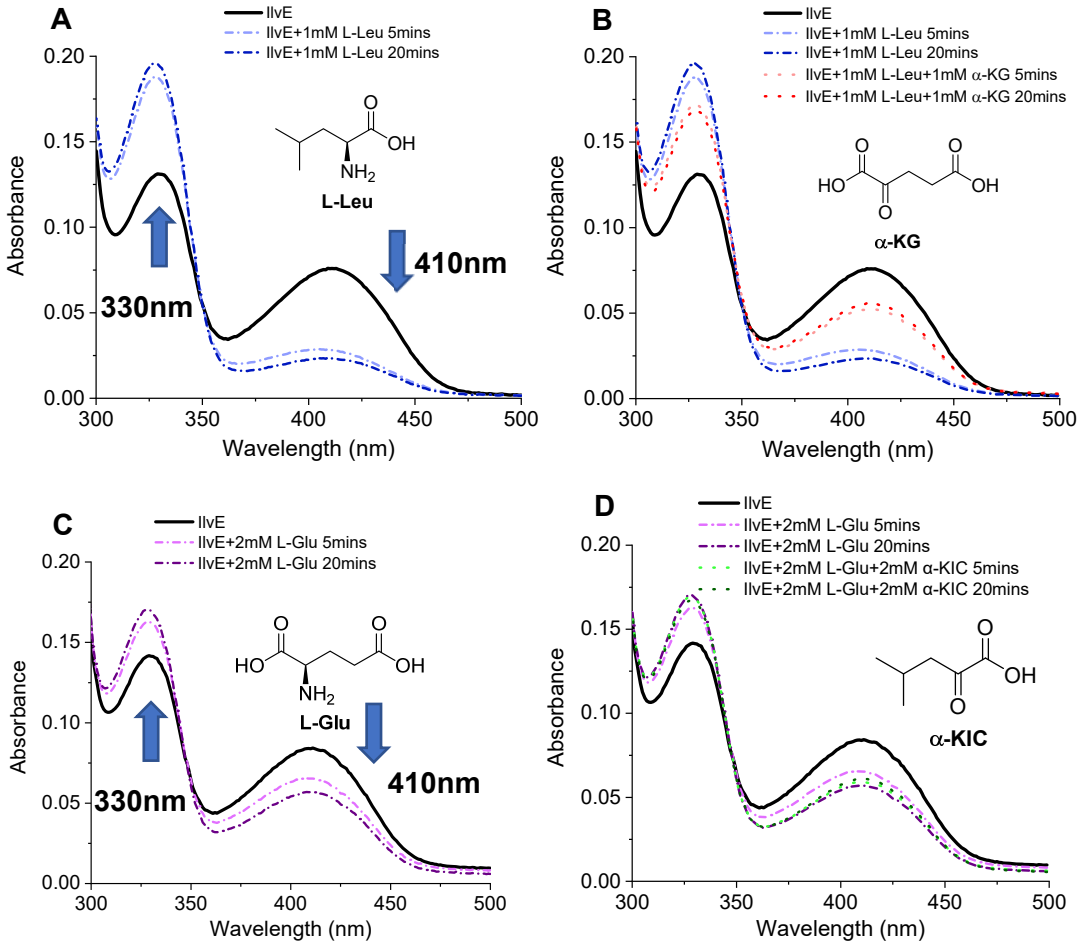

Figure 3.3.2 UV-vis spectra of PgIlvE in the 'forward' and 'reverse' reaction. The absorbance changes of PgIlvE with addition of L-Leu (A), L-Leu + α-KG (B), L-Glu (C), L-Glu + α-KIC (D) over time. Each assay contained 20 μM PgIlvE.

As shown in Figure 3.3.2, the 'forward' direction (A-B) was studied by addition of 1 mM L-Leu and monitoring changes between 0-20 mins. This led to a decrease in the peak at 410 nm and formation of a broad absorbance with λ_{max} at 405 nm. At the same time, the peak at 330 nm was increased and shifted to a new peak at 328 nm. Then, after 1 mM of α-KG was added and the absorbance changes were monitored for another 20 mins, the PMP peak at 328 nm decreased and the PLP peak at 405 nm increased. Meanwhile, in the 'reverse' direction (C-D) for substrate L-Glu and α-KIC showed a similar pattern when compared to the spectra in the 'forward' direction. However, even when the concentrations of L-Glu and α-KIC were doubled compared to those of L-Leu and α-KG, it appeared that PgIlvE favours reaction with L-Leu and α-KG rather than with L-Glu and α-KIC. The K_d value of each substrate would be one of the best parameters for measuring the substrate preference of the enzyme but because of the fast substrate turnover the determination of K_d values was challenging.

3.4 Characterization of PgIlvE

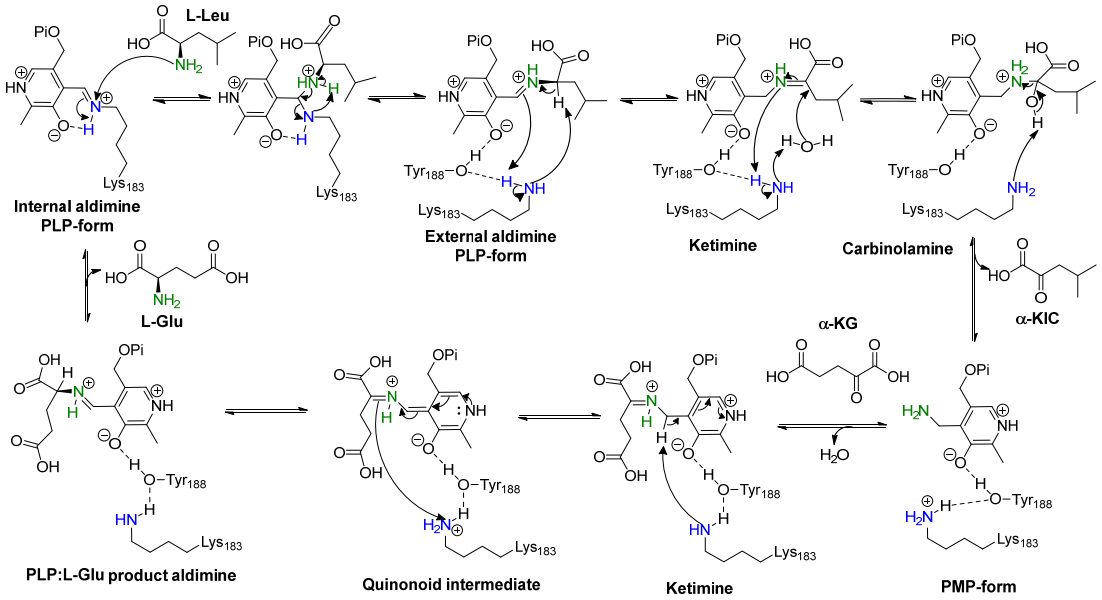

Figure 3.4.1 The proposed mechanism of PgIlvE reaction using L-Leu as amino donor and α-ketoglutaric acid (α-KG) as amino acceptor [178, 210].

The mechanism of PgIlvE could be proposed based on the classic PLP-dependent transaminase enzyme reaction (Figure 3.4.1) [178, 210]. In the first step of the reaction, the internal aldimine (PLP-form enzyme, bound to Lys183) undergoes transimination from an amino group in the amino donor (L-Leu as example here) to form the external aldimine (enzyme-substrate complex). A ketimine intermediate is formed is hydrolysed by water to become a carbinolamine [210]. The keto product (α-KIC) is released from the enzyme-substrate complex and the PLP-form of the enzyme is transformed into the PMP-form of the enzyme. Similar to the first step of the reaction, the PMP-form of the enzyme would react with the amino acceptor (α-KG) leading to the PLP:ketimine intermediate, which is then deprotonated to the quinonoid intermediate, which is converted to the quinonoid. This quinonoid is prontated to give the PLP:L-Glu external aldimine which releases the amino acid product (L-Glu) and returns into internal aldimine, PLP-bound form of the enzyme.

Four spectrophotometric coupled assays were developed for determining the PgIlvE activity in both directions. These assays used (i) glutamate dehydrogenase (GDH) from bovine liver (ii) colorimetric detection method via the NADH/mediator/tetrazolium route developed by Ward's group [260], (iii) oxoglutarate dehydrogenase/α-ketoglutarate dehydrogenase (OGH/KDH) from porcine heart, and (iv) leucine dehydrogenase (LeuDH) from *Bacillus cereus* [261, 262].

3.4.1 Coupled IlvE-GDH assay

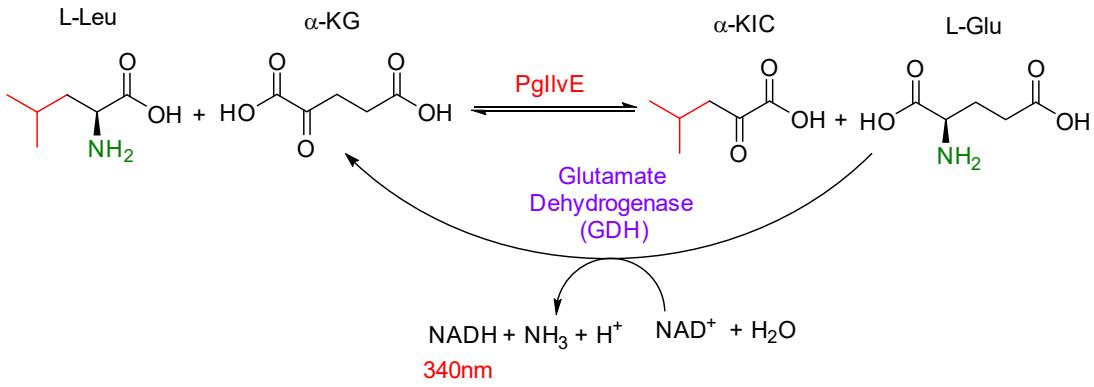

Figure 3.4.2 Schematic reaction of coupled IlvE/GDH assay in the 'forward' direction. In the presence of L-Glu, the NAD^+ is reduced to NADH by GDH to form α-KG and ammonia.

The PgIlvE activity in the 'forward' direction was tested by coupling with the GDH enzyme. GDH is a mitochondrial enzyme that indicates cell damage or necrotic hepatocytes caused by liver disease [263]. GDH catalyses conversion of L-Glu to α-KG in the presence of NAD^+, producing ammonia and NADH which leads to an increased absorbance at 340 nm (ε = 6200 $M^{-1}cm^{-1}$), as shown in Figure 3.4.2.

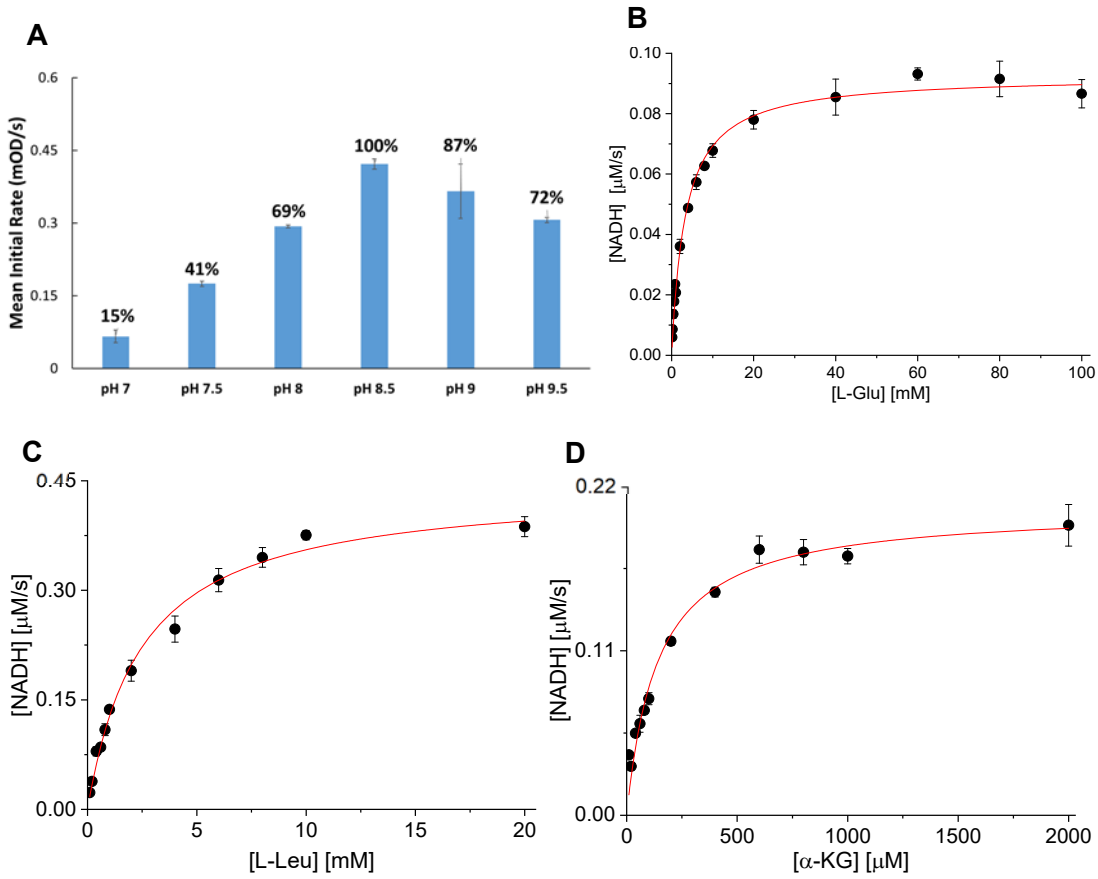

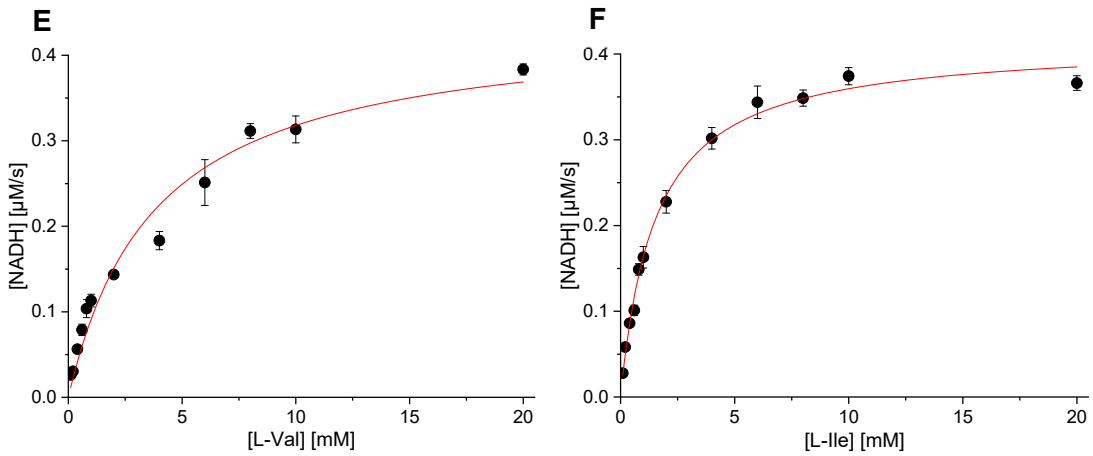

Figure 3.4.3 pH dependence and kinetic analysis of GDH alone and when coupled with PgIlvE. (A) The initial rate of GDH at different pH values. Each assay contained 0.2 U/mL GDH. (B) Kinetic analysis of GDH for L-Glu. Each assay contained 0.03 U/mL enzyme. (C-F) Kinetic analysis of PgIlvE for substrate L-Leu, α-KG, L-Val and L-Ile. Each assay contained 0.5 μM enzyme and variable concentration of substrates. All data were plotted as mean readings ±2-SD error bars.

The GDH reaction was optimized with buffers across a range of pH values and different concentrations of L-Glu as shown in the Figure 3.4.3 (A-B). The GDH had the best activity at pH 8.5 and 0.03 units/mL of GDH, which provided the K_M value of 3.35 ± 0.27 mM and V_{max} value of 0.16 ± 0.01 μM/s in good agreement with the published value (2.6 mM) [264]. The coupled PgIlvE/GDH assay was also carried out with different concentrations of GDH to obtain the minimum concentration required for the maximum speed of conversion from L-Glu to α-KG. The final optimized GDH concentration for the coupled IlvE/GDH assay was 3 units/mL GDH in 100 mM Tris buffer and 150 mM NaCl, pH 8.5 (buffer W).

Since it is a BCAT enzyme which binds *iso*-branched amino acids, the PgIlvE uses L-Leu as a substrate as well as L-Ile and L-Val. Under the optimized conditions of the coupled IlvE/GDH assay, the kinetic parameters for substrates in the 'forward' reaction, L-Leu, L-Val, L-Ile and α-KG, were successfully characterized as illustrated in Figure 3.4.3 (C-F). These are summarised in Table 3.4.1. For L-Leu, the K_M value was 2.48 ± 0.21 mM, the V_{max} value was 0.44 ± 0.01 μM/s, the k_{cat} value was 886 ± 24 × 10^{-3} s^{-1} and the k_{cat}/K_M value was 356.7 $M^{-1}s^{-1}$. For α-KG, the K_M value was 0.14 ± 0.01 mM, the V_{max} value was 0.21 ± 0.01 μM/s, the k_{cat} value was 410 ± 10 × 10^{-3} s^{-1} and the k_{cat}/K_M value was 2907.8 $M^{-1}s^{-1}$. For L-Val, the K_M value was 3.81 ± 0.47 mM, the V_{max} value was 0.44 ± 0.02 μM/s, the k_{cat} value was 439 ± 19 × 10^{-3} s^{-1} and the k_{cat}/K_M value was 110.2 $M^{-1}s^{-1}$. For L-Ile, the K_M value was 1.52 ± 0.10 mM, the V_{max} value was 0.41 ± 0.01 μM/s, the k_{cat} value was 414 ± 7 × 10^{-3} s^{-1} and the k_{cat}/K_M value was 271.4 $M^{-1}s^{-1}$.

Table 3.4.1 Kinetic parameters of different substrates by coupled IlvE/GDH assay.

Substrates	$k_{cat} \times 10^{-3}$ (s^{-1})	K_M (mM)	k_{cat}/K_M ($M^{-1}s^{-1}$)
L-Leu	886 ± 24	2.48 ± 0.21	356.7
L-Ile	414 ± 7	1.52 ± 0.10	271.4
L-Val	439 ± 19	3.81 ± 0.47	110.2
α-KG	410 ± 10	0.14 ± 0.01	2907.8

Within different amino acid substrates, the enzyme had a different reaction activity as illustrated in the Table 3.4.1. There was not a great difference in substrate affinity between the three BCAAs tested, even though L-Ile displayed the strongest affinity with PgIlvE. Nonetheless, L-Leu presented the best performance on both enzyme reaction rate and catalytic efficiency leading to L-Leu being the best BCAA substrate for PgIlvE in the 'forward' direction. PgIlvE also had a high substrate affinity with α-KG (140 μM K_M), however, the turnover rate of α-KG was approximately twice slower than L-Leu.

3.4.2 Colorimetric detection through the NADH/mediator/tetrazolium route (the XTT assay)

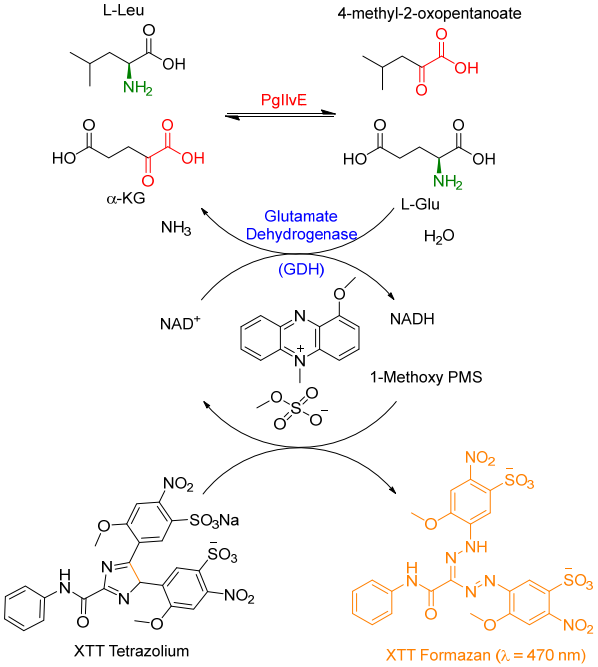

Figure 3.4.4 Schematic reaction of the assay. The amino group is transferred from L-Leu to the amino acceptor α-KG by PgIlvE. The NAD^+ is reduced to NADH by using GDH to catalyse conversion of the amino product, L-Glu. The NADH is oxidized to NAD^+ by 1-methoxy PMS and XTT tetrazolium salt.

Another way to assay the 'forward' reaction of PgIlvE is using the NADH/mediator/tetrazolium salt method suggested by Bommer *et al.* [260, 262]. This assay system is similar to the coupled IlvE/GDH assay, since it uses GDH to convert L-Glu into α-KG with the reduction of NAD^+ to NADH. A second electron transport mediator, 1-methoxy phenazine methosulfate (1-methoxy-PMS), is used to mediate conversion of the tetrazolium reagent, 2, 3-*bis*-(2-methoxy-4-nitro-5-sulfopenyl)-2H-tetrazolium-5-carboxanile (XTT), to the XTT formazan form via oxidation of NADH. The XTT formazan is measured at 470 nm by UV-Vis spectroscopy (Figure 3.3.4). The tetrazolium XTT reagent is commonly used to test mammalian cell viability and proliferation, and it was first mentioned by Scudiero *et al.* in 1988 during a study of cell growth and drug sensitivity in human and other tumour cell lines [265]. The XTT tetrazolium produces a water-soluble formazan whilst the traditional thiazolyl blue tetrazolium bromide (MTT) or iodonitrotetrazolium (INT) generates a non-soluble formazan that necessitated dissolving the dye in order to measure [266, 267]. Meanwhile, the assay has a high sensitivity allowing the minimum enzyme concentration of 0.01 µg/ml and a broad range of ATs that accept L-Glu [260].

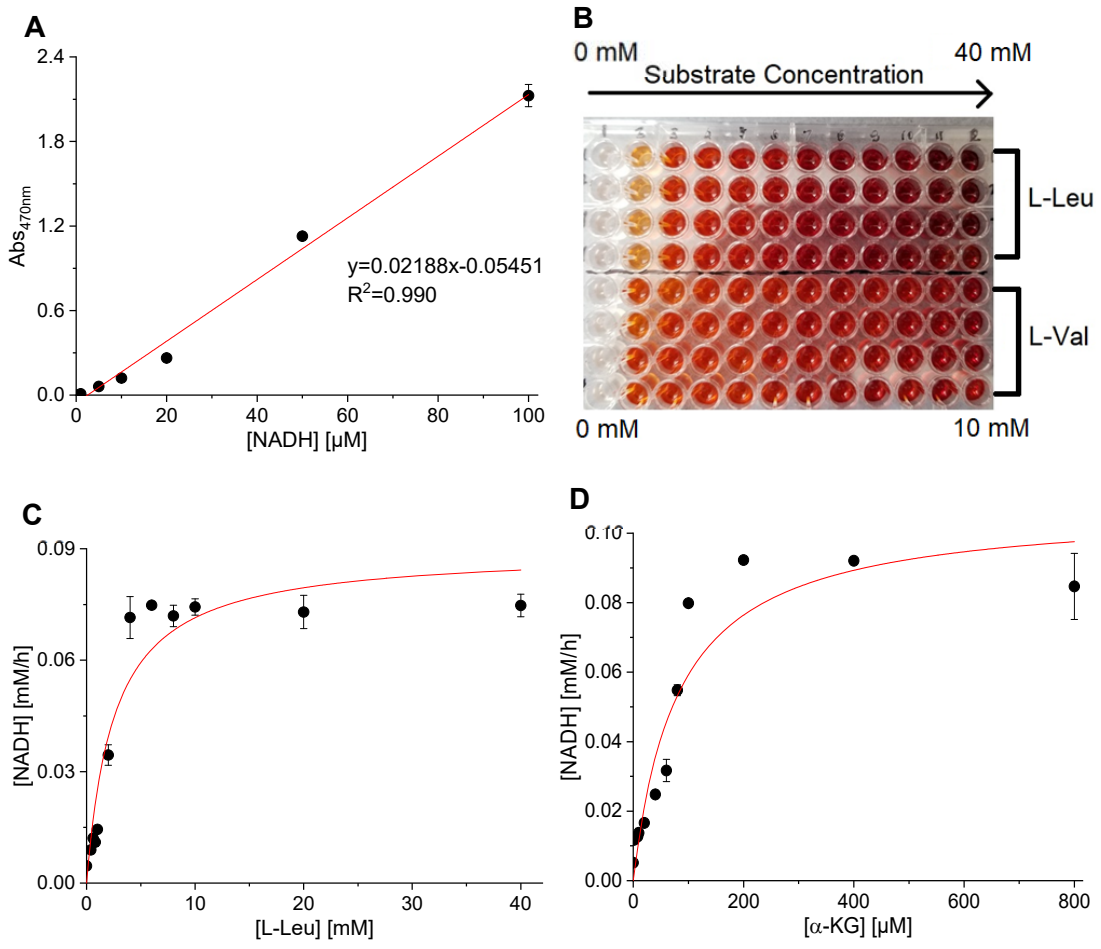

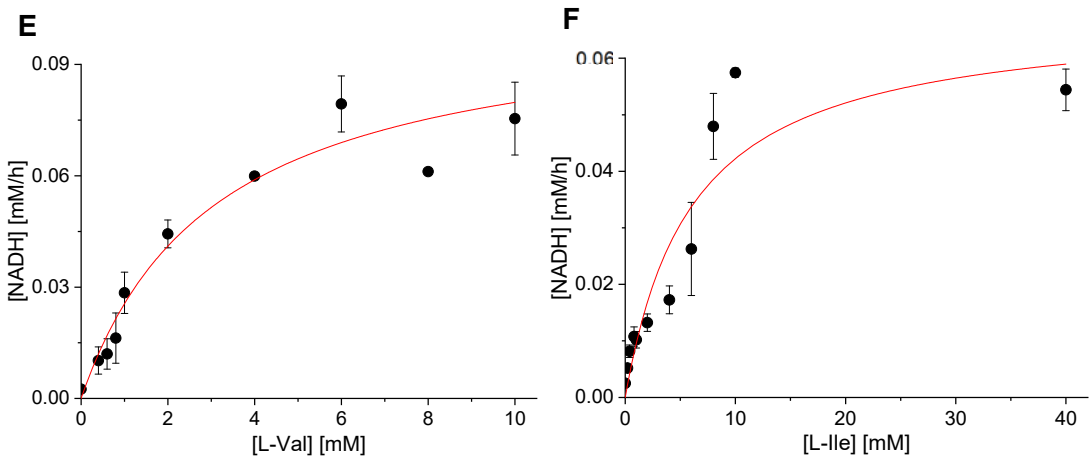

Figure 3.4.5 Characterization of recombinant PgIlvE by the XTT assay. (A) The calibration curve of NADH vs XTT formazan Abs_{470nm}. (B) The microplate of example reactions with L-Leu and L-Val. (C-F) Kinetic analysis of PgIlvE for substrate L-Leu, α-KG, L-Val and L-Ile. Each assay contained 0.5 μM enzyme and variable concentration of substrates. All data were plotted as mean readings ±2-SD error bars.

A calibration curve of NADH against XTT formazan absorbance at 470nm (Figure 3.4.5) was made, Abs_{470nm}=0.02188*[NADH]-0.05451, to compare the efficiently with other assays. In contrast to the continuous coupled IlvE/GDH assay, the XTT assay was an end point assay and enzyme activity was measured after 60 mins incubation with all reagents at 37 °C. As shown in the microplate in Figure 3.4.5, the vividly coloured XTT formazan could be observed with a gradient of substrate concentration (L-Leu or L-Val). After adjusting the reagents, the kinetic parameters of the substrates (L-Leu, L-Val, L-Ile and α-KG) were successfully calculated through Michaelis-Menten analysis in Figure 3.4.5.

Table 3.4.2 Kinetic parameters of different substrates by XTT assay

Substrates	k_{cat} (min^{-1})	K_M (mM)	k_{cat}/K_M ($M^{-1}s^{-1}$)
L-Leu	2.96 ± 0.13	2.54 ± 0.42	19.42
L-Ile	2.26 ± 0.21	6.08 ± 1.41	6.10
L-Val	3.46 ± 0.23	3.09 ± 0.53	18.66
α-KG	3.57 ± 0.27	0.08 ± 0.01	741.6

According to Table 3.4.2, there was not a great difference in substrate affinity between the amino donors with L-Ile displaying the weakest substrate affinity with PgIlvE. Compared to the data from the coupled IlvE/GDH assay, the BCAA substrate affinities from the XTT assay were in the 2.54 to ~6.0 mM range. In terms of the

reaction rate, they all displayed similar rates 2.3-3.5 min^{-1} which the fastest reaction is with L-Ile. However, the turnover numbers were all lower than the ones from the coupled IlvE/GDH assay, which was considerable since the XTT assay only measures the end point of absorbance that might a suffer time lag. The k_{cat} value of the coupled IlvE/GDH assay could be higher than expected since the PMP (330 nm) formed during the enzyme reaction might influence the measured NADH absorbance at 340 nm. The divergence between the assays also results in differences in k_{cat}/K_M values, even though the α-KG still had the best catalytic efficiency due to the low substrate affinity with the PgIlvE. Overall, L-Leu was still the best amino donor compared to other BCAAs in both assays.

Overall, these two methods can readily measure enzyme activity in the 'forward' direction, and both assays have their own advantages and disadvantages. For the coupled IlvE/GDH assay, the experiment is easily carried out and has a low demand for GDH and NADH. However, the absorbance at 340 nm may be affected by the PMP from the enzyme or the keto substrate, especially when there is a benzene ring attached. For the XTT assay, it is a coloured and sensitive detection even during the low efficiency reaction and the concentration of NAD^+ is maintained because of a self-recycling system. The UV-vis measurement at around 470 nm also prevented the interference from a high background. Nevertheless, for the XTT assay system, further optimisation was necessary to determine the initial rate of reaction. Meanwhile, the system required a high GDH concentration and other chemicals, notably the XTT tetrazolium salt was only slightly soluble in water at room temperature. Considering those factors, the XTT assay was more applicable for transaminases to readily test their substrate range.

3.4.3 Coupled IlvE/KDH assay

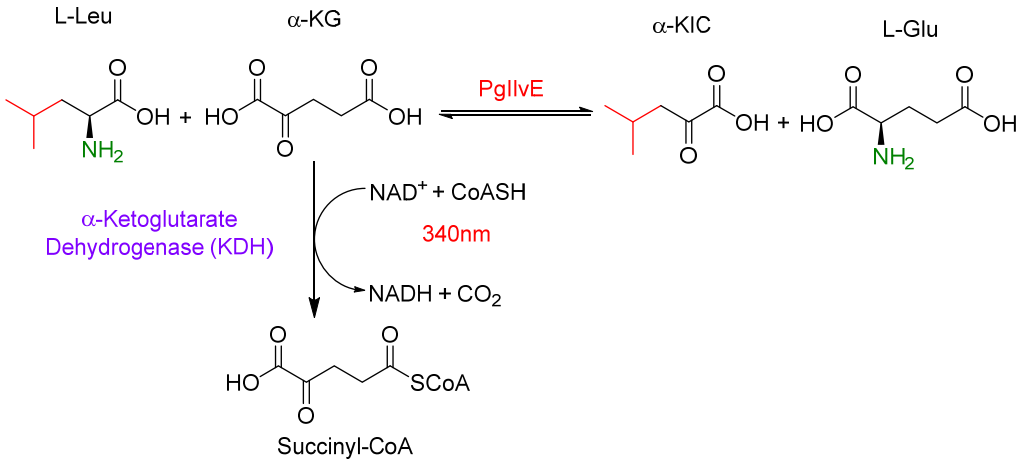

Figure 3.4.6 Schematic reaction of coupled IlvE/KDH assay in the 'reverse' direction. In the presence of α-KG, the NAD^+ is reduced to NADH by KDH to form succinyl-CoA.

The PgIlvE enzyme activity could also be monitored in the 'reverse' direction by using the KDH coupling enzymes, in which the keto product – α-KG was converted to succinyl-CoA with NAD^+ and CoASH (Figure 3.4.6). Thus, the reduction of NAD^+ to NADH would be measured at 340 nm to represent the reaction activity.

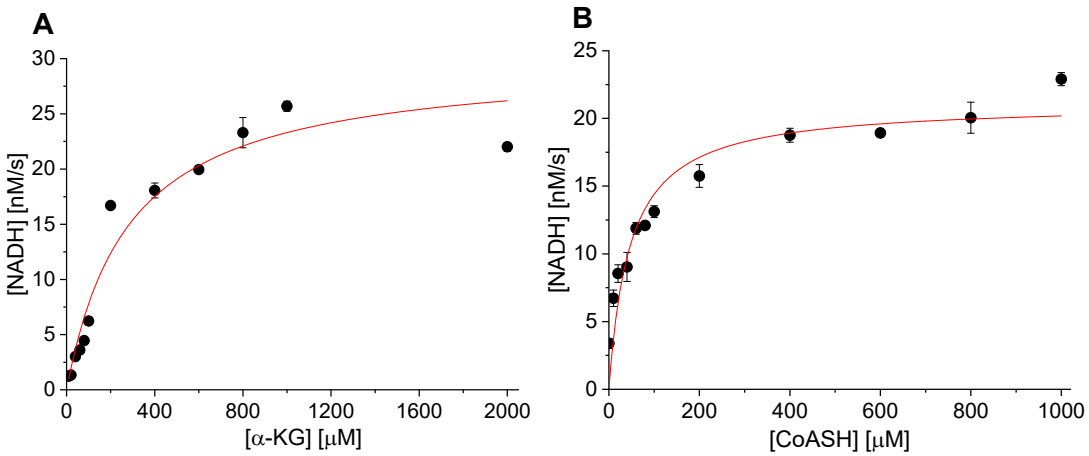

Figure 3.4.7 The kinetic analysis of KDH for substrate α-KG (A) and CoASH (B). Each assay contained 0.08 U/mL enzyme and variable concentrations of substrates. All data were plotted as mean readings ±2-SD error bars.

The KDH assay was characterized with different concentrations of α-KG and CoASH (Figure 3.4.7). Using 0.08 units/mL of KDH provided a K_M value of 0.28 ± 0.41 mM and V_{max} value of 0.03 ± 0.01 μM/s for α-KG; K_M value of 0.05 ± 0.01 mM and V_{max} value of 0.02 ± 0.01 μM/s for CoASH.

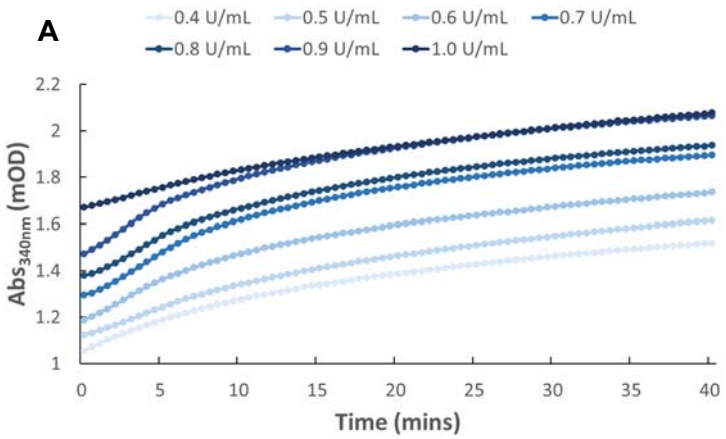

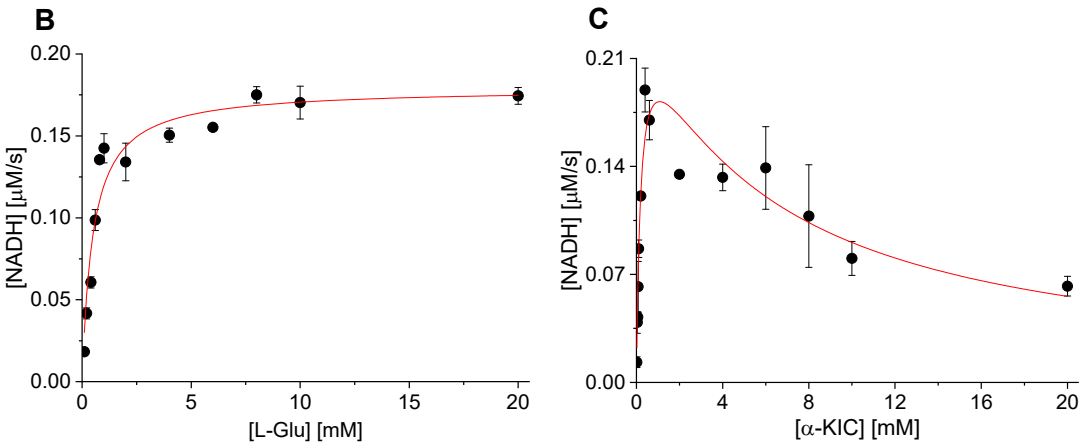

Figure 3.4.8 Characterization of the coupled IlvE/KDH assay. (A) The KDH concentration dependence of PgIlvE enzyme activity. Each assay contained with 1 μM PgIlvE, 0.4-1.0 U/mL GDH, 250 μM CoASH, 20 mM L-Glu, 1 mM α-KG, 1 mM NAD^+. (B-C) Kinetic analysis of PgIlvE for substrate L-Glu and α-KIC. Each assay contained 0.5 μM enzyme and variable concentration of substrates. All data were plotted as mean readings ±2-SD error bars.

The coupled IlvE/KDH assay was studied with different concentrations of KDH in order to achieve the maximum initial rate of the reaction. However, as displayed in Figure 3.4.8 (A), the enzyme showed high background absorbance. When the concentration of KDH was over 0.8 U/mL, the initial rate of reaction decreased, and there was the possibility that KDH could affect the PgIlvE reaction. Considering all these factors, the best concentration of KDH using in the coupled IlvE/KDH assay was 0.7 U/mL. The assay buffer was 100 mM Tris buffer and 150 mM NaCl, pH 8.0 (buffer Y). The kinetic parameters of PgIlvE in the 'reverse' direction were determined with both substrates, L-Glu and α-KIC (Figure 3.4.8 B-C). Interestingly, we observed substrate inhibition with α-KIC when the substrate concentration was over 0.6 mM, and the K_i value was 4.25 ± 0.81 mM. The K_M value was 0.28 ± 0.06 mM, the k_{cat} value was 0.63 ± 0.07 s^{-1} and the k_{cat}/K_M value was 2196.5 $M^{-1}s^{-1}$. Due to substrate inhibition, the concentration of α-KIC was adjusted to 400 μM for establishing the enzyme activity with L-Glu, which the K_M value was 0.50 ± 0.06 mM, the k_{cat} value was 0.36 ± 0.01 s^{-1} and the k_{cat}/K_M value was 723.2 $M^{-1}s^{-1}$. From the kinetic data, the PgIlvE showed good catalytic activity with the both substrates compared to all the BCAAs, but the reaction speed was limited. It was possible that the amino product, L-Leu, would interact with the enzyme to proceed to the first step of the reaction, producing α-KIC that might inhibit the assay system and slow down the overall enzyme activity. Unfortunately, the mechanism of substrate inhibition is unknown, and the hypothesis suggests another 'reverse' direction determination assay should be used – the coupled IlvE/LeuDH assay in the next section.

3.4.4 Coupled IlvE/LeuDH assay

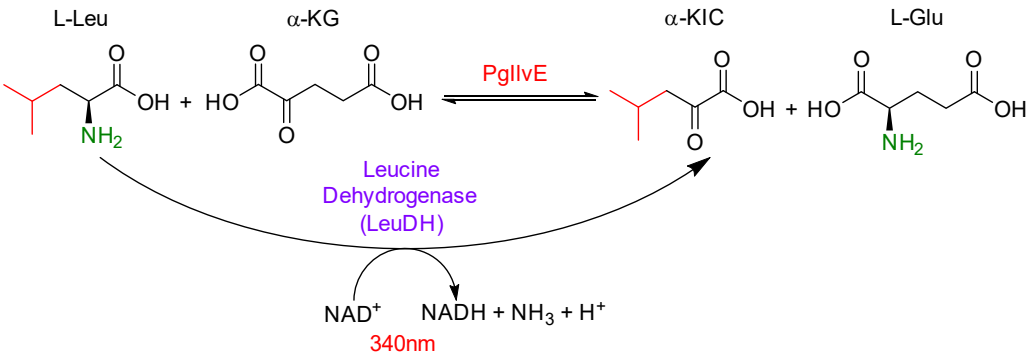

Figure 3.4.11 Schematic reaction of coupled IlvE/LeuDH assay in 'reverse' direction. In the presence of L-Leu, the NAD^+ is reduced to NADH by LeuDH to α-KIC formation.

There is another published assay [261], similar to the coupled GDH/IlvE assay, to measure the enzyme activity in the 'reverse' direction using LeuDH from *B. cereus* to react with the amino product L-Leu forming α-KIC (Figure 3.4.11).

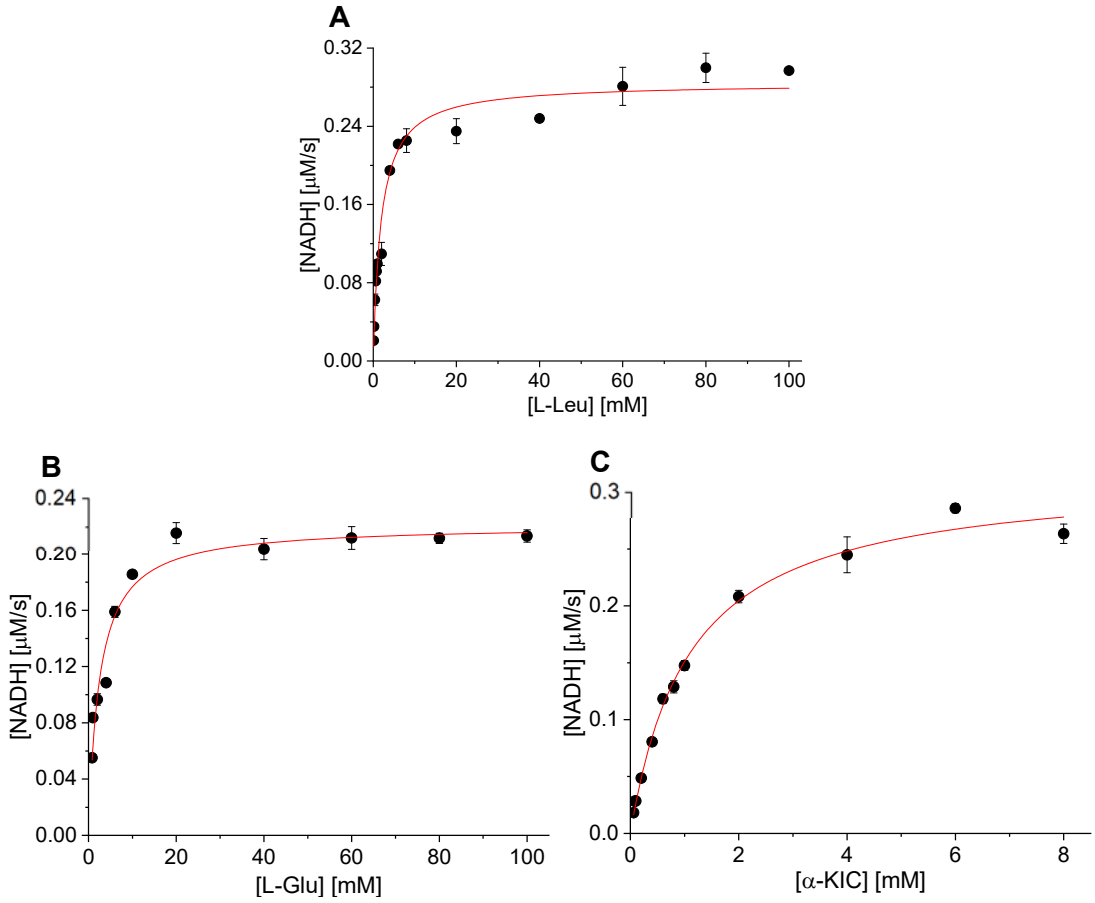

Figure 3.4.12 Kinetic analysis of LeuDH and recombinant PgIlvE using the coupled IlvE/LeuDH assay. (A) Kinetic analysis of LeuDH for L-Leu. Each assay contained 0.3 U/mL enzyme. (B-C) Kinetic analysis of PgIlvE for substrate L-Glu and α-KIC. Each assay contained 0.5 μM enzyme and variable concentration of substrates. All data were plotted as mean readings ±2-SD error bars.

With the same procedure as other three assays, the LeuDH was analysed with substrate L-Leu, giving the K_M value was 1.89 ± 0.18 mM with only 0.3 U/ml LeuDH (Figure 3.4.12). The LeuDH reaction was optimized according to the pH and substrate concentrations. It turned out that the LeuDH preferred basic conditions rather than neutral or acidic conditions and the best assay buffer condition was 100 mM CAPS, 150 mM NaCl, pH 11.0 (buffer Z). However, only 2 U/mL LeuDH was required to achieve the maximum reaction speed of the assay system.

Within the optimized condition, the enzyme activity with both substrates was calculated as shown in Figure 3.4.12. For L-Glu, the K_M value was 2.49 ± 0.23 mM, the V_{max} value was 0.22 ± 0.01 μM/s, the k_{cat} value was 0.44 ± 0.01 s^{-1} and the k_{cat}/K_M value was 177.6 $M^{-1}s^{-1}$. For α-KIC, the K_M value was 1.09 ± 0.07 mM, the V_{max} value was 0.32 ± 0.01 μM/s, the k_{cat} value was 0.63 ± 0.01 s^{-1} and the k_{cat}/K_M value was 579.3 $M^{-1}s^{-1}$. In the coupled IlvE/LeuDH assay, PgIlvE still maintained good substrate affinity and turnover rates with both substrates compared to the 'forward' direction, and there was no substrate inhibition appeared with α-KIC. It was suggested that α-KIC might affect with KDH rather than PgIlvE.

Table 3.4.3 Comparison of PgIlvE activity between the coupled IlvE/KDH assay and the coupled IlvE/LeuDH assay.

Substrates	**IlvE/KDH assay**		**IlvE/LeuDH assay**	
	L-Glu	**α-KIC**	**L-Glu**	**α-KIC**
K_M **(mM)**	0.50 ± 0.06	0.28 ± 0.06	2.49 ± 0.23	1.09 ± 0.07
k_{cat} **(s^{-1})**	0.36 ± 0.01	0.63 ± 0.07	0.44 ± 0.01	0.63 ± 0.01
k_{cat}/K_M **($M^{-1}s^{-1}$)**	723.2	2196.5	177.6	579.3
K_i **(mM)**	None	4.25 ± 0.81	None	None

In comparing the two assays used for the 'reverse' direction of PgIlvE (Table 3.4.3), the coupled IlvE/KDH assay showed the enzyme had better substrate affinities with both substrates, however, the turnover number between them were virtually the same. Potentially, the coupling enzyme, KDH or LeuDH, might have an unfavourable interaction with both substrates, as it was known that high concentrations of α-KIC could inhibit with KDH enzyme. It was unclear which assay would be better, since they were both indirect assays and were processed in different buffers and pHs that could also affect the enzyme performance. For the coupled IlvE/KDH assay, the high background absorbance obtained from the KDH itself provided challenging for optimizing the assay condition and measuring the accurate initial rate of the reaction.

Concerning the cost of the reagents, the KDH assay has a price of KDH (£7.62 per unit) and CoASH (£3.14 per mg), on the other hand, the LeuDH only costs £0.81 per unit. In contrast, with the coupled LeuDH/IlvE assay, the LeuDH also favours basic conditions, however this impacts the NAD^+ stability in the solution [268]. It has a weak interaction with high concentrations of L-Glu.

The PgIlvE was screened with different natural L-AAs to examine the substrate specificity. In the 'forward' direction, only BCAAs showed the activity, undoubtedly, L-Glu was the only natural L-AA that carried out the 'reverse' direction. It was also assumed that the PgIlvE only accept relevant branched chain keto acids, such as α-KIC from L-Leu, 3-methyl-2-oxopentanoic acid from L-Ile, α-ketoisovaleric acid from L-Val, or α-KG for the transaminase cycle system. It was highly likely that the enzyme possessed specific residues which only recognized the BCAAs or L-Glu and those relevant keto acids.

In comparison to the IlvE or BCAT from the other species (Table 3.4.4), different IlvE/BCATs display a different preference with different BCAAs. For example PgIlvE has a similar substrate affinity compared with *E. coli* BCAT for L-Leu, but is more similar to human BCAT2 for the L-Val substrate. Moreover, most BCATs display a higher substrate affinity with α-KIC acid rather than other substrates. However, there is a wide variation in the enzyme rates across the species and PgIlvE appears to have the lowest turnover number for all the substrates.

In conclusion, the four assays presented above were screened, then optimised, for their ability to measure PgIlvE activity, two for the 'forward' direction and two for the 'reverse' direction. Each of them showed different kinetic activities, and technical advantages and disadvantages. Therefore, the assay used for obtaining the best results is dependent on the aim of determination, the direction of reaction and the variety of substrates.

Table 3.4.4 The enzymatic activity of IlvE or BCAT from different species [182, 192, 200, 214, 269-272].

Species		*P. gingivalis*	*M. tuberculosis*	*E. coli*	*H. sapiens (BCAT1)*[g]	*H. sapiens (BCAT2)*[h]
K_M (mM)	L-Leu	2.48 ± 0.21[i]	6.02 ± 0.94[b]	2.2[d]	0.60 ± 0.04	1.60 ± 0.1
	L-Val	3.81 ± 0.47[i]	5.79 ± 0.99[b]	2.7[d]	2.4 ± 0.09	7.78 ± 0.3
	L-Ile	1.52 ± 0.10[i]	6.16 ± 1.14[b]	0.42[d]	0.77 ± 0.02	1.30 ± 0.1
	L-Glu	2.49 ± 0.23[j]	1.30 ± 0.20[c]	21.8 ± 1.26[e]	ND[a]	22.7 ± 1.1
	α-KG	0.14 ± 0.01[i]	6.95 ± 1.44[b]	6.6[f]	ND[a]	8.3 ± 1.7
	α-KIC	1.09 ± 0.07[j]	0.24 ± 0.03[c]	0.08 ± 0.01[e]	0.06 ± 0.01	0.3 ± 0.1
k_{cat} (s^{-1})	L-Leu	0.89 ± 0.02[i]	8.96 ± 0.56[b]	48[d]	132 ± 7	337 ± 4
	L-Val	0.44 ± 0.02[i]	7.88 ± 0.53[b]	19[d]	122 ± 9	290 ± 4
	L-Ile	0.41 ± 0.01[i]	9.56 ± 0.72[b]	48[d]	172 ± 8	371 ± 3
	L-Glu	0.44 ± 0.01[j]	8.90 ± 0.40[c]	53.5 ± 1.62[e]	ND[a]	277 ± 7
	α-KG	0.41 ± 0.01[i]	8.53 ± 0.74[b]	78[f]	ND[a]	340 ± 43
	α-KIC	0.63 ± 0.01 [j]	9.10 ± 0.40[c]	24.7 ± 0.87[e]	309 ± 11	810 ± 30

[a] Not determined; [b] Venos's paper HPLC assay; [c] Amorim's paper GDH coupling assay; [d] Inoue's paper GDH coupling assay; [e] Yu's paper HGDH coupling acid; [f] Kagamiyama's charpter GDH coupling assay; [g] Davoodi's paper NADH fluorescence; [h] Yennawar's paper radioactive assay; [i] GDH coupling assay; [j] LeuDH coupling assay.

3.5 A study of PgIlvE inhibitors

As a PLP-dependent enzyme, it was thought that the PgIlvE could be inhibited by inhibitors such as cycloserine (enantiomers LCS and DCS) in a similar way to that discussed for SPT. Blanchard's goup had recently published a study of the mechanism of inhibition of the *M. tuberculosis* IlvE (MtIlvE) by LCS and DCS. This included the determination of the crystal structure of IlvE in complex with DCS (PDB code: 5U3F) so the aim was to carry out a comparative study with PgIlvE [204, 214]. As well as CS, various IlvE/BCATs have also been studied with other general PLP inhibitors (Figure 3.5.1), such as O-benzylhydroxylamine (BHA) for *M. smegmatis* IlvE, pharmaceutical anticonvulsant drug gabapentin and 4-methyl-5-oxohexanoic acid (ERG240) for *H. sapiens* BCAT1 – they were investigated for their mechanism of inhibition, and in some cases, crystal structures of the inhibitor-bound structure has been determined [202, 205, 273]. The idea of 4-methylbenzyl hydrazine (4-MBH) being an inhibitor was originally from Lightcap's paper in 1996 which provided evidence that the isomer 3-hydroxybenzyl hydrazine (3-MBH) displayed inhibition of γ-aminobutyric acid aminotransferase (GABA-AT), for which the K_i value was determined as 0.3 μM [274]. Therefore, in this section, we examined these potential inhibitors of PgIlvE.

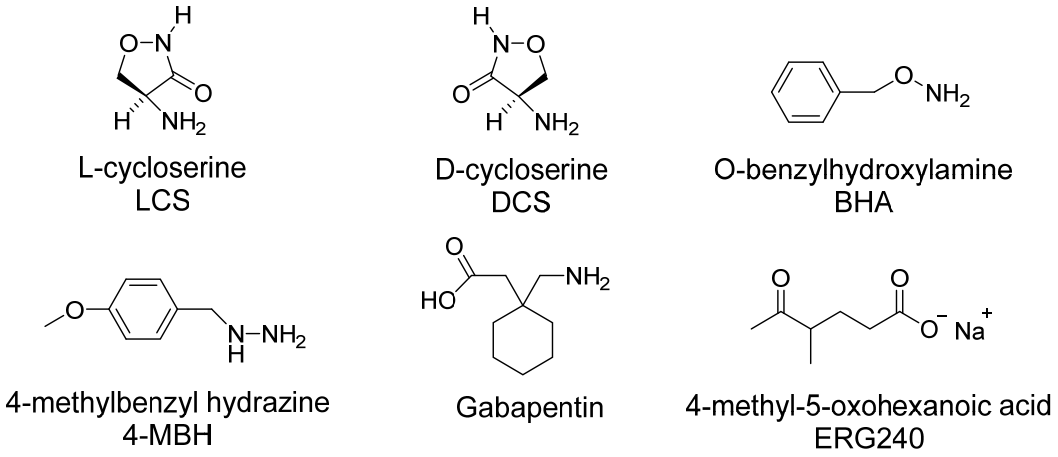

Figure 3.5.1 Chemical structure of inhibitors to IlvE/BCATs [202, 205, 214, 273].

Firstly, the PgIlvE was incubated with each of the potential inhibitors (0.5 mM) to observe the changes of the PLP cofactor by UV-vis spectroscopy as shown in Figure 3.5.2. This would give initial insight into whether the inhibitors were interacting with the enzyme. Over various times (0-20 hrs), the absorbance at 410 nm (internal aldimine, PLP-Lys183) decreased and the absorbance at 330 nm increased suggesting each inhibitor had bound. Beginning with CS, Franco and Blanchard [214],

had suggested that the inhibition mechanism for PgIlvE involved initial formation of the PLP-inhibitor external aldimine form before any further reaction. Comparing both enantiomers of CS with PgIlvE, it took around 45 mins for the enzyme to equilibrate with LCS (Figure 3.5.2 A). In contrast, with DCS it took around 9 hours for equilibration (Figure 3.5.2 B). This suggested that the LCS reacts with the enzyme faster than DCS. For inhibitor BHA, it took 3 hours to equilibrate with the enzyme (Figure 3.5.2 C). Moreover, it appeared that 4-MBH equilibrated with the enzyme over 6 hours (Figure 3.5.2 D). The detailed inhibition mechanism of PgIlvE will be discussed in the later section 3.5 with reference to a crystal structure of the PLP-LCS form.

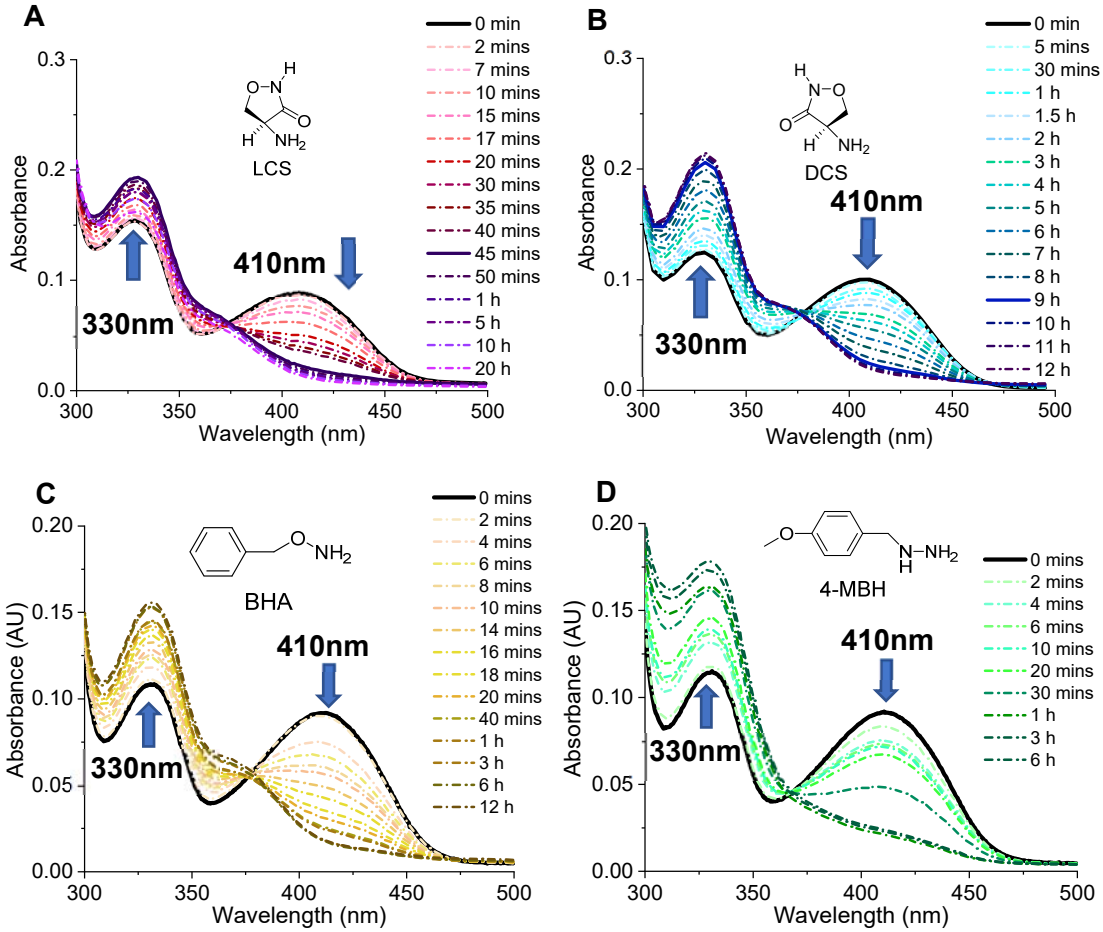

Figure 3.5.2 Absorption spectra of PgIlvE incubated with LCS (A), DCS (B), BHA (C) and MBH (D) overtime. Each assay contained 20 μM PgIlvE with 0.5 mM inhibitors.

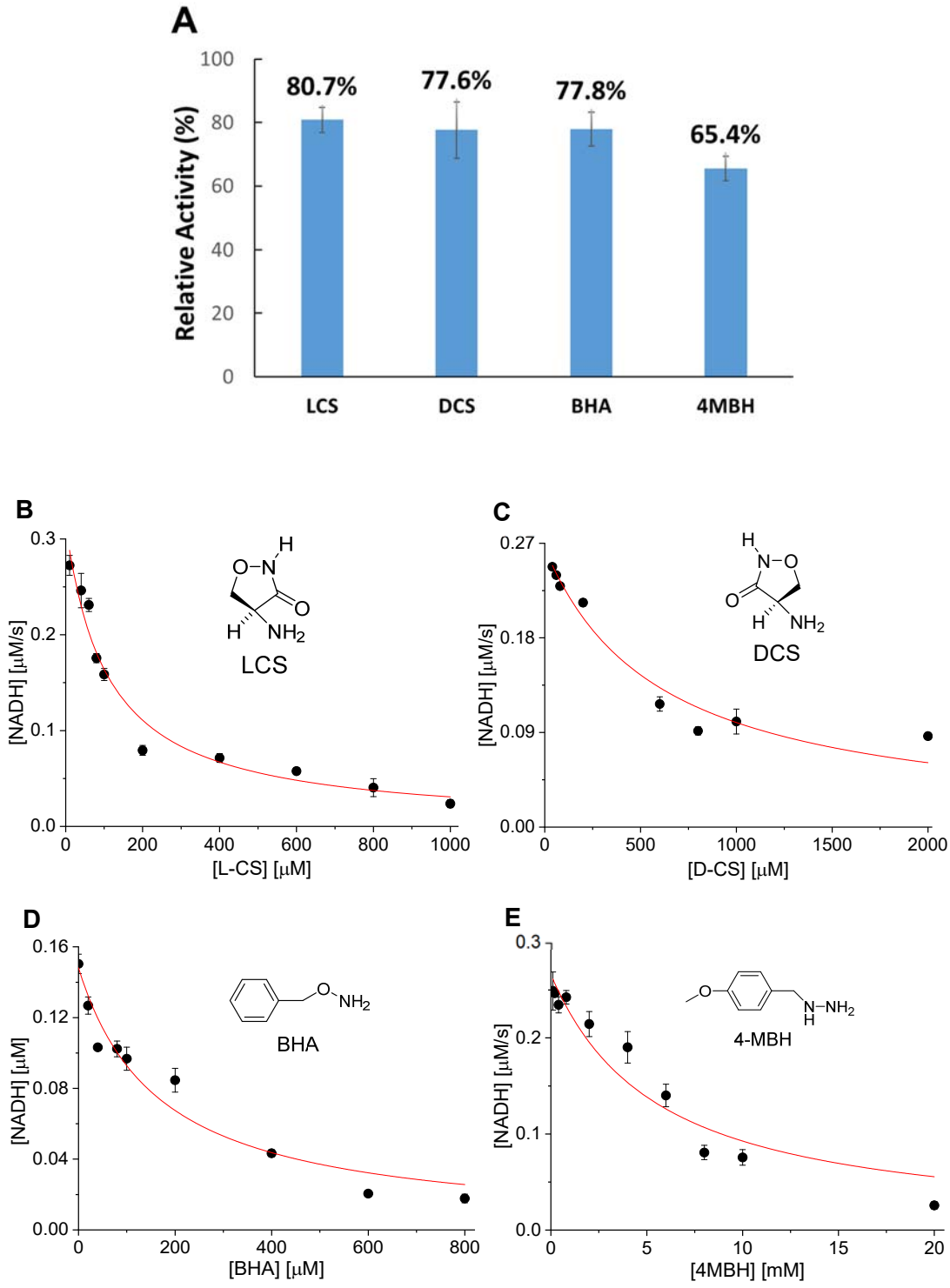

Figure 3.5.3 Inhibition study of PgIlvE with potential inhibitors. (A) Relative enzymatic activity recovery by dialysis. Each assay contained 0.5 μM PgIlvE and relative concentrations of inhibitors. (B-E) Inhibition analysis of PgIlvE with inhibitor LCS (B), DCS (C), BHA (D) and 4MBH (E) by the coupled IlvE/GDH assay. Each assay contained 0.5 μM PgIlvE and relative concentrations of inhibitors. All data were plotted as mean readings ±2-SD error bars.

$$Q = K_i \frac{K_m + S}{K_m} \quad (1)$$

$$Y = v_o\left(1 - \frac{([E]+X+Q) - \sqrt{([E]+X+Q)^2 - 4[E]X}}{2[E]}\right) \quad (2)$$

Analysis of the kinetics and the type of inhibition (reversible or irreversible) was carried out for all the inhibitors (Figure 3.5.3 A). The PgIlvE was initially incubated with LCS (200 μM), DCS (500 μM), BHA (200 μM) and 4MBH (4 mM) for 20 minutes, then dialysed for 24 hours against buffer W, which of note, included 50 μM PLP, before analysing the re-constituted enzyme with the coupled IlvE/GDH assay. It was observed that ~80% enzymatic activity was recovered after inhibition with LCS, ~77% activity was recovered for DCS and BHA, and ~65% for 4MBH, suggesting the inhibition mechanism of PgIlvE for each of the inhibitors was to a greater extent reversible. Earlier studies by Morrison and co-workers have provided a mathematical analysis to study how a reversible inhibitor effects the kinetics of enzymatic reactions. This has generated an equation, commonly referred to as the Morrison equation (2), to calculate the inhibitor constant (K_i) indicating how potent an inhibitor is [275-277]. Thus, all the inhibition activity would be examined with Morrison analysis using the coupled IlvE/GDH assay conditions in 'forward' reaction in order to determine the K_i.

Table 3.5.1 The inhibitor parameters of PgIlvE with different inhibitors.

Substrates	**LCS**	**DCS**	**BHA**	**4MBH**
K_i **(μM)**	60.70 ± 6.08	334.78 ± 33.2	93.45 ± 8.91	2890 ± 350

As illustrated in Figure 3.5.3 (B-E) and Table 3.5.1, different concentrations of inhibitors were plotted against relevant initial velocity (by measuring the concentration of NADH produced in the GDH coupled assay) were successfully fitted to a tight binding inhibition model. Calculated from the Morrison equation, the K_i value of LCS was 60.70 ± 6.08 μM and the K_i value of DCS was 334.78 ± 33.2 μM. Both the UV-vis studies and % inactivation agreed with the different stereospecificity of how the two different enantiomers inhibited PgIlvE. Blanchard and colleagues found that LCS is also a more of potent inhibitor of MtIlvE than DCS for, which the K_i value of LCS was reported as 88 μM, of interest the K_i value of DCS was not reported [214]. For inhibitor BHA, the inhibitor constant (K_i) was determined as 93.45 ± 8.91 μM. From Castell's paper [205], the K_i value of BHA was recorded as 65 μM for MtIlvE and 42 μM *for M. smegmatis* IlvE (MsIlvE) separately. For inhibitor 4MBH, the K_i value was determined as 2.89 ± 0.35 mM using Morrison equation to fit the data, showing the weakest inhibition with PgIlvE amongst all the inhibitors tested in this study.

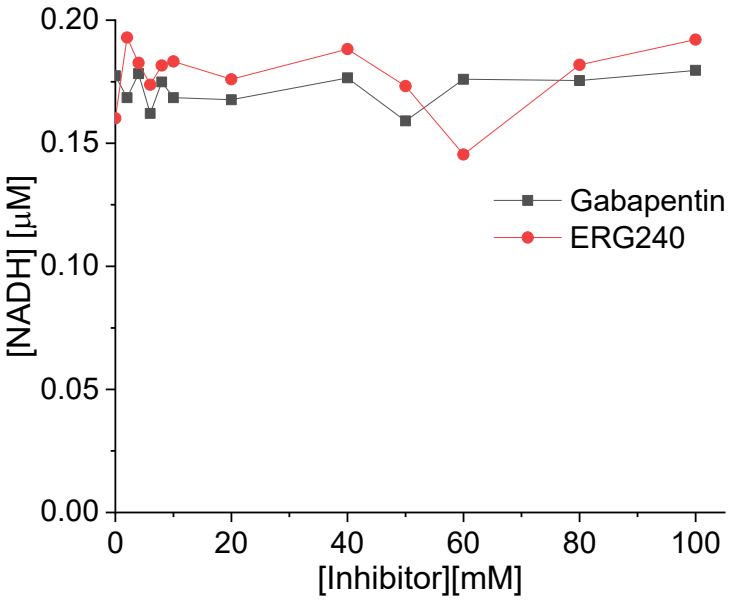

Figure 3.5.4 Inhibition study of PgIlvE with inhibitor gabapentin (black) and ERG240 (red) by the coupled GDH/IlvE assay.

Gabapentin (1-(Aminomethyl)cyclohexaneacetic acid, also know as brand name Neurontin, Fig. 3.5.1) is used as an anti-convulsant drug and it thought to act by inhibiting GABA AT. The inhibitor ERG240 (Fig. 3.5.1) is under current development for therapy of inflammatory conditions (e.g. arthritis). Both molecules were reported as cytosolic BCAT1 competitive inhibitors rather than mitochondrial BCAT2 inhibitors in human cells [273, 278]. Both compounds were analysed with PgIlvE, but unfortunately, there was no obvious inhibition observed through the activity assay (Figure 3.5.4).

In summary, the study of how bacterial PgIlvE interacts with the various inhibitors described suggests that PgIlvE inhibition displays similar mechanisms to those previously observed for both MtIlvE and human BCAT, even though there is relatively low (<40%) overall identity in the sequences (Table 3.1). That said, there are highly conserved residues in the active sites of all BCAT isoforms. Unfortunately, due to time limitations, none of the inhibitors were examined for half maximal inhibitory concentration (IC50) experiments with both substrates, L-Leu and α-KG. Therefore, it is uncertain to determine the types of inhibitions (competitive, uncompetitive or non-competitive). Furthermore, the inhibtors were not tested *in vivo* with *P.* gingivalis to determine if they displayed properties such as antimicrobial activity.

3.6 Structural analysis of PgIlvE

Determination of the 3D structure of an enzyme is the basis for understanding the details of its catalytic mechanism and potential development of medicinally-relevant drugs. As mentioned in section 3.1, a number of crystal structures of IlvE/BCATs has been studied and published in the PDB (Table 3.1.1). Therefore, obtaining the crystal structure of PgIlvE would allow comparative studies of other IlvE/BCAT enzymes. This work was carried out in collaboration with Dr. Jon Marles-Wright (Newcastle University).

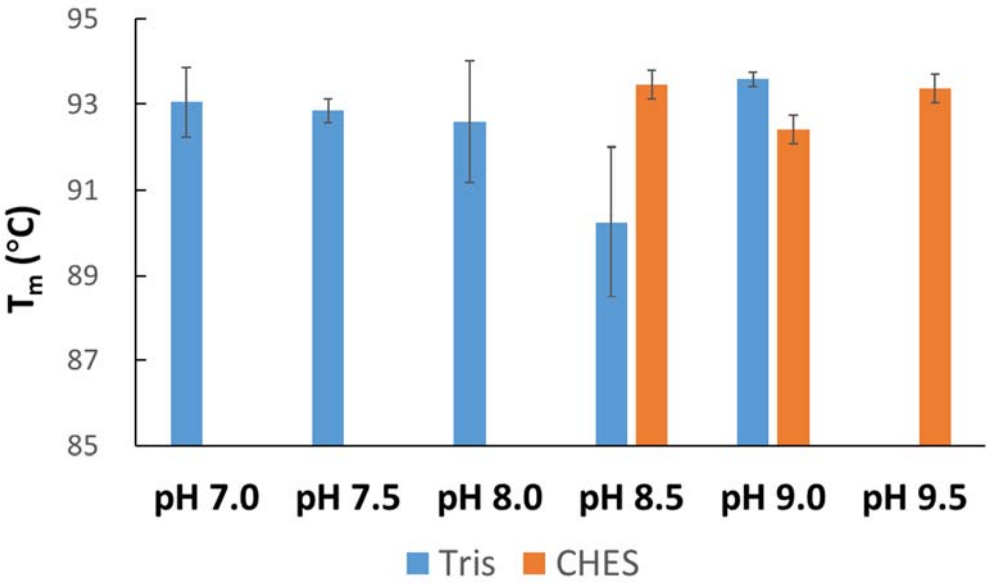

Figure 3.6.1 The thermal denaturation assay of PgIlvE with Tris and CHES buffer in different pH. T_m stands for melting temperature. Each essay contained 5 µM enzyme and all data were plotted as mean readings ±2-SD error bars.

To begin the route to the determination of the x-ray structure, diffraction-quality crystals are required. So, screens to identify conditions (pH, buffer, precipitant *etc.*) were carried out. The purified, recombinant PgIlvE WT tested by a thermal denaturation assay (TDA), a method used to measure the thermal stability of proteins through the transition unfolding temperature (T_m), in order to determine the best buffer for protein crystallography. We began by screening different pHs and used Tris or CHES buffers to analyse the range pH 7.0 - 9.5 (Figure 3.6.1). The T_m values of all buffers were over 90 °C, showing PgIlvE was an extremely stable enzyme giving promising results for protein crystallography. Concerning the chemical structure of Tris, which may interact with the PLP cofactor and remove the PLP from the protein and

the useful pH ranges of biological buffers chart at 25°C from the Sigma-Aldrich website, the final solution for all crystallizations was 100 mM CHES, 150 mM NaCl, pH 8.6 [279, 280].

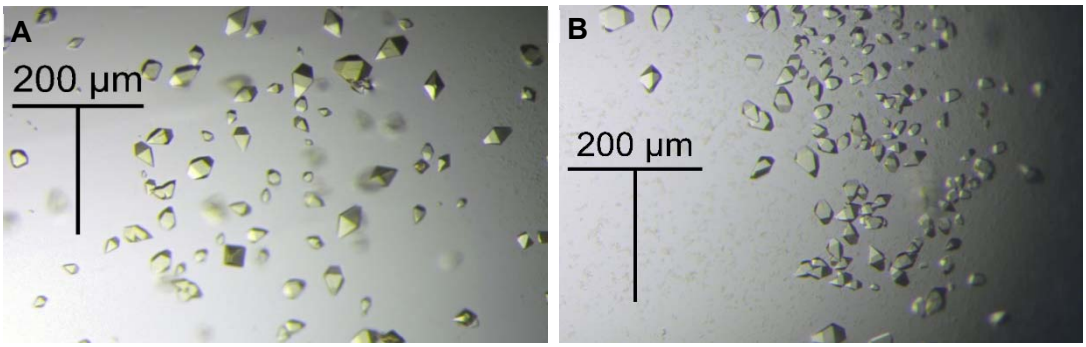

Figure 3.6.2 Crystal morphology of PglIvE WT from PEG/Ion Screen B12 (A) and PglIvE + L-Leu incubation from Structure Screen 1+2 D9 (B). Protein condition: 9 mg/ml PglIvE with/without 5mM L-Leu incubation. Precipitation condition: (A) 0.2 M lithium acetate dihydrate, 20% w/v polyethylene glycol (PEG) 3350, pH 7.9. (B) 4 M sodium formate.

In partnership with Dr. Jon Marles-Wright, crystallisation screening was performed under various precipitants' conditions from commercial screens (PEG/Ion, JCSC-plus, Midas and Structure Screen 1+2) via vapour diffusion of sitting drop method in 96 well plates setting by the Art Robbins Gryphon nano-litre pipetting robot. In order to observe the interaction between the substrates or inhibitors and the enzyme, all the substrates or inhibitors were incubated with the enzyme for at least 12 hours before setting the trails and crystallisation plates.

Approximately 9 mg/ml of PglIvE alone and PglIvE + L-Leu incubation were initially screened through the system. The positive crystals were observed under more than 20 different conditions in PEG/Ion, JCSC-plus and Structure Screen 1+2, as shown as in Figure 3.5.2. Due to the characteristics of PLP, the PglIvE formed yellow crystals, however the PglIvE + L-Leu incubation formed the colourless crystals. The colour changes suggested L-Leu binding. The condition of PEG/Ion Screen B12, which was 0.2 M lithium acetate dihydrate, 20% w/v polyethylene glycol (PEG) 3350, pH 7.9, was utilized for further optimization crystallography using the hanging drop method. Meanwhile, during the optimization stage, the enzyme was screened by incubation with the inhibitors LCS, DCS, BHA and 4MBH were also screened. After several days, potential crystals were chosen and freezed in cryoprotectant for X-ray diffraction analysis by Dr. Jon Marles-Wright. He also directed my attempts at structure solution by molecular replacement and refinement as best as possible. This was difficult to do remotely as I was in China and then in Edinburgh – the final models were refined by him.

The structure was determined in internal aldimine form, PLP:LCS and PLP:DCS, the initial model was built using Molrep [281-283], Phaser [284] and Refmac [285-288] in CCP4i [289] and the residues were checked and corrected with WinCoot with the highest homology structure found in the PDB which was *D. radiodurans* BCAT (3UYY [259]). However, the final confirmation of crystal structures and the crystal structure of external aldimine (PLP:Leu) are still in progress (October 2020). Therefore, those abnormal numbers in the Table 3.6.1 needs to be adjusted before publication. Therefore, the structures of the internal aldimine, PLP:LCS and PLP:DCS forms are shown and the refinement statistics data are given in Table 3.6.1. However, the interaction between enzyme and solvent would not be considered in the following discussion.

Table 3.6.1 Crystallographic data and refinement statistics for DCS, WT and LCS.

	DCS	WT	LCS
Wavelength (Å)	0.976	0.976	0.976
Resolution range (Å)	48.54 - 1.78	40.67 - 2.8	42.07 - 1.6
	(1.84 - 1.78)	(2.9 - 2.8)	(1.66 - 1.6)
Space group	C 1 2 1	P 21 21 21	P 21 21 21
a, b, c (Å)	207.16	77.82	80.09
	81.05	78.85	82.68
Unit cell	84.29	189.86	195.51
α, β, γ (°)	90	90	90
	110.40	90	90
	90	90	90
Total reflections	451590	187900	1241832
	(45601)	(19388)	(116202)
Unique reflections	124932	29361	171267
	(12437)	(2905)	(16903)
Multiplicity	3.6 (3.7)	6.4 (6.7)	7.3 (6.9)
Completeness (%)	99.67	98.84	99.92 (99.92)
	(99.75)	(99.38)	
Mean I/sigma(I)	40.89 (1.57)	34.85 (1.71)	28.13 (1.14)
Wilson B-factor (Å)	27.53	77.56	24.93
R-merge	0.092 (0.61)	0.27 (1.16)	0.17 (1.45)
R-meas	0.11 (0.71)	0.30 (1.26)	0.19 (1.57)
R-pim	0.06 (0.36)	0.12 (0.49)	0.067 (0.60)

CC1/2	0.99 (0.53)	0.94 (0.48)	0.98 (0.17)
CC*	1.00 (0.83)	0.98 (0.80)	0.99 (0.54)
Reflections used in refinement	124787 (12424)	29223 (2897)	171169 (16893)
Reflections used for R-free	6223 (662)	1412 (128)	8422 (841)
R-work	0.197 (0.27)	0.255 (0.39)	0.18 (0.31)
R-free	0.23 (0.30)	0.32 (0.40)	0.21 (0.33)
CC(work)	0.95 (0.63)	0.89 (0.45)	0.96 (0.33)
CC(free)	0.94 (0.73)	0.84 (0.53)	0.96 (0.42)
Number of non-hydrogen atoms	10980	10185	11990
Macromolecules	10224	10124	10670
Ligands	64	60	93
Solvent	692	1	1227
Protein residues	1309	1304	1345
RMS(bonds)	0.02	0.02	0.01
RMS(angles)	2.00	1.96	1.84
Ramachandran favored (%)	96.42	90.00	96.56
Ramachandran allowed (%)	2.88	8.49	2.92
Ramachandran outliers (%)	0.70	1.51	0.52
Rotamer outliers (%)	2.15	5.42	1.96
Clashscore	4.25	8.02	3.05
Average B-factor	35.47	90.39	32.79
Macromolecules	35.33	90.44	31.76
Ligands	27.83	83.49	30.85
Solvent	38.30	34.93	41.91

Statistics for the highest-resolution shell are shown in parentheses.

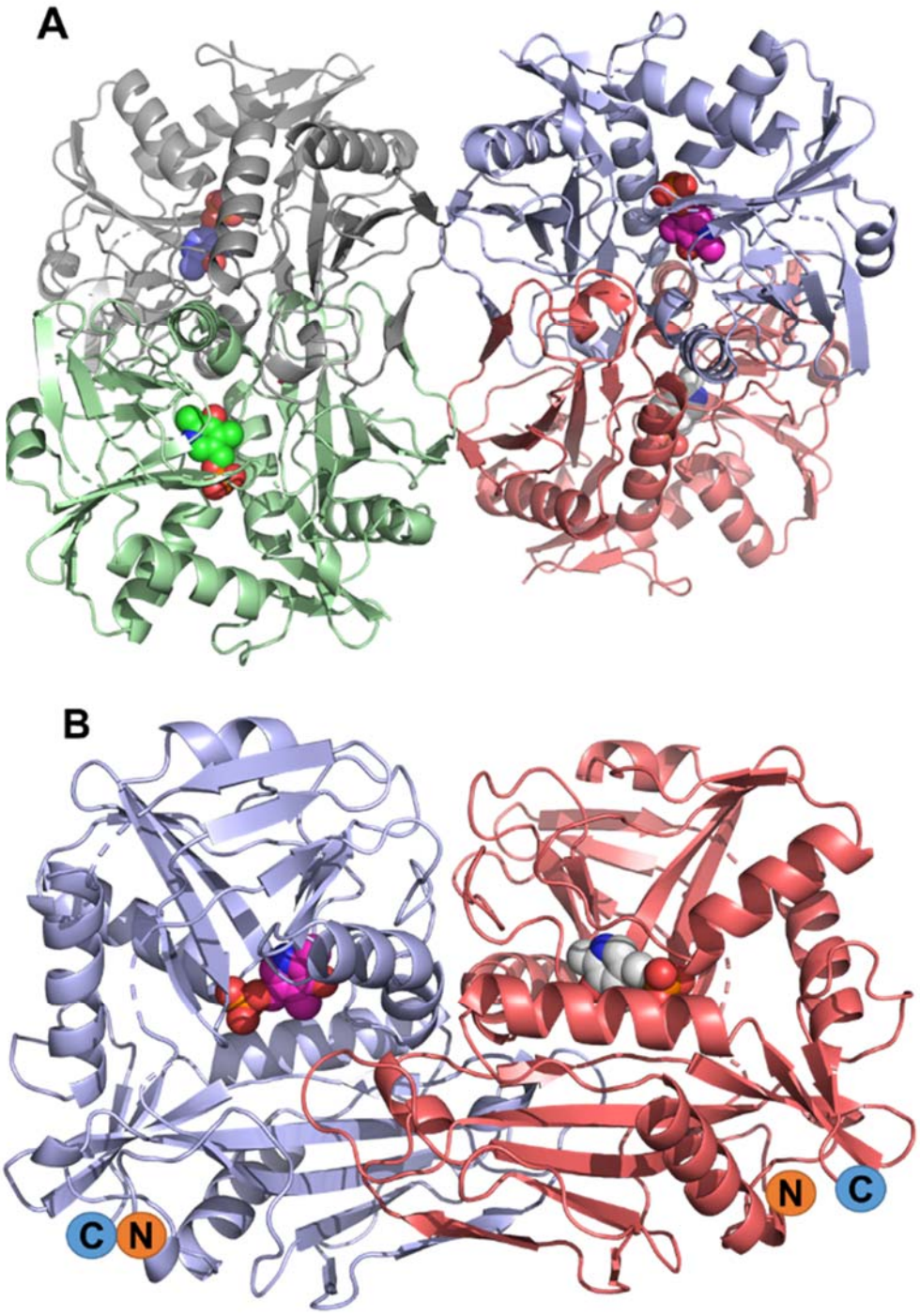

Figure 3.6.3 Crystal structure (at 2.80 Å resolution) of the recombinant PgIlvE internal aldimine form (A) The crystallographic unit cell containing four monomers. (B) the homodimer form (B). Each monomeric subunit is marked in a different colour and the PLP location is presented as solid spheres. The N- and C-termini are marked in (B).

The x-ray crystal structure of the internal aldimine form of PgIlvE was solved at 2.80 Å resolution (Figure 3.6.3). The PLP cofactor was clearly observed bound to Lys183. The crystallographic unit cell of PgIlvE contained two homodimers within four

monomeric chains. The homodimeric assembly agreed with the solution properties of the purified enzyme that suggested PgIlvE was a dimer of two monomer chains. Additionally, PgIlvE showed high homology in structure with other IlvE or BCATs. Aligning one chain of PgIlvE with others in the IlvE or BCAT family, the RMSD difference with *D. radiodurans* (PDB: 3UYY [259]) is 0.62 Å, with *S. mutans serotype c* (PDB: 4DQN [290]) is 0.66 Å, with MsIlvE (PDB: 3JZ6 [205]) is 0.84 Å and with MtIlvE (PDB: 3HT5 [204]) is 0.82 Å.

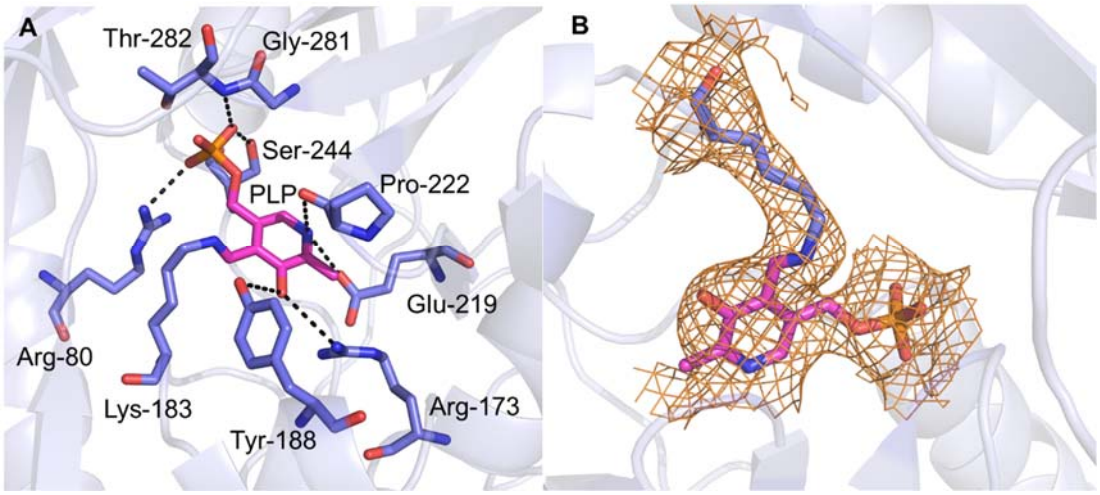

Figure 3.6.4 The position of PLP internal aldimine in the recombinant PgIlvE structure. (A) The interaction between PLP internal aldimine and residues in the active site. (B) The 2Fo-Fc density map contoured at 0.5 σ and carve radius at 2.5 Å.

Electron density for the PLP cofactor was clearly observed in the active site (Figure 3.6.4, 2Fo-Fc density map), the PLP cofactor was attached to the amine group of the Lys283 to as an internal aldimine. Apart from this, the -OH group of Tyr188 and the side-chain of Arg173 appeared to form hydrogen bonds with -OH group in the pyridine of PLP. The carbonyl group of Pro222 and the side chain of Glu219 engage in polar contacts with the amine of the pyridine ring to stabilise the PLP. Finally, the phosphate group of PLP displays polar contacts with the side-chain of Agr80, the – the side chain of Ser244 and the backbone peptide bond between Glu281 and Thr282. There appear to be no disulfides bonds in the PgIlvE structure. Even the closest two cysteines in each monomer chain from Cys48 were too far apart - the distance between them was 5.9 Å.

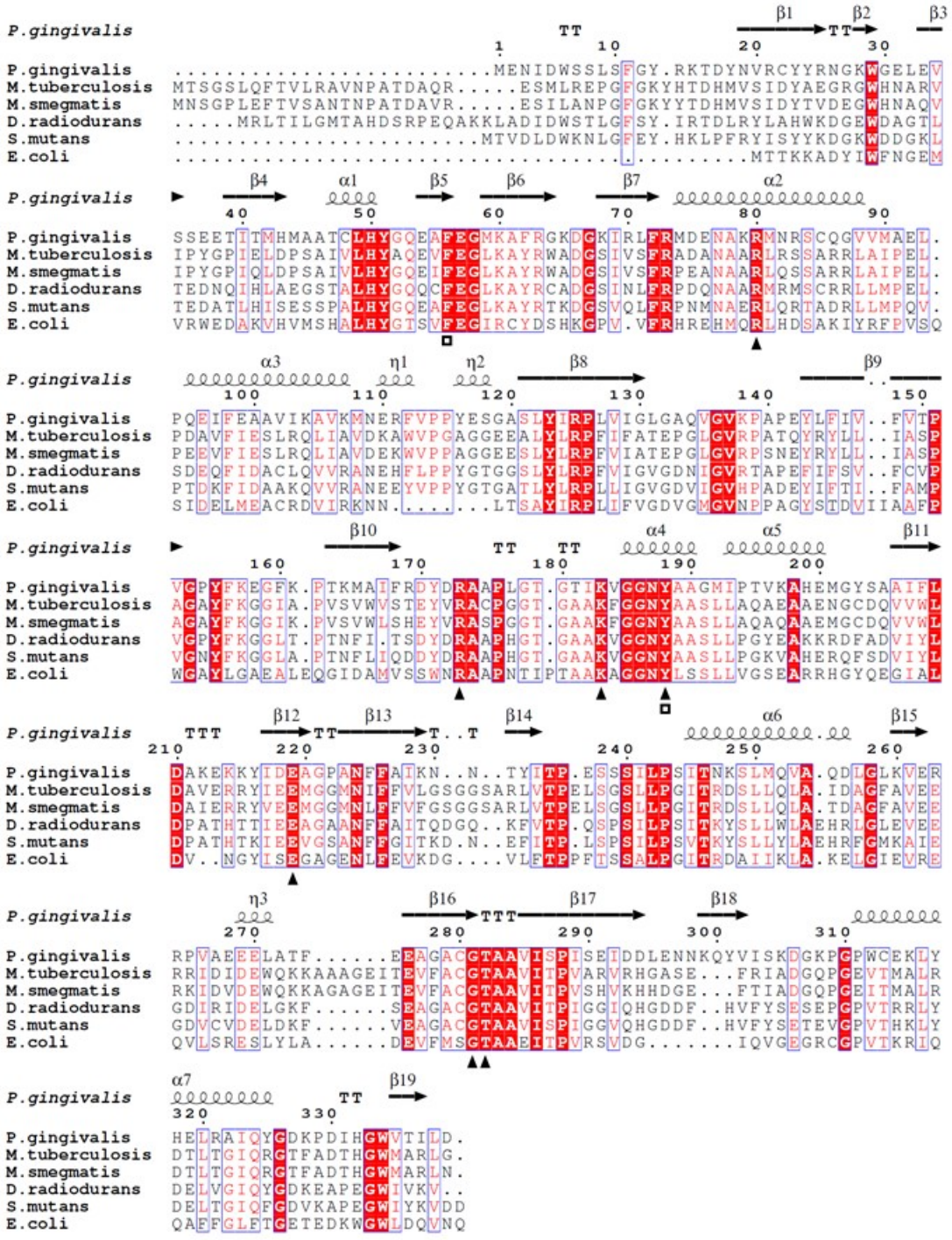

Figure 3.6.5 The sequence alignment of six bacterial IlvEs/BCATs numbered according to the *P. gingivalis* IlvE. The conserved residues that interact with the PLP cofactor are marked with a triangle below. Residues selected for site directed mutagenesis are marked with a square. The seconday structural elements (α-helix and β-sheet) are derived from the crystal structure of PgIlvE. Uniprot codes of each IlvE sequence are: *P. gingivalis* (Q7MV21), *M. tuberculosis* (P9WQ75), *M. smegmatis* (A0R066), *D. radiodurans* (Q9RTX5), *S. mutans serotype c* (Q8DTW7) and *E. coli* (P0AB80). The figure was generated with CLUSTAL Omega and annoted with EsPript 3.0.

The sequence of PgIlvE was aligned with other five bacterial IlvEs/BCATs (Figure 3.6.5), and residues Arg80, Arg173, Lys183, Tyr188, Glu219, Glu281 and Thr282 in PgIlvE were all conserved with the other IlvEs/BCATs. It is clear that Lys183 is the essential residue for IlvEs/BCATs since the enzyme uses this lysine to form the internal aldimine. Other conserved residues could also be essential for substrate binding and catalysing the transamination/aminotransferase activity, which can be explored using site-directed mutagenesis.

The crystal structure of the LCS-inhibited form of PgIlvE was also solved at 1.60 Å resolution (Figure 3.6.6). The PgIlvE: PLP:LCS protein structure consisted of four monomeric chains forming two homodimers in a similar manner as the structure of the PgIlvE PLP internal aldimine form. However, during the modelling stage, the electron density map suggested that two different structural forms of LCS were bound to the PLP cofactor (Figure 3.6.6 B and D). One structural form was the PLP:isoxazole form (ring-closed) and the other one was a ring-opened version of LCS, containing a -O-NH_2 group pointing at one direction and a carboxylate group pointing at the opposite direction. The PLP:isoxazole form is the most common adduct to be observed in PLP enzymes. For example, Olsen *et al.* and Peisach *et al.* both suggested the abstraction of the α-proton to give the aromatized CS adduct was carried out by the active site Lys in the LCS inactivation mechansims of γ-aminobutyric acid aminotransferase (GABA-AT) and DCS inactivation of D-amino acid aminotransferase (D-AAT) [291, 292]. In contrast, the phenomenon of a ring-opened version of CS has been reported in only a few PLP-dependent enzymes. Lowther *et al.* provided evidence for a ring-opened and decarboxylated version of CS on the SpSPT enzyme, resulting in PMP and β-aminooxyacetaldehyde. They observed the final product β-aminooxyacetaldehyde by MS analysis of dinitro-phenyl hydrazone adduct and in the x-ray crystal structure (PDB: 2XBN) [173]. Recently, Chiara *et al.* found the destruction of DCS in an alanine racemase and Gao *et al.* discovered a PMP-diketopiperazine adduct derived from the ring-opened form of CS in the PLP-dependent enzyme ForI from the biosynthetic pathway of the C-nucleoside antibiotic formycin [293, 294]. Therefore, all these findings suggested that upon incubation with PgIlvE the ring of CS would be broken down and the molecule would be rearranged into different structures.

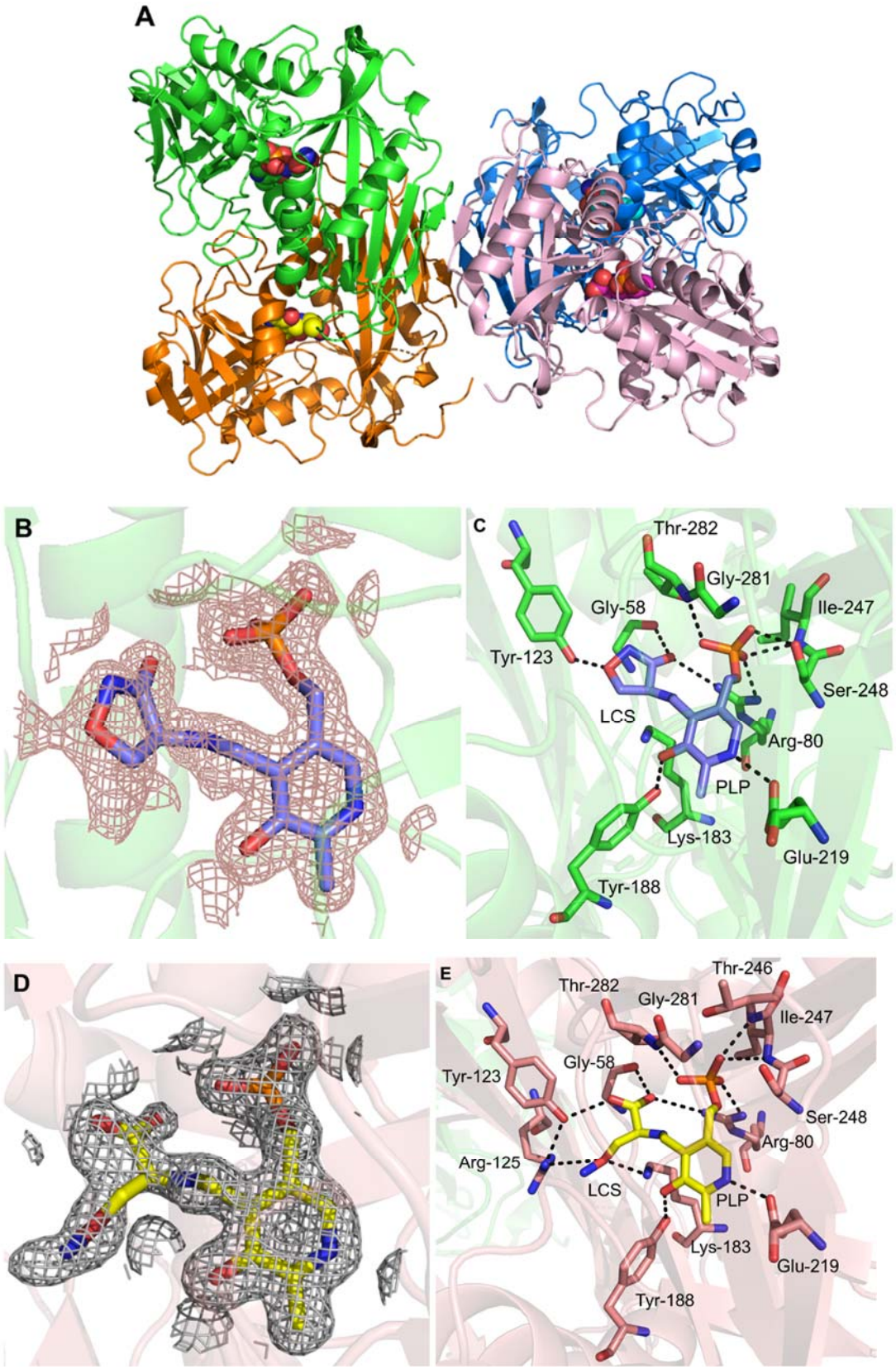

Figure 3.6.6 The x-ray crystal structure of the recombinant PglIvE in complex with a PLP:LCS form at 1.60 Å resolution. (A) Two homodimers in the crystallographic unit cell. The 2Fo-Fc map in chain A (B) and chain C (D) contoured at 1.0 σ and carve radius at 2.5 Å. (C) Crystal structure of PglIvE inhibited with LCS, showing ring-closed (C) and ring-opened (E) forms.

In the active site of the PglIvE PLP:LCS ring-closed version (Figure 3.6.6 C), the side chains of Arg88, Tyr188, Glu219, Gly281 and Thr282 still display polar contacts with the PLP cofactor in the same manner as the structure of PLP internal aldimine form. However, the phosphate group of the PLP cofactor appears to be shifted to form hydrogen bonds with the -OH group of Ser248 and the peptide backbone between Ser248 and Ile247. Furthermore, the keto group in the LCS ring interacts with both Gly58 and the side chain of Arg80. The -OH group of the Tyr123 side-chain engages in a polar contact with the oxygen in the LCS ring. All three of these residues stabilise the CS in the position of the active site. The Lys183 attached to PLP in the internal aldimine is clearly released from the PLP when LCS is connected to the PLP to form the external aldimine form (PLP:LCS).

Comparing the active site of the PLP:LCS ring-opened version (Figure 3.6.6 E), more residues were involved in stabilising the ring-opened form of the inhibitor. The Arg125 side chain is involved in forming hydrogen bonds with -O- group of ring-opened CS and the -OH of Tyr123. Meanwhile, the -O- group of the ring-opened CS is engaged in a polar contact with the amino side chain of Lys183, which was disconnected from the PLP. Additionally, the phosphate group of PLP was shifted again closer to the residues from Thr246 to Ser248, by forming a new hydrogen bond with the backbone amide bond between Thr246 and Ile247.

The x-ray crystal structure of the DCS-inhibited form of PglIvE was also solved at 1.78 Å resolution as shown as Figure 3.6.7. The protein crystal structure is composed of two homodimers within four monomeric chains in the crystallographic unit cell. Interestingly, instead of observing the PLP:DCS isoxazole form or a ring-opened form in the structure, density was found suggesting a PMP form in the active site according to the 2Fo-Fc map (Figure 3.6.7 B). However, it was not possible to locate the position of a CS-derived product such as the β-aminooxypyruvate or aldehyde. In addition, it was clear that the side chain of Lys183 is no longer forming a covalent bond with PLP that was observed in the PglIvE internal aldimine complex. The other residues, such as the side chains of Arg80, Tyr188, Glu219, Ser248, Gly281, Thr282, display polar contacts with the PMP cofactor similar to the protein structure of PLP internal aldimine form. However, the PMP appeared to be shifted and the Arg173 side chain was not in a hydrogen bond with -OH group of the pyridine ring.

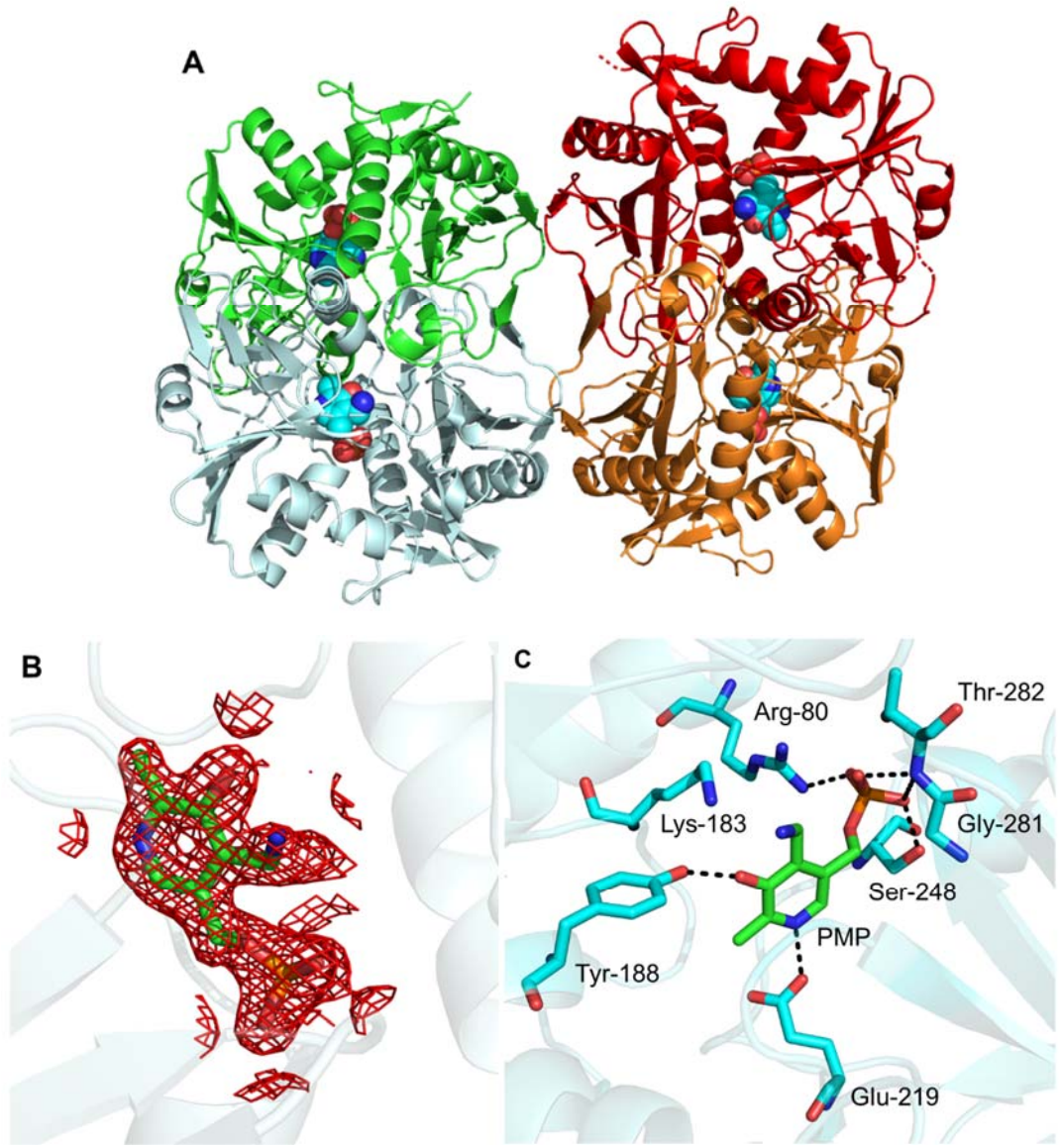

Figure 3.6.7 The x-ray structure of the recombinant PgIlvE in complex with PLP:DCS at 1.78 Å resolution. (A) Two homodimers in the crystallographic unit cell. (B) The 2Fo-Fc map contoured at 1.5 σ and carve radius at 2.5 Å. (C) Crystal structure of PgIlvE inhibited with DCS in the PMP form.

The structure of the covalent DCS-PMP adduct bound to MtIlvE was determined by Franco and Blanchard. DCS ring is showed as planar and aromatic, as previously observed for other enzyme systems. The research also confirmed the LCS and DCS-inhibited used MS analysis to show that the both LCS- and DCS-PMP complexes have the same mass. It is suggested that both enantiomers were converted to the same aromatized, isoxazole product [214]. Based on this work and studies shown above, a mechanism of CS inhibition of PgIlvE is proposed in the Figure 3.6.8. The internal aldimine was firstly combined with LCS or DCS to form the PLP:CS external aldimine form. Then, with the support of the side chain of Lys183, the PLP:CS

complex would be rearranged into the ketimine form, then the aromatized isoxazole form, which agreed with the ring-closed version of PLP:LCS crystal structure shown above. However, the ring-opened version of PLP:LCS and PMP were observed from the crystal structure results. It is worth noting that the breaking of bonds in CS or between PLP and CS could be caused by the high energy synchrotron radiation used in the X-ray diffraction analysis. In order to fully understand the inhibition mechanism, it is essential to carry out a full solution of the models by adding solvent molecules to discover the interaction between the active site and waters. This analysis is currently being carried out by the collaborator Dr. Jon Marles-Wright.

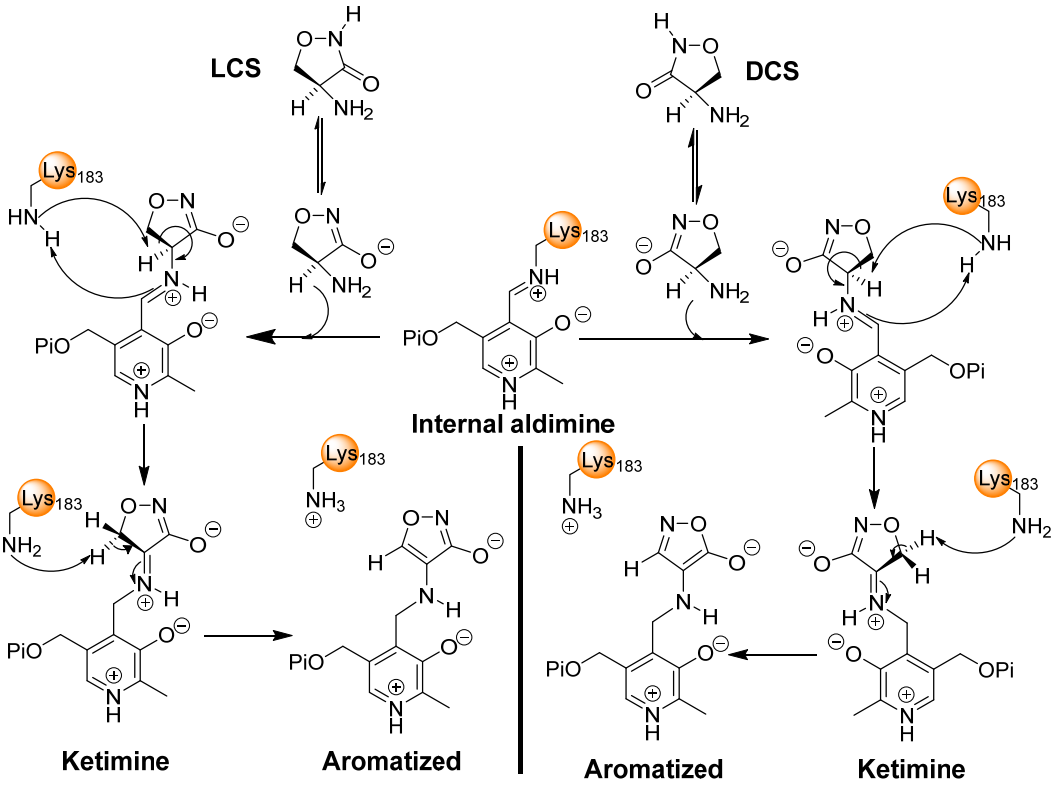

Figure 3.6.8 Proposed mechanism of CS inactivation of PgIlvE to form the PLP:aromatic isoxazole external aldminine.

3.7 Site mutagenesis study of PglIvE

During the x-ray crystal structural analysis of PglIvE (Section 3.6), it was also decided to carry out side-directed mutagenesis (SDM) to identify residues involved in substrate binding and catalysis. Based on Figure 3.7.1 and the reaction mechanism (Figure 3.4.1) of PglIvE, the -OH of the side chain of Tyr188 is close enough to provide a H-bond to the oxygen anion of the PLP cofactor and the amine of Lys183. The role of Tyr188 in the aminotransferase reaction was not known therefore, a mutant PglIvE Y188A was created to test what effect it would have on the activity of PglIvE. It was also noted in Franco and Blanchard's study [214] of MtIlvE that there was a potential Phe77 observed in the protein crystal structure (PDB: 1KT8) near to the main lysine residue of PLP that protected the active site from water molecules. The Phe residue was also a conserved residue in other BCATs – residue F56 in PglIvE from sequence alignment (Figure 3.6.5). Thus, the mutant PglIvE F56A was created and studied.

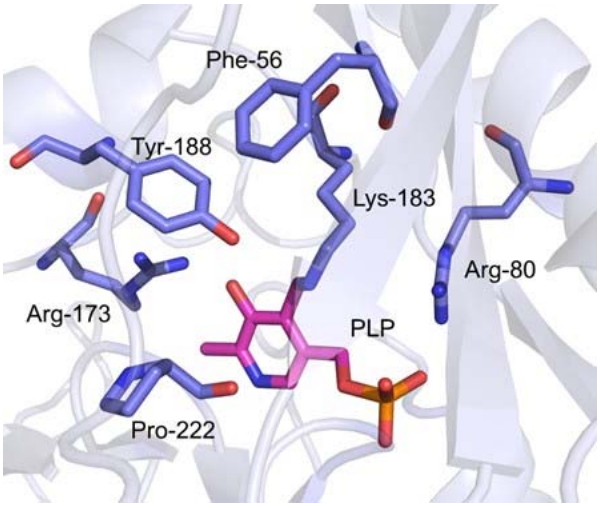

Figure 3.7.1 The structure of the PglIvE active site of the PLP internal aldimine form.

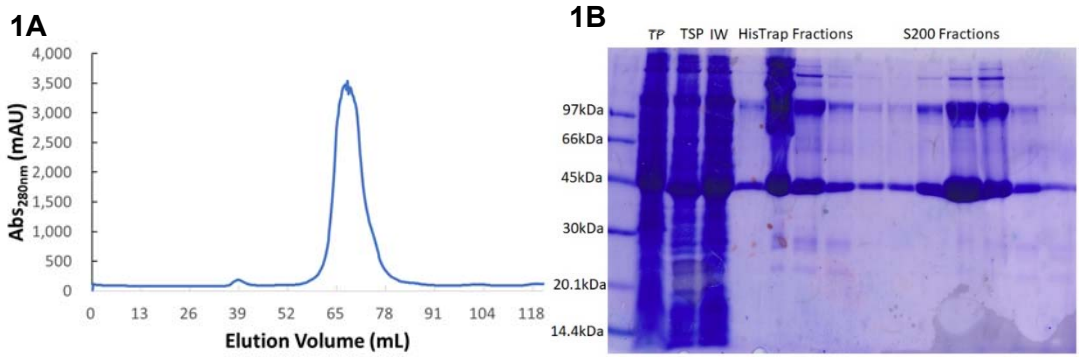

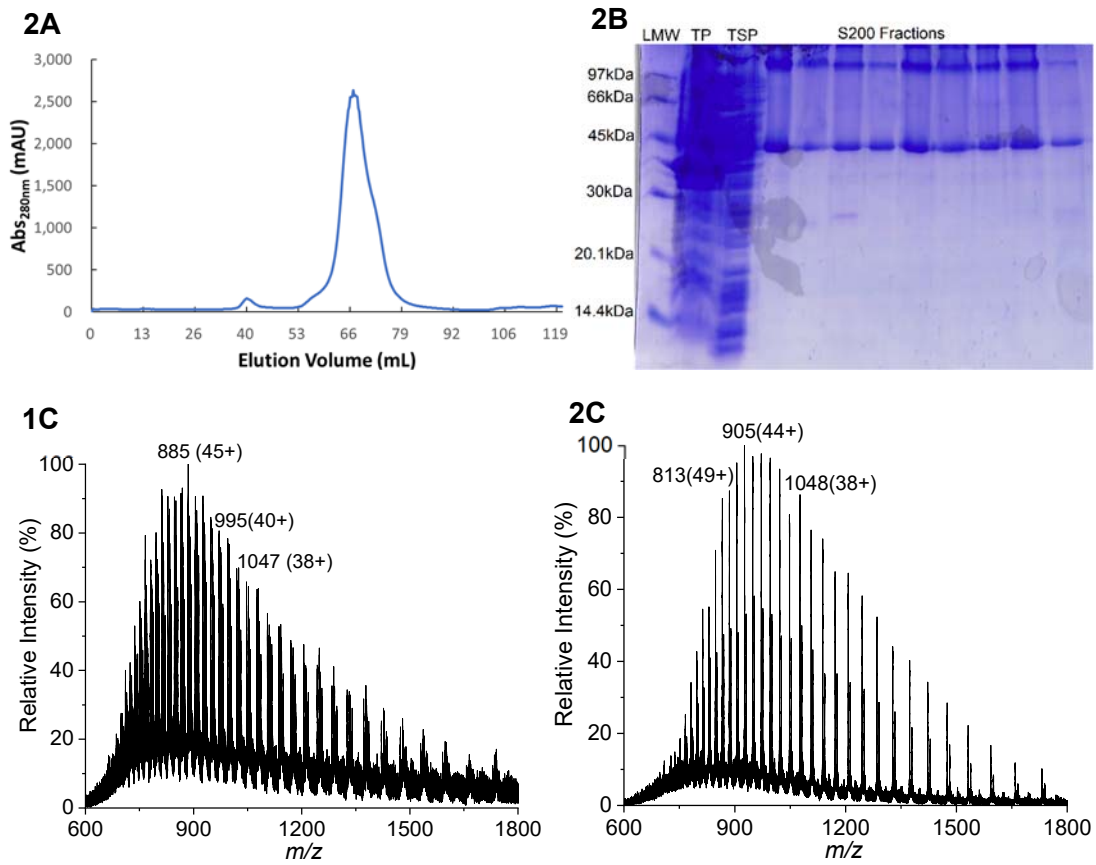

Figure 3.7.2 Mutants PglIvE Y188A (1) and F56A (2) purification and analysis. (A) Chromatogram from SES column. (B) 15% SDS-PAGE gel after SEC. LMW: Low molecular weight marker, S200 fraction: elution fractions from main peak. (C) The mass spectrum of recombinant PglIvE Y188A (1) with a mass of 36762.23 ± 0.78 Da, F56A (2) with a mass of 39782.87 ± 1.81 Da. All the enzyme concentrations were 10 μM.

The PglIvE mutants Y188A and F56A were readily expressed and purified with the same procedure as PglIvE WT described above, and both mutants showed similar UV-vis properties as the WT spectrum from the SEC column eluting at approximately 68 mL (Figure 3.7.2) representing a homodimer in solution. The SDS-PAGE analysis showed the protein with a monomeric mass of ~40kDa. Both mutants were further confirmed by LC-ESI-MS (Figure 3.7.2), giving a mass of 39762.23 ± 0.78 Da for Y188A and a mass of 39782.87 ± 1.81 Da for F56A. Both data were in keeping with the theoretical mass from the predicted recombinant protein sequence (39761.39 Da for Y188A, 39777.39 Da for F56A) without initial methionine (131.19 Da) and multiple forms of the enzyme were observed representing the glycosylation of the histidine tag [228, 229].

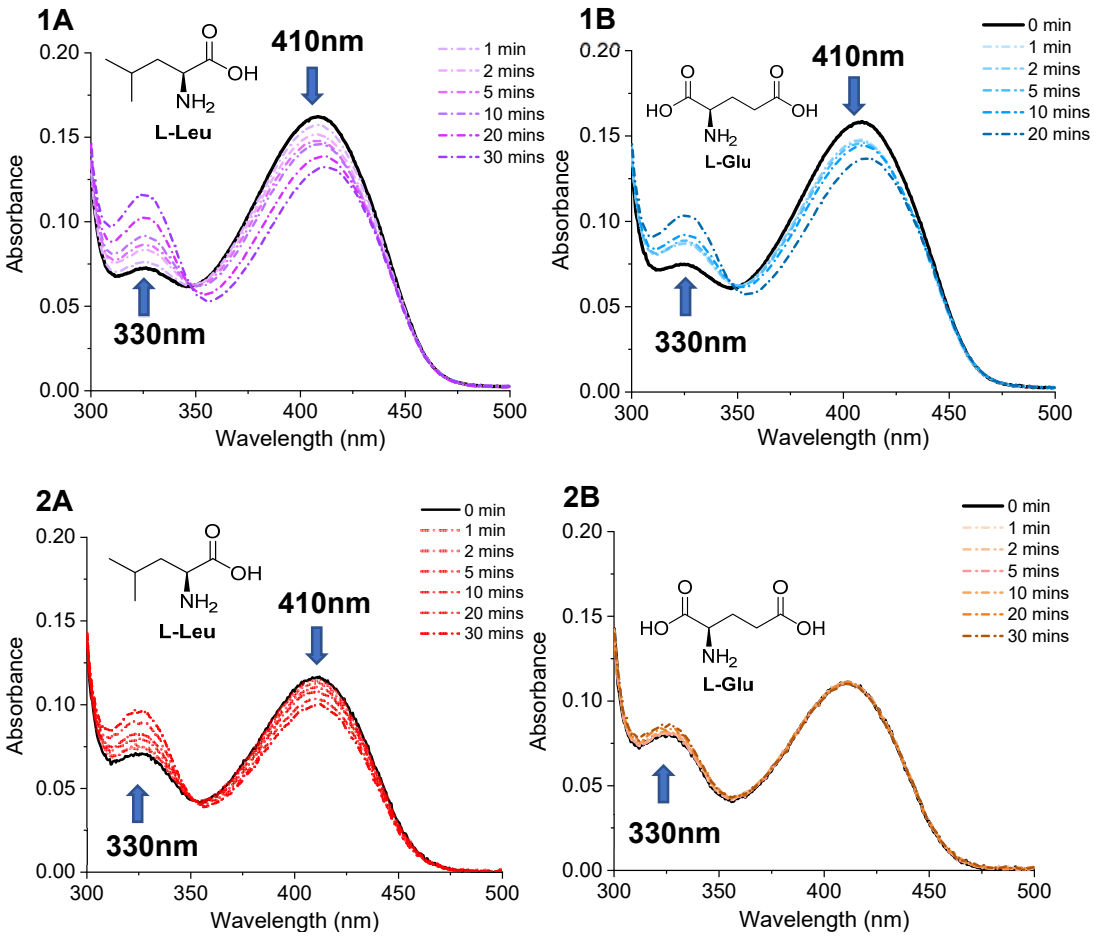

Figure 3.7.3 UV-vis analysis of the PglIvE mutants F56A (1) and Y188A (2). The absorbance changes of PglIvE with the addition of L-Leu (A) and L-Glu (B) over time. Each assay contained 20 μM PglIvE.

As shown in Figure 3.7.3, both mutant F56A (1) and Y188A (2) were studied by the addition of 1 mM L-Leu and 1mM L-Glu and monitoring changes between 0-20 mins. This led to a decrease in the peak at 410 nm and the formation of a broad absorbance with λ_{max} at 405 nm. At the same time, the peak at 330 nm was increased and shifted slightly to a new peak at 328 nm. However, the changes in the mutant Y188A were much less pronounced than in the mutant F56A, especially since almost no changes were noted when L-Glu was added to the Y188A mutant. Meanwhile, since the binding of L-Leu and L-Glu is the first step in the aminotransferase mechanism, it suggests that the Y188A mutation affected the PglIvE activity more severely than the F56A mutant.

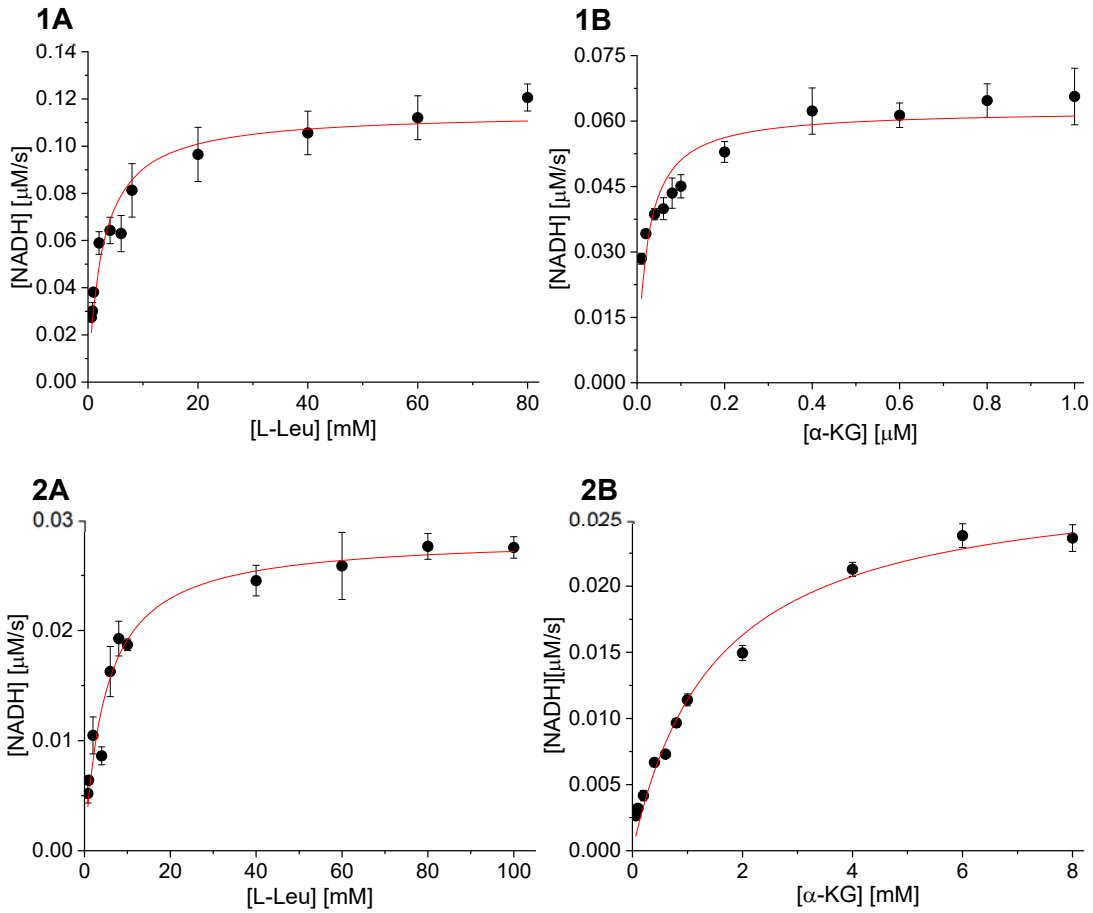

Figure 3.7.4 Kinetic analysis of PgIlvE mutants for substrate L-Leu (A) and α-KG (B) by the coupled IlvE/GDH assay. (1) F56A (2) Y188A. Each assay contained 1 or 15 μM enzyme and the variable concentration of L-Leu or α-KG. All data were plotted as mean readings ±2-SD error bars.

The enzyme activity of both PgIlvE mutants with substrates L-Leu and α-KG was analysed using the coupled IlvE/GDH assay as shown in Figure 3.7.4. Kinetic data derived using Michaelis-Menten analysis showed that there was a dramatic impact when the Tyr188 side chain was converted to Ala in mutant Y188A. In fact it was necessary to increase the enzyme concentration for the assay 30 fold from 0.5 μM to 15 μM in order to determine kinetic parameters. For substrate L-Leu, the K_M = 4.89 ± 0.49 mM, V_{max} = 0.03 ± 0.01 μM/s and the k_{cat} = 1.87 ± 0.05 × 10^{-3} s^{-1}. For substrate α-KG, the K_M = 1.50 ± 0.10 mM, V_{max} = 0.03 ± 0.01 μM/s and the k_{cat} = 1.87 ± 0.05 × 10^{-3} s^{-1}. In contrast, the F56A mutant was not as severely affected as the Tyr188Ala mutant, which gave kinetic parameters K_M = 2.67 ± 0.31 mM, V_{max} = 0.11 ± 0.01 μM/s and the k_{cat} = 0.11 ± 0.01 s^{-1} with substrate L-Leu and the K_M = 0.02 ± 0.01 mM, V_{max} = 0.06 ± 0.01 μM/s and the k_{cat} = 0.06 ± 0.01 s^{-1} with substrate α-KG.

Table 3.7.1 Comparison of enzymatic activities of PgIlvE WT, Y188A and F56A with substrates L-Leu and α-KG using the coupled IlvE/GDH assay.

Enzymes		WT	Y188A	F56A
K_M (mM)	L-Leu	2.48 ± 0.21	4.89 ± 0.49	2.67 ± 0.31
	α-KG	0.14± 0.01	1.50 ± 0.10	0.02 ± 0.01
$k_{cat} \times 10^{-3}$ (s^{-1})	L-Leu	886 ± 24	1.87 ± 0.05	110 ± 10
	α-KG	410 ± 10	1.87 ± 0.05	60 ± 10
k_{cat}/K_M ($M^{-1}s^{-1}$)	L-Leu	356.7	0.380	42.7
	α-KG	2907.8	1.24	3100

Contrasting with the PgIlvE WT (Table 3.7.1), the Y188A mutant showed not only weaker substrate affinity with L-Leu (~twice as weak) and α-KG (~10 times weaker), but also the catalytic activity was essentially abolished since the turnover was reduced by ~470 (L-Leu) and ~220 fold (α-KG). In contrast, the F56A mutant only showed a stronger affinity with α-KG compared to the WT, however, the turnover number of each substrate was approximately 8 times slower than the WT. Thus, the mutant F56A only affected the catalytic efficiency of L-Leu and not α-KG.

In summary, the Phe56 residue of PgIlvE did play a role in the enzyme activity possibly by affecting the hydrophobic nature of the active site and the interaction with the substrates, in agreement with that found for the equivalent Phe77 residue in MtIlvE. Additionally, in our study of PgIlvE, the -OH group of the side-chain of Y188 plays essential role in both the catalytic activity and substrate binding according to both kinetic analysis and UV-vis results. Further structural studies of the PgIlvE Y188F mutant might reveal how the removal of this side chain has impacted on the position and orientation of the PLP cofactor. Furthermore, a crystal structure of the wild type PgIlvE in complex with a PLP:substrate external aldimine may provide insight into this residue interacts with both BCAA and α-KG substrates and reveal a role in the catalytic mechanism.

Chapter 4 3-Ketodihydrosphingsine reductase (KDSR)

4.1 Cloning, expression and purification of *S. Cerevisiae* KDSR (ScKDSR)

In the core, conserved SL biosynthetic pathway, after the first committed SPT-catalysed reaction, a key second step is the conversion of the 3-KDS intermediate to DHS. This reduction is catalysed by a 3-KDS reductase (KDSR) and the eukaryotic enzymes are found in the ER. The membrane-bound nature of the KDSRs made them technically difficult to study e.g. an x-ray crystal structure has not been determined of a KDSR. Furthermore, there has not been a soluble, bacterial KDSR isolated to date that can be used as a model for the isozymes from a higher organism in a similar way that the bacterial SPT has been used as a model for the membrane-bound SPT complexes.

As mentioned in Introduction 1.4, in 1998 Beeler, Dunn *et al.* characterised the *S. cerevisiae* yeast KDSR (encoded by the TSC10/YBR265w gene) and in the ~20 years since then more KDSRs have been discovered in mammals (including humans) and fungi [215-217]. The KDSRs can be classified as members of the short chain dehydrogenase/reductase (SDR) superfamily. This superfamily represents one of the largest protein superfamilies known to date and they can catalyse NAD(P)(H) dependent reactions with a substrate spectrum ranging from polyols, retinoids, steroids and fatty acids. Without a structure it is unclear how these KDSR enzymes catalyse the stereospecific reduction of 3-KDS with the NADPH cofactor. Therefore, to begin a study of the yeast KDSR, sequence alignment analysis was carried out between the characterised KDSRs (Figure 4.1.1 A). Although these KDSRs display low identity (15%~30%) with the yeast KDSR, they showed a conserved motif (YXXXK), which was considered as the catalytic site for the SDR family [295]. Furthermore, the Lys and Ser side chains were proposed to support a proton transfer from Tyr to the substrate [296]. The other conserved motif (GXXXGXG) near to the N terminus was suggested to form the NADPH-binding domain or Rossman fold [297]. Additionally, Beeler *et al.* prediected a 38 aa hydrophobic anchor/membrane-binding domain near to the C terminus of KDSR to allow interaction with the ER membrane. Therefore to aid in soluble expression, this domain was removed and a truncated his-tag version had been cloned from a plasmid gifted by Prof. Teresa Dunn and expressed in *E. coli* by a previous group member, Dr. Jonathan Lowther (Figure 4.1.1 B). However, no biochemical data on the purified yeast KDSR had been published.

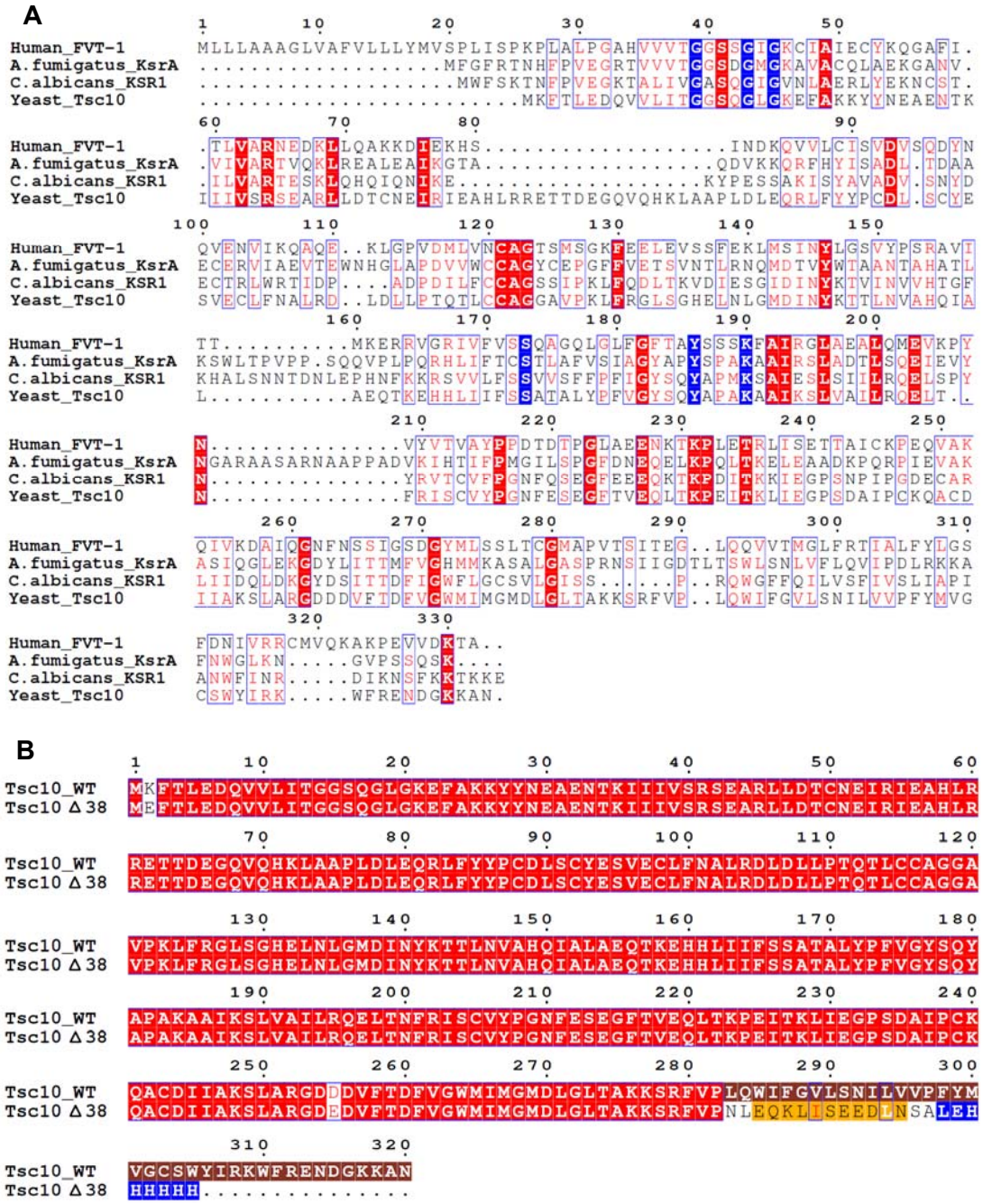

Figure 4.1.1 Sequence alignment of KDSRs. (A) from human, fungi (*A. fumigatus* and *C. albicans*) and and yeast. The essential residues were highlighted as blue. (B) between yeast KDSR WT and truncated-his-tag version. The truncated part was highlighted in brown; the his-tag was highlighted in blue; the Myc-tag was highlighted in orange. The alignment was produced by Clustal Omega and annotated using ESPript 3.0.

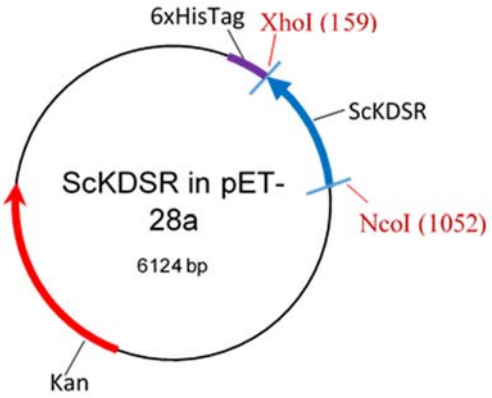

Figure 4.1.2 Plasmid map of *S. Cerevisiae* KDSR in pET-28a

Therefore, this project was based on establishing the activity of the yeast enzyme known as ScKDSR, which had already been cloned into a C-terminal 6xHis-tag in a pET-28a plasmid with NcoI and XhoI restriction sites (Figure 4.1.1). The other goal was to couple the KDSR with SPT and directly monitor KDS formation by converson to DHS at the same time as oxidation of NADPH at 340 nm.

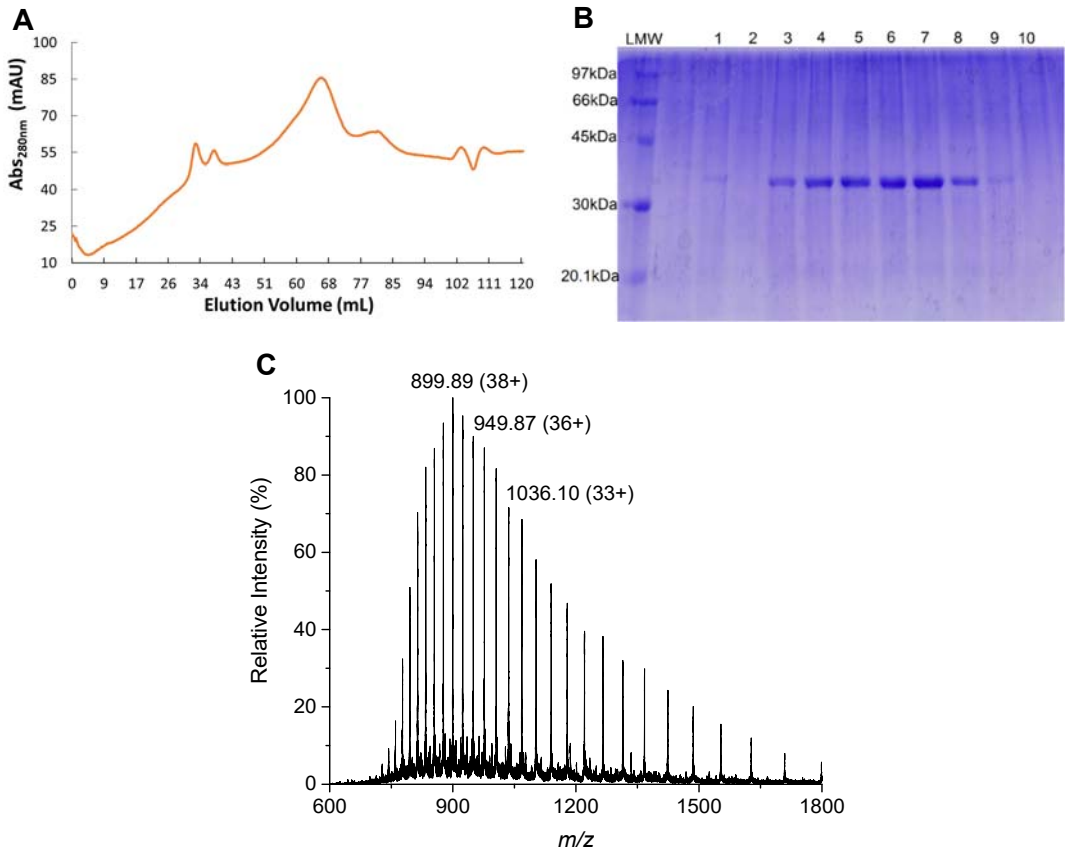

Figure 4.1.3 ScKDSR purification and analysis. (A) Chromatogram from SES column. (B) 12% SDS-PAGE gel after SEC. LMW: Low molecular weight marker, Lane 1-10: elution fractions from 33-87 mL. (C) The mass spectrum of recombinant ScKDSR (10 μM) with a mass of 34159.95 ± 1.49 Da.

The ScKDSR expressed well (band at ~34 kDa in SDS-PAGE) and in soluble form in *E. coli* BL21 (DE3) for 4 hours at 30 °C after being induced with 0.1 mM IPTG. An EDTA-free protease inhibitor tablet (Roche) was added before the sonication and the ScKDSR was isolated by HisTrap using buffer M and N, then was loaded on a calibrated HiPrep™ 16/60 Sephacryl™ S-300 SEC with buffer G, and typical protein yields were ~5 mg/L culture. According to the chromatogram, the protein appeared to be aggregated because of several elution peaks from the SEC column and only one clear band on each section analysed by SDS-PAGE gel (Figure 4.1.3). The protein quaternary structure was unpredictable even after using the standard calibration (Appendix 8.2). The pure ScKDSR was analysed by denaturing LC-ESI-MS and the resulting mass spectrum (Figure 4.1.3) showed several peaks, representing many charge states of the protein. The protein mass was determined using the maximum entropy algorithm from smoothed and centroided data, shown as 34159.95 ± 1.49 Da, and was within 0.05% of the theoretical mass of 34176.04 Da calculated from recombinant protein sequence by using ExPaSy ProtParam tool.

The ScKDSR catalyses the stereospecific NADPH-dependent reduction of 3-KDS to produce DHS – also known as L-erythro-dihydrosphingosine or (2*R*, 3*S*)-2-aminooctadecane-1,3-diol. Based on the SDR mechanism suggested by Filling *et al.*, it is possible that the ScKDSR catalyses hydride attack on the 3-KDS substrate carbonyl from the NAPDH. The enzyme uses the –OH of the Tyr180 side chain as the proton donor which is replenished through a water channel as shown in Figure 4.1.4 [298]. More details of the proposed catalytic mechanism will be discussed with a ScKDSR model in Section 4.5. Therefore, the kinetic parameters of the enzyme can be characterized by monitoring decreasing absorbance of NADPH at the wavelength 340 nm (ε_{Max} = 6200 M^{-1} cm^{-1}).

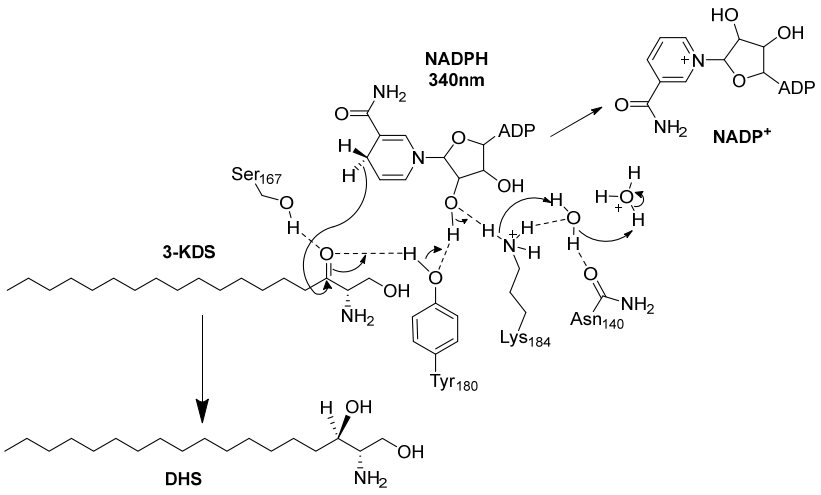

Figure 4.1.4 Proposed mechanism of ScKDSR [298]

4.2 Characterization and activity of KDSR

As well as monitoring the oxidation of the NADPH cofactor it was also key to measure the reduction of the 3-KDS to DHS directly using MS This was achieved by incubation of the recombinant ScKDSR with 3-KDS and NADPH and then analysis of the products in comparison to commercial standards and the appropriate controls (Figure 4.2.1).

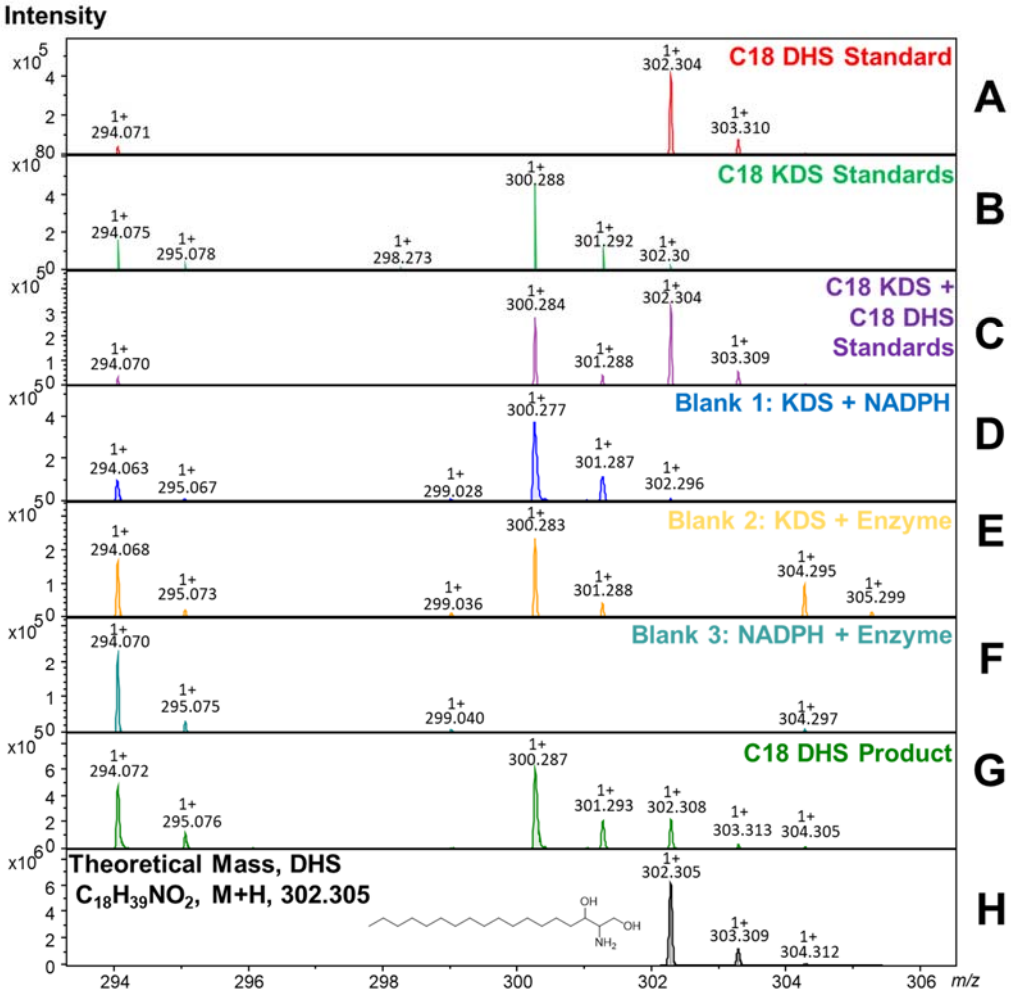

Figure 4.2.1 MALDI-ToF analysis of the recombinant ScKDSR reaction products using C18 3-KDS and NADPH substrates. (A) C18 DHS standard (B) C18 3-KDS standard (C) C18 KDS + C18 DHS standards (D-E) negative controls (G) Full assay of ScKDSR reaction (H) Theoretical mass spectrum. Each assay contained 100 μM ScKDSR, 250 μM NADPH and 100 μM 3-KDS. The data was analysed on positive mode in triplicates.

The product C18 DHS (302.305 Da) produced from the KDSR reaction was successfully detected by MALDI-ToF-MS (Figure 4.2.1). In the positive ion mode MALDI-ToF-MS analysis of the standards (panel A and B in the spectra), it was

observed as one main peak due to the quasi-molecular ion $[M+H]^+$ as well as one ^{13}C isotope peaks $[M+H]^+$ +1 amu. The relative abundance of this ion is ~20% of the base peak due to the presence of the ^{13}C isotope (natural abundance 1.1%), Therefore, even if the isotope peak $[M+H+2]^+$ (*m/z* 302.30) of C18 3-KDS overlapped with the main peak $[M+H]^+$ (*m/z* 302.30) of C18 DHS, there was still a ion count at *m/z* = 302.30 and the other two isotope peaks (*m/z* 303.30 and *m/z* 304.31) were also present in the DHS product spectrum (Panel C in the spectra, Figure 4.2.1). The Data Analysis Bruker software also allows calculation of the theoretical mass spectrum based on the chemical formula of the DHS species (C18H39NO2) for the $[M+H]^+$ ion and the associated isotope peaks (panel H in Figure 4.2.1). The experimental data is in good agreement with the predicted values and, when combined the negative controls (panels D-F in Figure 4.2.1), provide good supporting data that the ScKDSR is active (panel G in Figure 4.2.1).

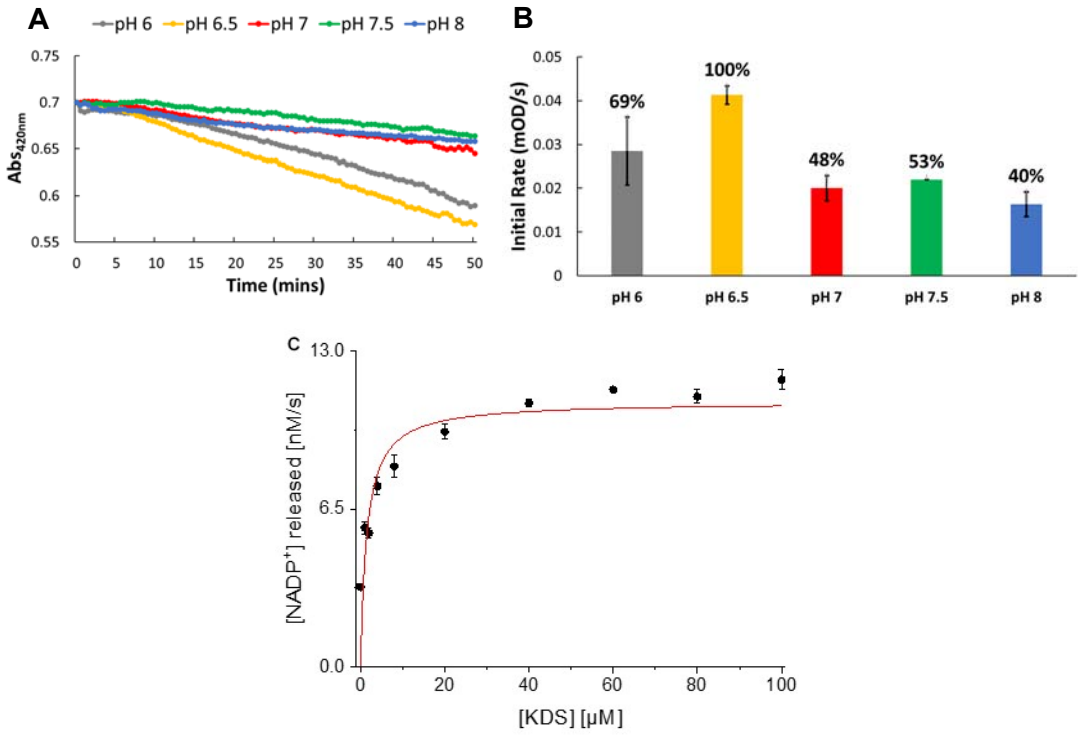

Figure 4.2.2 pH dependence and kinetic analysis of recombinant KDSR by NADH assay. (A) The absorbance against time in different pH. (B) Comparison of initial rate in different pH. Each assay contained 90 nM enzyme. (C) Kinetic analysis for substrate 3-KDS. Each assay contained 90 nM enzyme and variable concentration of 3-KDS. All data were plotted as mean readings ±2-SD error bars.

Before characterising the kinetic parameters of KDSR, the enzyme was firstly tested with a range of pH values between 6.0 and 8.0 in 0.5 increments to determine the optimal assay conditions. As shown in Figure 4.2.2, the highest reaction rate was observed at pH 6.5. Fresh solutions were prepared before the assay to avoid NADPH degradation each time [299]. The other problem which occurred during the assay was the hydrophobicity of the substrate 3-KDS and ther product DHS because of the long alkyl chain, and according to the safety data sheet from the provider company Matreya LLC, ethanol, methanol or chloroform was necessary to dissolve 3-KDS. For this assay, 10 mM KDS was dissolved in 50% ethanol to form a maximum stock concentration made for the kinetic assay.

With the optimized assay conditions, several typical reactions were carried out at multiple substrate (C18 3-KDS) concentrations (0-100 μM). Kinetic parameters were determined by using Michaelis-Menten analysis (Figure 4.2.2), which resulted in a determination for KDS; K_M = 1.51 ± 0.31 μM, V_{max} = 10.90 ± 0.46 nM/s, and k_{cat} = 0.12 ± 0.01 s^{-1}. Noticeably, at 0 point on the x axis, there was still an initial rate around 3.25 nM/s, which was considered as the background rate in the assay.

Table 4.2.1 Kinetic parameters of KDS for different KDSRs [216, 217].

Species	k_{cat} (s^{-1})	K_M (μM)	k_{cat}/K_M ($mM^{-1}s^{-1}$)
HsFVT-1	ND[a]	3	ND[a]
CaKSR1Δ39p	0.11	9	12.22
ScKDSR	0.12 ± 0.01	1.51 ± 0.31	79.47

[a] Not determined

In a summary (Table 4.2.1), Fornarotto *et al.* [217] determined kinetic parameters with a truncated version of CaKSR1 which cut off 39 amino acids. Kihara's group [216] only determined the estimated K_M value of human FVT-1 as 3 μM for KDS. Compared to the ScKDSR, both enzymes bound the substrate with lower affinity (high K_M). One possible influence on the catalytic rate could be the use of detergent which will be discussed below.

As well as obtaining biochemical data for ScKDSR, another goal was to couple the enzyme in an assay with bacterial and other SPTs. This meant that the conditions for both enzymes had to be compatible – however, it had been reported that ScKDSR, especially the ER-bound forms, required the addition of detergents for activity. Our method of expression had removed the predicted C-terminal membrane-binding domain and the enzyme was soluble when expressed in *E. coli*. Therefore, as a check,

the ScKDSR activity was tested with different detergents and different concentrations (Figure 4.2.3). In general, all the detergents showed different effects on the assay. All the initial rates with detergents (0.5~8 nM/s) were slower than the one without detergent (12.5 nM/s). In the previous study of the recombinant *C. albicans* enzyme (CaKSR1), Fornarotto *et al.* [217] used the detergent 0.5% CHAPS in their KDSR assay. However, from Figure 4.2.3, the initial rate of ScKDSR with 0.5% CHAPS was only 3.9 nM/s, showing the enzymatic activity had been lowered to ~31%. Additionally, detergents DDM and TDM had less influence on the ScKDSR enzyme (4~8 nM/s), which still retained 32%~65% enzymatic activity. It was found that 2% DDM (8.2 nM/s) was the best detergent condition for measuring KDSR activity, and by increasing the KDSR concentration in the SPT coupling assay might minimize the influence of the detergent.

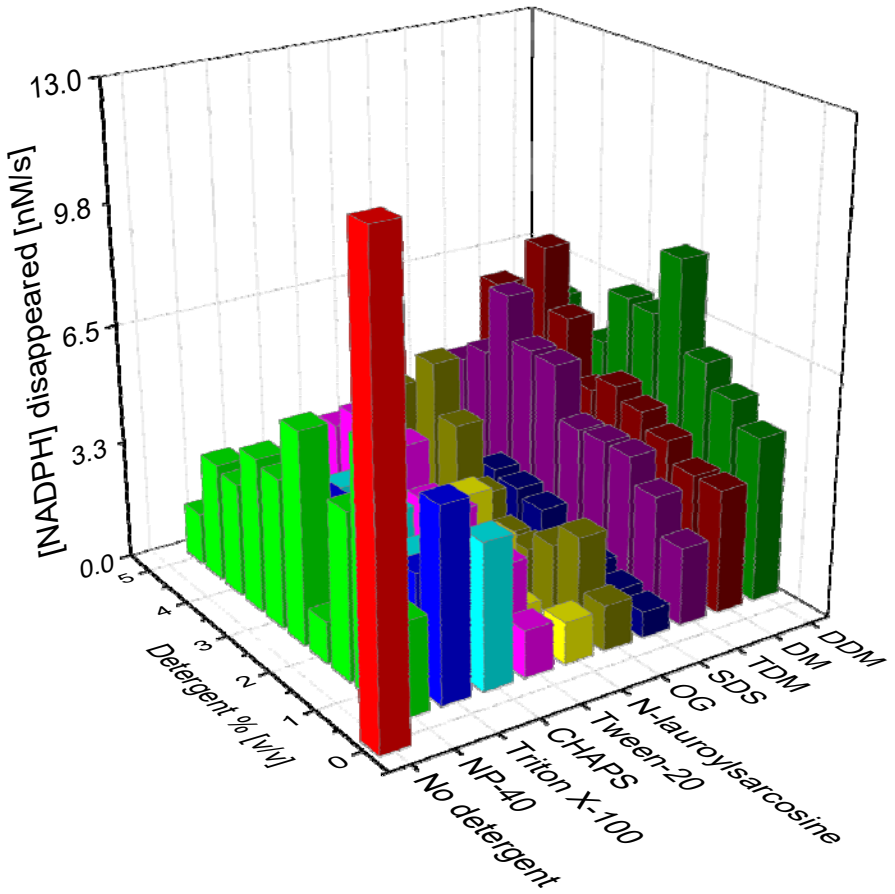

Figure 4.2.3 Detergent screening of KDSR WT activity by the NADPH assay. Each assay contained with 90 nM enzyme, 200 μM NADPH, 60 μM KDS (0.6% ethanol).

4.3 KDSR and human disease

As mentioned in the introduction, a rare, inherited syndrome of skin pathology and recessive progressive symmetric erythrokeratoderma, had been recently identified. This disease is characterized by severe lesions of thick, scaly skin on the face and genitals, as well as thickened, red, and scaly skin on the hands and feet. It has been associated with reduced ceramide levels and linked to mutations in human KDSR [221-223]. As shown in the Figure 4.3.1, different mutations or deletions across the full length of KDSR gene and led to the dysfunction of the encoded enzyme.

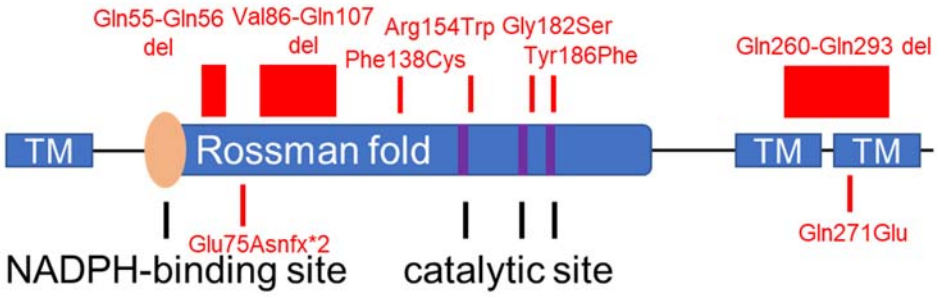

Figure 4.3.1 KDSR mutations/deletions reported in the pathogenic patients [221-223, 300].

Therefore, it is intriguing to use the ScKDSR as a model for the human isoform and by site-directed mutagenesis study the influence of the disease-causing mutations on substrate binding and catalysis.

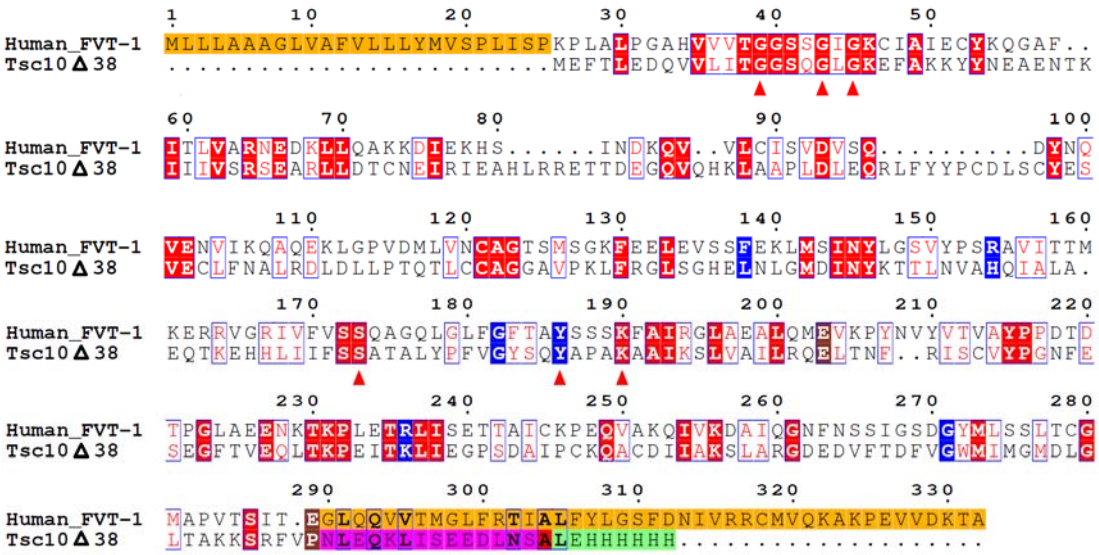

Figure 4.3.2 Sequence alignment of human and yeast KDSR. The KDSR mutations found in patients were highlighted in blue; the truncated part of ScKDSR was highlighted in pink; the his-tag was highlighted in green; the predicted membrane-binding domain was highlighted in orange; the predicted mutations were highlighted in brown; the essential residues were labelled with red triangles. The alignment was produced by Clustal Omega and annotated with EsPript 3.0.

First, an alignment of human FVT-1 and ScKDSR was prepared (Figure 4.3.2), there are extra residues at the beginning and end of the sequence of FVT-1, which is predicted as the ER membrane-binding sequence. According to the published KDSR papers, apart from the codon deletion, there are actually five mutated sites found in the thrombocytopenia patients, which are F138C, R154W [301], G182S, Y186F [222] and G271E in the FVT-1 [221]. Furthermore, in a recent study by Huber *et al.*, the mutations E198K and E289K were predicted to have an impact on the function of KDSR [300]. However, only three of the mutated sites are conserved in both the human and yeast KDSR sequences. Therefore those mutations, corresponding to ScKDSR G176S, Y180F and G263E, will be the main subject of study and discussion in the following section.

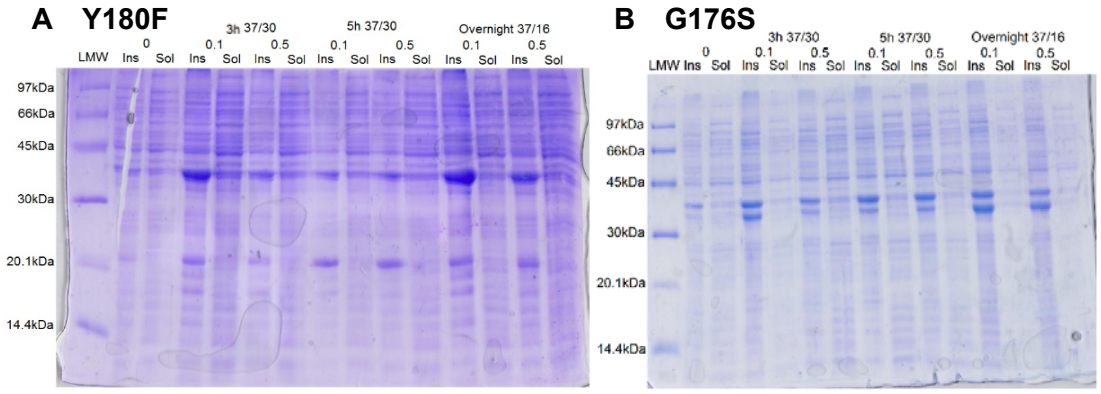

Figure 4.3.3 Test expression of ScKDSR mutants Y180F (A) and G176S (B) in *E.coli* BL21 (DE3). LMW: Low Molecular Weight marker. Ins: Insoluble. Sol: Soluble. The test conditions were varied from 0, 0.1, 0.5 mM concentration of IPTG added, 30 or 16 °C after induction, 3h, 5h, overnight growth after induction. The expected molecular weight of recombinant protein was around ~36kDa.

The equivalent ScKDSR mutant mimics, G176S, Y180F and G263E were successfully cloned by PCR and confirmed by DNA sequencing. All three mutants were tested in different expression conditions, regrettably, Y180F and G176S failed to express or were insoluble in expression strains such BL21 (DE3) (Figure 4.3.3), C41 (DE3), C43 (DE3), and Rosetta-gami 2 (DE3) cells with LB media or 2YT media or the addition of sorbitol [302]. The impact of these mutations on the ScKDSR suggest Y180 and G176 are essential residues either for protein expression or folding, because both changed codons, TTT for Y180F and AGC for G176S, were not rare codons in *E.coli* expression.

4.4 Expression, purification and characterization of ScKDSR G263E

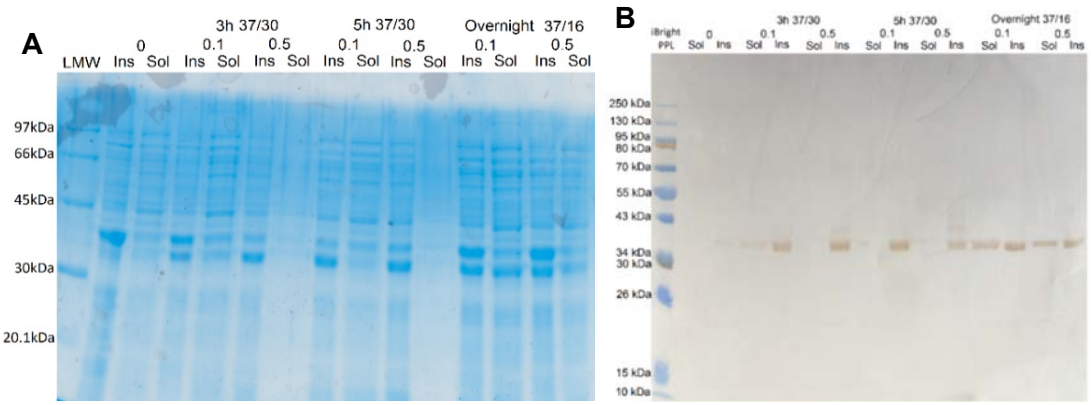

Figure 4.4.1 Expression test for ScKDSR mutant G263E in *E.coli* BL21 (DE3). (A) 12% SDS-gel analysis. (B) Western blotting analysis. LMW: Low Molecular Weight marker. Ins: Insoluble. Sol: Soluble. iBright PPL: iBright Prestained Protein Ladder (ThermoFisher). The expected molecular weight of recombinant protein was around ~36kDa.

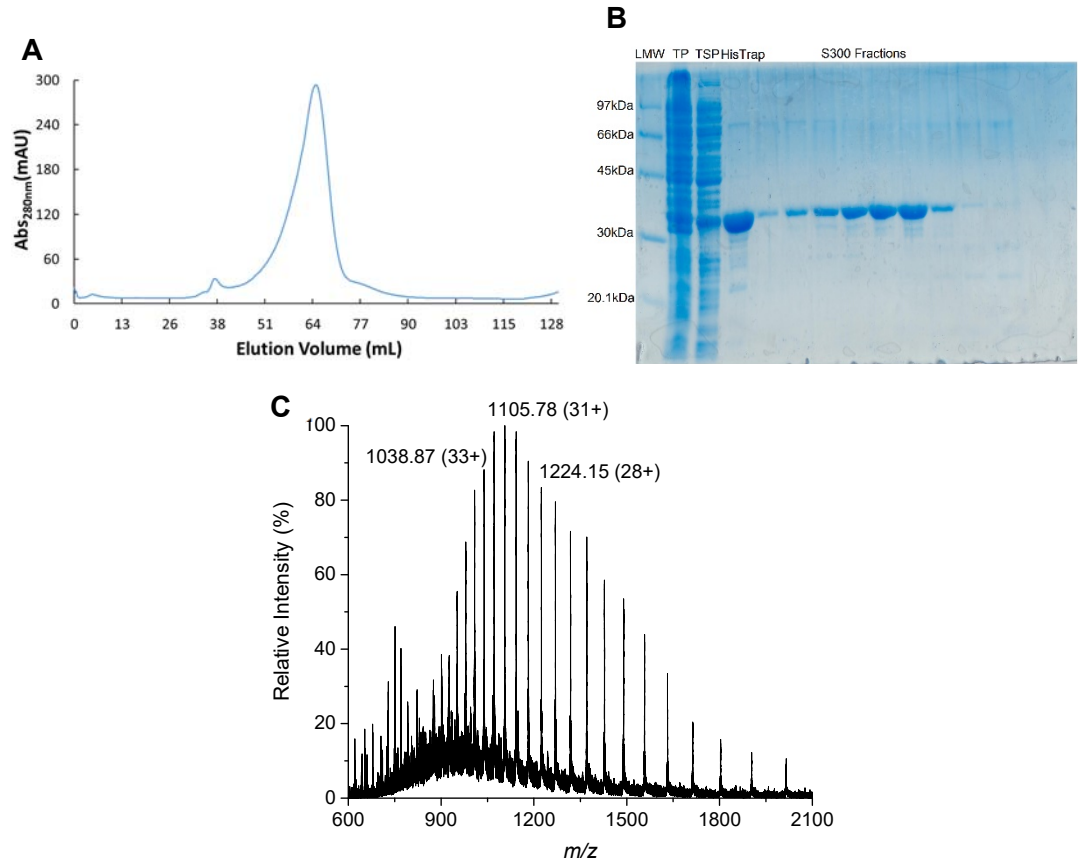

Figure 4.4.2 ScKDSR G263E mutant purification and analysis. (A) Chromatogram from SES column. (B) 12% SDS-PAGE gel after SEC. LMW: Low molecular weight marker, S300 Fraction: elution fractions from 38-90 mL. (C) The mass spectrum of recombinant ScKDSR G263E (10 μM) with a mass of 34248.61 ± 1.51 Da.

In contrast to the other mutants, ScKDSR mutant G263E was well expressed and soluble in *E. coli* BL21 (DE3) via overnight expression at 16 °C after induction of 0.1 or 0.5 mM IPTG. This was proved by 12% SDS-PAGE analysis and western blotting analysis for his-tag protein (Figure 4.4.1). Compared to the ScKDSR WT, the mutant G263E behaved differently during isolation (Figure 4.4.2 A). From the SEC chromatogram, the aggregation was absent as the mutant eluted with one sharp peak at ~65 mL. Therefore, by using a S300 calibration curve, the KDSR G263E behaved as a trimer in solution. However, the elution peak was still broad which could be a mixture of dimer or trimer. The protein mass was measured as 34248.61 ± 1.00 Da (Figure 4.4.2 C) using ESI-MS, which was in good agreement as theoretical mass of 34248.10 Da from ExPaSy ProtParam tool.

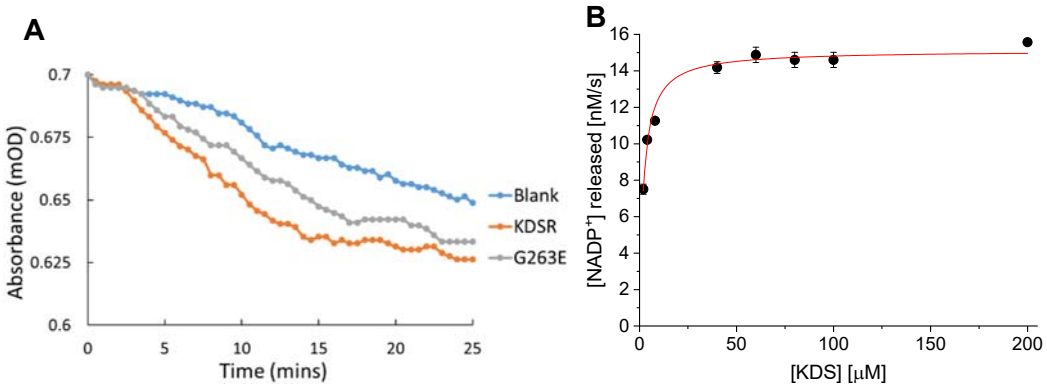

Figure 4.4.3 Characterization of ScKDSR G263E mutant by the NADH assay. (A) The absorbance vs time dot-line plot of KDSR WT, mutant G263E and blank samples. (B) Kinetic analysis of the mutant G263E. Each assay contained with 200 nM enzyme and variable concentration of KDSs. All data were plotted as mean readings ±2-SD error bars.

Table 4.4.1 Kinetic parameters of KDSR WT and mutant G263E by NAPDH assay.

Parameters	WT	G263E
K_M (μM)	1.51 ± 0.31	1.94 ± 0.22
k_{cat} (s^{-1})	0.12 ± 0.01	0.08 ± 0.01
k_{cat}/K_M ($mM^{-1}s^{-1}$)	79.47	41.23

Using the same NADPH assay for the WT enzyme (Figure 4.4.3 and Table 4.4.1), the mutant activity was measured as 1.5 times slower in comparison with the WT activity, with a lower k_{cat} = 0.08 ± 0.01 s^{-1}. However, there was no large difference in affinity with the substrate KDS, the K_M = 1.94 ± 0.22 μM for mutant and 1.51 ± 0.31 μM for WT. The catalytic efficiency (k_{cat}/K_M) showed that the mutant was reduced ~50% compared to the WT enzyme. This result agreed with Takeichi's study that the cellular DHS concentration was decreased due to the G271E mutation in human FVT-1 but the molecular details of this impact are unknown [221].

4.5 Crystallography study

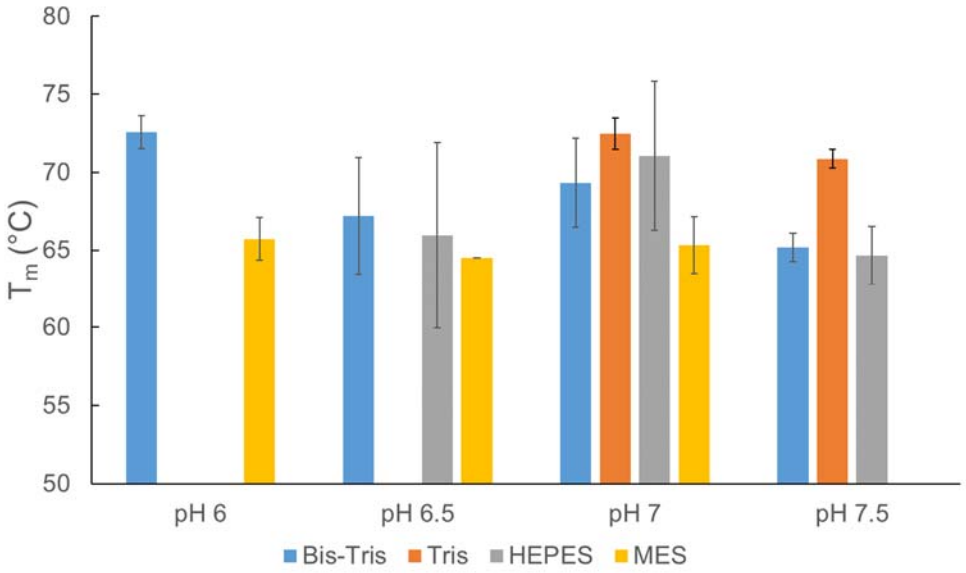

Figure 4.5.1 The thermal denaturation assay of KDSR G263E with a range of buffer and pH. T_m stands for melting temperature. Each essay contained 5 μM enzyme and all data were plotted as mean readings ±2-SD error bars.

Homogenous protein is desirable to begin screening for the optimal conditions for growing diffraction-quality crystals. We compared the purification of ScKDSR WT and the G263E mutant. Considering the S300 profiles of both WT and G263E, the mutant G263E was taken forward for crystal trials (both in Edinburgh and in collaboration with Prof. Jim Naismith, Oxford). Firstly, the mutant G263E was tested by TDA assay to identify suitable buffers for protein stabilisation, which could aid the crystallisation process or improve on existing crystal quality (Figure 4.5.1). Considering the pH range of the buffer and the fact that the optimal pH for KDSR activity is 6.5, there was no need to test buffer Tris at pH 6.0 or 6.5, MES at pH 7.5 and HEPES at pH 6.0. Both Bis-Tris pH 6.0 and Tris pH 7.0 were chosen as desirable buffers for mutant ScKDSR G263E, which gave high T_m values of around 72.57 ± 1.05 °C for Bis-Tris pH 6.0 and 72.47 ± 0.99 °C for Tris pH 7.0 respectively compared to other conditions. Moreover, Tris pH 7.5 also obtained T_m around 70.88 ± 0.6 °C, showing Tris could be the best buffer for G263E stabilisation. In contrast MES buffer was the worst for the enzyme at all pH values with an average T_m of 65 °C. Therefore the buffer for the crystallography condition screen of the mutant G263E was processed using buffer 50 mM Tris, 150 mM NaCl, pH 7.0. Unfortunately, by the end of my PhD studies, diffraction-quality ScKDSR crystals had not been solved. Therefore, it was decided that we should attempt to build a structural model to understand the catalytic mechanism of this important enzyme.

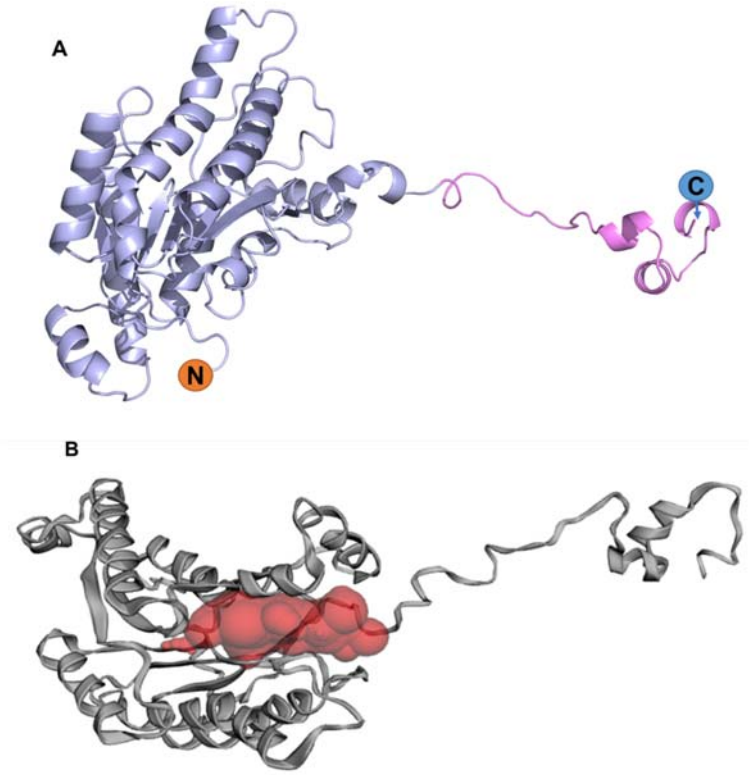

Figure 4.5.2 The homology model of ScKDSR (also known as Tsc10). (A) The protein was modelled as a monomer, the prediected membrane binding domain was labelled as light pink and the enzymatic catalytic was labelled as slate blue. (B) The possible NADPH binding pocket is shown in red.

Because Swiss-Model was based on one template to the build protein model in using conserved residues, and the ScKDSR (Tsc10) had less 25% identity and 41% similarity with all the SDR homologues in PDB Bank, we used RosettaCM software to carry out multi-template comparative modelling to enhance the modelling accurary using multiple templates. The four structure templates of the most similar protein sequences compared to ScKDSR were identified, which are 3RIH (41%) [303], 3WOH (38%) [304], 3F5S (38%) [305] and 3F5Q (38%) [306]. A homology model was built and shown in Figure 4.5.2 A. The total score given from the Rosetta software is -539.819. For a refined structure of this size, a score of -370 to -1,110 is typical, and the lower the score, the more stable the structure is likely to be as a given protein. The RMSD of the model with each template is quite close except with 3WOH, which are 3.03 and others are 1.12 (3RIH), 1.98 (3F5S) and 1.96 (3F5Q). Therefore, the model still is judged as good enough to begin to understand the mechanism of the ScKDSR. The model consisted of a N-terminal catalytic domain and a membrane binding domain at the C terminus. By using a computed atlas of surface topography of protein (CASTp) online service [307], a possible pocket was identified for NAPDH binding in the catalytic domain (Figure 4.5.2 B). Next, the catalytic domain was zoomed on by deleting the membrane domain and trying to dock NAPDH into the structural model by using

AutoDock Vina [308].

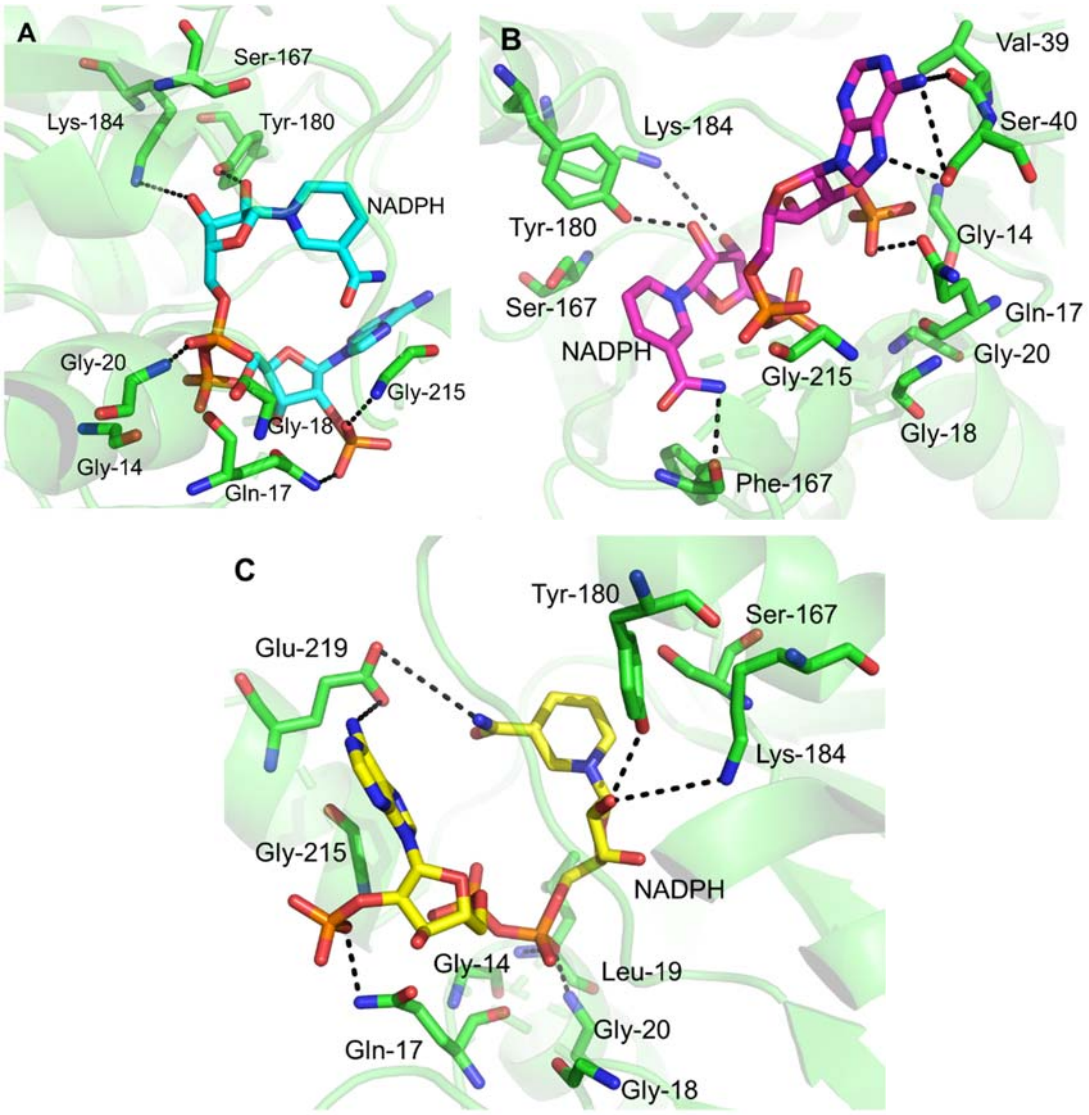

Figure 4.5.3 The best three possible NADPH docking positions in ScKDSR using AutoDock Vina.

After running the docking tests, we found that the three most possible NADPH positions in ScKDSR (Figure 4.5.3). Based on the reaction of KDS reduction and the proposed catalytic mechanism of ScKDSR (Figure 4.2.1), the residues of Tyr180 and Lys184 display polar contacts with both the -OH group in the ribose ring close to the pyridine ring (Figure 4.5.3 A). Also the Gly20 is proposed to form a hydrogen bond with a phosphate group. Morover, the other two Gly14 and Gly20 residues in the motif of the NADPH-binding domain are quite far away if they are to engage with NADPH. Such an interaction could be mediated by a water molecule to connect these two glycines and the phosphate group – such interactions have been observed in other SDR family crystal structures. Of interest, in all possible NADPH binding positions, the side chain of Gln17 would form a hydrogen bond with the additional phosphate bond in the 2' position of the ribose ring. In the human FVT-1 and CaKSR1 sequences,

this resodues is not conserved, it is Ser and Asp respectively, which of which still have a potential H-bond donor to allow for binding with NADPH. Therefore, Gln17 could be one of the essential residues to stabilise the NADPH binding. Furthermore, this could be same as Gly215 since Gly215 is also a conserved residue between the species.

In binding mode B (Figure 4.5.3 B), the adenine moiety seems to have a polar contact with the -C=O group of both the Val39 and Ser40 residues. Also the $-NH_2$ group attached to the pyridine ring has a polar contact with the -C=O group of Phe167. In position C (Figure 4.5.3 C), both adenine moiety and $-NH_2$ group linked to the pyridine have a polar contact with Glu219, and the phosphate group would have a polar contact with Leu19. Thus, it seems the NADPH is much more stable in position B and C instead of position A. Considering the catalytic reduction mechanism, the the NADPH provides the hydride. The KDS would bind to the enzyme and the keto group of KDS would have a polar contact with Ser167 plus the hydrogen in the pyridine group would transfer KDS, the position B seems to be the best position for KDS docking. It was also gratifying to observe the Tyr180 close to the substrates in all the models – it would be interesting to mutate this and other side-chains to test their roles in the KDSR reaction. In Section 4.4, we found the mutant G263E changed the expression level and enzymatic activity compared to ScKDSR WT. However, from the potential model, the Gly263 is in a loop that is far away from the possible pocket or possible NADPH positions. The reason for this requires further study – it could be that KDS and NADPH binding causes large conformational changes in the enzyme.

Chapter 5 Conclusion and future work

At the outset of this work detailed information about the complete SL biosynthetic pathways in various microbes was unknown. An inspection of the comprehensive LipidMaps database (www.lipidmaps.org/) reveals little information on the genes, enzymes and pathways associated with both bacterial SL biosynthesis and degradation. To expand our knowledge of SLs and Cers biosynthesis from these species we have undertaken a number of biochemical studies of key enzymes involved in the "core" SL biosynthesis.

Overall, three different types of key enzymes (SPT, IlvE/BCAT and KDSR) involved in SL biosynthesis from *B. fragilis*, *P. gingivalis* and *S. cerevisiae* have been studied. An investigation into BfSPT led to the discovery of substrate inhibition with high concentrations of C16-CoA of over 80 μM. Therefore, novel kinetic parameters of BfSPT with optimized concentrations of C16-CoA were determined. Furthermore, Val353 of BfSPT was proposed to control the C16-CoA interaction with the PLP:L-Ser external aldimine complex. This was not expected as the equivalent residue, Arg378 of SpSPT, was previously shown to be responsible for stabilization of the carboxylate of the serine substrate.

In a collaborative study with oral microbiologist Prof. Mary Ellen Davey (University of Florida), a novel PgSPT was characterised and a full biochemical analysis was carried out with both substrates (L-Ser and C16-CoA), as well as inhibitors such as LCS and DCS. The KDS products derived from straight-chain C14-C18 acyl-CoA substrates and amino acid substrates (Gly, L-Ala and L-Ser) produced by BfSPT and PgSPT were determined by MALDI-ToF-MS. Moreover, we found by mutagenesis analysis of residues in a conserved non-catalytic loop (PAXXP) in the bacterial SPTs influenced both the affinity and catalytic activity with the common substrates L-Ser and C16-CoA. Additionally, a relationship between the position of the 6His affinity tag (N- and C- terminus) and PgSPT activity, which had not been previously discussed in the literature, was observed. The position of this tag may control substrate inhibition observed with high concentrations of C16-CoA. Crystal trials were screened but no diffraction-quality crystals were obtained. Instead, a hypothetical homology model of the 3D structure of the PgSPT PLP:L-Ser external aldimine complex was constructed and the essential residues around the active site and the conserved loop were studied by comparison with other SPT isoforms from the Protein Data Bank (PDB) database. Future analysis of SPT enzymes would focus on the function of the loop (PAXXP), as well as understanding the binding domain of the acyl-CoA by solving the crystal structure of SPT with this substrate bound.

At the same time, in collaboration with Davey, a SPT mutant strain of *P. gingivalis*

(ΔPG1780) was constructed and incubated with THP1 macrophages. The mutant strain was unable to synthesise SLs and elicited a robust immune response in these cells compared to a wild type strain. This suggests that the ability of *P. gingivalis* to synthesise SLs is central to its ability to manipulate the host inflammatory response, and they demonstrate the integral importance of SLs in the physiology of *P. gingivalis* (F.G. Rocha, **P. Tang**, *et al.*, *Journal of Dental Research*, 2020, 99, 568-576) [232]. Future studies are aimed at investigating the exact molecular details of what roles these SLs play in mediating the bacterial/host immune response.

To investigate the origin of the *iso*-Me branch of the odd-numbered acyl chain of bacterial SLs, we explored a PLP-dependent amino transferase (IlvE/BCAT) predicted to be involved in metabolism of branched chain amino acids. The *P. gingivalis* IlvE (PG1290) was identified by sequence/homology analysis, cloned, purified and characterised. The enzyme followed a similar substrate binding and catalytic activity as other well-known transaminases (e.g. from *M. tuberculosis*), except this reversible enzyme used BCAAs and L-Glu AA substrates and converted them to the corresponding keto acids. We optimised four different coupled enzyme kinetic assay; two assays for the 'forward' direction and two assays for the 'reverse' direction, to determine the enzyme activity for different purposes. Studies of the interaction between PgIlvE with inhibitors, LCS and DCS suggested that the PgIlvE inhibition mechanism was similar to the human BCAT2 inhibition mechanism. Furthermore, in collaboration with Dr. Jon Marles-Wright (University of Newcastle) with the supporting evidence of crystal structures of PgIlvE (PLP-internal aldimine form, PLP:LCS ring-opened and ring-closed form and PMP form in DCS structures), an understanding of the catalytic mechanism and inhibition mechanism has been improved. Through the PgIlvE crystal structure, two new mutants (F56A and Y188A) were prepared and studied. It was also established that Tyr188 plays an essential role in catalysis and F56 appears to play an important role in defining the hydrophobicity of the active site.

Further investigations of PgIlvE would uncover the essential residues involved in defining the substrate specificity. To explore the role of IlvE in the biosynthesis of *P. gingivalis* SLs, PgIlvE mutant cells will be prepared and mass spectrometry used to determine if the SLs retained their *iso*-Me branch. Furthermore, labelling of the *iso*-Me branched SL pool in *P. gingivalis* with isotope-labelled (e.g. ^{13}C) BCAA precursors will allow metabolic tracking of these amino acids into the mature SLs.

Since a bacterial, Gram-negative KDSR has not been identified, an alternative KDSR from the yeast *S. cerevisiae* (ScKDSR) was expressed and purified. Sequence analysis suggested the enzyme contained a transmembrane domain (TMD) at the C-terminus. A truncated recombinant version of ScKDSR was isolated from *E. coli* and

assayed using a NADPH-dependent spectrophotometric assay. The C18 DHS products derived from the C18 KDS substrate were detected using a MS method. Interestingly, we also found that the use of detergent affects the catalytic activity of ScKDSR. A recently discovered genetic dysfunction in human KDSR causes a Mendelian disorder termed a “recessive progressive symmetric erythrokeratoderma”. The exact details of how these KDSR mutants lead to a KDS to DHS imbalance and cause a skin disorder. The human and yeast KDSR homologs show high sequence homology so to explore this further several mutant mimics of disease-causing mutations were created and their biochemistry studied (ScKDSR G176S, Y180F and G263E). Certain mutants changed the characteristics of ScKDSR expression, solubility (Y180F and G176S mutants), protein folding and enzyme activity (G263E mutant). Moreover, we built a homology model of ScKDSR based on multiple templates of the SDR superfamily as crystal trails were not successful. Three possible NADPH docking positions were explored and provided more information about the relationship between the essential residues for KDS and NADPH binding in ScKDSR.

Further research into ScKDSR would aim to acquire a high resolution crystal structure of the enzyme, coupled with a detailed study of the catalytic mechanism by docking the substrates KDS and NADPH into the structural models. Future work is also aimed at finally identifying a bacterial KDSR homologue and studying both its biochemical properties and its role in bacterial SL biosynthesis.

To that end a new collaboration has been initiated with groups of Dr. Eric Klein (Rutgers University) and Prof. Ziqiang Guan (Duke University) using the fresh-water, Gram-negative microbe *Caulobacter crescentus*. It was recently discovered a novel bacterial GSL specie present under the phosphate starvation condition and proposed several enzymes involved into ceramide synthesis of *C. crescentus* [309]. Olea-Ozuna *et al.* suggested five structural genes of *C. crescentus* for ceramide synthesis and sensitivity towards the antibiotic polymyxin B [310]. Based on those biological and bioinformatic analysis, we are able to predict more key enzymes, such as SPT, KDSR, SK and CerS in the genome sequence of *C. crescentus* as shown in Figure 5.1.

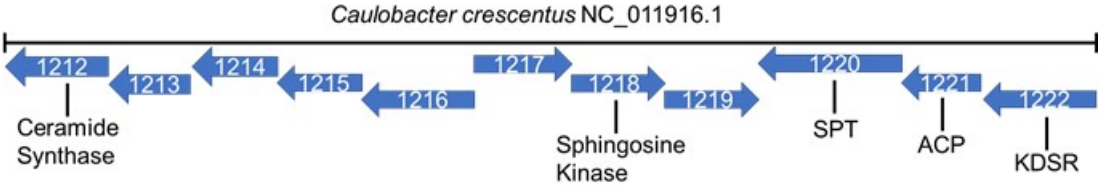

Figure 5.1 The genomic context of genes related to SL biosynthesis in *C. crescentus*. (inspired from Stankeviciute *et al.* and Olea-Ozuna *et al.* [309, 310]).

Cloning, expression and characterization of predicted enzymes with this operon *C. crescentus* and exploring their homologues in other species would lead to a big progress to identify and understand the unique bacterial SLs biosynthesis pathway.

At the end of this work it is now possible to propose a working SL biosynthetic pathway that explains how *iso*-Me SLs are formed in those human bacteria as shown in Figure 5.2 [45, 100, 311]. The studied enzymes (gene PG1290, BF2461 and PG1780) in this thesis indicated the transformation of the *iso*-Me group from BCAAs through SLs pathways and metabolism.

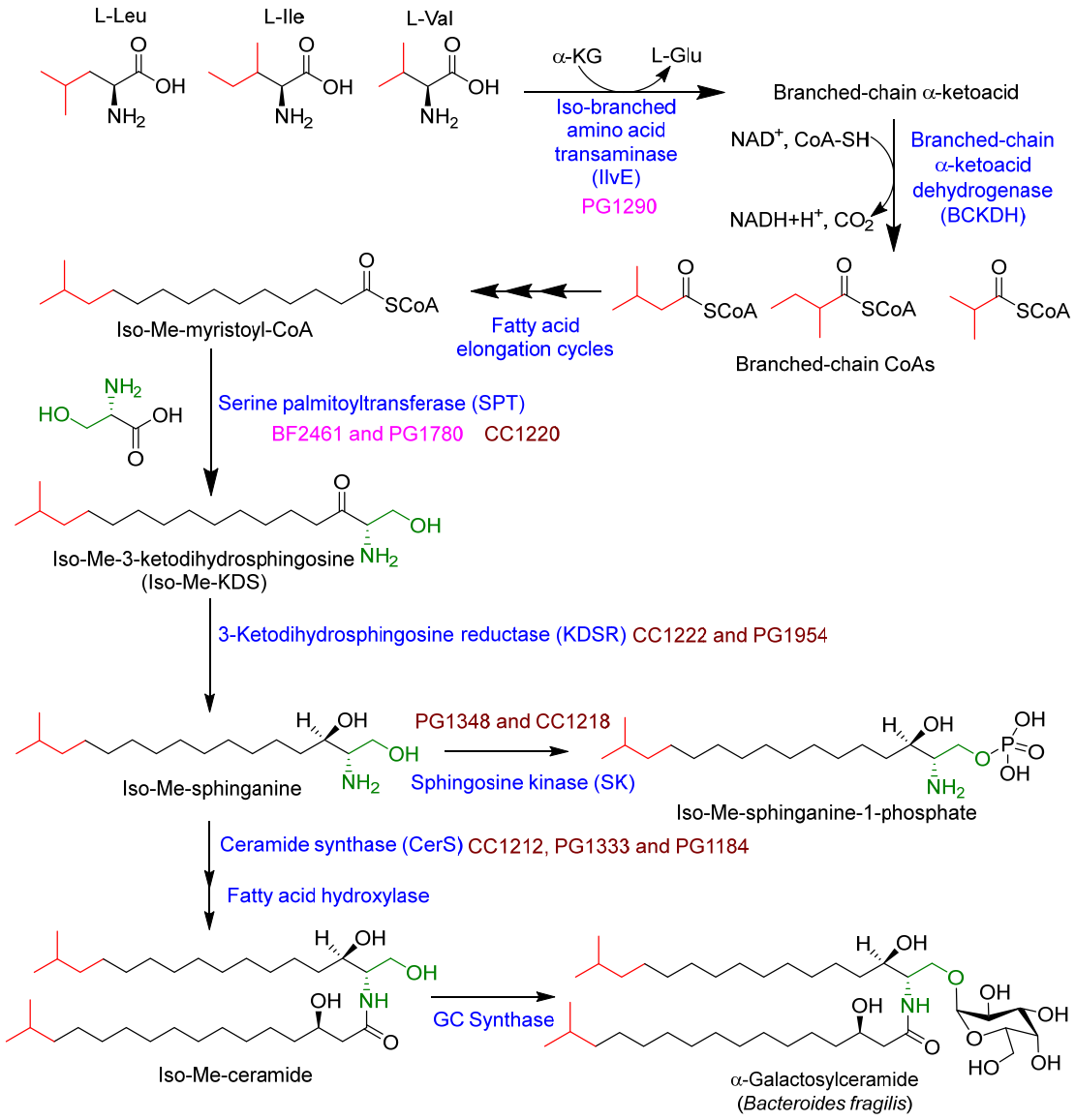

Figure 5.2 A current proposed pathway for the biosynthesis of *iso*-branched SLs in microbial systems. The studied genes are coloured in pink, and putative genes are coloured in brown. (inspired by Wieland Brown *et al.*, Hannich *et al.* and Harrison *et al.* [45, 100, 311]).

In this figure, we included those potential genes from *C. crescentus* and *P. gingivalis* (Figure 5.1; CC1212, CC1218, CC1220, CC1222, PG1184, PG1333, and PG1348) predicted by our collaborators Dr. Eric Klein (Rutgers University) and Prof. Mary Ellen Davey (University of Florida). The enzymes encoded by these genes are currently being characterized and are not discussed in this thesis. However, it worth noting that the predicted CC1214 gene product has been expressed and purified from *E. coli* and been shown to display CerS activity. Of interest the enzyme appears to use KDS as a substrate, rather than DHS which is used by the higher order CerSs isolated to date. This suggests that the biosynthetic order in *C. crescentus* is different compared to the pathway in mammals, plants and yeast. Overall, this thesis provides a foundation to characterise the remaining 'hidden' enzymes in core biosynthetic pathway of microbial SLs related in transport and regulation.

Chapter 6 Materials and Methodology

6.1 Materials & Regents

All chemicals and reagents were purchased from Sigma-Aldrich, Fisher Scientific or Biorad except those stated. The BfSPT gene and ScKDSR gene were provided from previous group members and the PgSPT and PgIlvE genes were provided by Dr. Mary E. Davey (University of Florida, Gainesville). The pERSRCTEVC10HIS plasmid was provided by University of St. Andrews.

6.1.1 Plasmid vector

Table 6.1.1 The information of plasmid vector

Plasmid	Bacterial Resistance	Application
pGEM	Ampicillin	Provides stock of DNA for cloning into different expression vectors
pET-28a	Kanamycin	Expression of a N- or C-terminal His-tagged protein
pETHISTEV_	Kanamycin	Expression of a N-terminal His_6-tagged protein
pEBSRCTEVC10HIS	Ampicillin	Expression of a C-terminal His_{10}-tagged protein

6.1.2 Antibiotic solution

All antibiotics stock solutions were dissolved in distilled water and filtered through sterile filter (0.2 mm), before being stored at -20°C for further use.

Table 6.1.2 The making protocol of antibiotic stock solutions

Antibiotics	Making Protocol
Kanamycin	A 30 mg/ml stock solution was made, and the relative volume added into media to give a final concentration of 30 μg/ml
Ampicillin	A 100 mg/ml stock solution was made, and the relative volume added into media to give a final concentration of 100 μg/ml
Chloramphenicol	A 10 mg/ml stock solution was made in ethanol and the relative volume added into media to give a final concentration of 10 μg/ml

6.1.3 Competent cell used

Table 6.1.3 The cell lines, genotype, application of bacterial strains

Species	Cell lines	Genotype	Application	Volume
E.coli	DH5α™ (Invitrogen)	F-Φ80 *lac*ZΔM15 Δ(lac2YA-*arg*F) U169 *rec*A1 *end*A1 *hsd*R17(r_k^- m_k^+) *pho*A *sup*E44λ- *thi*-1 *gyr*A96 *rel*A1	Transformation, plasmid storage	25 μl
E.coli	BL21 (DE3) (New England BioLabs*inc*)	*fhu*A2 *[lon] omp*T *gal* [*λ sBamHIo* Δ*EcoRI-B int::(lacI::PlacUV5::T7 gene1) i21* Δ*nin5*] *[dcm]* Δ*hsd*S	Transformation, protein expression,	10 μl
E.coli	BL21-Gold (DE3) (Agilent)	*E. coli B F– ompT hsdS(rB – mB –) dcm+ Tetr gal endA Hte*	Protein expression	25 μl
E.coli	C2987 (New England BioLabs*inc*)	*fhuA2 Δ(argF-lacZ)U169 phoA glnV44 Φ80 Δ(lacZ)M15 gyrA96 recA1 relA1 endA1 thi-1 hsdR17*	High efficiency transformation, plasmid storage	10 μl
E.coli	C41 (DE3) (Agilent)	*F– ompT gal dcm hsdSB(rB- mB-)(DE3)*	Protein expression	25 μl
E.coli	C43 (DE3) (Agilent)	*F– ompT gal dcm hsdSB(rB- mB-)(DE3)*	Protein expression,	25 μl
E.coli	Rosetta (DE3) (Novagen)	F- *ompT hsdS*B(r_B^- m_B^-) *gal dcm* (DE3) pRARE (Cam^R)	Protein expression	20 μl
E.coli	Rosetta-gami 2 (DE3) (Novagen)	Δ(*ara-leu*)*7697* Δ*lacX74* Δ*phoA Pvu*II *phoR araD139 ahpC galE galK rpsL* F′[*lac*+ *lacIq pro*] *gor522*::Tn*10 trxB* pRARE2 (Cam^R, Str^R, Tet^R)	Protein expression	20 μl

6.1.4 Growth media & agar

All growth media and agars were dissolved in distilled water and autoclaved. The media and agar, was stored at 4°C until used.

Table 6.1.4 The composition of growth media and agars

	Ingredients
LB	Tryptone: 10 g/L; yeast extract: 5 g/L; sodium chloride (NaCl): 10 g/L.
SOC Broth	Tryptone: 20 g/L; yeast extract: 5 g/L; NaCl: 10 mM; potassium chloride (KCl): 2.5 mM; magnesium chloride ($MgCl_2$): 10 mM; magnesium sulphate ($MgSO_4$):10 mM; glucose: 2% w/v.
LB Agar	Tryptone: 10 g/L; yeast extract: 5 g/L; NaCl: 10 g/L; Agar (15 g/L)
2xYT	Tryptone: 16 g/L; yeast extract: 10 g/L; sodium chloride (NaCl): 5 g/L
LB + sorbitol	LB media + 5 mM sorbitol

6.1.5 PCR primers

Name	5'-3' Primer Sequence
PgSPT C'HisTev Forward	AACCCCATGGGCGGAAAATTGTTA
PgSPT C'HisTev Reverse	AATTCTCGAGCAGGACACCGTTCTG
BfSPT V353R Forward	AATCCAGTTCGGCCTCCCGCATGTTCTCCGA
BfSPT V353R Reverse	GCGGGAGGCCGAACTGGATTTACAAACA
KDSR G176S Forward	GTGAGCTATTCCCAGTATGCGCCTGCAAAAG
KDSR G176S Reverse	AATAGCTCACAAATGGGTAAAGCGCGGTGG
KDSR Y180F Forward	GCTATTCCCAGTTTGCGCAAAAGCTGC
KDSR Y180F Reverse	GCAGCTTTTGCGCAAACTGGGAATAGC
KDSR G263E Forward	TGTCGAATGGATGATAATGGGGATGGA
KDSR G263E Reverse	ATCCATTCGACAAAATCTGTAAAAACGTCTTCAT
PgSPT V358C Forward	CGGCGTGCGCTCCGTCCGACACCCTTA
PgSPT V358C Reverse	GGACGGAGCGCACGCCGGAGAGACCACCG
PgSPT V358A Forward	CGGCGGCAGCTCCGTCCGACACCCTTAT
PgSPT V358A Reverse	ACGGAGCTGCCGCCGGAGAGACCACCG
PgSPT A359S Forward	GCGGTATCTCCGTCCGACACCCTTATTCGC
PgSPT A359S Reverse	GGACGGAGATACCGCCGGAGAGACCACCGG
PgSPT DM Forward	GTGCTCTCCGTCCGACACCCTTATTCGCTTTT
PgSPT DM Reverse	GACGGAGAGCACGCCGGAGAGACCAC
PgIlvE pGEM-T Easy Forward	GGCCCATATGGAAAATATCGATTGGTCATC
PgIlvE pGEM-T Easy Reverse	AACCGGATCCTTAGTCGAGGATTGTCAC
PgIlvE Y188A Forward	TAACGCTGCAGCCGGTATGATCCCCAC
PgIlvE Y188A Reverse	CTGCAGCGTTACCGCCCACTTTGATCGTA
PgIlvE F56A Forward	AGCAGCTGAAGGGATGAAGGCTTTCCGT
PgIlvE F56A Reverse	TTCAGCTGCTTCCTGTCCGTAGTGGAGAC

6.1.6 Experimental buffers

Each buffer was made by following the components listed below and filtered before being used and stored at 4°C. The PLP was added prior to nickel affinity chromatography and size column chromatography.

Table 6.1.5 The composition of experimental buffers

Buffers	Ingredients
20mM KPhos pH 7.5	Monobasic potassium phosphate (KH_2PO_4): 0.00396 moles/L; Dibasic potassium phosphate (K_2HPO_4): 0.01604 moles/L
Buffer A	20 mM KPhos; 150 mM NaCl; 25 μM PLP; 10 mM Imidazole; pH 7.5
Buffer B	20 mM KPhos; 150 mM NaCl; 25 μM PLP; 300 mM Imidazole; pH 7.5
Buffer C	20 mM KPhos; 150 mM NaCl; 25 μM PLP; 10% w/v Glycerol; pH 7.5
Buffer D	20 mM KPhos; 150 mM NaCl; 25 μM PLP; pH 7.5
Buffer E	50 mM HEPES; 250 mM NaCl; 25 μM PLP; 30 mM Imidazole; pH 7
Buffer F	50 mM HEPES; 250 mM NaCl; 25 μM PLP; 300 mM Imidazole; pH 7
Buffer G	20 mM KPhos; 150 mM NaCl; pH 7.5
Buffer H	50 mM HEPES; 250 mM NaCl; 25 μM PLP; 10% w/v Glycerol; pH 7
Buffer I	48 mM Tris; 39 mM Glycine; 20% Methanol; 0.2% SDS
Buffer J	1L Phosphate buffered saline (PBS, 0.05 M Phosphate Buffer, 13.5 mM KCl, 0.685 M NaCl, pH 7.4) ; 0.1% Tween 20
Buffer K	50% v/v H_2O; 40% v/v methanol; 10% v/v acetic acid; 0.25% w/v Coomassie brilliant blue R250
Buffer L	50% v/v H_2O; 40% v/v methanol; 10% v/v acetic acid
Buffer M	20 mM KPhos; 150 mM NaCl; 30 mM Imidazole; pH 7
Buffer N	20 mM KPhos; 150 mM NaCl; 300 mM Imidazole; pH 7
Buffer O	50 mM HEPES; 150 mM NaCl; pH 6.5 (KDS assay)
Buffer P	100 mM HEPES; 250 mM NaCl; pH 7 (SPT assay)
Buffer Q	20 mM KPhos; 500 mM NaCl; 50 μM PLP; 30 mM Imidazole; pH 7.5
Buffer R	20 mM KPhos; 500 mM NaCl; 50 μM PLP; 500 mM Imidazole; pH 7.5
Buffer S	100 mM CHES; 150 mM NaCl; 50 μM PLP; 30 mM Imidazole; pH 8.6
Buffer T	100 mM CHES; 150 mM NaCl; 50 μM PLP; 500 mM Imidazole; pH 8.6
Buffer U	20 mM KPhos; 500 mM NaCl; 50 μM PLP; pH 7.5
Buffer V	100 mM CHES; 150 mM NaCl; 50 μM PLP; pH 8.6
Buffer W	100 mM Tris; 150 mM NaCl; 50 μM PLP; pH 8.5 (GDH assay)
Buffer X	100 mM Kphos; 50 μM PLP; pH 8 (XTT assay)

Buffer Y	100 mM Tris; 150 mM NaCl; 50 μM PLP; pH 8 (KDH/ODH assay)
Buffer Z	100 mM CHES, 150 mM NaCl; 50 μM PLP; pH 11.0 (LeuDH assay)
Buffer 0	50 mM Tris-HCl; 25 μM PLP; pH 7.5
Buffer 1	50 mM Tris-HCl; 1 M NaCl; 25 μM PLP; pH 7.5

6.2 Methodology

6.2.1 Transformation of Competent E.coli

The required aliquot of competent cells was removed from -80°C and defrosted. Once defrosted, plasmid DNA (~200 μg) was added to the aliquot and placed on ice for 30 minutes. Then, the mixture was heat-shocked for 40 seconds at 42°C before cooling on ice. SOC media (200 μl) was immediately added and the mixture was placed on the shaker (200 rpm) at 37°C for at least an hour. After that, the cells were plated on the LB antibiotics plate and left in the incubator for overnight at 37°C.

6.2.2 Polymerase chain reaction (PCR) and site-directed mutagenesis

5X Phusion HF buffer (10 μl), DNA template (1 μl, 100 ng/μl), forward primer (2.5 μl, 10 μM), reverse primer (2.5 μl, 10 μM), dNTPs (1.0 μl, 10 mM), Phusion DNA Polymerase (1 μl) were combined with together. DMSO (1.5 μl) was added to one reaction and diluted to 50 μl by dH_2O, and the other reaction was directly diluted to 50 μl by dH_2O.

Table 6.2.1 The details of PCR condition

Step	Temperature/°C	Time	Number of Cycles
Initial Denaturation	98	30 seconds	1
Denaturation	98	10 seconds	
Annealing	45-72	30 seconds	35
Extension	72	30 seconds/kb	
Final Extension	72	10 minutes	1

6.2.3 Digestion by restriction endonuclease

Template DNA (50 μl), restriction CutSmart buffer (6 μl, 10x from New England Biolabs), and restriction enzyme (2 μl) were combined together for a typical restriction digestion. The mixture was incubated at 37°C for at least 2 hours before being separated by gel electrophoresis.

6.2.4 Ligation to Expression Vector

Insert DNA (2 μl), restricted vector (6 μl), T4 DNA ligase reaction buffer (1 μl, 10x from New England Biolabs), T4 DNA ligase (1 μl, New England Biolabs) were mixed together and placed at room temperature for 15 minutes or 4°C overnight. The final product was transformed into C2987 host cells.

6.2.5 DNA purification using ThermoFisher Scientific GeneJET plasmid miniprep kit

An overnight inoculation liquid culture (10 mL) with desired colonies was centrifuged for 10 minutes at 3500 rpm to obtain a cell pellet. The pellet was resuspended with 250 μl resuspension solution containing RNase A and transferred to an Eppendorf tube. A 250 μl lysis solution was then added and mixed thoroughly by inverting the tube 4-6 times. The mixture was neutralized by adding 350 μl neutralization solution and inverted 4-6 times. After centrifuging for 5 minutes at 13000 rpm, the supernatant was transferred into the supplied GeneJET spin column by pipetting and centrifuged for 1 minute 13000 rpm. The flow-through was discarded and 500 μl wash solution with ethanol was added into the GeneJET spin column. The column was centrifuged for 1 minute at 13000 rpm, and the flow-through was discarded. After repeating the wash procedure, the spin column was centrifuged for an additional one minute at 13000 rpm to prevent residual ethanol in plasmid preps. The GeneJET spin column was transferred into a fresh 1.5 mL Eppendorf tube and 50 μl elution buffer was added to the centre of GeneJET spin column to elute the plasmid DNA. The column was incubated at room temperature for 2 minutes and then centrifuge for 2 minutes at 13000 rpm. Finally, the column was discarded, and purified plasmid DNA was stored at -20°C for further investigation.

6.2.6 DNA extraction from agarose gel using ThermoFisher Scientific GeneJET gel extraction kit

The DNA in agarose gel was observed under the Ultraviolet light (254 nm) and the required fragment was excised using a clean scalpel blade and transferred into a pre-weighed 1.5 mL Eppendorf tube. The binding buffer (1:1 volume: gel weight) was added to the gel slice and the mixture was incubated at 50-60°C for at least 10 minutes until the gel was completely dissolved. The gel solution was transferred to the GeneJET purification column and centrifuged for 1 minute at 13000 rpm. Another 100 µl of binding buffer was added to the GeneJET purification column, and the column was centrifuged for 1 minute at 13000 rpm. Then, the flow-through liquid was discarded and 700 μl of wash buffer was added to the column to centrifuge for 1 minute at 13000 rpm. After removing the residual wash buffer by centrifuging for an additional 1 minute at 13000 rpm, the GeneJET purification column was transferred into a clean 1.5 mL microcentrifuge tube and the elution buffer (50 µl) was added to the centre of the purification column membrane. The DNA was obtained by centrifuging the column for 1 minute at 13000 rpm and stored at -20°C until required.

6.2.7 PCR product cleaning by using ThermoFisher Scientific GeneJET gel extraction and DNA cleanup kit

The PCR products (50 μl) were digested by the relevant restriction enzyme for 2 hours and adjusted to 200 μl with water before using the kit. 100 μl of binding buffer and 300 μl of ethanol were added and mixed by pipetting. The mixture was transferred to the DNA purification column and was centrifuged for 1 minute at 13000 rpm. The supernatant was discarded and 200 μl of prewash buffer was added before centrifuging for 1 minute at 13000 rpm. 700 μl of wash buffer was added and the column was centrifuged again for 1 minute at 13000 rpm. After repeating the wash buffer step, the supernatant was discarded and the column was centrifuged for an additional 1 minute to get rid of residual wash buffer. Finally, transferring the column into a clean 1.5 mL microcentrifuge tube, 10 μl of elution buffer was added into centre of column membrane; the column was centrifuged for 1 minute at 13000 rpm and the purified DNA was stored at -20°C until required.

6.2.8 Analytical digestion by restriction endonuclease

7 μl of required template DNA, 1 μl of restriction CutSmart buffer and the restriction enzyme were mixed to make it a total 10 μl solution. The mixture was incubated at 37°C for 2 hours before being analysed by gel electrophoresis.

6.2.9 Gel electrophoresis

Agarose (1% w/v) was added to TAE buffer and microwaved until all the agarose was in solution, and the GelRed™ (3 μl, Biotium) was added after the gel had cooled to 50°C. The solution was mixed and poured into the gel casting and allowed to solidify for at least 30 minutes at room temperature. For each test sample, 2 μl DNA loading dye (5 x buffer, Biolab) and 10 μl were combined. After the gel was immersed into TAE buffer (89 mM Tris pH 7.6, 89 mM boric acid and 2 mM EDTA), samples were loaded into the walls and 5 μl of DNA ladder as a maker was also loaded into the gel. Good separation was achieved by running the gel at a constant voltage (100 V) and the bands were observed under the UV light condition.

6.2.10 Bacterial glycerol stock solution for long-term storage

A bacterial liquid culture was inoculated for at least 8 hours and 500 μl of sterile 50% glycerol and 500 μl culture were combined into a 2 mL crew top tube. The glycerol stock tube was frozen by liquid nitrogen and kept at -80°C for long-term storage.

6.2.11 Large scale over-expression in E.coli

One colony was inoculated in LB broth (2 x 200 mL) containing kanamycin (30 μg/mL) and was grown overnight at 37°C with shaking (250 rpm). The inoculant was divided into LB broth (8 x 500 mL) with kanamycin (30 μg/mL), starting with OD_{600} of 0.1. After the OD_{600} reached 0.6~0.8, 0.1 mM of isopropyl β-D-1-thiogalactopyranoside (IPTG) was added into growth media and the protein was left to express for 5 hours at 30°C. Cells were centrifuged at 7000 rpm for 10 minutes at 4°C and were resuspend in phosphate-buffered saline (PBS) buffer. Cells were centrifuge at 3500 rpm at 4°C for 10 minutes before being stored at -20°C until further investigation.

6.2.12 Cell lysis by sonication

This method was carried out on ice. The cell pellet was defrosted for 10 minutes and suspended in wash buffer. After using a Soniprep 150 for sonicating the cells for around 10 cycles (30 seconds on, 30 seconds off) while the sample was kept on ice to diminish the generated heat. Cell debris was removed by centrifugation (14000 rpm, 30 minutes, 4°C), and the supernatant was retained for enzyme purification.

6.2.13 Cell lysis by lysozyme for expression test

A stock of lysozyme (30 μg/mL) was prepared in PBS solution. A 10 mL overnight small culture was centrifuged at 3500 rpm for 10 minutes at 4°C. The supernatant was discarded and the cell pellet was suspended into 1 mL Eppendorf tube. After centrifuging in a microcentrifuge tube (13000 rpm, 2 minutes) and discarding the supernatant, 50 μl of lysozyme was added into pellet and the cell was suspended by pipetting or vortexing. After being left for 45 minutes, the cell was centrifuged again at 13000 rpm for 2 minutes. The supernant (soluble protein) combined with 50 μl SDS 2xSample buffer and the pellet (insoluble protein) mixed with 50 μl H_2O and 50 μl SDS 2xSample buffer were analysed by SDS-PAGE.

6.2.14 Ni-NTA agarose affinity chromatography

The HisTrap™ FF column (1 mL, GE Healthcare Life Science) was attached to an ÄKTA purifier (GE Healthcare). Then, the column was washed by water and wash buffer individually for 10 minutes (0.3 MPa, 1.0 mL/min). The injection loop was washed by water and wash buffer separately and the purified protein was injected into the loop. After the sample was loaded onto the column, the column was washed by wash buffer for at least 20 minutes to get rid of unbound protein. Elution buffer was pumped onto the column using a gradient increase for 40 minutes, and during this time, the fractions (3 mL each) were collected in glass tube. The tubes with peaks

shown in the chromatogram were collected and analysed by SDS-PAGE. The HisTrap™ FF column was washed by wash buffer, water and 20% ethanol for storage/re-use.

6.2.15 Anion exchange chromatography

The HiTrap Q HP column (1 mL, GE Healthcare Life Science) was attached to an ÄKTA purifier (GE Healthcare), the column was washed with water and wash buffer individually for 10 minutes (0.3 MPa, 1.0 mL/min). The injection loop was washed with water and wash buffer separately and then the purified protein was injected into the loop. After the sample was loaded onto the column, it was washed with wash buffer for at least 20 minutes to get rid of unbound protein. Elution buffer was pumped onto the column with a gradient increase for 40 minutes, and during this time, the fractions (3 mL each) were collected in glass tube. The tubes with peaks shown in the chromatogram were collected and analysed by SDS-PAGE. The HiTrap Q HP column was washed by wash buffer, water and 20% ethanol for storage/re-use.

6.2.16 Size exclusion chromatography

The HiLoad™ 16/600 Superdex™ 200 pg column (120 mL) or HiPrep™ 16/60 Sephacryl™ S-300 column was attached to an ÄKTA purifier (GE Healthcare), the column was equilibrated with water and buffer for 140 minutes (0.3 MPa, 1.0 mL/min). The injection loop was washed with water and buffer separately and the concentrated protein (up to 1 mL) was injected into the loop. After loading the protein onto the column, the protein was eluted with buffer for 140 minutes which was collected in 3 mL fractions. The fractions with desired peaks shown in the chromatogram were collected and analysed by SDS-PAGE. The protein was concentrated using a spin-column and the column was equilibrated with water for maintenance.

6.2.17 Sodium dodecyl sulfate-polyacrylamide gel electrophoresis (SDS-PAGE)

A typical gel (6 mL) was made of a 4 mL 15% running gel, which contained 1.425 mL H_2O, 1.5 mL 40% bis-acrylamide, 1 mL 1.5 M Tris pH 8.8, 37.5 μl 10% w/v SDS, 75 μl ammonium persulfate (APS) and 5 μl tetramethylethylenediamine (TEMED), and 2 mL 6% stacking gel, which consisted of 0.725 mL H_2O, 187.5 μl 40% bis-acrylamide, 312.5 μl 0.5 M Tris pH 6.8, 12.5 μl 10% w/v SDS, 25 μl APS and 1.25 μl TEMED. All protein samples were denatured by the addition of SDS 2xSample buffer (2.5 mL 0.5 M Tris pH 8.8, 2 mL Glycerol, 4 mL 10% w/v SDS, 0.5 mL 0.1% w/v bromophenol blue and 1 mL β-mercaptoethanol) and boiled at 90-100°C for 10 minutes. The samples were centrifuged at 11000 rpm for 1 minute before being loaded onto the gel. After low molecular weight maker (5 μl, LMW-SDS Marker Kit, GE Healthcare) was also loaded, the gel was run for 60 minutes at a constant voltage of

200 volts in the TGS buffer (BIO-RAD, 25 mM Tris, 192 mM Glycerol, 0.1% w/v SDS, pH 8.3). The protein bands were observed by staining the gel with Coomassie Blue stain buffer K for overnight and detaining with buffer L until excess blue was removed.

6.2.18 Western blotting for His-tag protein

Protein samples were separated by SDS-PAGE and the filter papers and membrane were immersed in Buffer I. After the SDS-PAGE finished in, the order of a fibre pad, a filter paper, a gel, a membrane, a filter paper and a fibre pad were placed on the cassette. The cassette module was run in buffer I with a constant voltage of 100V for an hour. The membrane was immersed into a skimmed 0.1% fat milk solution to reduce the background proteins for an hour. After that, the membrane was washed with buffer J for 5 minutes each and 30 minutes in total. The membrane was submerged in 10 µl Monoclonal Anti-polyHistidine antibody for an hour and then was washed with buffer J for 5 minutes each and 30 minutes in total. The protein peaks were visualized by using ECL™ Prime Western Blotting Detection Reagent Kit (GE Healthcare) under the laser scanner chemiluminescent mode.

6.2.19 Quick start™ bradford protein assay

50 µl of water was added to a Bradford solution as a blank and a series of standards (0.25, 0.5, 1.0 and 1.4 mg/mL) were made. The calibration curve was plotted by measuring the absorbance at 595 nm using a UV spectrometer. A diluted protein sample was then loaded into the Bradford solution and the concentration of the protein was calculated from the calibration curve and protein molecular weight.

6.2.20 Desalting and buffer exchange of proteins by using PD-10 desalting column

The top cap was removed and the column storage solution was poured off from the PD-10 desalting column (GE Healthcare). The sealed end was then cut at the notch. 25 mL of equilibration buffer was loaded onto the column until the packed bed was completely covered. 2.5 mL of sample was loaded onto column. After the sample had been loaded on the packed bed, a collection tube was placed under the column and 3.5 mL of equilibration buffer was used to elute the protein. The protein was stored in the -80°C for further investigation.

6.2.21 Spectroscopic measurements

All UV-vis spectra was obtained on a Cary 50 UV-Vis spectrophotometer and analysed using Cary WinUV software (Varian). The PLP enzymes were dialysed through a PD-10 desalting column with buffer G before any spectroscopic analysis. The machine was blanked with buffer G and the analysis was taken at room temperature.

6.2.22 Determination of dissociation constants (K_d) for substrates

A typical binding assay consisted of a certain enzyme in buffer G. Various concentrations of amino acids were added. The reaction mixture was allowed to equilibrate for 20 - 25 minutes at room temperature. Assays were analysed in 1 cm pathlength cuvettes. Baseline correction was adjusted before acquiring spectra. The acquired spectra was normalized by the maximum of the 280nm peak to diminish the error from dilution of the sample with addition of the substrate solution. The K_d value was calculated from different plots of ΔA_{425} versus amino acids concentrations by fitting to a hyperbolic saturation curve (Equation 6-1) on Omega 2019.

$$\Delta A_{obs} = \frac{\Delta A_{MAX} \times [Amino\ Acid]}{K_d + [Amino\ Acid]}$$

Equation 6.1 K_d calculation formula

(ΔA_{obs} represents the observed change in absorbance at 425 nm, ΔA_{MAX} is the maximal absorbance change, [$Amino\ Acid$] is amino acid concentration, and the K_d is the dissociation constant)

6.2.23 Determination of kinetic constants (K_M) for SPT by using 5, 5'-dithiobis-2-nitrobenzoic acid (DTNB) assay

The SPT activity was determined by monitoring the release of CoASH from the reaction of C16-CoA with L-Ser as suggested by Raman's paper [159]. The principle (Figure 5.2.1) of the assay is that the thiol group on the CoA will react with 5,5'-dithiobis-2-nitrobenzoic acid (DTNB, Ellman's reagent) in order to break the disulphide bond and generate the coloured TNB^- anion measured at 412 nm (λ_{max} = 412nm; ε = 14,150/$M^{-1}cm^{-1}$).

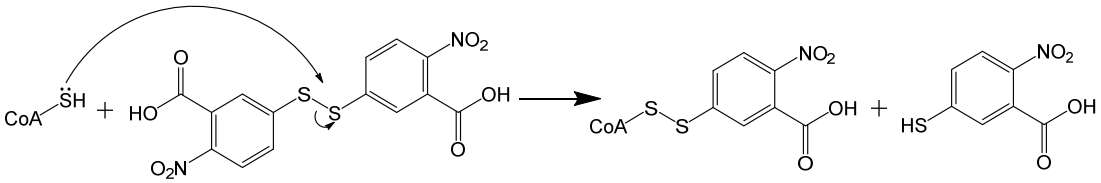

Figure 6.2.1 The reaction of DTNB with CoASH

The kinetic assay was carried out in a 96 wells microtiter plate contained 0.4 mM DTNB (100 μl), SPT enzyme (20 μl), deionized water (40 μl), L-Ser (20 μl), palmitoyl-CoA (20 μl). When measuring various concentration of L-Ser (0.1-100 mM), the concentration of palmitoyl-CoA was maintained at 250 μM. When measuring different concentration of palmitoyl-CoA (1-1000 μM), the concentration of L-Ser was maintained at 20 mM. The absorbance was monitored by plate reader at 412 nm in 1 min intervals for 60 minutes in total at 30 °C. The kinetic constant was calculated from the Michaelis-Menten equation by plotting rate versus concentration using Origin 2019.

$$v = \frac{V_{MAX} \times [S]}{K_M + [S]}$$

Equation 6.2 Michaelis-Menten equation

(v is relative reaction rate, [S] is substrate concentration, and the K_M is the substrate concentration at which the reaction rate is half of V_{MAX}, V_{MAX} represents the maximum rate achieved by the system)

6.2.24 Determination of kinetic constants (K_M) for IlvE with the coupled IlvE/GDH assay

The IlvE activity of the 'forward' direction was determined by monitoring the production of NADH from the reduction of NAD^+ generating an increase in absorbance at 340 nm (ε = 6,220 $M^{-1}cm^{-1}$) (Figure 3.3.2). The enzyme kinetic assay was carried out in a 96 well microtiter plate containing GDH (20 μl), ilvE enzyme (20 μl), BCAAs (20 μl), α-KG (20 μl), NAD^+ (20 μl) and buffer W (100 μl). The absorbance was monitored by the plate reader at 340 nm at 0.5 min intervals for 60 minutes in total at 30 °C. The kinetic constant was calculated from the Michaelis-Menten equation by plotting rate versus concentration using Origin 2019.

6.2.25 Determination of kinetic constants (K_M) for IlvE with the XTT assay [260]

The IlvE activity of the 'forward' direction was determined by monitoring the production of XTT formazan from XTT Tetrazolium generating an increase in absorbance at 470 nm (Figure 3.3.4). A calibration curve was made with NADH (0-100 μM) against $absorbance_{470nm}$ in buffer X. The enzyme kinetic assay was carried out in a 96 well microtiter plate contained GDH (20 μl), ilvE enzyme (20 μl), BCAAs (20 μl), α-KG (20 μl), NAD^+ (20 μl), XTT (20 μl), PMS (20 μl) and buffer W (60 μl). The absorbance was monitored by a plate reader at 470 nm at the end point of the assay after an hour at 30 °C. The kinetic constant was calculated from the Michaelis-Menten equation by plotting rate versus concentration using Origin 2019.

6.2.26 Determination of kinetic constants (K_M) for IlvE with coupled IlvE/KDH(ODH) assay

The IlvE activity of the 'reverse' direction was also determined by monitoring the production of NADH from the reduction of NAD^+ generating an increase in absorbance at 340 nm (ε = 6,220 $M^{-1}cm^{-1}$) (Figure 3.3.6). The enzyme kinetic assay was carried out in a 96 wells microtiter plate containing KDH/ODH (20 μl), ilvE enzyme (20 μl), BCAAs (20 μl), α-KG (20 μl), CoASH (20 μl), NAD^+ (20 μl) and buffer W (80 μl). The absorbance was monitored by the plate reader at 340 nm at 0.5 min intervals for 60 minutes in total at 30 °C. The kinetic constant was calculated from the Michaelis-Menten equation by plotting rate versus concentration using Origin 2019.

6.2.27 Determination of kinetic constants (K_M) for IlvE with coupled IlvE/LeuDH assay

The IlvE activity of the 'reverse' direction was also determined by monitoring the production of NADH from the reduction of NAD^+ generating an increase in absorbance at 340 nm (ε = 6,220 $M^{-1}cm^{-1}$) (Figure 3.3.11). The enzyme kinetic assay was carried out in a 96 well microtiter plate containing LeuDH (20 μl), ilvE enzyme (20 μl), BCAAs (20 μl), a-KG (20 μl), NAD^+ (20 μl) and buffer W (100 μl). The absorbance was monitored by the plate reader at 340 nm at 0.5 min intervals for 60 minutes in total at 30 °C. The kinetic constant was calculated from the Michaelis-Menten equation by plotting rate versus concentration using Origin 2019.

6.2.28 Determination of kinetic constants (K_M) for KDSR with NADPH assay

The KDSR activity was determined by monitoring the reduction of NADPH from the reduction of $NADP^+$ generating a decrease in absorbance at 340 nm (ε = 6,220 $M^{-1}cm^{-1}$) (Figure 4.2.1). The enzyme kinetic assay was carried out in a 96 well microtiter plate containING KDSR enzyme (20 μl), KDS (20 μl) and buffer O (160 μl) containing 250 μM NADPH. The KDS stock solution was made as 1 mM in 2:8 (v/v) ethanol/buffer O. The absorbance was monitored by the plate reader at 340 nm at 0.5 min intervals for 60 minutes in total at 30 °C. The kinetic constant was calculated from the Michaelis-Menten equation by plotting rate versus concentration using Origin 2019.

6.2.29 Determination of inhibitor constants (K_i).

The enzyme was incubated with different concentrations of inhibitors for 20 mins at room temperature. Then, the enzyme kinetic assay was carried out in a 96 well microtiter plate. For SPT inhibition, the DTNB assay was carried out and for IlvE inhibition, the coupled IlvE/GDH assay was carried out. The absorbance was monitored by the plate reader at relative wavelengths in 0.5 min intervals for 60 minutes in total at 30 °C. The inhibitor constants were calculated from equation 5.3 for irreversible inhibition or Morrison tight-binding inhibition equation for reversible inhibition.

$$A = A_0 e^{-k_{obs}t} \quad (1)$$

$$k_{obs} = \frac{k_{inact}[Inhibitor]}{K_i + [Inhibitor]} \quad (2)$$

Equation 6.3 Irreversible inhibition equation.

(A is absorbance, A_0 is time-zero absorbance, t is the time period, k_{obs} is observed constant, e is numerical constant, the [inhibitor] is inhibitor concentration, K_i is the inhibitor concentration, k_{inact} represents the rate of enzyme inactivation)

6.2.30 Liquid Chromatography-Mass Spectrometry (LC-MS) for Protein Identification

The total protein concentration was determined by Bradford assay and diluted with relative buffer to a concentration of 5-10 μM plus filtering with 0.45 μm filter for LC-MS. LC-MS was analysed on the Waters Synapt G2-Si ion mobility instrument with the LC column Thermo Proswift RP 4H coupled to an electrospray ionisation (ESI) source. The LC gradient started at 5% acetonitrile and 95% water with 0.1% formic acid and ran to 95% acetonitrile over 15 mins.

6.2.31 Confirming Protein Sequence by Using Mass Spectrometric Analysis of Tryptic Peptides

The total protein concentration was determined by the Bradford assay and diluted with relative buffer to 50 μg. 50 μl of 8 M urea was added into the sample and incubated at room temperature for 2 hours. 5 mM dithiothreitol (DTT) was added and incubated for 30 mins at room temperature. Then 15 mM iodacetamide was added and incubated at room temperature in the dark for 30 mins. Next 15 mM DTT was added and incubated at room temperature for 30 mins. The urea in the samples was diluted down to less than 1 M and 450 μl of 50 mM ammonium bicarbonate was added to the mixture. The trypsin was added to the sample in a ratio of 1:50 (Trypsin to protein w/w) and the sample was incubated overnight at 37°C. The next day, the sample was cleaned using C18 100 μl ziptips, then washed in 0.2% formic acid and eluted in 60% acetonitrile (ACN) with 0.2% formic acid (FA). The resulting peptide mixture was diluted and analysed by FT-ICR-MS with nanomate infusion in positive ion mode and the resulting data processed and calibrated using Bruker data analysis, MS fit and prosight lite.

6.2.32 Measuring SLs using Matrix-Assisted Laser Desorption/Ionization-Time-of-Flight-Mass Spectroscopy (MALDI-TOF-MS).

The samples were obtained from the kinetic assay and desalted using OMIX C4 pipette tips. Samples were eluted in 100% ACN containing 0.2% FA. 1 μL of matrix seed (20 mg/mL apha-cyano-4-hydroxycinnamic acid (CHCA) in methanol/acetone (2:3)) was spotted onto a MTP 384 ground steel plate and left to air dry. The sample was then mixed with matrix (20 mg/mL CHCA in 50% ACN within 0.25% trifluoroacetic acid (TFA)) in a 1:1 ratio, and 1 μL of this mixture was spotted on top of CHCA-acetone layer and left to air-dry. The sample was analysed in reflector mode using a calibrated Bruker UltrafleXtreme MALDI-TOF-MS. The analysis was carried out in positive ion mode. The laser power was adjusted to provide optimum signal. 500 laser shots were used per sample and each spectrum was a sum of over 5000 shots. Spectra were acquired over a range of 200-1500 *m/z*. The data acquisition software used was Flex

Control version 3.4. The data was analysed using Data Analysis version 4.4 software.

6.2.33 Thermal Denaturation Assay (TDA)

The fresh enzyme was prepared day before the assay and the concentration of the sample was calculated as 1000/$MW_{protein\ monomer}$ μM. The concentration of the sypro orange (5000X stock in DMSO) sample was made as 10X in the protein purification buffer. The enzyme (5 μl), the test buffer (20 μl) and the sypro orange sample (25 μl) were mixed in MicroAmp™ Fast Optical 96-Well Reaction Plate. The test plate was sealed with adhesive film and centrifuged for 5 minutes at 500 rpm. Then the plate was put into TOptical Thermocycler (Biometra) and the method was set up on the TOptical software. The assay was run under a temperature gradient of 20°C - 90°C for an hour. Finally, the data was collected and analysed in TOptical software and Microsoft Excel 365.

6.2.34 Robot screening of enzyme crystallography.

Recombinant enzyme was purified and concentrated to 8~10 mg/mL before the experiment. The robot screening experiment was carried out in 96 MRC plates (Swissci) with 0.2 μL of enzyme and 0.2 μL of different precipitant solutions by the nano-litre pipetting robot (Art Robbins Gryphon). The precipitant solutions were from commercially available screens, such as PEG/Ion, JCSG+, Midas and Structure Screen 1+2 from Molecular Dimensions Limited and Hampton Industrial Limited. The enzyme was crystallised by hanging-drop vapour diffusion and the plates were left at 18°C. After one week, the MRC plates were examined under the microscope to see whether enzyme crystals had formed.

6.2.35 Enzyme crystallography optimization.

Once the enzyme crystals were spotted out from robot screening, the optimization experiment was then set up in a 24 well crystallography plate with 1 mL crystallization solution with different conditions. The crystallization conditions were further optimized by changing the pH, concentration of precipitant, and concentration of salt. The enzyme with same concentration from robot screening. After that, the enzyme was sent to X-ray diffraction to obtain the electron density map for structural modelling.

References

1. Mcilwain, H., *A Treatise on the Chemical Constitution of the Brain - Thudichum,Jlw.* Isis, 1964. **55**(180): p. 249-250.
2. Sourkes, T.L., *How Thudichum came to study the brain.* Journal of the History of the Neurosciences, 1993. **2**(2): p. 107-119.
3. Carter, H.E., F.J. Glick, W.P. Norris, and G.E. Phillips, *Biochemistry of the Sphingolipides .3. Structure of Sphingosine.* Journal of Biological Chemistry, 1947. **170**(1): p. 285-294.
4. Carter, H.E., *Synthesis of alpha-amino-beta-hydroxy-n-butyric acids.* Journal of Biological Chemistry, 1936. **112**(2): p. 769-773.
5. Carter, H.E., W.P. Norris, and H.E. Rockwell, *Biochemistry of the Sphingolipides .4. Synthesis of Compounds Related To Sphingosine.* Journal of Biological Chemistry, 1947. **170**(1): p. 295-299.
6. Law, J.H. and R.K. Yu, *Introduction to thematic series on sphingolipids in honor of Professor Herbert E. Carter (1910-2007).* Journal of Lipid Research, 2008. **49**(5): p. 907-908.
7. Carter, H.E. and C.G. Humiston, *Biochemistry of the Sphingolipides .5. The Structure of Sphingine.* Journal of Biological Chemistry, 1951. **191**(2): p. 727-733.
8. Carter, H.E., O. Nalbandov, and P.A. Tavormina, *Biochemistry of the Sphingolipides .6. The O-Methyl Ethers of Sphingosine.* Journal of Biological Chemistry, 1951. **192**(1): p. 197-207.
9. Carter, H.E. and Y. Fujino, *Biochemistry of the Sphingolipides .9. Configuration of Cerebrosides.* Journal of Biological Chemistry, 1956. **221**(2): p. 879-883.
10. Carter, H.E., W.P. Norris, F.J. Glick, G.E. Phillips, and R. Harris, *Biochemistry of the Sphingolipides .2. Isolation of Dihydrosphingosine from the Cerebroside Fractions of Beef Brain and Spinal Cord.* Journal of Biological Chemistry, 1947. **170**(1): p. 269-283.
11. Carter, H.E., W.D. Celmer, D.S. Galanos, R.H. Gigg, W.E.M. Lands, J.H. Law, K.L. Mueller, T. Nakayama, H.H. Tomizawa, and E. Weber, *Biochemistry of the Sphingolipides .10. Phytoglycolipide, a Complex Phytosphingosine-Containing Lipide from Plant Seeds.* Journal of the American Oil Chemists Society, 1958. **35**(7): p. 335-343.
12. Carter, H.E., R.C. Gaver, and R.K. Yu, *A novel branched-chain sphingolipid base from Crithidia fasciculata.* Biochem Biophys Res Commun, 1966. **22**(3): p. 316-20.
13. Carter, H.E. and C.B. Hirschberg, *Phytosphingosines and Branched Sphingosines in Kidney.* Biochemistry, 1968. **7**(6): p. 2296-+.
14. Merrill, A.H., Jr., *Sphingolipid and glycosphingolipid metabolic pathways in the era of sphingolipidomics.* Chem Rev, 2011. **111**(10): p. 6387-422.
15. Fahy, E., S. Subramaniam, H.A. Brown, C.K. Glass, A.H. Merrill, R.C. Murphy, C.R.H. Raetz, D.W. Russell, Y. Seyama, W. Shaw, T. Shimizu, F. Spener, G. van Meer, M.S. VanNieuwenhze, S.H. White, J.L. Witztum, and E.A. Dennis, *A comprehensive classification system for lipids.* European Journal of Lipid Science and Technology, 2005. **107**(5): p. 337-364.
16. Merrill, A.H., Jr., M.D. Wang, M. Park, and M.C. Sullards, *(Glyco)sphingolipidology: an amazing challenge and opportunity for systems biology.* Trends Biochem Sci, 2007. **32**(10): p. 457-68.
17. Bartke, N. and Y.A. Hannun, *Bioactive sphingolipids: metabolism and function.* J Lipid Res, 2009. **50 Suppl**: p. S91-6.
18. Hannun, Y.A. and L.M. Obeid, *Sphingolipids and their metabolism in physiology and disease.* Nature Reviews Molecular Cell Biology, 2018. **19**(3): p. 175-191.
19. Wartewig, S. and R.H.H. Neubert, *Properties of Ceramides and their impact on the stratum corneum structure: A review.* Skin Pharmacology and Physiology, 2007. **20**(5): p. 220-229.

20. Huwiler, A., T. Kolter, J. Pfeilschifter, and K. Sandhoff, *Physiology and pathophysiology of sphingolipid metabolism and signaling.* Biochim Biophys Acta, 2000. **1485**(2-3): p. 63-99.
21. Buccoliero, R. and A.H. Futerman, *The roles of ceramide and complex sphingolipids in neuronal cell function.* Pharmacol Res, 2003. **47**(5): p. 409-19.
22. Pettus, B.J., C.E. Chalfant, and Y.A. Hannun, *Ceramide in apoptosis: an overview and current perspectives.* Biochim Biophys Acta, 2002. **1585**(2-3): p. 114-25.
23. Ohanian, J. and V. Ohanian, *Sphingolipids in mammalian cell signalling.* Cell Mol Life Sci, 2001. **58**(14): p. 2053-68.
24. Heinrich, M., M. Wickel, W. Schneider-Brachert, C. Sandberg, J. Gahr, R. Schwandner, T. Weber, P. Saftig, C. Peters, J. Brunner, M. Kronke, and S. Schutze, *Cathepsin D targeted by acid sphingomyelinase-derived ceramide.* EMBO J, 1999. **18**(19): p. 5252-63.
25. van Blitterswijk, W.J., *Hypothesis: ceramide conditionally activates atypical protein kinases C, Raf-1 and KSR through binding to their cysteine-rich domains*. Biochem J, 1998. **331 (Pt 2)**: p. 679-80.
26. Trayssac, M., Y.A. Hannun, and L.M. Obeid, *Role of sphingolipids in senescence: implication in aging and age-related diseases*. Journal of Clinical Investigation, 2018. **128**(7): p. 2702-2712.
27. Miazek, K., S. Lebecque, M. Hamaidia, A. Paul, S. Danthine, L. Willems, M. Frederich, E. De Pauw, M. Deleu, A. Richel, and D. Goffin, *Sphingolipids: promising lipid-class molecules with potential applications for industry. A review.* Biotechnologie Agronomie Societe Et Environnement, 2016. **20**: p. 321-336.
28. Norris, G.H. and C.N. Blesso, *Dietary and Endogenous Sphingolipid Metabolism in Chronic Inflammation.* Nutrients, 2017. **9**(11).
29. Slotte, J.P. and B. Ramstedt, *The functional role of sphingomyelin in cell membranes*. European Journal of Lipid Science and Technology, 2007. **109**(10): p. 977-981.
30. Osawa, Y., H. Uchinami, J. Bielawski, R.F. Schwabe, Y.A. Hannun, and D.A. Brenner, *Roles for C16-ceramide and sphingosine 1-phosphate in regulating hepatocyte apoptosis in response to tumor necrosis factor-alpha.* J Biol Chem, 2005. **280**(30): p. 27879-87.
31. Cuschieri, J., E. Bulger, J. Billgrin, I. Garcia, and R.V. Maier, *Acid Sphingomyelinase Is Required for Lipid Raft TLR4 Complex Formation.* Surgical Infections, 2007. **8**(1): p. 91-106.
32. Garcia-Ruiz, C., J.M. Mato, D. Vance, N. Kaplowitz, and J.C. Fernandez-Checa, *Acid sphingomyelinase-ceramide system in steatohepatitis: A novel target regulating multiple pathways.* Journal of Hepatology, 2015. **62**(1): p. 219-233.
33. Mari, M., A. Colell, A. Morales, F. Caballero, A. Moles, A. Fernandez, O. Terrones, G. Basanez, B. Antonsson, C. Garcia-Ruiz, and J.C. Fernandez-Checa, *Mechanism of mitochondrial glutathione-dependent hepatocellular susceptibility to TNF despite NF-kappa B activation.* Gastroenterology, 2008. **134**(5): p. 1507-1520.
34. Avota, E., M.N. de Lira, and S. Schneider-Schaulies, *Sphingomyelin Breakdown in T Cells: Role of Membrane Compartmentalization in T Cell Signaling and Interference by a Pathogen.* Frontiers in Cell and Developmental Biology, 2019. **7**.
35. Hailemariam, T.K., C. Huan, J. Liu, Z. Li, C. Roman, M. Kalbfeisch, H.H. Bui, D.A. Peake, M.S. Kuo, G. Cao, R. Wadgaonkar, and X.C. Jiang, *Sphingomyelin synthase 2 deficiency attenuates NFkappaB activation.* Arterioscler Thromb Vasc Biol, 2008. **28**(8): p. 1519-26.
36. Gowda, S., C. Yeang, S. Wadgaonkar, F. Anjum, N. Grinkina, M. Cutaia, X.C. Jiang, and R. Wadgaonkar, *Sphingomyelin synthase 2 (SMS2) deficiency attenuates LPS-induced lung injury.* Am J Physiol Lung Cell Mol Physiol, 2011. **300**(3): p. L430-40.
37. Liu, J., C. Huan, M. Chakraborty, H. Zhang, D. Lu, M.S. Kuo, G. Cao, and X.C. Jiang, *Macrophage sphingomyelin synthase 2 deficiency decreases atherosclerosis in mice.* Circ Res, 2009. **105**(3): p. 295-303.
38. D'Angelo, G., S. Capasso, L. Sticco, and D. Russo, *Glycosphingolipids: synthesis and*

functions. FEBS J, 2013. **280**(24): p. 6338-53.
39. Russo, D., L. Capolupo, J.S. Loomba, L. Sticco, and G. D'Angelo, *Glycosphingolipid metabolism in cell fate specification.* J Cell Sci, 2018. **131**(24).
40. Hakomori, S., *Structure, organization, and function of glycosphingolipids in membrane.* Current Opinion in Hematology, 2003. **10**(1): p. 16-24.
41. Lieberman, R.L., *Sneak peak at galactocerebrosidase, Krabbe disease's lysosomal hydrolase.* Proceedings of the National Academy of Sciences of the United States of America, 2011. **108**(37): p. 15017-15018.
42. Pandey, M.K., T.A. Burrow, R. Rani, L.J. Martin, D. Witte, K.D. Setchell, M.A. Mckay, A.F. Magnusen, W.J. Zhang, B. Liou, J. Kohl, and G.A. Grabowski, *Complement drives glucosylceramide accumulation and tissue inflammation in Gaucher disease.* Nature, 2017. **543**(7643): p. 108-+.
43. Wu, D., G.W. Xing, M.A. Poles, A. Horowitz, Y. Kinjo, B. Sullivan, V. Bodmer-Narkevitch, O. Plettenburg, M. Kronenberg, M. Tsuji, D.D. Ho, and C.H. Wong, *Bacterial glycolipids and analogs as antigens for CD1d-restricted NKT cells.* Proceedings of the National Academy of Sciences of the United States of America, 2005. **102**(5): p. 1351-1356.
44. Krziwon, C., U. Zahringer, K. Kawahara, B. Weidemann, S. Kusumoto, E.T. Rietschel, H.D. Flad, and A.J. Ulmer, *Glycosphingolipids from Sphingomonas-Paucimobilis Induce Monokine Production in Human Mononuclear-Cells.* Infection and Immunity, 1995. **63**(8): p. 2899-2905.
45. Harrison, P.J., T.M. Dunn, and D.J. Campopiano, *Sphingolipid biosynthesis in man and microbes.* Nat Prod Rep, 2018. **35**(9): p. 921-954.
46. Merrill, A.H., Jr., *De novo sphingolipid biosynthesis: a necessary, but dangerous, pathway.* J Biol Chem, 2002. **277**(29): p. 25843-6.
47. Di Pardo, A., A. Basit, A. Armirotti, E. Amico, S. Castaldo, G. Pepe, F. Marracino, F. Buttari, A.F. Digilio, and V. Maglione, *De novo Synthesis of Sphingolipids Is Defective in Experimental Models of Huntington's Disease.* Frontiers in Neuroscience, 2017. **11**.
48. Hanada, K., *Serine palmitoyltransferase, a key enzyme of sphingolipid metabolism.* Biochim Biophys Acta, 2003. **1632**(1-3): p. 16-30.
49. Gault, C.R., L.M. Obeid, and Y.A. Hannun, *An overview of sphingolipid metabolism: from synthesis to breakdown.* Adv Exp Med Biol, 2010. **688**: p. 1-23.
50. Riebeling, C., J.C. Allegood, E. Wang, A.H. Merrill, and A.H. Futerman, *Two mammalian longevity assurance gene (LAG1) family members, trh1 and trh4, regulate dihydroceramide synthesis using different fatty acyl-CoA donors.* Journal of Biological Chemistry, 2003. **278**(44): p. 43452-43459.
51. Fabrias, G., J. Munoz-Olaya, F. Cingolani, P. Signorelli, J. Casas, V. Gagliostro, and R. Ghidoni, *Dihydroceramide desaturase and dihydrosphingolipids: debutant players in the sphingolipid arena.* Prog Lipid Res, 2012. **51**(2): p. 82-94.
52. Colacios, C., F. Sabourdy, N. Andrieu-Abadie, B. Ségui, and T. Levade, *Basics of Sphingolipid Metabolism and Signalling*, in *Bioactive Sphingolipids in Cancer Biology and Therapy*, Y.A. Hannun, et al., Editors. 2015, Springer International Publishing: Cham. p. 1-20.
53. Wijesinghe, D.S., A. Massiello, P. Subramanian, Z. Szulc, A. Bielawska, and C.E. Chalfant, *Substrate specificity of human ceramide kinase.* J Lipid Res, 2005. **46**(12): p. 2706-16.
54. Momoi, T., Y. Benyoseph, and H.L. Nadler, *Substrate-Specificities of Acid and Alkaline Ceramidases in Fibroblasts from Patients with Farber Disease and Controls.* Biochemical Journal, 1982. **205**(2): p. 419-425.
55. Yu, F.P.S., S. Amintas, T. Levade, and J.A. Medin, *Acid ceramidase deficiency: Farber disease and SMA-PME.* Orphanet Journal of Rare Diseases, 2018. **13**.
56. Alemany, R., C.J. van Koppen, K. Danneberg, M. Ter Braak, and D. Meyer Zu Heringdorf, *Regulation and functional roles of sphingosine kinases.* Naunyn Schmiedebergs Arch Pharmacol, 2007. **374**(5-6): p. 413-28.

57. Serra, M. and J.D. Saba, *Sphingosine 1-phosphate lyase, a key regulator of sphingosine 1-phosphate signaling and function.* Adv Enzyme Regul, 2010. **50**(1): p. 349-62.
58. Ikeda, M., A. Kihara, and Y. Igarashi, *Sphingosine-1-phosphate lyase SPL is an endoplasmic reticulum-resident, integral membrane protein with the pyridoxal 5 '-phosphate binding domain exposed to the cytosol.* Biochemical and Biophysical Research Communications, 2004. **325**(1): p. 338-343.
59. Morgan, A.R., D. Turic, L. Jehu, G. Hamilton, P. Hollingworth, V. Moskvina, L. Jones, S. Lovestone, C. Brayne, D.C. Rubinsztein, B. Lawlor, M. Gill, M.C. O'Donovan, M.J. Owen, and J. Williams, *Association studies of 23 positional/functional candidate genes on chromosome 10 in late-onset Alzheimer's disease.* Am J Med Genet B Neuropsychiatr Genet, 2007. **144B**(6): p. 762-70.
60. Santos, A.X.S. and H. Riezman, *Yeast as a model system for studying lipid homeostasis and function.* FEBS Letters, 2012. **586**(18): p. 2858-2867.
61. Guillas, I., J.C. Jiang, C. Vionnet, C. Roubaty, D. Uldry, R. Chuard, J. Wang, S.M. Jazwinski, and A. Conzelmann, *Human homologues of LAG1 reconstitute Acyl-CoA-dependent ceramide synthesis in yeast.* J Biol Chem, 2003. **278**(39): p. 37083-91.
62. Schorling, S., B. Vallee, W.P. Barz, H. Riezman, and D. Oesterhelt, *Lag1p and Lac1p are essential for the Acyl-CoA-dependent ceramide synthase reaction in Saccharomyces cerevisae.* Mol Biol Cell, 2001. **12**(11): p. 3417-27.
63. Megyeri, M., H. Riezman, M. Schuldiner, and A.H. Futerman, *Making Sense of the Yeast Sphingolipid Pathway.* J Mol Biol, 2016. **428**(24 Pt A): p. 4765-4775.
64. Haak, D., K. Gable, T. Beeler, and T. Dunn, *Hydroxylation of Saccharomyces cerevisiae ceramides requires Sur2p and Scs7p.* J Biol Chem, 1997. **272**(47): p. 29704-10.
65. Clay, L., F. Caudron, A. Denoth-Lippuner, B. Boettcher, S. Buvelot Frei, E.L. Snapp, and Y. Barral, *A sphingolipid-dependent diffusion barrier confines ER stress to the yeast mother cell.* Elife, 2014. **3**: p. e01883.
66. Cowart, L.A. and L.M. Obeid, *Yeast sphingolipids: recent developments in understanding biosynthesis, regulation, and function.* Biochim Biophys Acta, 2007. **1771**(3): p. 421-31.
67. Kondo, N., Y. Ohno, M. Yamagata, T. Obara, N. Seki, T. Kitamura, T. Naganuma, and A. Kihara, *Identification of the phytosphingosine metabolic pathway leading to odd-numbered fatty acids.* Nat Commun, 2014. **5**: p. 5338.
68. Dunn, T.M., D.V. Lynch, L.V. Michaelson, and J.A. Napier, *A post-genomic approach to understanding sphingolipid metabolism in Arabidopsis thaliana.* Ann Bot, 2004. **93**(5): p. 483-97.
69. Markham, J.E., J. Li, E.B. Cahoon, and J.G. Jaworski, *Separation and identification of major plant sphingolipid classes from leaves.* J Biol Chem, 2006. **281**(32): p. 22684-94.
70. Tafesse, F.G., P. Ternes, and J.C. Holthuis, *The multigenic sphingomyelin synthase family.* J Biol Chem, 2006. **281**(40): p. 29421-5.
71. Michaelson, L.V., J.A. Napier, D. Molino, and J.-D. Faure, *Plant sphingolipids: Their importance in cellular organization and adaption.* Biochimica et biophysica acta, 2016. **1861**(9 Pt B): p. 1329-1335.
72. Sperling, P., S. Franke, S. Luthje, and E. Heinz, *Are glucocerebrosides the predominant sphingolipids in plant plasma membranes?* Plant Physiol Biochem, 2005. **43**(12): p. 1031-8.
73. Kawaguchi, M., H. Imai, M. Naoe, Y. Yasui, and M. Ohnishi, *Cerebrosides in Grapevine Leaves: Distinct Composition of Sphingoid Bases Among the Grapevine Species Having Different Tolerances to Freezing Temperature.* Bioscience, Biotechnology, and Biochemistry, 2000. **64**(6): p. 1271-1273.
74. Mashima, R., T. Okuyama, and M. Ohira, *Biosynthesis of long chain base in sphingolipids in animals, plants and fungi.* Future Science OA. **0**(0): p. FSO434.
75. Borner, G.H., D.J. Sherrier, T. Weimar, L.V. Michaelson, N.D. Hawkins, A. Macaskill, J.A. Napier, M.H. Beale, K.S. Lilley, and P. Dupree, *Analysis of detergent-resistant membranes*

in Arabidopsis. Evidence for plasma membrane lipid rafts. Plant Physiol, 2005. **137**(1): p. 104-16.
76. Luttgeharm, K.D., E.B. Cahoon, and J.E. Markham, *A mass spectrometry-based method for the assay of ceramide synthase substrate specificity.* Anal Biochem, 2015. **478**: p. 96-101.
77. Luttgeharm, K.D., A.N. Kimberlin, R.E. Cahoon, R.L. Cerny, J.A. Napier, J.E. Markham, and E.B. Cahoon, *Sphingolipid metabolism is strikingly different between pollen and leaf in Arabidopsis as revealed by compositional and gene expression profiling.* Phytochemistry, 2015. **115**: p. 121-129.
78. Wu, J.X., J. Li, Z. Liu, J. Yin, Z.Y. Chang, C. Rong, J.L. Wu, F.C. Bi, and N. Yao, *The Arabidopsis ceramidase AtACER functions in disease resistance and salt tolerance.* Plant J, 2015. **81**(5): p. 767-80.
79. Rennie, E.A., B. Ebert, G.P. Miles, R.E. Cahoon, K.M. Christiansen, S. Stonebloom, H. Khatab, D. Twell, C.J. Petzold, P.D. Adams, P. Dupree, J.L. Heazlewood, E.B. Cahoon, and H.V. Scheller, *Identification of a Sphingolipid α-Glucuronosyltransferase That Is Essential for Pollen Function in Arabidopsis.* The Plant Cell, 2014. **26**(8): p. 3314-3325.
80. Msanne, J., M. Chen, K.D. Luttgeharm, A.M. Bradley, E.S. Mays, J.M. Paper, D.L. Boyle, R.E. Cahoon, K. Schrick, and E.B. Cahoon, *Glucosylceramides are critical for cell-type differentiation and organogenesis, but not for cell viability in Arabidopsis.* Plant J, 2015. **84**(1): p. 188-201.
81. Cacas, J.L., C. Bure, F. Furt, J.P. Maalouf, A. Badoc, S. Cluzet, J.M. Schmitter, E. Antajan, and S. Mongrand, *Biochemical survey of the polar head of plant glycosylinositolphosphoceramides unravels broad diversity.* Phytochemistry, 2013. **96**: p. 191-200.
82. Dutilleul, C., G. Benhassaine-Kesri, C. Demandre, N. Rézé, A. Launay, S. Pelletier, J.-P. Renou, A. Zachowski, E. Baudouin, and I. Guillas, *Phytosphingosine-phosphate is a signal for AtMPK6 activation and Arabidopsis response to chilling.* New Phytologist, 2012. **194**(1): p. 181-191.
83. Worrall, D., Y.-K. Liang, S. Alvarez, G.H. Holroyd, S. Spiegel, M. Panagopulos, J.E. Gray, and A.M. Hetherington, *Involvement of sphingosine kinase in plant cell signalling.* The Plant Journal, 2008. **56**(1): p. 64-72.
84. Gupta, R.S. and E. Lorenzini, *Phylogeny and molecular signatures (conserved proteins and indels) that are specific for the Bacteroidetes and Chlorobi species*. BMC evolutionary biology, 2007. **7**: p. 71-71.
85. Heaver, S.L., E.L. Johnson, and R.E. Ley, *Sphingolipids in host–microbial interactions.* Current Opinion in Microbiology, 2018. **43**: p. 92-99.
86. Ley, R.E., M. Hamady, C. Lozupone, P.J. Turnbaugh, R.R. Ramey, J.S. Bircher, M.L. Schlegel, T.A. Tucker, M.D. Schrenzel, R. Knight, and J.I. Gordon, *Evolution of mammals and their gut microbes*. Science (New York, N.Y.), 2008. **320**(5883): p. 1647-1651.
87. Olsen, I. and E. Jantzen, *Sphingolipids in Bacteria and Fungi.* Anaerobe, 2001. **7**(2): p. 103-112.
88. Stoffel, W., K. Dittmar, and R. Wilmes, *Sphingolipid metabolism in Bacteroideaceae.* Hoppe Seylers Z Physiol Chem, 1975. **356**(6): p. 715-25.
89. Kato, M., Y. Muto, K. Tanaka-Bandoh, K. Watanabe, and K. Ueno, *Sphingolipid composition in Bacteroides species.* Anaerobe, 1995. **1**(2): p. 135-9.
90. Turnbaugh, P.J., R.E. Ley, M. Hamady, C.M. Fraser-Liggett, R. Knight, and J.I. Gordon, *The human microbiome project*. Nature, 2007. **449**(7164): p. 804-10.
91. Petersen, C. and J.L. Round, *Defining dysbiosis and its influence on host immunity and disease.* Cell Microbiol, 2014. **16**(7): p. 1024-33.
92. Grassme, H., V. Jendrossek, A. Riehle, G. von Kurthy, J. Berger, H. Schwarz, M. Weller, R. Kolesnick, and E. Gulbins, *Host defense against Pseudomonas aeruginosa requires ceramide-rich membrane rafts.* Nat Med, 2003. **9**(3): p. 322-30.

93. Hanada, K., *Sphingolipids in infectious diseases.* Jpn J Infect Dis, 2005. **58**(3): p. 131-48.
94. Wieland Brown, L.C., C. Penaranda, P.C. Kashyap, B.B. Williams, J. Clardy, M. Kronenberg, J.L. Sonnenburg, L.E. Comstock, J.A. Bluestone, and M.A. Fischbach, *Production of alpha-galactosylceramide by a prominent member of the human gut microbiota.* PLoS Biol, 2013. **11**(7): p. e1001610.
95. An, D., S.F. Oh, T. Olszak, J.F. Neves, F.Y. Avci, D. Erturk-Hasdemir, X. Lu, S. Zeissig, R.S. Blumberg, and D.L. Kasper, *Sphingolipids from a symbiotic microbe regulate homeostasis of host intestinal natural killer T cells.* Cell, 2014. **156**(1-2): p. 123-33.
96. Brown, E.M., X. Ke, D. Hitchcock, S. Jeanfavre, J. Avila-Pacheco, T. Nakata, T.D. Arthur, N. Fornelos, C. Heim, E.A. Franzosa, N. Watson, C. Huttenhower, H.J. Haiser, G. Dillow, D.B. Graham, B.B. Finlay, A.D. Kostic, J.A. Porter, H. Vlamakis, C.B. Clish, and R.J. Xavier, *Bacteroides-Derived Sphingolipids Are Critical for Maintaining Intestinal Homeostasis and Symbiosis.* Cell Host Microbe, 2019. **25**(5): p. 668-680 e7.
97. Moye, Z.D., K. Valiuskyte, F.E. Dewhirst, F.C. Nichols, and M.E. Davey, *Synthesis of Sphingolipids Impacts Survival of Porphyromonas gingivalis and the Presentation of Surface Polysaccharides.* Front Microbiol, 2016. **7**: p. 1919.
98. Heung, L.J., C. Luberto, and M. Del Poeta, *Role of sphingolipids in microbial pathogenesis.* Infect Immun, 2006. **74**(1): p. 28-39.
99. Kawahara, K., U. Seydel, M. Matsuura, H. Danbara, E.T. Rietschel, and U. Zahringer, *Chemical structure of glycosphingolipids isolated from Sphingomonas paucimobilis.* FEBS Lett, 1991. **292**(1-2): p. 107-10.
100. Hannich, J.T., D. Mellal, S. Feng, A. Zumbuehl, and H. Riezman, *Structure and conserved function of iso-branched sphingoid bases from the nematode Caenorhabditis elegans.* Chemical Science, 2017. **8**(5): p. 3676-3686.
101. Nichols, F.C., X. Yao, B. Bajrami, J. Downes, S.M. Finegold, E. Knee, J.J. Gallagher, W.J. Housley, and R.B. Clark, *Phosphorylated dihydroceramides from common human bacteria are recovered in human tissues.* PLoS One, 2011. **6**(2): p. e16771.
102. Nichols, F.C., B. Riep, J. Mun, M.D. Morton, T. Kawai, F.E. Dewhirst, and M.B. Smith, *Structures and biological activities of novel phosphatidylethanolamine lipids of Porphyromonas gingivalis.* J Lipid Res, 2006. **47**(4): p. 844-53.
103. White, D.C., A.N. Tucker, and C.C. Sweeley, *Characterization of the iso-branched sphinganines from the ceramide phospholipids of Bacteroides melaninogenicus.* Biochim Biophys Acta, 1969. **187**(4): p. 527-32.
104. White, D.C. and A.N. Tucker, *Ceramide phosphorylglycerol phosphate a new sphingolipid found in bacteria.* Lipids, 1970. **5**(1): p. 56-62.
105. Chitwood, D.J., W.R. Lusby, M.J. Thompson, J.P. Kochansky, and O.W. Howarth, *The glycosylceramides of the nematode Caenorhabditis elegans contain an unusual, branched-chain sphingoid base.* Lipids, 1995. **30**(6): p. 567-73.
106. Cutler, R.G., K.W. Thompson, S. Camandola, K.T. Mack, and M.P. Mattson, *Sphingolipid metabolism regulates development and lifespan in Caenorhabditis elegans.* Mechanisms of Ageing and Development, 2014. **143-144**: p. 9-18.
107. György, P. and R.E. Eckardt, *Further investigations on vitamin B(6) and related factors of the vitamin B(2) complex in rats. Parts I and II.* The Biochemical journal, 1940. **34**(8-9): p. 1143-1154.
108. Percudani, R. and A. Peracchi, *A genomic overview of pyridoxal-phosphate-dependent enzymes.* EMBO Rep, 2003. **4**(9): p. 850-4.
109. Metzler, D.E., M. Ikawa, and E.E. Snell, *A General Mechanism for Vitamin B6-catalyzed Reactions1.* Journal of the American Chemical Society, 1954. **76**(3): p. 648-652.
110. Martino, L., N. Budisa, and R. Contestabile. *PLP-dependent Enzymes: a Powerful Tool for Metabolic Synthesis of Non-canonical Amino Acids 1.* 2013.
111. Lowther, J., J.H. Naismith, T.M. Dunn, and D.J. Campopiano, *Structural, mechanistic and regulatory studies of serine palmitoyltransferase.* Biochem Soc Trans, 2012. **40**(3): p. 547-

54.
112. Dunathan, H.C., *Conformation and reaction specificity in pyridoxal phosphate enzymes.* Proc Natl Acad Sci U S A, 1966. **55**(4): p. 712-6.
113. Major, D.T. and J. Gao, *A combined quantum mechanical and molecular mechanical study of the reaction mechanism and alpha-amino acidity in alanine racemase.* J Am Chem Soc, 2006. **128**(50): p. 16345-57.
114. Grishin, N.V., M.A. Phillips, and E.J. Goldsmith, *Modeling of the spatial structure of eukaryotic ornithine decarboxylases.* Protein Sci, 1995. **4**(7): p. 1291-304.
115. Percudani, R. and A. Peracchi, *The B6 database: a tool for the description and classification of vitamin B6-dependent enzymatic activities and of the corresponding protein families.* BMC Bioinformatics, 2009. **10**: p. 273.
116. Milano, T., A. Paiardini, I. Grgurina, and S. Pascarella, *Type I pyridoxal 5′-phosphate dependent enzymatic domains embedded within multimodular nonribosomal peptide synthetase and polyketide synthase assembly lines.* BMC Structural Biology, 2013. **13**(1): p. 26.
117. Liang, J., Q. Han, Y. Tan, H. Ding, and J. Li, *Current Advances on Structure-Function Relationships of Pyridoxal 5′-Phosphate-Dependent Enzymes.* Frontiers in Molecular Biosciences, 2019. **6**(4).
118. Schneider, G., H. Käck, and Y. Lindqvist, *The manifold of vitamin B₆ dependent enzymes.* Structure, 2000. **8**(1): p. R1-R6.
119. Yoshimura, T., K.-H. Jhee, and K. Soda, *Stereospecificity for the Hydrogen Transfer and Molecular Evolution of Pyridoxal Enzymes.* Bioscience, Biotechnology, and Biochemistry, 1996. **60**(2): p. 181-187.
120. Cohen, P., T. Duewer, and E.H. Fischer, *Phosphorylase from Dogfish Skeletal Muscle. Purification and a Comparison of Its Physical Properties to Those of Rabbit Muscle Phosphorylase.* Biochemistry, 1971. **10**(14): p. 2683-2694.
121. Berkovitch, F., E. Behshad, K.-H. Tang, E.A. Enns, P.A. Frey, and C.L. Drennan, *A locking mechanism preventing radical damage in the absence of substrate, as revealed by the x-ray structure of lysine 5,6-aminomutase.* Proceedings of the National Academy of Sciences of the United States of America, 2004. **101**(45): p. 15870-15875.
122. Berkovitch, F., E. Behshad, K.-H. Tang, E.A. Enns, P.A. Frey, and C.L. Drennan, *A locking mechanism preventing radical damage in the absence of substrate, as revealed by the x-ray structure of lysine 5,6-aminomutase.* Proceedings of the National Academy of Sciences of the United States of America, 2004. **101**(45): p. 15870.
123. Lepore, B.W., F.J. Ruzicka, P.A. Frey, and D. Ringe, *The x-ray crystal structure of lysine-2,3-aminomutase from Clostridium subterminale.* Proceedings of the National Academy of Sciences of the United States of America, 2005. **102**(39): p. 13819-13824.
124. Wu, R., R. Sanishvili, B.R. Belitsky, J.I. Juncosa, H.V. Le, H.J.S. Lehrer, M. Farley, R.B. Silverman, G.A. Petsko, D. Ringe, and D. Liu, *PLP and GABA trigger GabR-mediated transcription regulation in Bacillus subtilis via external aldimine formation.* Proceedings of the National Academy of Sciences of the United States of America, 2017. **114**(15): p. 3891-3896.
125. Hilario, E., Caulkins, B.G., Young, R.P., Dunn, M.F., Mueller, L.J., Fan, L., *Crystal structure of Tryptophan Synthase from Salmonella typhimurium in complex with F9 ligand and the product L-Tryptophan in the beta-site.* http://www.rcsb.org/structure/5CGQ.
126. Au, K., J. Ren, T.S. Walter, K. Harlos, J.E. Nettleship, R.J. Owens, D.I. Stuart, and R.M. Esnouf, *Structures of an alanine racemase from Bacillus anthracis (BA0252) in the presence and absence of (R)-1-aminoethylphosphonic acid (L-Ala-P).* Acta crystallographica. Section F, Structural biology and crystallization communications, 2008. **64**(Pt 5): p. 327-333.
127. Lepore, B.W., D. Liu, Y. Peng, M. Fu, C. Yasuda, J.M. Manning, R.B. Silverman, and D. Ringe, *Chiral Discrimination among Aminotransferases: Inactivation by 4-Amino-4,5-*

dihydrothiophenecarboxylic Acid. Biochemistry, 2010. **49**(14): p. 3138-3147.
128. Kyriakis, E., T.G.A. Solovou, S. Kun, K. Czifrák, B. Szőcs, L. Juhász, É. Bokor, G.A. Stravodimos, A.L. Kantsadi, D.S.M. Chatzileontiadou, V.T. Skamnaki, L. Somsák, and D.D. Leonidas, *Probing the β-pocket of the active site of human liver glycogen phosphorylase with 3-(C-β-d-glucopyranosyl)-5-(4-substituted-phenyl)-1, 2, 4-triazole inhibitors*. Bioorganic Chemistry, 2018. **77**: p. 485-493.
129. Lepore, B.W., F.J. Ruzicka, P.A. Frey, and D. Ringe, *The x-ray crystal structure of lysine-2,3-aminomutase from Clostridium subterminale*. Proceedings of the National Academy of Sciences of the United States of America, 2005. **102**(39): p. 13819-13824.
130. Futerman, A.H. and H. Riezman, *The ins and outs of sphingolipid synthesis*. Trends in Cell Biology, 2005. **15**(6): p. 312-318.
131. Snell, E.E., S.J. Dimari, and R.N. Brady, *Biosynthesis of sphingosine and dihydrosphingosine by cell-free systems from Hansenula ciferri*. Chemistry and Physics of Lipids, 1970. **5**(1): p. 116-138.
132. Stoffel, W., *Studies on the biosynthesis and degradation of sphingosine bases.* Chemistry and Physics of Lipids, 1970. **5**(1): p. 139-158.
133. Hanada, K., T. Hara, M. Nishijima, O. Kuge, R.C. Dickson, and M.M. Nagiec, *A mammalian homolog of the yeast LCB1 encodes a component of serine palmitoyltransferase, the enzyme catalyzing the first step in sphingolipid synthesis.* J Biol Chem, 1997. **272**(51): p. 32108-14.
134. Nagiec, M.M., J.A. Baltisberger, G.B. Wells, R.L. Lester, and R.C. Dickson, *The LCB2 gene of Saccharomyces and the related LCB1 gene encode subunits of serine palmitoyltransferase, the initial enzyme in sphingolipid synthesis*. Proc Natl Acad Sci U S A, 1994. **91**(17): p. 7899-902.
135. Yasuda, S., M. Nishijima, and K. Hanada, *Localization, topology, and function of the LCB1 subunit of serine palmitoyltransferase in mammalian cells.* J Biol Chem, 2003. **278**(6): p. 4176-83.
136. Gable, K., H. Slife, D. Bacikova, E. Monaghan, and T.M. Dunn, *Tsc3p is an 80-amino acid protein associated with serine palmitoyltransferase and required for optimal enzyme activity.* J Biol Chem, 2000. **275**(11): p. 7597-603.
137. Breslow, D.K., S.R. Collins, B. Bodenmiller, R. Aebersold, K. Simons, A. Shevchenko, C.S. Ejsing, and J.S. Weissman, *Orm family proteins mediate sphingolipid homeostasis*. Nature, 2010. **463**(7284): p. 1048-53.
138. Brice, S.E., C.W. Alford, and L.A. Cowart, *Modulation of sphingolipid metabolism by the phosphatidylinositol-4-phosphate phosphatase Sac1p through regulation of phosphatidylinositol in Saccharomyces cerevisiae.* J Biol Chem, 2009. **284**(12): p. 7588-96.
139. Han, S., M.A. Lone, R. Schneiter, and A. Chang, *Orm1 and Orm2 are conserved endoplasmic reticulum membrane proteins regulating lipid homeostasis and protein quality control.* Proc Natl Acad Sci U S A, 2010. **107**(13): p. 5851-6.
140. Roelants, F.M., D.K. Breslow, A. Muir, J.S. Weissman, and J. Thorner, *Protein kinase Ypk1 phosphorylates regulatory proteins Orm1 and Orm2 to control sphingolipid homeostasis in Saccharomyces cerevisiae*. Proc Natl Acad Sci U S A, 2011. **108**(48): p. 19222-7.
141. Han, G., S.D. Gupta, K. Gable, D. Bacikova, N. Sengupta, N. Somashekarappa, R.L. Proia, J.M. Harmon, and T.M. Dunn, *The ORMs interact with transmembrane domain 1 of Lcb1 and regulate serine palmitoyltransferase oligomerization, activity and localization*. Biochimica et Biophysica Acta (BBA) - Molecular and Cell Biology of Lipids, 2019. **1864**(3): p. 245-259.
142. Braun, P.E., P. Morell, and N.S. Radin, *Synthesis of C18- and C20-dihydrosphingosines, ketodihydrosphingosines, and ceramides by microsomal preparations from mouse brain.* J Biol Chem, 1970. **245**(2): p. 335-41.
143. Kanfer, J.N. and S. Bates, *Sphingolipid metabolism II. The biosynthesis of 3-keto-*

dihydrosphingosine by a partially-purified enzyme from rat brain. Lipids, 1970. **5**(8): p. 718-720.

144. Hanada, K., T. Hara, and M. Nishijima, *Purification of the Serine Palmitoyltransferase Complex Responsible for Sphingoid Base Synthesis by Using Affinity Peptide Chromatography Techniques.* Journal of Biological Chemistry, 2000. **275**(12): p. 8409-8415.
145. Hornemann, T., S. Richard, M.F. Rutti, Y. Wei, and A. von Eckardstein, *Cloning and initial characterization of a new subunit for mammalian serine-palmitoyltransferase.* J Biol Chem, 2006. **281**(49): p. 37275-81.
146. Han, G., S.D. Gupta, K. Gable, S. Niranjanakumari, P. Moitra, F. Eichler, R.H. Brown, Jr., J.M. Harmon, and T.M. Dunn, *Identification of small subunits of mammalian serine palmitoyltransferase that confer distinct acyl-CoA substrate specificities.* Proc Natl Acad Sci U S A, 2009. **106**(20): p. 8186-91.
147. Hornemann, T., A. Penno, M.F. Rutti, D. Ernst, F. Kivrak-Pfiffner, L. Rohrer, and A. von Eckardstein, *The SPTLC3 subunit of serine palmitoyltransferase generates short chain sphingoid bases.* J Biol Chem, 2009. **284**(39): p. 26322-30.
148. Zhao, L., S. Spassieva, K. Gable, S.D. Gupta, L.Y. Shi, J. Wang, J. Bielawski, W.L. Hicks, M.P. Krebs, J. Naggert, Y.A. Hannun, T.M. Dunn, and P.M. Nishina, *Elevation of 20-carbon long chain bases due to a mutation in serine palmitoyltransferase small subunit b results in neurodegeneration.* Proc Natl Acad Sci U S A, 2015. **112**(42): p. 12962-7.
149. Bejaoui, K., C. Wu, M.D. Scheffler, G. Haan, P. Ashby, L. Wu, P. de Jong, and R.H. Brown, Jr., *SPTLC1 is mutated in hereditary sensory neuropathy, type 1.* Nat Genet, 2001. **27**(3): p. 261-2.
150. Dawkins, J.L., D.J. Hulme, S.B. Brahmbhatt, M. Auer-Grumbach, and G.A. Nicholson, *Mutations in SPTLC1, encoding serine palmitoyltransferase, long chain base subunit-1, cause hereditary sensory neuropathy type I.* Nat Genet, 2001. **27**(3): p. 309-12.
151. Beattie, A.E., S.D. Gupta, L. Frankova, A. Kazlauskaite, J.M. Harmon, T.M. Dunn, and D.J. Campopiano, *The pyridoxal 5'-phosphate (PLP)-dependent enzyme serine palmitoyltransferase (SPT): effects of the small subunits and insights from bacterial mimics of human hLCB2a HSAN1 mutations.* Biomed Res Int, 2013. **2013**: p. 194371.
152. Thomas, P.K., *Hereditary sensory neuropathies.* Brain Pathol, 1993. **3**(2): p. 157-63.
153. Ikushiro, H., H. Hayashi, and H. Kagamiyama, *A water-soluble homodimeric serine palmitoyltransferase from Sphingomonas paucimobilis EY2395T strain. Purification, characterization, cloning, and overproduction.* J Biol Chem, 2001. **276**(21): p. 18249-56.
154. Ikushiro, H., M.M. Islam, H. Tojo, and H. Hayashi, *Molecular Characterization of Membrane-Associated Soluble Serine Palmitoyltransferases from Sphingobacterium multivorum and Bdellovibrio stolpii.* Journal of Bacteriology, 2007. **189**(15): p. 5749-5761.
155. Wexler, H.M., *Bacteroides: the good, the bad, and the nitty-gritty.* Clin Microbiol Rev, 2007. **20**(4): p. 593-621.
156. An, D., C. Na, J. Bielawski, Y.A. Hannun, and D.L. Kasper, *Membrane sphingolipids as essential molecular signals for Bacteroides survival in the intestine.* Proc Natl Acad Sci U S A, 2011. **108 Suppl 1**: p. 4666-71.
157. Mun, J., A. Onorato, F.C. Nichols, M.D. Morton, A.I. Saleh, M. Welzel, and M.B. Smith, *Structural confirmation of the dihydrosphinganine and fatty acid constituents of the dental pathogen Porphyromonas gingivalis.* Org Biomol Chem, 2007. **5**(23): p. 3826-33.
158. Yard, B.A., L.G. Carter, K.A. Johnson, I.M. Overton, M. Dorward, H. Liu, S.A. McMahon, M. Oke, D. Puech, G.J. Barton, J.H. Naismith, and D.J. Campopiano, *The structure of serine palmitoyltransferase; gateway to sphingolipid biosynthesis.* J Mol Biol, 2007. **370**(5): p. 870-86.
159. Raman, M.C., K.A. Johnson, B.A. Yard, J. Lowther, L.G. Carter, J.H. Naismith, and D.J. Campopiano, *The external aldimine form of serine palmitoyltransferase: structural,*

kinetic, and spectroscopic analysis of the wild-type enzyme and HSAN1 mutant mimics. J Biol Chem, 2009. **284**(25): p. 17328-39.
160. Raman, M.C., K.A. Johnson, D.J. Clarke, J.H. Naismith, and D.J. Campopiano, *The serine palmitoyltransferase from Sphingomonas wittichii RW1: An interesting link to an unusual acyl carrier protein.* Biopolymers, 2010. **93**(9): p. 811-22.
161. Ikushiro, H., M.M. Islam, A. Okamoto, J. Hoseki, T. Murakawa, S. Fujii, I. Miyahara, and H. Hayashi, *Structural insights into the enzymatic mechanism of serine palmitoyltransferase from Sphingobacterium multivorum.* J Biochem, 2009. **146**(4): p. 549-62.
162. Shiraiwa, Y., H. Ikushiro, and H. Hayashi, *Multifunctional role of His159in the catalytic reaction of serine palmitoyltransferase.* J Biol Chem, 2009. **284**(23): p. 15487-95.
163. Ikushiro, H. and H. Hayashi, *Mechanistic enzymology of serine palmitoyltransferase.* Biochim Biophys Acta, 2011. **1814**(11): p. 1474-80.
164. Lowther, J., G. Charmier, M.C. Raman, H. Ikushiro, H. Hayashi, and D.J. Campopiano, *Role of a conserved arginine residue during catalysis in serine palmitoyltransferase.* FEBS Lett, 2011. **585**(12): p. 1729-34.
165. Ikushiro, H., S. Fujii, Y. Shiraiwa, and H. Hayashi, *Acceleration of the substrate Calpha deprotonation by an analogue of the second substrate palmitoyl-CoA in Serine Palmitoyltransferase.* J Biol Chem, 2008. **283**(12): p. 7542-53.
166. Dunathan, H.C., *Conformation and reaction specificity in pyridoxal phosphate enzymes.* Proceedings of the National Academy of Sciences of the United States of America, 1966. **55**(4): p. 712-716.
167. Kerbarh, O., D.J. Campopiano, and R.L. Baxter, *Mechanism of alpha-oxoamine synthases: identification of the intermediate Claisen product in the 8-amino-7-oxononanoate synthase reaction.* Chem Commun (Camb), 2006(1): p. 60-2.
168. Harrison, P.J., K. Gable, N. Somashekarappa, V. Kelly, D.J. Clarke, J.H. Naismith, T.M. Dunn, and D.J. Campopiano, *Use of isotopically labeled substrates reveals kinetic differences between human and bacterial serine palmitoyltransferase*. J Lipid Res, 2019. **60**(5): p. 953-962.
169. Zweerink, M.M., A.M. Edison, G.B. Wells, W. Pinto, and R.L. Lester, *Characterization of a novel, potent, and specific inhibitor of serine palmitoyltransferase.* J Biol Chem, 1992. **267**(35): p. 25032-8.
170. Kluepfel, D., J. Bagli, H. Baker, M.P. Charest, and A. Kudelski, *Myriocin, a new antifungal antibiotic from Myriococcum albomyces.* J Antibiot (Tokyo), 1972. **25**(2): p. 109-15.
171. Aragozzini, F., P.L. Manachini, R. Craveri, B. Rindone, and C. Scolastico, *Structure of thermozymocidin.* Experientia, 1972. **28**(8): p. 881-2.
172. Wadsworth, J.M., D.J. Clarke, S.A. McMahon, J.P. Lowther, A.E. Beattie, P.R. Langridge-Smith, H.B. Broughton, T.M. Dunn, J.H. Naismith, and D.J. Campopiano, *The chemical basis of serine palmitoyltransferase inhibition by myriocin.* J Am Chem Soc, 2013. **135**(38): p. 14276-85.
173. Lowther, J., B.A. Yard, K.A. Johnson, L.G. Carter, V.T. Bhat, M.C. Raman, D.J. Clarke, B. Ramakers, S.A. McMahon, J.H. Naismith, and D.J. Campopiano, *Inhibition of the PLP-dependent enzyme serine palmitoyltransferase by cycloserine: evidence for a novel decarboxylative mechanism of inactivation.* Mol Biosyst, 2010. **6**(9): p. 1682-93.
174. Medlock, K.A. and A.H. Merrill, Jr., *Inhibition of serine palmitoyltransferase in vitro and long-chain base biosynthesis in intact Chinese hamster ovary cells by beta-chloroalanine.* Biochemistry, 1988. **27**(18): p. 7079-84.
175. Lowther, J., A.E. Beattie, P.R.R. Langridge-Smith, D.J. Clarke, and D.J. Campopiano, *l-Penicillamine is a mechanism-based inhibitor of serine palmitoyltransferase by forming a pyridoxal-5′-phosphate-thiazolidine adduct*. MedChemComm, 2012. **3**(8): p. 1003-1008.
176. Holecek, M., *Branched-chain amino acids in health and disease: metabolism, alterations in blood plasma, and as supplements.* Nutr Metab (Lond), 2018. **15**: p. 33.

177. Brosnan, J.T. and M.E. Brosnan, *Branched-chain amino acids: enzyme and substrate regulation.* J Nutr, 2006. **136**(1 Suppl): p. 207s-11s.
178. Amorim Franco, T.M., S. Hegde, and J.S. Blanchard, *Chemical Mechanism of the Branched-Chain Aminotransferase IlvE from Mycobacterium tuberculosis.* Biochemistry, 2016. **55**(45): p. 6295-6303.
179. Ichihara, A. and E. Koyama, *Transaminase of branched chain amino acids. I. Branched chain amino acids-alpha-ketoglutarate transaminase.* J Biochem, 1966. **59**(2): p. 160-9.
180. Taylor, R.T. and W.T. Jenkins, *Leucine aminotransferase. II. Purification and characterization.* J Biol Chem, 1966. **241**(19): p. 4396-405.
181. Hutson, S., *Structure and function of branched chain aminotransferases.* Prog Nucleic Acid Res Mol Biol, 2001. **70**: p. 175-206.
182. Davoodi, J., P.M. Drown, R.K. Bledsoe, R. Wallin, G.D. Reinhart, and S.M. Hutson, *Overexpression and characterization of the human mitochondrial and cytosolic branched-chain aminotransferases.* J Biol Chem, 1998. **273**(9): p. 4982-9.
183. Suryawan, A., J.W. Hawes, R.A. Harris, Y. Shimomura, A.E. Jenkins, and S.M. Hutson, *A molecular model of human branched-chain amino acid metabolism.* Am J Clin Nutr, 1998. **68**(1): p. 72-81.
184. Yennawar, N., J. Dunbar, M. Conway, S. Hutson, and G. Farber, *The structure of human mitochondrial branched-chain aminotransferase.* Acta Crystallogr D Biol Crystallogr, 2001. **57**(Pt 4): p. 506-15.
185. Yennawar, N.H., M.E. Conway, H.P. Yennawar, G.K. Farber, and S.M. Hutson, *Crystal structures of human mitochondrial branched chain aminotransferase reaction intermediates: ketimine and pyridoxamine phosphate forms.* Biochemistry, 2002. **41**(39): p. 11592-601.
186. Islam, M.M., M. Nautiyal, R.M. Wynn, J.A. Mobley, D.T. Chuang, and S.M. Hutson, *Branched-chain amino acid metabolon: interaction of glutamate dehydrogenase with the mitochondrial branched-chain aminotransferase (BCATm).* J Biol Chem, 2010. **285**(1): p. 265-76.
187. Ashby, E.L., M. Kierzkowska, J. Hull, P.G. Kehoe, S.M. Hutson, and M.E. Conway, *Altered Expression of Human Mitochondrial Branched Chain Aminotransferase in Dementia with Lewy Bodies and Vascular Dementia.* Neurochem Res, 2017. **42**(1): p. 306-319.
188. Ananieva, E.A., J.N. Bostic, A.A. Torres, H.R. Glanz, S.M. McNitt, M.K. Brenner, M.P. Boyer, A.K. Addington, and S.M. Hutson, *Mice deficient in the mitochondrial branched-chain aminotransferase (BCATm) respond with delayed tumour growth to a challenge with EL-4 lymphoma.* Br J Cancer, 2018. **119**(8): p. 1009-1017.
189. Rajendram, R., V.R. Preedy, and V.B. Patel, *Branched chain amino acids in clinical nutrition*. Nutrition and health. 2015, New York: Humana Press. volumes.
190. Rudman, D. and A. Meister, *Transamination in Escherichia coli.* J Biol Chem, 1953. **200**(2): p. 591-604.
191. Norton, J.E. and J.R. Sokatch, *Purification and partial characterization of the branched chain amino acid transaminase of Pseudomonas aeruginosa.* Biochim Biophys Acta, 1970. **206**(2): p. 261-9.
192. Venos, E.S., M.H. Knodel, C.L. Radford, and B.J. Berger, *Branched-chain amino acid aminotransferase and methionine formation in Mycobacterium tuberculosis.* BMC Microbiol, 2004. **4**: p. 39.
193. Yvon, M., E. Chambellon, A. Bolotin, and F. Roudot-Algaron, *Characterization and role of the branched-chain aminotransferase (BcaT) isolated from Lactococcus lactis subsp. cremoris NCDO 763.* Appl Environ Microbiol, 2000. **66**(2): p. 571-7.
194. Saito, M., K. Nishimura, S. Wakabayashi, T. Kurihara, and Y. Nagata, *Purification of branched-chain amino acid aminotransferase from Helicobacter pylori NCTC 11637.* Amino Acids, 2007. **33**(3): p. 445-9.
195. Bezsudnova, E.Y., K.M. Boyko, and V.O. Popov, *Properties of Bacterial and Archaeal*

Branched-Chain Amino Acid Aminotransferases. Biochemistry (Mosc), 2017. **82**(13): p. 1572-1591.
196. Kaiser, J.C., S. Sen, A. Sinha, B.J. Wilkinson, and D.E. Heinrichs, *The role of two branched-chain amino acid transporters in Staphylococcus aureus growth, membrane fatty acid composition and virulence.* Mol Microbiol, 2016. **102**(5): p. 850-864.
197. Singh, V.K., D.S. Hattangady, E.S. Giotis, A.K. Singh, N.R. Chamberlain, M.K. Stuart, and B.J. Wilkinson, *Insertional inactivation of branched-chain alpha-keto acid dehydrogenase in Staphylococcus aureus leads to decreased branched-chain membrane fatty acid content and increased susceptibility to certain stresses.* Appl Environ Microbiol, 2008. **74**(19): p. 5882-90.
198. Kaiser, J.C. and D.E. Heinrichs, *Branching Out: Alterations in Bacterial Physiology and Virulence Due to Branched-Chain Amino Acid Deprivation.* mBio, 2018. **9**(5).
199. Conway, M.E., N. Yennawar, R. Wallin, L.B. Poole, and S.M. Hutson, *Human mitochondrial branched chain aminotransferase: structural basis for substrate specificity and role of redox active cysteines.* Biochim Biophys Acta, 2003. **1647**(1-2): p. 61-5.
200. Yennawar, N.H., M.M. Islam, M. Conway, R. Wallin, and S.M. Hutson, *Human mitochondrial branched chain aminotransferase isozyme: structural role of the CXXC center in catalysis.* J Biol Chem, 2006. **281**(51): p. 39660-71.
201. Hu, L.Y., P.A. Boxer, S.R. Kesten, H.J. Lei, D.J. Wustrow, D.W. Moreland, L. Zhang, K. Ahn, T.R. Ryder, X. Liu, J.R. Rubin, K. Fahnoe, R.T. Carroll, S. Dutta, D.C. Fahnoe, A.W. Probert, R.L. Roof, M.F. Rafferty, C.R. Kostlan, J.D. Scholten, M. Hood, X.D. Ren, G.P. Schielke, T.Z. Su, C.P. Taylor, A. Mistry, P. McConnell, C. Hasemann, and J. Ohren, *The design and synthesis of human branched-chain amino acid aminotransferase inhibitors for treatment of neurodegenerative diseases.* Bioorg Med Chem Lett, 2006. **16**(9): p. 2337-40.
202. Goto, M., I. Miyahara, K. Hirotsu, M. Conway, N. Yennawar, M.M. Islam, and S.M. Hutson, *Structural determinants for branched-chain aminotransferase isozyme-specific inhibition by the anticonvulsant drug gabapentin.* J Biol Chem, 2005. **280**(44): p. 37246-56.
203. Okada, K., K. Hirotsu, M. Sato, H. Hayashi, and H. Kagamiyama, *Three-dimensional structure of Escherichia coli branched-chain amino acid aminotransferase at 2.5 A resolution.* J Biochem, 1997. **121**(4): p. 637-41.
204. Tremblay, L.W. and J.S. Blanchard, *The 1.9 A structure of the branched-chain amino-acid transaminase (IlvE) from Mycobacterium tuberculosis.* Acta Crystallogr Sect F Struct Biol Cryst Commun, 2009. **65**(Pt 11): p. 1071-7.
205. Castell, A., C. Mille, and T. Unge, *Structural analysis of mycobacterial branched-chain aminotransferase: implications for inhibitor design.* Acta Crystallogr D Biol Crystallogr, 2010. **66**(Pt 5): p. 549-57.
206. Okada, K., K. Hirotsu, H. Hayashi, and H. Kagamiyama, *Structures of Escherichia coli branched-chain amino acid aminotransferase and its complexes with 4-methylvalerate and 2-methylleucine: induced fit and substrate recognition of the enzyme.* Biochemistry, 2001. **40**(25): p. 7453-63.
207. Rocha, J.F., A.F. Pina, S.F. Sousa, and N.M.F.S.A. Cerqueira, *PLP-dependent enzymes as important biocatalysts for the pharmaceutical, chemical and food industries: a structural and mechanistic perspective.* Catalysis Science & Technology, 2019. **9**(18): p. 4864-4876.
208. Karsten, W.E., T. Ohshiro, Y. Izumi, and P.F. Cook, *Reaction of serine-glyoxylate aminotransferase with the alternative substrate ketomalonate indicates rate-limiting protonation of a quinonoid intermediate.* Biochemistry, 2005. **44**(48): p. 15930-6.
209. Cassimjee, K.E., B. Manta, and F. Himo, *A quantum chemical study of the omega-transaminase reaction mechanism.* Org Biomol Chem, 2015. **13**(31): p. 8453-64.
210. Amorim Franco, T.M. and J.S. Blanchard, *Bacterial Branched-Chain Amino Acid Biosynthesis: Structures, Mechanisms, and Drugability.* Biochemistry, 2017. **56**(44): p.

5849-5865.
211. Selwan, E.M. and A.L. Edinger, *Branched chain amino acid metabolism and cancer: the importance of keeping things in context.* Translational Cancer Research, 2017: p. S578-S584.
212. Papathanassiu, A.E., J.-H. Ko, M. Imprialou, M. Bagnati, P.K. Srivastava, H.A. Vu, D. Cucchi, S.P. McAdoo, E.A. Ananieva, C. Mauro, and J. Behmoaras, *BCAT1 controls metabolic reprogramming in activated human macrophages and is associated with inflammatory diseases.* Nature Communications, 2017. **8**(1): p. 16040.
213. Ananieva, E.A., C.H. Patel, C.H. Drake, J.D. Powell, and S.M. Hutson, *Cytosolic branched chain aminotransferase (BCATc) regulates mTORC1 signaling and glycolytic metabolism in CD4+ T cells.* J Biol Chem, 2014. **289**(27): p. 18793-804.
214. Amorim Franco, T.M., L. Favrot, O. Vergnolle, and J.S. Blanchard, *Mechanism-Based Inhibition of the Mycobacterium tuberculosis Branched-Chain Aminotransferase by d- and l-Cycloserine.* ACS Chem Biol, 2017. **12**(5): p. 1235-1244.
215. Beeler, T., D. Bacikova, K. Gable, L. Hopkins, C. Johnson, H. Slife, and T. Dunn, *The Saccharomyces cerevisiae TSC10/YBR265w gene encoding 3-ketosphinganine reductase is identified in a screen for temperature-sensitive suppressors of the Ca2+-sensitive csg2Delta mutant.* J Biol Chem, 1998. **273**(46): p. 30688-94.
216. Kihara, A. and Y. Igarashi, *FVT-1 is a mammalian 3-ketodihydrosphingosine reductase with an active site that faces the cytosolic side of the endoplasmic reticulum membrane.* J Biol Chem, 2004. **279**(47): p. 49243-50.
217. Fornarotto, M., L. Xiao, Y. Hou, K.A. Koch, E. Chang, R.M. O'Malley, T.A. Black, M.B. Cable, and S.S. Walker, *Sphingolipid biosynthesis in pathogenic fungi: identification and characterization of the 3-ketosphinganine reductase activity of Candida albicans and Aspergillus fumigatus.* Biochim Biophys Acta, 2006. **1761**(1): p. 52-63.
218. Chao, D.Y., K. Gable, M. Chen, I. Baxter, C.R. Dietrich, E.B. Cahoon, M.L. Guerinot, B. Lahner, S. Lu, J.E. Markham, J. Morrissey, G. Han, S.D. Gupta, J.M. Harmon, J.G. Jaworski, T.M. Dunn, and D.E. Salt, *Sphingolipids in the root play an important role in regulating the leaf ionome in Arabidopsis thaliana.* Plant Cell, 2011. **23**(3): p. 1061-81.
219. Gupta, S.D., K. Gable, G. Han, A. Borovitskaya, L. Selby, T.M. Dunn, and J.M. Harmon, *Tsc10p and FVT1: topologically distinct short-chain reductases required for long-chain base synthesis in yeast and mammals.* J Lipid Res, 2009. **50**(8): p. 1630-40.
220. Park, K.H., Z.W. Ye, J. Zhang, S.M. Hammad, D.M. Townsend, D.C. Rockey, and S.H. Kim, *3-ketodihydrosphingosine reductase mutation induces steatosis and hepatic injury in zebrafish.* Sci Rep, 2019. **9**(1): p. 1138.
221. Takeichi, T., A. Torrelo, J.Y.W. Lee, Y. Ohno, M.L. Lozano, A. Kihara, L. Liu, Y. Yasuda, J. Ishikawa, T. Murase, A.B. Rodrigo, P. Fernandez-Crehuet, Y. Toi, J. Mellerio, J. Rivera, V. Vicente, D.P. Kelsell, Y. Nishimura, Y. Okuno, D. Kojima, Y. Ogawa, K. Sugiura, M.A. Simpson, W.H.I. McLean, M. Akiyama, and J.A. McGrath, *Biallelic Mutations in KDSR Disrupt Ceramide Synthesis and Result in a Spectrum of Keratinization Disorders Associated with Thrombocytopenia.* J Invest Dermatol, 2017. **137**(11): p. 2344-2353.
222. Boyden, L.M., N.G. Vincent, J. Zhou, R. Hu, B.G. Craiglow, S.J. Bayliss, I.S. Rosman, A.W. Lucky, L.A. Diaz, L.A. Goldsmith, A.S. Paller, R.P. Lifton, S.J. Baserga, and K.A. Choate, *Mutations in KDSR Cause Recessive Progressive Symmetric Erythrokeratoderma.* Am J Hum Genet, 2017. **100**(6): p. 978-984.
223. Bursztejn, A.C., R. Happle, L. Charbit, J. Kusel, S. Leclerc-Mercier, S. Hadj-Rabia, S. Fraitag, A. Zimmer, and J. Fischer, *The PERIOPTER syndrome (periorificial and ptychotropic erythrokeratoderma): a new Mendelian disorder of cornification.* J Eur Acad Dermatol Venereol, 2019. **33**(1): p. e1-e3.
224. Youssefian, L., A. Touati, H. Vahidnezhad, A.H. Saeidian, S. Sotoudeh, S. Zeinali, and J. Uitto, *Erythrokeratoderma: a manifestation associated with multiple types of ichthyoses with different gene defects.* Br J Dermatol, 2018. **178**(3): p. e219-e221.

225. Johnson, E.L., S.L. Heaver, J.L. Waters, B.I. Kim, A. Bretin, A.L. Goodman, A.T. Gewirtz, T.S. Worgall, and R.E. Ley, *Sphingolipids produced by gut bacteria enter host metabolic pathways impacting ceramide levels.* Nature Communications, 2020. **11**(1): p. 2471.
226. Bower, E., *Bacterial Sphingolipid Biosynthesis*, in *Department of Chemistry*. 2011, University of Edinburgh.
227. Mykhaylyk, B., *Structural and Mechanistic Studies of Serine Palmitoyltransferase from Bacteriodes fragilis – A Representative of Key Enzyme Controlling Sphingolipid Biosynthesis in Human Microbiome*, in *Department of Chemistry.* 2017, University of Edinburgh.
228. Geoghegan, K.F., H.B. Dixon, P.J. Rosner, L.R. Hoth, A.J. Lanzetti, K.A. Borzilleri, E.S. Marr, L.H. Pezzullo, L.B. Martin, P.K. LeMotte, A.S. McColl, A.V. Kamath, and J.G. Stroh, *Spontaneous alpha-N-6-phosphogluconoylation of a "His tag" in Escherichia coli: the cause of extra mass of 258 or 178 Da in fusion proteins.* Anal Biochem, 1999. **267**(1): p. 169-84.
229. Bonissone, S., N. Gupta, M. Romine, R.A. Bradshaw, and P.A. Pevzner, *N-terminal protein processing: a comparative proteogenomic analysis.* Mol Cell Proteomics, 2013. **12**(1): p. 14-28.
230. Ikushiro, H., M.M. Islam, H. Tojo, and H. Hayashi, *Molecular characterization of membrane-associated soluble serine palmitoyltransferases from Sphingobacterium multivorum and Bdellovibrio stolpii.* J Bacteriol, 2007. **189**(15): p. 5749-61.
231. Eisenthal, R., M.J. Danson, and D.W. Hough, *Catalytic efficiency and kcat/KM: a useful comparator?* Trends Biotechnol, 2007. **25**(6): p. 247-9.
232. Rocha, F.G., Z.D. Moye, G. Ottenberg, P. Tang, D.J. Campopiano, F.C. Gibson, and M.E. Davey, *Porphyromonas gingivalis Sphingolipid Synthesis Limits the Host Inflammatory Response.* Journal of Dental Research, 2020. **99**(5): p. 568-576.
233. Aframian, D.J., T. Davidowitz, and R. Benoliel, *The distribution of oral mucosal pH values in healthy saliva secretors.* Oral Dis, 2006. **12**(4): p. 420-3.
234. Penno, A., M.M. Reilly, H. Houlden, M. Laura, K. Rentsch, V. Niederkofler, E.T. Stoeckli, G. Nicholson, F. Eichler, R.H. Brown, A. von Eckardstein, and T. Hornemann, *Hereditary Sensory Neuropathy Type 1 Is Caused by the Accumulation of Two Neurotoxic Sphingolipids.* Journal of Biological Chemistry, 2010. **285**(15): p. 11178-11187.
235. Ferreira, C.R., S.M.I. Goorden, A. Soldatos, H.M. Byers, J.M.M. Ghauharali-van der Vlugt, F.S. Beers-Stet, C. Groden, C.D. van Karnebeek, W.A. Gahl, F.M. Vaz, X. Jiang, and H.J. Vernon, *Deoxysphingolipid precursors indicate abnormal sphingolipid metabolism in individuals with primary and secondary disturbances of serine availability.* Molecular Genetics and Metabolism, 2018. **124**(3): p. 204-209.
236. Ikushiro, H., H. Hayashi, and H. Kagamiyama, *Reactions of serine palmitoyltransferase with serine and molecular mechanisms of the actions of serine derivatives as inhibitors.* Biochemistry, 2004. **43**(4): p. 1082-92.
237. Kuzmic, P., *DynaFit--a software package for enzymology.* Methods Enzymol, 2009. **467**: p. 247-280.
238. Kitz, R. and I.B. Wilson, *Esters of Methanesulfonic Acid as Irreversible Inhibitors of Acetylcholinesterase.* Journal of Biological Chemistry, 1962. **237**(10): p. 3245-&.
239. Strelow, J.M., *A Perspective on the Kinetics of Covalent and Irreversible Inhibition.* SLAS Discov, 2017. **22**(1): p. 3-20.
240. Webster, S.P., D. Alexeev, D.J. Campopiano, R.M. Watt, M. Alexeeva, L. Sawyer, and R.L. Baxter, *Mechanism of 8-Amino-7-oxononanoate Synthase: Spectroscopic, Kinetic, and Crystallographic Studies.* Biochemistry, 2000. **39**(3): p. 516-528.
241. Lendrihas, T., G.A. Hunter, and G.C. Ferreira, *Targeting the active site gate to yield hyperactive variants of 5-aminolevulinate synthase.* The Journal of biological chemistry, 2010. **285**(18): p. 13704-13711.
242. Booth, W.T., C.R. Schlachter, S. Pote, N. Ussin, N.J. Mank, V. Klapper, L.R. Offermann, C.

Tang, B.K. Hurlburt, and M. Chruszcz, *Impact of an N-terminal Polyhistidine Tag on Protein Thermal Stability.* ACS Omega, 2018. **3**(1): p. 760-768.
243. Karav, S., E. Talak, M. Tuncer, and A. Özleyen, *The Effect of Fusion Tags on Enzyme Specificity and Protein Purification Efficiency.* 2017. **6**: p. 2319-1473.
244. Esen, H., S. Alpdağtaş, M. Mervan Çakar, and B. Binay, *Tailoring of recombinant FDH: effect of histidine tag location on solubility and catalytic properties of Chaetomium thermophilum formate dehydrogenase (CtFDH).* Preparative Biochemistry & Biotechnology, 2019. **49**(5): p. 529-534.
245. Majorek, K.A., M.L. Kuhn, M. Chruszcz, W.F. Anderson, and W. Minor, *Double trouble-Buffer selection and His-tag presence may be responsible for nonreproducibility of biomedical experiments.* Protein Sci, 2014. **23**(10): p. 1359-68.
246. Yu, X., X. Wang, and P.C. Engel, *The specificity and kinetic mechanism of branched-chain amino acid aminotransferase from Escherichia coli studied with a new improved coupled assay procedure and the enzyme's potential for biocatalysis*. Febs j, 2014. **281**(1): p. 391-400.
247. Meng, L., Y. Liu, X. Yin, H. Zhou, J. Wu, M. Wu, and L. Yang, *Effects of His-tag on Catalytic Activity and Enantioselectivity of Recombinant Transaminases.* Applied Biochemistry and Biotechnology, 2020. **190**(3): p. 880-895.
248. Lucast, L.J., R.T. Batey, and J.A. Doudna, *Large-scale purification of a stable form of recombinant tobacco etch virus protease.* Biotechniques, 2001. **30**(3): p. 544-6, 548, 550 passim.
249. Carson, M., D.H. Johnson, H. McDonald, C. Brouillette, and L.J. Delucas, *His-tag impact on structure.* Acta Crystallogr D Biol Crystallogr, 2007. **63**(Pt 3): p. 295-301.
250. Waterhouse, A., M. Bertoni, S. Bienert, G. Studer, G. Tauriello, R. Gumienny, F.T. Heer, T.A.P. de Beer, C. Rempfer, L. Bordoli, R. Lepore, and T. Schwede, *SWISS-MODEL: homology modelling of protein structures and complexes.* Nucleic Acids Res, 2018. **46**(W1): p. W296-w303.
251. Guex, N., M.C. Peitsch, and T. Schwede, *Automated comparative protein structure modeling with SWISS-MODEL and Swiss-PdbViewer: a historical perspective.* Electrophoresis, 2009. **30 Suppl 1**: p. S162-73.
252. Bienert, S., A. Waterhouse, T.A. de Beer, G. Tauriello, G. Studer, L. Bordoli, and T. Schwede, *The SWISS-MODEL Repository-new features and functionality.* Nucleic Acids Res, 2017. **45**(D1): p. D313-d319.
253. Studer, G., C. Rempfer, A.M. Waterhouse, R. Gumienny, J. Haas, and T. Schwede, *QMEANDisCo-distance constraints applied on model quality estimation.* Bioinformatics, 2020. **36**(6): p. 1765-1771.
254. Bertoni, M., F. Kiefer, M. Biasini, L. Bordoli, and T. Schwede, *Modeling protein quaternary structure of homo- and hetero-oligomers beyond binary interactions by homology.* Sci Rep, 2017. **7**(1): p. 10480.
255. Borthwick, J.A., N. Ancellin, S.M. Bertrand, R.P. Bingham, P.S. Carter, C.W. Chung, I. Churcher, N. Dodic, C. Fournier, P.L. Francis, A. Hobbs, C. Jamieson, S.D. Pickett, S.E. Smith, D.O. Somers, C. Spitzfaden, C.J. Suckling, and R.J. Young, *Structurally Diverse Mitochondrial Branched Chain Aminotransferase (BCATm) Leads with Varying Binding Modes Identified by Fragment Screening.* J Med Chem, 2016. **59**(6): p. 2452-67.
256. Deng, H., J. Zhou, F. Sundersingh, J.A. Messer, D.O. Somers, M. Ajakane, C.C. Arico-Muendel, A. Beljean, S.L. Belyanskaya, R. Bingham, E. Blazensky, A.B. Boullay, E. Boursier, J. Chai, P. Carter, C.W. Chung, A. Daugan, Y. Ding, K. Herry, C. Hobbs, E. Humphries, C. Kollmann, V.L. Nguyen, E. Nicodeme, S.E. Smith, N. Dodic, and N. Ancellin, *Discovery and Optimization of Potent, Selective, and in Vivo Efficacious 2-Aryl Benzimidazole BCATm Inhibitors.* ACS Med Chem Lett, 2016. **7**(4): p. 379-84.
257. Deng, H., J. Zhou, F.S. Sundersingh, J. Summerfield, D. Somers, J.A. Messer, A.L. Satz, N. Ancellin, C.C. Arico-Muendel, K.L. Sargent Bedard, A. Beljean, S.L. Belyanskaya, R.

Bingham, S.E. Smith, E. Boursier, P. Carter, P.A. Centrella, M.A. Clark, C.W. Chung, C.P. Davie, J.L. Delorey, Y. Ding, G.J. Franklin, L.C. Grady, K. Herry, C. Hobbs, C.S. Kollmann, B.A. Morgan, L.J. Pothier Kaushansky, and Q. Zhou, *Discovery, SAR, and X-ray Binding Mode Study of BCATm Inhibitors from a Novel DNA-Encoded Library.* ACS Med Chem Lett, 2015. **6**(8): p. 919-24.

258. Bertrand, S.M., N. Ancellin, B. Beaufils, R.P. Bingham, J.A. Borthwick, A.B. Boullay, E. Boursier, P.S. Carter, C.W. Chung, I. Churcher, N. Dodic, M.H. Fouchet, C. Fournier, P.L. Francis, L.A. Gummer, K. Herry, A. Hobbs, C.I. Hobbs, P. Homes, C. Jamieson, E. Nicodeme, S.D. Pickett, I.H. Reid, G.L. Simpson, L.A. Sloan, S.E. Smith, D.O. Somers, C. Spitzfaden, C.J. Suckling, K. Valko, Y. Washio, and R.J. Young, *The Discovery of in Vivo Active Mitochondrial Branched-Chain Aminotransferase (BCATm) Inhibitors by Hybridizing Fragment and HTS Hits.* J Med Chem, 2015. **58**(18): p. 7140-63.
259. Chen, C.D., C.H. Lin, P. Chuankhayan, Y.C. Huang, Y.C. Hsieh, T.F. Huang, H.H. Guan, M.Y. Liu, W.C. Chang, and C.J. Chen, *Crystal structures of complexes of the branched-chain aminotransferase from Deinococcus radiodurans with alpha-ketoisocaproate and L-glutamate suggest the radiation resistance of this enzyme for catalysis.* J Bacteriol, 2012. **194**(22): p. 6206-16.
260. Bommer, M. and J.M. Ward, *A 1-step microplate method for assessing the substrate range of l-alpha-amino acid aminotransferase.* Enzyme Microb Technol, 2013. **52**(4-5): p. 218-25.
261. Cooper, A.J., M. Conway, and S.M. Hutson, *A continuous 96-well plate spectrophotometric assay for branched-chain amino acid aminotransferases.* Anal Biochem, 2002. **308**(1): p. 100-5.
262. Bottone, E.J., *Bacillus cereus, a volatile human pathogen.* Clin Microbiol Rev, 2010. **23**(2): p. 382-98.
263. O., E.G., *Animal Clinical Chemistry: A Practical Handbook for Toxicologists and Biomedical Researchers*. 2nd Edition ed. 2009, Boca Raton: CRC Press. 368.
264. Bailey, J., E.T. Bell, and J.E. Bell, *Regulation of bovine glutamate dehydrogenase. The effects of pH and ADP.* J Biol Chem, 1982. **257**(10): p. 5579-83.
265. Scudiero, D.A., R.H. Shoemaker, K.D. Paull, A. Monks, S. Tierney, T.H. Nofziger, M.J. Currens, D. Seniff, and M.R. Boyd, *Evaluation of a soluble tetrazolium/formazan assay for cell growth and drug sensitivity in culture using human and other tumor cell lines.* Cancer Res, 1988. **48**(17): p. 4827-33.
266. Hansen, M.B., S.E. Nielsen, and K. Berg, *Re-examination and further development of a precise and rapid dye method for measuring cell growth/cell kill.* J Immunol Methods, 1989. **119**(2): p. 203-10.
267. Rej, R., *A convenient continuous-rate spectrophotometric method for determination of amino acid substrate specificity of aminotransferases: application to isoenzymes of aspartate aminotransferase.* Anal Biochem, 1982. **119**(1): p. 205-10.
268. Lowry, O.H., J.V. Passonneau, and M.K. Rock, *The stability of pyridine nucleotides.* J Biol Chem, 1961. **236**: p. 2756-9.
269. Zheng, X., Y. Cui, T. Li, R. Li, L. Guo, D.-F. Li, and B. Wu, *Biochemical and structural characterization of a highly active branched-chain amino acid aminotransferase from Pseudomonas sp. for efficient biosynthesis of chiral amino acids.* bioRxiv, 2019: p. 559120.
270. Kagamiyama, H. and H. Hayashi, *Branched-chain amino-acid aminotransferase of Escherichia coli.* Methods Enzymol, 2000. **324**: p. 103-13.
271. Inoue, K., S. Kuramitsu, K. Aki, Y. Watanabe, T. Takagi, M. Nishigai, A. Ikai, and H. Kagamiyama, *Branched-chain amino acid aminotransferase of Escherichia coli: overproduction and properties.* J Biochem, 1988. **104**(5): p. 777-84.
272. Yu, X., X. Wang, and P.C. Engel, *The specificity and kinetic mechanism of branched-chain amino acid aminotransferase from Escherichia coli studied with a new improved coupled assay procedure and the enzyme's potential for biocatalysis.* FEBS J, 2014. **281**(1): p. 391-

400.
273. Papathanassiu, A.E., J.H. Ko, M. Imprialou, M. Bagnati, P.K. Srivastava, H.A. Vu, D. Cucchi, S.P. McAdoo, E.A. Ananieva, C. Mauro, and J. Behmoaras, *BCAT1 controls metabolic reprogramming in activated human macrophages and is associated with inflammatory diseases*. Nat Commun, 2017. **8**: p. 16040.
274. Lightcap, E.S. and R.B. Silverman, *Slow-binding inhibition of gamma-aminobutyric acid aminotransferase by hydrazine analogues.* J Med Chem, 1996. **39**(3): p. 686-94.
275. Morrison, J.F., *Kinetics of the reversible inhibition of enzyme-catalysed reactions by tight-binding inhibitors*. Biochim Biophys Acta, 1969. **185**(2): p. 269-86.
276. Williams, J.W. and J.F. Morrison, *The kinetics of reversible tight-binding inhibition.* Methods Enzymol, 1979. **63**: p. 437-67.
277. Copeland, R.A., *Tight Binding Inhibitors*, in *Enzymes: A Practical Introduction to Structure, Mechanism, and Data Analysis.*, R.A. Copeland, Editor. 2002, Wiley-VCH, Inc.: Wiley-VCH, Inc. p. 305-317.
278. Grankvist, N., K.A. Lagerborg, M. Jain, and R. Nilsson, *Gabapentin Can Suppress Cell Proliferation Independent of the Cytosolic Branched-Chain Amino Acid Transferase 1 (BCAT1).* Biochemistry, 2018. **57**(49): p. 6762-6766.
279. Serpico, A., *Biocatalytic application of rare PLP-dependent aminotransferases for the synthesis of high value amino acids and amines*, in *Chemistry*. 2018, University of Edinburgh: 2018. p. 198.
280. Sigma-Aldrich. *Buffer Reference Center*. 2019 [cited 2019 9th September]; Available from: https://www.sigmaaldrich.com/life-science/core-bioreagents/biological-buffers/learning-center/buffer-reference-center.html.
281. Stein, N., *CHAINSAW: a program for mutating pdb files used as templates in molecular replacement*. Journal of Applied Crystallography, 2008. **41**(3): p. 641-643.
282. Evans, P., *Scaling and assessment of data quality.* Acta Crystallographica Section D, 2006. **62**(1): p. 72-82.
283. Evans, P.R., *An introduction to data reduction: space-group determination, scaling and intensity statistics*. Acta Crystallogr D Biol Crystallogr, 2011. **67**(Pt 4): p. 282-92.
284. McCoy, A.J., R.W. Grosse-Kunstleve, P.D. Adams, M.D. Winn, L.C. Storoni, and R.J. Read, *Phaser crystallographic software.* Journal of Applied Crystallography, 2007. **40**(4): p. 658-674.
285. Kovalevskiy, O., R.A. Nicholls, F. Long, A. Carlon, and G.N. Murshudov, *Overview of refinement procedures within REFMAC5: utilizing data from different sources.* Acta crystallographica. Section D, Structural biology, 2018. **74**(Pt 3): p. 215-227.
286. Nicholls, R.A., M. Tykac, O. Kovalevskiy, and G.N. Murshudov, *Current approaches for the fitting and refinement of atomic models into cryo-EM maps using CCP-EM.* Acta Crystallographica Section D, 2018. **74**(6): p. 492-505.
287. Murshudov, G.N., P. Skubak, A.A. Lebedev, N.S. Pannu, R.A. Steiner, R.A. Nicholls, M.D. Winn, F. Long, and A.A. Vagin, *REFMAC5 for the refinement of macromolecular crystal structures*. Acta Crystallographica Section D, 2011. **67**(4): p. 355-367.
288. Murshudov, G.N., A.A. Vagin, and E.J. Dodson, *Refinement of Macromolecular Structures by the Maximum-Likelihood Method.* Acta Crystallographica Section D, 1997. **53**(3): p. 240-255.
289. Winn, M.D., C.C. Ballard, K.D. Cowtan, E.J. Dodson, P. Emsley, P.R. Evans, R.M. Keegan, E.B. Krissinel, A.G. Leslie, A. McCoy, S.J. McNicholas, G.N. Murshudov, N.S. Pannu, E.A. Potterton, H.R. Powell, R.J. Read, A. Vagin, and K.S. Wilson, *Overview of the CCP4 suite and current developments.* Acta Crystallogr D Biol Crystallogr, 2011. **67**(Pt 4): p. 235-42.
290. Ruan, J., J. Hu, A. Yin, W. Wu, X. Cong, X. Feng, and S. Li, *Structure of the branched-chain aminotransferase from Streptococcus mutans.* Acta Crystallogr D Biol Crystallogr, 2012. **68**(Pt 8): p. 996-1002.
291. Olson, G.T., M. Fu, S. Lau, K.L. Rinehart, and R.B. Silverman, *An Aromatization Mechanism*

of Inactivation of γ-Aminobutyric Acid Aminotransferase for the Antibiotic l-Cycloserine. Journal of the American Chemical Society, 1998. **120**(10): p. 2256-2267.
292. Peisach, D., D.M. Chipman, P.W. Van Ophem, J.M. Manning, and D. Ringe, *d-Cycloserine Inactivation of d-Amino Acid Aminotransferase Leads to a Stable Noncovalent Protein Complex with an Aromatic Cycloserine-PLP Derivative*. Journal of the American Chemical Society, 1998. **120**(10): p. 2268-2274.
293. Gao, S., H. Liu, V. de Crécy-Lagard, W. Zhu, N.G.J. Richards, and J.H. Naismith, *PMP–diketopiperazine adducts form at the active site of a PLP dependent enzyme involved in formycin biosynthesis.* Chemical Communications, 2019. **55**(96): p. 14502-14505.
294. de Chiara, C., M. Homšak, G.A. Prosser, H.L. Douglas, A. Garza-Garcia, G. Kelly, A.G. Purkiss, E.W. Tate, and L.P.S. de Carvalho, *d-Cycloserine destruction by alanine racemase and the limit of irreversible inhibition.* Nature Chemical Biology, 2020. **16**(6): p. 686-694.
295. Jörnvall, H., B. Persson, M. Krook, S. Atrian, R. Gonzalez-Duarte, J. Jeffery, and D. Ghosh, *Short-chain dehydrogenases/reductases (SDR).* Biochemistry, 1995. **34**(18): p. 6003-6013.
296. Duax, W.L., J.F. Griffin, and D. Ghosh, *The fascinating complexities of steroid-binding enzymes.* Curr Opin Struct Biol, 1996. **6**(6): p. 813-23.
297. Ghosh, D., Z. Wawrzak, C.M. Weeks, W.L. Duax, and M. Erman, *The refined three-dimensional structure of 3 alpha,20 beta-hydroxysteroid dehydrogenase and possible roles of the residues conserved in short-chain dehydrogenases.* Structure, 1994. **2**(7): p. 629-40.
298. Filling, C., K.D. Berndt, J. Benach, S. Knapp, T. Prozorovski, E. Nordling, R. Ladenstein, H. Jörnvall, and U. Oppermann, *Critical residues for structure and catalysis in short-chain dehydrogenases/reductases.* J Biol Chem, 2002. **277**(28): p. 25677-84.
299. Wu, J.T., L.H. Wu, and J.A. Knight, *Stability of NADPH: effect of various factors on the kinetics of degradation.* Clin Chem, 1986. **32**(2): p. 314-9.
300. Huber, M., E. Chiticariu, D. Bachmann, L. Flatz, and D. Hohl, *Palmoplantar Keratoderma with Leukokeratosis Anogenitalis Caused by KDSR Mutations.* Journal of Investigative Dermatology, 2020. **140**(8): p. 1662-1665.e1.
301. Bariana, T.K., V. Labarque, J. Heremans, C. Thys, M. De Reys, D. Greene, B. Jenkins, L. Grassi, D. Seyres, F. Burden, D. Whitehorn, O. Shamardina, S. Papadia, K. Gomez, N. BioResource, C. Van Geet, A. Koulman, W.H. Ouwehand, C. Ghevaert, M. Frontini, E. Turro, and K. Freson, *Sphingolipid dysregulation due to lack of functional KDSR impairs proplatelet formation causing thrombocytopenia.* Haematologica, 2018.
302. Prasad, S., P.B. Khadatare, and I. Roy, *Effect of chemical chaperones in improving the solubility of recombinant proteins in Escherichia coli.* Appl Environ Microbiol, 2011. **77**(13): p. 4603-9.
303. Baugh, L., I. Phan, D.W. Begley, M.C. Clifton, B. Armour, D.M. Dranow, B.M. Taylor, M.M. Muruthi, J. Abendroth, J.W. Fairman, D. Fox, 3rd, S.H. Dieterich, B.L. Staker, A.S. Gardberg, R. Choi, S.N. Hewitt, A.J. Napuli, J. Myers, L.K. Barrett, Y. Zhang, M. Ferrell, E. Mundt, K. Thompkins, N. Tran, S. Lyons-Abbott, A. Abramov, A. Sekar, D. Serbzhinskiy, D. Lorimer, G.W. Buchko, R. Stacy, L.J. Stewart, T.E. Edwards, W.C. Van Voorhis, and P.J. Myler, *Increasing the structural coverage of tuberculosis drug targets.* Tuberculosis (Edinb), 2015. **95**(2): p. 142-8.
304. Wang, H., H. Zhang, Y. Zou, Y. Mi, S. Lin, Z. Xie, Y. Yan, and H. Zhang, *Structural insight into the tetramerization of an iterative ketoreductase siam through aromatic residues in the interfaces.* PLoS One, 2014. **9**(6): p. e97996.
305. Malashkevich, V.N., Toro, R., Sauder, J.M., Burley, S.K., Almo, S.C., *CRYSTAL STRUCTURE OF putativte short chain dehydrogenase from Shigella flexneri 2a str. 301.* To be published, 2008.
306. Malashkevich, V.N., Toro, R., Sauder, J.M., Burley, S.K., Almo, S.C., *Crystal structure of an uncharacterized protein.* TO BE PUBLISHED, 2008.

307. Tian, W., C. Chen, X. Lei, J. Zhao, and J. Liang, *CASTp 3.0: computed atlas of surface topography of proteins.* Nucleic Acids Research, 2018. **46**(W1): p. W363-W367.
308. Trott, O. and A.J. Olson, *AutoDock Vina: improving the speed and accuracy of docking with a new scoring function, efficient optimization, and multithreading.* Journal of computational chemistry, 2010. **31**(2): p. 455-461.
309. Stankeviciute, G., Z. Guan, H. Goldfine, and E.A. Klein, *Caulobacter crescentus Adapts to Phosphate Starvation by Synthesizing Anionic Glycoglycerolipids and a Novel Glycosphingolipid.* mBio, 2019. **10**(2): p. e00107-19.
310. Olea-Ozuna, R.J., S. Poggio, EdBergström, E. Quiroz-Rocha, D.A. García-Soriano, D.X. Sahonero-Canavesi, J. Padilla-Gómez, L. Martínez-Aguilar, I.M. López-Lara, J. Thomas-Oates, and O. Geiger, *Five structural genes required for ceramide synthesis in Caulobacter and for bacterial survival.* Environmental Microbiology. **n/a**(n/a).
311. Wieland Brown, L.C., C. Penaranda, P.C. Kashyap, B.B. Williams, J. Clardy, M. Kronenberg, J.L. Sonnenburg, L.E. Comstock, J.A. Bluestone, and M.A. Fischbach, *Production of α-Galactosylceramide by a Prominent Member of the Human Gut Microbiota.* PLOS Biology, 2013. **11**(7): p. e1001610.

Appendix

Appendix 8.1 Calibration curve of the HiLoad 16/60 Superdex 200 prep grade column

Standards	Elution vol (Ve)	Vol 0 (dextran blue)	Vol t	Ve/Vo	Mr (kDa)	Mr (Dalton)	Ln (Dalton)	Kav	Lg (Dalton)
Ovalbumin	78.48	40.97	110	1.92	43	43000	10.67	0.54	4.63
Conalbumin	74.57	40.97	110	1.82	75	75000	11.23	0.49	4.88
Aldolase	67.22	40.97	110	1.64	158	158000	11.97	0.38	5.20
Ferritin	56.19	40.97	110	1.37	440	440000	12.99	0.22	5.64

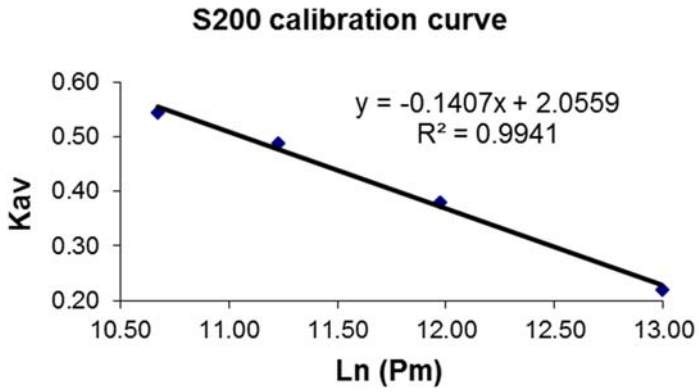

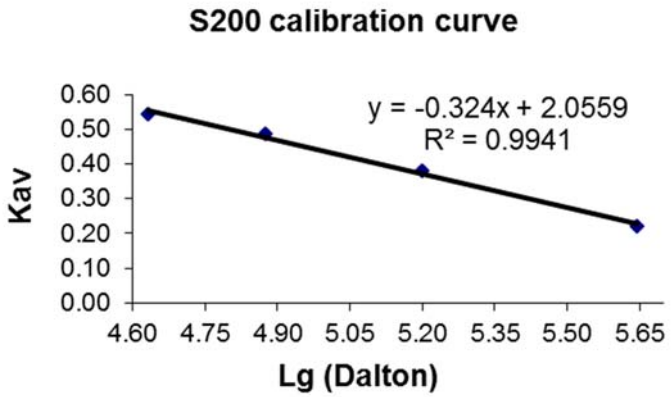

The MW of the protein is estimated as follows:

$$MW = 10^{\frac{K_{av} - 2.0559}{-0.1407}}$$

$$K_{av} = \frac{V_e - V_o}{V_t - V_o}$$

Where:

MW is measured in Da

V_e = Elution volume

V_o = Void volume

V_t = Total bed volume

Appendix 8.2 Calibration curve of the HiPrep™ 16/60 Sephacryl™ S-300 column

Standards	Elution vol (Ve)	Vol 0 (dextran blue)	Vol t	Ve/Vo	Mr (kDa)	Mr (Dalton)	Ln (Dalton)	Kav	Lg (Dalton)
Ovalbumin	69.48	36.9	120	1.883	43	43000	10.669	0.392	4.633
Conablumin	64.29	36.9	120	1.742	75	75000	11.225	0.330	4.875
Aldolase	51.11	36.9	120	1.385	158	158000	11.970	0.171	5.199
Ferritin	42.99	36.9	120	1.165	440	440000	12.995	0.073	5.643
Thyroglobulin	37.94	36.9	120	1.028	669	669000	13.414	0.012	5.825

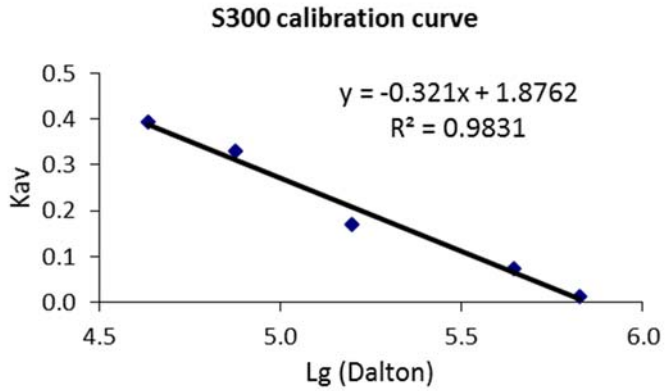

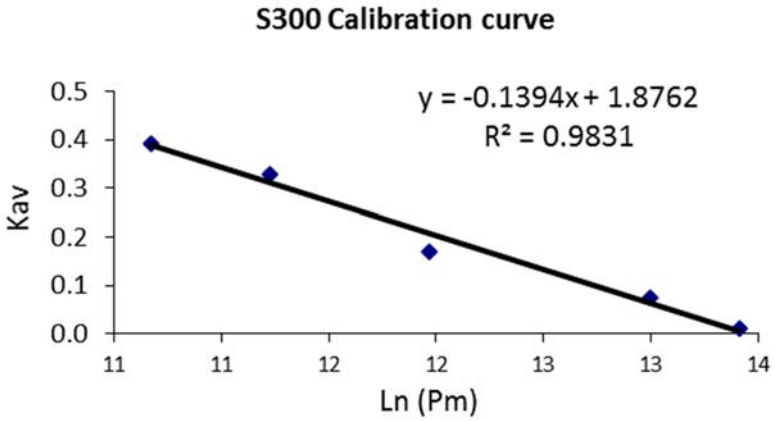

The MW of the protein is estimated as follows:

$$MW = 10^{\frac{K_{av} - 1.8762}{-0.1394}}$$

$$K_{av} = \frac{V_e - V_o}{V_t - V_o}$$

Where:

MW is measured in Da

V_e = Elution volume

V_o = Void volume

V_t = Total bed volume

Appendix 8.3 The DNA and amino acid sequences of recombinant proteins

>DNA sequence of KDSR

```
   1 ATGGAGTTTA CGTTAGAAGA CCAAGTTGTG TTGATCACTG GTGGTTCACA
  51 AGGTCTTGGA AAGGAATTCG CCAAAAAATA TTATAATGAG GCTGAAAACA
 101 CAAAGATTAT TATCGTCAGT AGGTCAGAGG CTAGACTGCT GGACACATGC
 151 AACGAAATTA GGATTGAAGC TCACCTGAGA AGGGAAACCA CTGACGAGGG
 201 CCAAGTGCAA CATAAGTTGG CTGCGCCCTT GGACCTTGAG CAACGGTTAT
 251 TTTACTACCC ATGCGACTTG TCCTGCTACG AATCCGTGGA ATGTTTGTTC
 301 AATGCCCTGA GAGACTTGGA TTTACTCCCT ACACAAACGT TATGCTGTGC
 351 AGGGGGGGCT GTTCCTAAGT TATTTCGTGG GCTAAGCGGA CATGAGTTGA
 401 ACTTGGGTAT GGACATCAAC TATAAAACAA CTTTGAACGT GGCACATCAG
 451 ATTGCCCTTG CAGAGCAAAC CAAGGAACAC CACCTCATCA TCTTTTCTAG
 501 TGCCACCGCG CTTTACCCAT TTGTGGGCTA TTCCCAGTAT GCGCCTGCAA
 551 AAGCTGCAAT CAAATCACTG GTAGCAATCT TAAGACAAGA ACTGACGAAC
 601 TTCCGTATCA GTTGTGTTTA TCCTGGTAAT TTTGAAAGCG AAGGTTTCAC
 651 TGTAGAGCAG CTAACGAAAC CCGAAATTAC AAAGTTGATC GAAGGCCCCT
 701 CAGACGCTAT CCCATGCAAA CAAGCATGTG ATATCATTGC CAAGTCGCTG
 751 GCCAGAGGTG ATGAAGACGT TTTTACAGAT TTTGTCGGAT GGATGATAAT
 801 GGGGATGGAC CTTGGGCTCA CCGCAAAGAA AAGCCGCTTT GTTCCGAATC
 851 TAGAACAAAA ACTCATCTCA GAAGAGGATC TGAATAGCGC CCTCGAGCAC
 901 CACCACCACC ACCAC
```

>Amino acid sequence of KDSR

```
   1 MEFTLEDQVV LITGGSQGLG KEFAKKYYNE AENTKIIIVS RSEARLLDTC
  51 NEIRIEAHLR RETTDEGQVQ HKLAAPLDLE QRLFYYPCDL SCYESVECLF
 101 NALRDLDLLP TQTLCCAGGA VPKLFRGLSG HELNLGMDIN YKTTLNVAHQ
 151 IALAEQTKEH HLIIFSSATA LYPFVGYSQY APAKAAIKSL VAILRQELTN
 201 FRISCVYPGN FESEGFTVEQ LTKPEITKLI EGPSDAIPCK QACDIIAKSL
 251 ARGDEDVFTD FVGWMIMGMD LGLTAKKSRF VPNLEQKLIS EEDLNSALEH
 301 HHHHH
```

(C-terminal His_6 tag in red)

> DNA sequence of KDSR G263E

```
   1 ATGGAGTTTA CGTTAGAAGA CCAAGTTGTG TTGATCACTG GTGGTTCACA
  51 AGGTCTTGGA AAGGAATTCG CCAAAAAATA TTATAATGAG GCTGAAAACA
 101 CAAAGATTAT TATCGTCAGT AGGTCAGAGG CTAGACTGCT GGACACATGC
 151 AACGAAATTA GGATTGAAGC TCACCTGAGA AGGGAAACCA CTGACGAGGG
 201 CCAAGTGCAA CATAAGTTGG CTGCGCCCTT GGACCTTGAG CAACGGTTAT
 251 TTTACTACCC ATGCGACTTG TCCTGCTACG AATCCGTGGA ATGTTTGTTC
 301 AATGCCCTGA GAGACTTGGA TTTACTCCCT ACACAAACGT TATGCTGTGC
 351 AGGGGGGGCT GTTCCTAAGT TATTTCGTGG GCTAAGCGGA CATGAGTTGA
 401 ACTTGGGTAT GGACATCAAC TATAAAACAA CTTTGAACGT GGCACATCAG
 451 ATTGCCCTTG CAGAGCAAAC CAAGGAACAC CACCTCATCA TCTTTTCTAG
 501 TGCCACCGCG CTTTACCCAT TTGTGGGCTA TTCCCAGTAT GCGCCTGCAA
 551 AAGCTGCAAT CAAATCACTG GTAGCAATCT TAAGACAAGA ACTGACGAAC
 601 TTCCGTATCA GTTGTGTTTA TCCTGGTAAT TTTGAAAGCG AAGGTTTCAC
 651 TGTAGAGCAG CTAACGAAAC CCGAAATTAC AAAGTTGATC GAAGGCCCCT
 701 CAGACGCTAT CCCATGCAAA CAAGCATGTG ATATCATTGC CAAGTCGCTG
 751 GCCAGAGGTG ATGAAGACGT TTTTACAGAT TTTGTCGAAT GGATGATAAT
 801 GGGGATGGAC CTTGGGCTCA CCGCAAAGAA AAGCCGCTTT GTTCCGAATC
 851 TAGAACAAAA ACTCATCTCA GAAGAGGATC TGAATAGCGC CCTCGAGCAC
 901 CACCACCACC ACCAC
```

> Amino acid sequence of KDSR G263E

```
   1 MEFTLEDQVV LITGGSQGLG KEFAKKYYNE AENTKIIIVS RSEARLLDTC
  51 NEIRIEAHLR RETTDEGQVQ HKLAAPLDLE QRLFYYPCDL SCYESVECLF
 101 NALRDLDLLP TQTLCCAGGA VPKLFRGLSG HELNLGMDIN YKTTLNVAHQ
 151 IALAEQTKEH HLIIFSSATA LYPFVGYSQY APAKAAIKSL VAILRQELTN
 201 FRISCVYPGN FESEGFTVEQ LTKPEITKLI EGPSDAIPCK QACDIIAKSL
```

```
 251 ARGDEDVFTD FVEWMIMGMD LGLTAKKSRF VPNLEQKLIS EEDLNSALEH
 301 HHHHH
```

(C-terminal His_6 tag in red, the mutated site in blue)

> DNA sequence of BfSPT

```
   1 ATGGGATTAT TACAAGAGAA GTTAGCTAAA TACGACCTCC CTCAGCAGAT
  51 AAAGGCTAAA GGCGTATATC CATACTTTCG TTGTATCGAA AGTGAACAGA
 101 ACACAGAGGT GATAATGAGT GGCAGAAAGG TGTTAATGTT TGGCTCAAAC
 151 TCATACTTAG GCCTGACTAA TCATCCGAAA GTAATTGAAG CTGCTGTTGA
 201 AGCTACCCGC AAATATGGTA CAGGTTGCGC CGGATCGCGT TTTCTGAACG
 251 GTACACTCGA CCTCCATCTT CAATTGGAGA AAGAATTGGC CGAATTTGTT
 301 GGTAAAGAAG ATGCTATCAT TTATTCTACC GGATTTCAGG TAAATCTGGG
 351 TGTGGTTTCG TGTGTGACAG GTCGTGAAGA TTATGTGATC TGTGATGAAC
 401 TTGACCACGC TTCTATTGTT GAAGGACGCC GCCTTTCTTT TTCTACCATT
 451 CTTAAGTTCA AGCATAACGA TATGGAATCT CTTGAGAAAG AGTTGCAGAA
 501 ATGTCGTCCT GATGCAGTGA AACTGATTGT AGTAGATGGA GTATTCAGTA
 551 TGGAGGGTGA TATTGCCAAT TTGCCTGAGA TCGTCCGTTT GTCTAAAAAA
 601 TATGATGCTA ATATCATGGT AGATGAAGCG CATGGACTGG GAGTTTTGGG
 651 TAATCACGGA CGCGGTACTT GTGATCATTT CGGATTGACT AAAGAGGTGG
 701 ATCTTATTAT GGGTACATTC AGTAAGTCAT TGGCCGCTAT CGGTGGCTTT
 751 ATTGCAGCAG ACGAGTCCAT CATTAATTAT TTGCGTCACA ATTCACGTTC
 801 ATATATCTTT AGTGCAAGTA ATACGCCTGC TGCTACAGCT GCCGCTCGTG
 851 CTGCACTTCA GATTATGAAA AACGAACCGG AACGTATTGA GCATTTGTGG
 901 GATATAACCA ATTACTCTTT AAAGTGTTTC CGTGAACTTG GTTTTGAGAT
 951 CGGACATACC TCCACTCCTA TCATTCCTCT ATATGTACGT GATATGGAGA
1001 AGACATTTAT GGTAACTAAG ATGTTATTTG ACGAAGGTGT GTTTGTAAAT
1051 CCAGTTGTGC CTCCCGCATG TTCTCCGAAC GATACGTTGA TTCGTTTCTC
1101 GTTGATGGCT ACACACTCTA AAGAACAGAT TGATTTTGCT
```

>Amino acid sequence of BfSPT

```
   1 MGLLQEKLAK YDLPQQIKAK GVYPYFRCIE SEQNTEVIMS GRKVLMFGSN
  51 SYLGLTNHPK VIEAAVEATR KYGTGCAGSR FLNGTLDLHL QLEKELAEFV
 101 GKEDAIIYST GFQVNLGVVS CVTGREDYVI CDELDHASIV EGRRLSFSTI
 151 LKFKHNDMES LEKELQKCRP DAVKLIVVDG VFSMEGDIAN LPEIVRLSKK
 201 YDANIMVDEA HGLGVLGNHG RGTCDHFGLT KEVDLIMGTF SKSLAAIGGF
 251 IAADESIINY LRHNSRSYIF SASNTPAATA AARAALQIMK NEPERIEHLW
 301 DITNYSLKCF RELGFEIGHT STPIIPLYVR DMEKTFMVTK MLFDEGVFVN
 351 PVVPPACSPN DTLIRFSLMA THSKEQIDFA IGKLVKCFKA LDLLEHHHHH
 401 H
```

(C-terminal His_6 tag in red)

> DNA sequence of BfSPT V353R

```
   1 ATGGGATTAT TACAAGAGAA GTTAGCTAAA TACGACCTCC CTCAGCAGAT
  51 AAAGGCTAAA GGCGTATATC CATACTTTCG TTGTATCGAA AGTGAACAGA
 101 ACACAGAGGT GATAATGAGT GGCAGAAAGG TGTTAATGTT TGGCTCAAAC
 151 TCATACTTAG GCCTGACTAA TCATCCGAAA GTAATTGAAG CTGCTGTTGA
 201 AGCTACCCGC AAATATGGTA CAGGTTGCGC CGGATCGCGT TTTCTGAACG
 251 GTACACTCGA CCTCCATCTT CAATTGGAGA AAGAATTGGC CGAATTTGTT
 301 GGTAAAGAAG ATGCTATCAT TTATTCTACC GGATTTCAGG TAAATCTGGG
 351 TGTGGTTTCG TGTGTGACAG GTCGTGAAGA TTATGTGATC TGTGATGAAC
 401 TTGACCACGC TTCTATTGTT GAAGGACGCC GCCTTTCTTT TTCTACCATT
 451 CTTAAGTTCA AGCATAACGA TATGGAATCT CTTGAGAAAG AGTTGCAGAA
 501 ATGTCGTCCT GATGCAGTGA AACTGATTGT AGTAGATGGA GTATTCAGTA
 551 TGGAGGGTGA TATTGCCAAT TTGCCTGAGA TCGTCCGTTT GTCTAAAAAA
 601 TATGATGCTA ATATCATGGT AGATGAAGCG CATGGACTGG GAGTTTTGGG
 651 TAATCACGGA CGCGGTACTT GTGATCATTT CGGATTGACT AAAGAGGTGG
 701 ATCTTATTAT GGGTACATTC AGTAAGTCAT TGGCCGCTAT CGGTGGCTTT
 751 ATTGCAGCAG ACGAGTCCAT CATTAATTAT TTGCGTCACA ATTCACGTTC
 801 ATATATCTTT AGTGCAAGTA ATACGCCTGC TGCTACAGCT GCCGCTCGTG
 851 CTGCACTTCA GATTATGAAA AACGAACCGG AACGTATTGA GCATTTGTGG
```

```
 901 GATATAACCA ATTACTCTTT AAAGTGTTTC CGTGAACTTG GTTTTGAGAT
 951 CGGACATACC TCCACTCCTA TCATTCCTCT ATATGTACGT GATATGGAGA
1001 AGACATTTAT GGTAACTAAG ATGTTATTTG ACGAAGGTGT GTTTGTAAAT
1051 CCAGTTCGGC CTCCCGCATG TTCTCCGAAC GATACGTTGA TTCGTTTCTC
1101 GTTGATGGCT ACACACTCTA AAGAACAGAT TGATTTTGCT ATCGGTAAGT
1151 TAGTGAAATG TTTCAAGGCA CTTGATCTTC TCGAGCACCA CCACCACCAC
1201 CACTGA
```

>Amino acid sequence of BfSPT V353R

```
   1 MGLLQEKLAK YDLPQQIKAK GVYPYFRCIE SEQNTEVIMS GRKVLMFGSN
  51 SYLGLTNHPK VIEAAVEATR KYGTGCAGSR FLNGTLDLHL QLEKELAEFV
 101 GKEDAIIYST GFQVNLGVVS CVTGREDYVI CDELDHASIV EGRRLSFSTI
 151 LKFKHNDMES LEKELQKCRP DAVKLIVVDG VFSMEGDIAN LPEIVRLSKK
 201 YDANIMVDEA HGLGVLGNHG RGTCDHFGLT KEVDLIMGTF SKSLAAIGGF
 251 IAADESIINY LRHNSRSYIF SASNTPAATA AARAALQIMK NEPERIEHLW
 301 DITNYSLKCF RELGFEIGHT STPIIPLYVR DMEKTFMVTK MLFDEGVFVN
 351 PVRPPACSPN DTLIRFSLMA THSKEQIDFA IGKLVKCFKA LDLLEHHHHH
 401 H
```

(C-terminal His_6 tag in red, the mutated site in blue)

> DNA sequence of C-terminal pETHis_{10}PgSPT

```
   1 ATGGGCGGAA AATTGTTACA GGATAAATTG GATCAGTATA CCGAGCCGCA
  51 AAAGGCACAA GCCGCAGGTA TTTACCCTTA TTTCAGAAAA ATCGAAAGTG
 101 ATCAGGATAC CGAGGTCGTT ATCGATGGTC GGAAAGTCCT CATGTTCGGC
 151 TCCAATGCAT ATCTGGGACT GACGAACCAC CCGAAAGTCA AGGAGGCAGC
 201 TATCGAAGCG ACAAAGAAGT ACGGTACGGG CTGTGCCGGC TCCCGCTTCC
 251 TCAACGGCAC ACTCGATATT CACCTCGAAC TGGAAAAACG GCTGGCCGAG
 301 TTCGTCGGCA AGGAAGATGC CATCAGCTTC TCTACCGGCT TCCAAGTGAA
 351 TCTGGGCGTT GTCTCCTGCA TCACCGGCCG CGAGGATTAT ATCATCTGGG
 401 ACGAGTTGGA TCATGCTTCG ATCATCGAGG GTATTCGCCT TTCATTCAGC
 451 ACGAAGTTAA AGTACAAGCA TAATGATATG GTTTCTCTGG AGAAGCGGCT
 501 CCAGCAGTGC GACCACGGAG AAGATCAAAC TGATTGTGGT CCGATGGTGT
 551 CTTTCAGTAT GGAGGGTGAT GTCTGCAATC TGCCCGAAAT CGTTCGCCTC
 601 GCCAAGCGAT ACAACGCCAA TGTGATGGTG GACGAAGCTC ACGGTATCGG
 651 CGTGATGGGC GACCACGGAC GCGGCGTCTG CAATCACTTC GGTCTGACCG
 701 ACGAAGTGGA CTTGATCATG GGTACTTTCA GCAAATCTTT CGCTTCGCTC
 751 GGAGGGTTTA TTGCAGGAGA CAAGAGCGTT ATCAACTACC TGCGCCACCA
 801 CGCCCGATCC TATATTTTCA GTGCCAGCTG TACGCCGGCC TCTACGGCAG
 851 CGGCAGCAGC TGCTCTGGAC ATTATGTTTA GCGAACCGGA GCGTTTAGCC
 901 CGATTGTGGG AGCTGACGCA CTACTCATTG AACGCATTCC GCAGTCTTGG
 951 ATTCGAAATA GGTCATACAT CGACACCTAT TATCCCGCTT TTTATCCGCA
1001 ACAACGAGAA GACATTCCAA ATAACCCGAG ACGCTTTCGA AGAAGGGGTA
1051 TTCGTCAATC CGGTGGTCTC TCCGGCGGTA GCTCCGTCCG ACACCCTTAT
1101 TCGCTTTTCA CTCATGGCTA CGCATACGAA GGAGCAACTC GACTTTGCCA
1151 TCGAAAAGCT GCATAAGGTA TTCAAGCAGA ACGGTGTCCT GCTCGAGGAA
1201 AACCTGTATT TTCAGGGCAC GCATCATCAT CATCACCACC ACCACCACCA
1251 CTGA
```

> Amino acid sequence of C-terminal pETHis_{10}PgSPT

```
   1 MGKLLQDKLA QYTEPQKAQA AGIYPYFRKI ESDQDTEVVI DGRKVLMFGS
  51 NAYLGLTNHP KVKEAAIEAT KKYGTGCAGS RFLNGTLDIH LELEKRLAEF
 101 VGKEDAISFS TGFQVNLGVV SCITGREDYI IWDELDHASI IEGIRLSFST
 151 KLKYKHNDMG SLEKRLQQCD PEKIKLIVVD GVFSMEGDVC NLPEIVRLAK
 201 RYNANVMVDE AHGIGVMGDH GRGVCNHFGL TDEVDLIMGT FSKSFASLGG
 251 FIAGDKSVIN YLRHHARSYI FSASCTPAST AAAAAALDIM FSEPERLARL
 301 WELTHYSLNA FRSLGFEIGH TSTPIIPLFI RNNEKTFQIT RDAFEEGVFV
 351 NPVVSPAVAP SDTLIRFSLM ATHTKEQLDF AIEKLHKVFK QNGVLEENL
 401 YFQGAHHHHH HHHHH
```

(C-terminal His_6 tag in red)

> DNA sequence of C-terminal pETHis$_{10}$PgSPT V358C

```
   1 ATGGGAAAAT TGTTACAGGA TAAATTGGCT CAGTATACCG AGCCGCAAAA
  51 GGCACAAGCC GCAGGTATTT ACCCTTATTT CAGAAAAATC GAAAGTGATC
 101 AGGATACCGA GGTCGTTATC GATGGTCGGA AAGTCCTCAT GTTCGGCTCC
 151 AATGCATATC TGGGACTGAC GAACCACCCG AAAGTCAAGG AGGCAGCTAT
 201 CGAAGCGACA AAGAAGTACG GTACGGGCTG TGCCGGCTCC CGCTTCCTCA
 251 ACGGCACACT CGATATTCAC CTCGAACTGG AAAAACGGCT GGCCGAGTTC
 301 GTCGGCAAGG AAGATGCCAT CAGCTTCTCT ACCGGCTTCC AAGTGAATCT
 351 GGGCGTTGTC TCCTGCATCA CCGGCCGCGA GGATTATATC ATCTGGGACG
 401 AGTTGGATCA TGCTTCGATC ATCGAGGGTA TTCGCCTTTC ATTCAGCACG
 451 AAGTTAAAGT ACAAGCATAA TGATATGGGT TCTCTGGAGA AGCGGCTCCA
 501 GCAGTGCGAC CCGGAGAAGA TCAAACTGAT TGTGGTCGAT GGTGTCTTCA
 551 GTATGGAGGG TGATGTCTGC AATCTGCCCG AAATCGTTCG CCTCGCCAAG
 601 CGATACAACG CCAATGTGAT GGTGGACGAA GCTCACGGTA TCGGCGTGAT
 651 GGGCGACCAC GGACGCGGCG TCTGCAATCA CTTCGGTCTG ACCGACGAAG
 701 TGGACTTGAT CATGGGTACT TTCAGCAAAT CTTTCGCTTC GCTCGGAGGG
 751 TTTATTGCAG GAGACAAGAG CGTTATCAAC TACCTGCGCC ACCACGCCCG
 801 ATCCTATATT TTCAGTGCCA GCTGTACGCC GGCCTCTACG GCAGCGGCAG
 851 CAGCTGCTCT GGACATTATG TTTAGCGAAC CGGAGCGTTT AGCCCGATTG
 901 TGGGAGCTGA CGCACTACTC ATTGAACGCA TTCCGCAGTC TTGGATTCGA
 951 AATAGGTCAT ACATCGACAC CTATTATCCC GCTTTTTATC CGCAACAACG
1001 AGAAGACATT CCAAATAACC CGAGACGCTT TCGAAGAAGG GGTATTCGTC
1051 AATCCGGTGG TCTCTCCGGC GTGCGCTCCG TCCGACACCC TTATTCGCTT
1101 TTCACTCATG GCTACGCATA CGAAGGAGCA ACTCGACTTT GCCATCGAAA
1151 AGCTGCATAA GGTATTCAAG CAGAACGGTG TCCTG
```

> Amino acid sequence of C-terminal pETHis$_{10}$PgSPT V358C

```
   1 MGKLLQDKLA QYTEPQKAQA AGIYPYFRKI ESDQDTEVVI DGRKVLMFGS
  51 NAYLGLTNHP KVKEAAIEAT KKYGTGCAGS RFLNGTLDIH LELEKRLAEF
 101 VGKEDAISFS TGFQVNLGVV SCITGREDYI IWDELDHASI IEGIRLSFST
 151 KLKYKHNDMG SLEKRLQQCD PEKIKLIVVD GVFSMEGDVC NLPEIVRLAK
 201 RYNANVMVDE AHGIGVMGDH GRGVCNHFGL TDEVDLIMGT FSKSFASLGG
 251 FIAGDKSVIN YLRHHARSYI FSASCTPAST AAAAAALDIM FSEPERLARL
 301 WELTHYSLNA FRSLGFEIGH TSTPIIPLFI RNNEKTFQIT RDAFEEGVFV
 351 NPVVSPACAP SDTLIRFSLM ATHTKEQLDF AIEKLHKVFK QNGVLLEENL
 401 YFQGAHHHHH HHHHH
```

(C-terminal His$_{10}$ tag in red, the mutated site in blue)

> DNA sequence of C-terminal pETHis$_{10}$PgSPT V358A

```
   1 ATGGGAAAAT TGTTACAGGA TAAATTGGCT CAGTATACCG AGCCGCAAAA
  51 GGCACAAGCC GCAGGTATTT ACCCTTATTT CAGAAAAATC GAAAGTGATC
 101 AGGATACCGA GGTCGTTATC GATGGTCGGA AAGTCCTCAT GTTCGGCTCC
 151 AATGCATATC TGGGACTGAC GAACCACCCG AAAGTCAAGG AGGCAGCTAT
 201 CGAAGCGACA AAGAAGTACG GTACGGGCTG TGCCGGCTCC CGCTTCCTCA
 251 ACGGCACACT CGATATTCAC CTCGAACTGG AAAAACGGCT GGCCGAGTTC
 301 GTCGGCAAGG AAGATGCCAT CAGCTTCTCT ACCGGCTTCC AAGTGAATCT
 351 GGGCGTTGTC TCCTGCATCA CCGGCCGCGA GGATTATATC ATCTGGGACG
 401 AGTTGGATCA TGCTTCGATC ATCGAGGGTA TTCGCCTTTC ATTCAGCACG
 451 AAGTTAAAGT ACAAGCATAA TGATATGGGT TCTCTGGAGA AGCGGCTCCA
 501 GCAGTGCGAC CCGGAGAAGA TCAAACTGAT TGTGGTCGAT GGTGTCTTCA
 551 GTATGGAGGG TGATGTCTGC AATCTGCCCG AAATCGTTCG CCTCGCCAAG
 601 CGATACAACG CCAATGTGAT GGTGGACGAA GCTCACGGTA TCGGCGTGAT
 651 GGGCGACCAC GGACGCGGCG TCTGCAATCA CTTCGGTCTG ACCGACGAAG
 701 TGGACTTGAT CATGGGTACT TTCAGCAAAT CTTTCGCTTC GCTCGGAGGG
 751 TTTATTGCAG GAGACAAGAG CGTTATCAAC TACCTGCGCC ACCACGCCCG
 801 ATCCTATATT TTCAGTGCCA GCTGTACGCC GGCCTCTACG GCAGCGGCAG
 851 CAGCTGCTCT GGACATTATG TTTAGCGAAC CGGAGCGTTT AGCCCGATTG
 901 TGGGAGCTGA CGCACTACTC ATTGAACGCA TTCCGCAGTC TTGGATTCGA
 951 AATAGGTCAT ACATCGACAC CTATTATCCC GCTTTTTATC CGCAACAACG
1001 AGAAGACATT CCAAATAACC CGAGACGCTT TCGAAGAAGG GGTATTCGTC
1051 AATCCGGTGG TCTCTCCGGC GGCAGCTCCG TCCGACACCC TTATTCGCTT
```

```
1101 TTCACTCATG GCTACGCATA CGAAGGAGCA ACTCGACTTT GCCATCGAAA
1151 AGCTGCATAA GGTATTCAAG CAGAACGGTG TCCTG
```

> Amino acid sequence of C-terminal pETHis$_{10}$PgSPT V358A

```
   1 MGKLLQDKLA QYTEPQKAQA AGIYPYFRKI ESDQDTEVVI DGRKVLMFGS
  51 NAYLGLTNHP KVKEAAIEAT KKYGTGCAGS RFLNGTLDIH LELEKRLAEF
 101 VGKEDAISFS TGFQVNLGVV SCITGREDYI IWDELDHASI IEGIRLSFST
 151 KLKYKHNDMG SLEKRLQQCD PEKIKLIVVD GVFSMEGDVC NLPEIVRLAK
 201 RYNANVMVDE AHGIGVMGDH GRGVCNHFGL TDEVDLIMGT FSKSFASLGG
 251 FIAGDKSVIN YLRHHARSYI FSASCTPAST AAAAAALDIM FSEPERLARL
 301 WELTHYSLNA FRSLGFEIGH TSTPIIPLFI RNNEKTFQIT RDAFEEGVFV
 351 NPVVSPAAAP SDTLIRFSLM ATHTKEQLDF AIEKLHKVFK QNGVLLEENL
 401 YFQGAHHHHH HHHHH
```

(C-terminal His$_{10}$ tag in red, the mutated site in blue)

> DNA sequence of C-terminal pETHis$_{10}$PgSPT A359S

```
   1 ATGGGAAAAT TGTTACAGGA TAAATTGGCT CAGTATACCG AGCCGCAAAA
  51 GGCACAAGCC GCAGGTATTT ACCCTTATTT CAGAAAAATC GAAAGTGATC
 101 AGGATACCGA GGTCGTTATC GATGGTCGGA AAGTCCTCAT GTTCGGCTCC
 151 AATGCATATC TGGGACTGAC GAACCACCCG AAAGTCAAGG AGGCAGCTAT
 201 CGAAGCGACA AAGAAGTACG GTACGGGCTG TGCCGGCTCC CGCTTCCTCA
 251 ACGGCACACT CGATATTCAC CTCGAACTGG AAAAACGGCT GGCCGAGTTC
 301 GTCGGCAAGG AAGATGCCAT CAGCTTCTCT ACCGGCTTCC AAGTGAATCT
 351 GGGCGTTGTC TCCTGCATCA CCGGCCGCGA GGATTATATC ATCTGGGACG
 401 AGTTGGATCA TGCTTCGATC ATCGAGGGTA TTCGCCTTTC ATTCAGCACG
 451 AAGTTAAAGT ACAAGCATAA TGATATGGGT TCTCTGGAGA AGCGGCTCCA
 501 GCAGTGCGAC CCGGAGAAGA TCAAACTGAT TGTGGTCGAT GGTGTCTTCA
 551 GTATGGAGGG TGATGTCTGC AATCTGCCCG AAATCGTTCG CCTCGCCAAG
 601 CGATACAACG CCAATGTGAT GGTGGACGAA GCTCACGGTA TCGGCGTGAT
 651 GGGCGACCAC GGACGCGGCG TCTGCAATCA CTTCGGTCTG ACCGACGAAG
 701 TGGACTTGAT CATGGGTACT TTCAGCAAAT CTTTCGCTTC GCTCGGAGGG
 751 TTTATTGCAG GAGACAAGAG CGTTATCAAC TACCTGCGCC ACCACGCCCG
 801 ATCCTATATT TTCAGTGCCA GCTGTACGCC GGCCTCTACG GCAGCGGCAG
 851 CAGCTGCTCT GGACATTATG TTTAGCGAAC CGGAGCGTTT AGCCCGATTG
 901 TGGGAGCTGA CGCACTACTC ATTGAACGCA TTCCGCAGTC TTGGATTCGA
 951 AATAGGTCAT ACATCGACAC CTATTATCCC GCTTTTTATC CGCAACAACG
1001 AGAAGACATT CCAAATAACC CGAGACGCTT TCGAAGAAGG GGTATTCGTC
1051 AATCCGGTGG TCTCTCCGGC GGTCTCTCCG TCCGACACCC TTATTCGCTT
1101 TTCACTCATG GCTACGCATA CGAAGGAGCA ACTCGACTTT GCCATCGAAA
1151 AGCTGCATAA GGTATTCAAG CAGAACGGTG TCCTG
```

> Amino acid sequence of C-terminal pETHis$_{10}$PgSPT A359S

```
   1 MGKLLQDKLA QYTEPQKAQA AGIYPYFRKI ESDQDTEVVI DGRKVLMFGS
  51 NAYLGLTNHP KVKEAAIEAT KKYGTGCAGS RFLNGTLDIH LELEKRLAEF
 101 VGKEDAISFS TGFQVNLGVV SCITGREDYI IWDELDHASI IEGIRLSFST
 151 KLKYKHNDMG SLEKRLQQCD PEKIKLIVVD GVFSMEGDVC NLPEIVRLAK
 201 RYNANVMVDE AHGIGVMGDH GRGVCNHFGL TDEVDLIMGT FSKSFASLGG
 251 FIAGDKSVIN YLRHHARSYI FSASCTPAST AAAAAALDIM FSEPERLARL
 301 WELTHYSLNA FRSLGFEIGH TSTPIIPLFI RNNEKTFQIT RDAFEEGVFV
 351 NPVVSPAVSP SDTLIRFSLM ATHTKEQLDF AIEKLHKVFK QNGVLLEENL
 401 YFQGAHHHHH HHHHH
```

(C-terminal His$_{10}$ tag in red, the mutated site in blue)

> DNA sequence of C-terminal pETHis$_{10}$PgSPT DM V358C A359S

```
   1 ATGGGAAAAT TGTTACAGGA TAAATTGGCT CAGTATACCG AGCCGCAAAA
  51 GGCACAAGCC GCAGGTATTT ACCCTTATTT CAGAAAAATC GAAAGTGATC
 101 AGGATACCGA GGTCGTTATC GATGGTCGGA AAGTCCTCAT GTTCGGCTCC
 151 AATGCATATC TGGGACTGAC GAACCACCCG AAAGTCAAGG AGGCAGCTAT
 201 CGAAGCGACA AAGAAGTACG GTACGGGCTG TGCCGGCTCC CGCTTCCTCA
```

```
 251 ACGGCACACT CGATATTCAC CTCGAACTGG AAAAACGGCT GGCCGAGTTC
 301 GTCGGCAAGG AAGATGCCAT CAGCTTCTCT ACCGGCTTCC AAGTGAATCT
 351 GGGCGTTGTC TCCTGCATCA CCGGCCGCGA GGATTATATC ATCTGGGACG
 401 AGTTGGATCA TGCTTCGATC ATCGAGGGTA TTCGCCTTTC ATTCAGCACG
 451 AAGTTAAAGT ACAAGCATAA TGATATGGGT TCTCTGGAGA AGCGGCTCCA
 501 GCAGTGCGAC CCGGAGAAGA TCAAACTGAT TGTGGTCGAT GGTGTCTTCA
 551 GTATGGAGGG TGATGTCTGC AATCTGCCCG AAATCGTTCG CCTCGCCAAG
 601 CGATACAACG CCAATGTGAT GGTGGACGAA GCTCACGGTA TCGGCGTGAT
 651 GGGCGACCAC GGACGCGGCG TCTGCAATCA CTTCGGTCTG ACCGACGAAG
 701 TGGACTTGAT CATGGGTACT TTCAGCAAAT CTTTCGCTTC GCTCGGAGGG
 751 TTTATTGCAG GAGACAAGAG CGTTATCAAC TACCTGCGCC ACCACGCCCG
 801 ATCCTATATT TTCAGTGCCA GCTGTACGCC GGCCTCTACG GCAGCGGCAG
 851 CAGCTGCTCT GGACATTATG TTTAGCGAAC CGGAGCGTTT AGCCCGATTG
 901 TGGGAGCTGA CGCACTACTC ATTGAACGCA TTCCGCAGTC TTGGATTCGA
 951 AATAGGTCAT ACATCGACAC CTATTATCCC GCTTTTTATC CGCAACAACG
1001 AGAAGACATT CCAAATAACC CGAGACGCTT TCGAAGAAGG GGTATTCGTC
1051 AATCCGGTGG TCTCTCCGGC GTGCTCTCCG TCCGACACCC TTATTCGCTT
1101 TTCACTCATG GCTACGCATA CGAAGGAGCA ACTCGACTTT GCCATCGAAA
1151 AGCTGCATAA GGTATTCAAG CAGAACGGTG TCCTG
```

> Amino acid sequence of C-terminal pETHis$_{10}$PgSPT DM V358C A359S

```
   1 MGKLLQDKLA QYTEPQKAQA AGIYPYFRKI ESDQDTEVVI DGRKVLMFGS
  51 NAYLGLTNHP KVKEAAIEAT KKYGTGCAGS RFLNGTLDIH LELEKRLAEF
 101 VGKEDAISFS TGFQVNLGVV SCITGREDYI IWDELDHASI IEGIRLSFST
 151 KLKYKHNDMG SLEKRLQQCD PEKIKLIVVD GVFSMEGDVC NLPEIVRLAK
 201 RYNANVMVDE AHGIGVMGDH GRGVCNHFGL TDEVDLIMGT FSKSFASLGG
 251 FIAGDKSVIN YLRHHARSYI FSASCTPAST AAAAAALDIM FSEPERLARL
 301 WELTHYSLNA FRSLGFEIGH TSTPIIPLFI RNNEKTFQIT RDAFEEGVFV
 351 NPVVSPACSP SDTLIRFSLM ATHTKEQLDF AIEKLHKVFK QNGVLLEENL
 401 YFQGAHHHHH HHHHH
```

(C-terminal His$_{10}$ tag in red, the mutated site in blue)

> DNA sequence of N-terminal pETHis$_6$PgSPT

```
 -74 ATGTCGTACT ACCATCACCA TCACCATCAC GATTACGACA TCCCAACGAC
 -24 CGAAAACCTG TATTTTCAGG GCGCCATGGG AAAATTGTTA CAGGATAAAT
  26 TGGCTCAGTA TACCGAGCCG CAAAAGGCAC AAGCCGCAGG TATTTACCCT
  76 TATTTCAGAA AAATCGAAAG TGATCAGGAT ACCGAGGTCG TTATCGATGG
 126 TCGGAAAGTC CTCATGTTCG GCTCCAATGC ATATCTGGGA CTGACGAACC
 176 ACCCGAAAGT CAAGGAGGCA GCTATCGAAG CGACAAAGAA GTACGGTACG
 226 GGCTGTGCCG GCTCCCGCTT CCTCAACGGC ACACTCGATA TTCACCTCGA
 276 ACTGGAAAAA CGGCTGGCCG AGTTCGTCGG CAAGGAAGAT GCCATCAGCT
 326 TCTCTACCGG CTTCCAAGTG AATCTGGGCG TTGTCTCCTG CATCACCGGC
 376 CGCGAGGATT ATATCATCTG GGACGAGTTG GATCATGCTT CGATCATCGA
 426 GGGTATTCGC CTTTCATTCA GCACGAAGTT AAAGTACAAG CATAATGATA
 476 TGGGTTCTCT GGAGAAGCGG CTCCAGCAGT GCGACCCGGA GAAGATCAAA
 526 CTGATTGTGG TCGATGGTGT CTTCAGTATG GAGGGTGATG TCTGCAATCT
 576 GCCCGAAATC GTTCGCCTCG CCAAGCGATA CAACGCCAAT GTGATGGTGG
 626 ACGAAGCTCA CGGTATCGGC GTGATGGGCG ACCACGGACG CGGCGTCTGC
 676 AATCACTTCG GTCTGACCGA CGAAGTGGAC TTGATCATGG GTACTTTCAG
 726 CAAATCTTTC GCTTCGCTCG GAGGGTTTAT TGCAGGAGAC AAGAGCGTTA
 776 TCAACTACCT GCGCCACCAC GCCCGATCCT ATATTTTCAG TGCCAGCTGT
 826 ACGCCGGCCT CTACGGCAGC GGCAGCAGCT GCTCTGGACA TTATGTTTAG
 876 CGAACCGGAG CGTTTAGCCC GATTGTGGGA GCTGACGCAC TACTCATTGA
 926 ACGCATTCCG CAGTCTTGGA TTCGAAATAG GTCATACATC GACACCTATT
 976 ATCCCGCTTT TTATCCGCAA CAACGAGAAG ACATTCCAAA TAACCCGAGA
1026 CGCTTTCGAA GAAGGGGTAT TCGTCAATCC GGTGGTCTCT CCGGCGGTAG
1076 CTCCGTCCGA CACCCTTATT CGCTTTTCAC TCATGGCTAC GCATACGAAG
1126 GAGCAACTCG ACTTTGCCAT CGAAAAGCTG CATAAGGTAT TCAAGCAGAA
1176 CGGTGTCCTG TAA
```

> Amino acid sequence of N-terminal pETHis$_6$PgSPT

```
-24 MSYYHHHHHH DYDIPTTENL YFQGAMGKLL QDKLAQYTEP QKAQAAGIYP
 26 YFRKIESDQD TEVVIDGRKV LMFGSNAYLG LTNHPKVKEA AIEATKKYGT
 76 GCAGSRFLNG TLDIHLELEK RLAEFVGKED AISFSTGFQV NLGVVSCITG
126 REDYIIWDEL DHASIIEGIR LSFSTKLKYK HNDMGSLEKR LQQCDPEKIK
176 LIVVDGVFSM EGDVCNLPEI VRLAKRYNAN VMVDEAHGIG VMGDHGRGVC
226 NHFGLTDEVD LIMGTFSKSF ASLGGFIAGD KSVINYLRHH ARSYIFSASC
276 TPASTAAAAA ALDIMFSEPE RLARLWELTH YSLNAFRSLG FEIGHTSTPI
326 IPLFIRNNEK TFQITRDAFE EGVFVNPVVS PAVAPSDTLI RFSLMATHTK
376 EQLDFAIEKL HKVFKQNGVL
```

(N-terminal His_6 tag in red)

> DNA sequence of N-terminal pETHis_6PgIlvE

```
-57 ATGGGCAGCA GCCATCATCA TCATCATCAC AGCAGCGGCC TGGTGCCGCG
 -7 CGGCAGCCCA TATGGAAAAT ATCGATTGGT CATCGCTCTC ATTCGGTTAT
 43 AGGAAGACCG ACTACAACGT GCGCTGTTAC TATCGCAACG GCAAGTGGGG
 93 AGAGCTTGAA GTATCCTCAG AGGAAACGAT CACGATGCAC ATGGCTGCCA
143 CTTGTCTCCA CTACGGACAG GAAGCATTCG AAGGGATGAA GGCTTTCCGT
193 GGCAAAGATG GCAAGATCCG CCTCTTCCGC ATGGATGAGA ATGCCAAGCG
243 CATGAACAGA TCATGCCAAG GTGTGGTAAT GGCCGAGCTG CCGCAGGAAA
293 TCTTCGAAGC AGCTGTAATC AAGGCCGTAA AGATGAACGA GCGTTTCGTT
343 CCTCCTTACG AAAGCGGAGC TTCTCTTTAC ATCCGTCCGC TTGTTATCGG
393 ACTGGGTGCA CAAGTGGGTG TGAAGCCGGC TCCCGAGTAT CTCTTCATCG
443 TCTTTGTAAC GCCCGTAGGG CCGTATTTCA AAGAAGGATT CAAACCGACC
493 AAGATGGCCA TCTTCCGCGA CTATGACCGT GCAGCTCCTC TGGGTACGGG
543 TACGATCAAA GTGGGCGGTA ACTATGCAGC CGGTATGATC CCCACAGTGA
593 AAGCTCACGA AATGGGCTAC TCTGCAGCTA TCTTCTTGGA TGCCAAAGAA
643 AAGAAGTACA TAGACGAAGC CGGTCCGGCC AACTTCTTCG CCATCAAGAA
693 CAATACTTAT ATCACTCCCG AATCCAGCTC TATCCTGCCC TCTATCACAA
743 ACAAGAGTCT GATGCAGGTG GCTCAGGATC TGGGTCTGAA GGTAGAGCGT
793 CGTCCGGTAG CCGAAGAAGA GCTTGCTACT TTCGAAGAAG CAGGTGCTTG
843 TGGTACGGCA GCCGTGATCA GCCCTATCTC CGAGATTGAC GACTTGGAGA
893 ACAACAAACA GTACGTCATC AGCAAGGACG GCAAACCGGG TCCGTGGTGT
943 GAAAAGCTCT ATCACGAACT TCGTGCCATC CAGTATGGCG ACAAGCCCGA
993 CATTCATGGT TGGGTGACAA TCCTCGACTA A
```

> Amino acid sequence of N-terminal pETHis_6 PgIlvE

```
-19 MGSSHHHHHH SSGLVPRGSH MENIDWSSLS FGYRKTDYNV RCYYRNGKWG
 31 ELEVSSEETI TMHMAATCLH YGQEAFEGMK AFRGKDGKIR LFRMDENAKR
 81 MNRSCQGVVM AELPQEIFEA AVIKAVKMNE RFVPPYESGA SLYIRPLVIG
131 LGAQVGVKPA PEYLFIVFVT PVGPYFKEGF KPTKMAIFRD YDRAAPLGTG
181 TIKVGGNYAA GMIPTVKAHE MGYSAAIFLD AKEKKYIDEA GPANFFAIKN
231 NTYITPESSS ILPSITNKSL MQVAQDLGLK VERRPVAEEE LATFEEAGAC
281 GTAAVISPIS EIDDLENNKQ YVISKDGKPG PWCEKLYHEL RAIQYGDKPD
331 IHGWVTILD
```

(N-terminal His_6 tag in red)

> DNA sequence of N-terminal pETHis_6PgIlvE Y188A

```
-57 ATGGGCAGCA GCCATCATCA TCATCATCAC AGCAGCGGCC TGGTGCCGCG
 -7 CGGCAGCCCA TATGGAAAAT ATCGATTGGT CATCGCTCTC ATTCGGTTAT
 43 AGGAAGACCG ACTACAACGT GCGCTGTTAC TATCGCAACG GCAAGTGGGG
 93 AGAGCTTGAA GTATCCTCAG AGGAAACGAT CACGATGCAC ATGGCTGCCA
143 CTTGTCTCCA CTACGGACAG GAAGCATTCG AAGGGATGAA GGCTTTCCGT
193 GGCAAAGATG GCAAGATCCG CCTCTTCCGC ATGGATGAGA ATGCCAAGCG
243 CATGAACAGA TCATGCCAAG GTGTGGTAAT GGCCGAGCTG CCGCAGGAAA
293 TCTTCGAAGC AGCTGTAATC AAGGCCGTAA AGATGAACGA GCGTTTCGTT
343 CCTCCTTACG AAAGCGGAGC TTCTCTTTAC ATCCGTCCGC TTGTTATCGG
393 ACTGGGTGCA CAAGTGGGTG TGAAGCCGGC TCCCGAGTAT CTCTTCATCG
443 TCTTTGTAAC GCCCGTAGGG CCGTATTTCA AAGAAGGATT CAAACCGACC
493 AAGATGGCCA TCTTCCGCGA CTATGACCGT GCAGCTCCTC TGGGTACGGG
543 TACGATCAAA GTGGGCGGTA ACGCTGCAGC CGGTATGATC CCCACAGTGA
593 AAGCTCACGA AATGGGCTAC TCTGCAGCTA TCTTCTTGGA TGCCAAAGAA
643 AAGAAGTACA TAGACGAAGC CGGTCCGGCC AACTTCTTCG CCATCAAGAA
```

```
693 CAATACTTAT ATCACTCCCG AATCCAGCTC TATCCTGCCC TCTATCACAA
743 ACAAGAGTCT GATGCAGGTG GCTCAGGATC TGGGTCTGAA GGTAGAGCGT
793 CGTCCGGTAG CCGAAGAAGA GCTTGCTACT TTCGAAGAAG CAGGTGCTTG
843 TGGTACGGCA GCCGTGATCA GCCCTATCTC CGAGATTGAC GACTTGGAGA
893 ACAACAAACA GTACGTCATC AGCAAGGACG GCAAACCGGG TCCGTGGTGT
943 GAAAAGCTCT ATCACGAACT TCGTGCCATC CAGTATGGCG ACAAGCCCGA
993 CATTCATGGT TGGGTGACAA TCCTCGACTA A
```

> Amino acid sequence of N-terminal pETHis$_6$ PgIlvE Y188A

```
-19 MGSSHHHHHH SSGLVPRGSH MENIDWSSLS FGYRKTDYNV RCYYRNGKWG
 31 ELEVSSEETI TMHMAATCLH YGQEAFEGMK AFRGKDGKIR LFRMDENAKR
 81 MNRSCQGVVM AELPQEIFEA AVIKAVKMNE RFVPPYESGA SLYIRPLVIG
131 LGAQVGVKPA PEYLFIVFVT PVGPYFKEGF KPTKMAIFRD YDRAAPLGTG
181 TIKVGGNAAA GMIPTVKAHE MGYSAAIFLD AKEKKYIDEA GPANFFAIKN
231 NTYITPESSS ILPSITNKSL MQVAQDLGLK VERRPVAEEE LATFEEAGAC
281 GTAAVISPIS EIDDLENNKQ YVISKDGKPG PWCEKLYHEL RAIQYGDKPD
331 IHGWVTILD
```

(N-terminal His$_6$ tag in red, the mutated site in blue)

> DNA sequence of N-terminal pETHis$_6$PgIlvE F56A

```
-57 ATGGGCAGCA GCCATCATCA TCATCATCAC AGCAGCGGCC TGGTGCCGCG
 -7 CGGCAGCCCA TATGGAAAAT ATCGATTGGT CATCGCTCTC ATTCGGTTAT
 43 AGGAAGACCG ACTACAACGT GCGCTGTTAC TATCGCAACG GCAAGTGGGG
 93 AGAGCTTGAA GTATCCTCAG AGGAAACGAT CACGATGCAC ATGGCTGCCA
143 CTTGTCTCCA CTACGGACAG GAAGCAGCTG AAGGGATGAA GGCTTTCCGT
193 GGCAAAGATG GCAAGATCCG CCTCTTCCGC ATGGATGAGA ATGCCAAGCG
243 CATGAACAGA TCATGCCAAG GTGTGGTAAT GGCCGAGCTG CCGCAGGAAA
293 TCTTCGAAGC AGCTGTAATC AAGGCCGTAA AGATGAACGA GCGTTTCGTT
343 CCTCCTTACG AAAGCGGAGC TTCTCTTTAC ATCCGTCCGC TTGTTATCGG
393 ACTGGGTGCA CAAGTGGGTG TGAAGCCGGC TCCCGAGTAT CTCTTCATCG
443 TCTTTGTAAC GCCCGTAGGG CCGTATTTCA AAGAAGGATT CAAACCGACC
493 AAGATGGCCA TCTTCCGCGA CTATGACCGT GCAGCTCCTC TGGGTACGGG
543 TACGATCAAA GTGGGCGGTA ACTATGCAGC CGGTATGATC CCCACAGTGA
593 AAGCTCACGA AATGGGCTAC TCTGCAGCTA TCTTCTTGGA TGCCAAAGAA
643 AAGAAGTACA TAGACGAAGC CGGTCCGGCC AACTTCTTCG CCATCAAGAA
693 CAATACTTAT ATCACTCCCG AATCCAGCTC TATCCTGCCC TCTATCACAA
743 ACAAGAGTCT GATGCAGGTG GCTCAGGATC TGGGTCTGAA GGTAGAGCGT
793 CGTCCGGTAG CCGAAGAAGA GCTTGCTACT TTCGAAGAAG CAGGTGCTTG
843 TGGTACGGCA GCCGTGATCA GCCCTATCTC CGAGATTGAC GACTTGGAGA
893 ACAACAAACA GTACGTCATC AGCAAGGACG GCAAACCGGG TCCGTGGTGT
943 GAAAAGCTCT ATCACGAACT TCGTGCCATC CAGTATGGCG ACAAGCCCGA
993 CATTCATGGT TGGGTGACAA TCCTCGACTA A
```

> Amino acid sequence of N-terminal pETHis$_6$ PgIlvE Y188A

```
-19 MGSSHHHHHH SSGLVPRGSH MENIDWSSLS FGYRKTDYNV RCYYRNGKWG
 31 ELEVSSEETI TMHMAATCLH YGQEAAEGMK AFRGKDGKIR LFRMDENAKR
 81 MNRSCQGVVM AELPQEIFEA AVIKAVKMNE RFVPPYESGA SLYIRPLVIG
131 LGAQVGVKPA PEYLFIVFVT PVGPYFKEGF KPTKMAIFRD YDRAAPLGTG
181 TIKVGGNYAA GMIPTVKAHE MGYSAAIFLD AKEKKYIDEA GPANFFAIKN
231 NTYITPESSS ILPSITNKSL MQVAQDLGLK VERRPVAEEE LATFEEAGAC
281 GTAAVISPIS EIDDLENNKQ YVISKDGKPG PWCEKLYHEL RAIQYGDKPD
331 IHGWVTILD
```

(N-terminal His$_6$ tag in red, the mutated site in blue)

Publication

Research Reports: Biological

Journal of Dental Research
2020, Vol. 99(5) 568–576

DOI: 10.1177/0022034520908784
journals.sagepub.com/home/jdr

Porphyromonas gingivalis Sphingolipid Synthesis Limits the Host Inflammatory Response

F.G. Rocha[1*], Z.D. Moye[1*], G. Ottenberg[1*], P. Tang[2*], D.J. Campopiano[2†], F.C. Gibson III[1†], and M.E. Davey[1†]

Abstract

Porphyromonas gingivalis, like other bacteria belonging to the phylum Bacteroidetes, synthesizes sphingolipids (SLs). However, their exact roles in microbial physiology and their potential role in mediating interactions with their eukaryotic host are unclear. Our working hypothesis for this study was that synthesis of SLs (host-like lipids) affords a mechanism that allows *P. gingivalis* to persist in homeostasis with its host. In a previous study, we deleted a gene (PG1780 in strain W83) predicted to encode a serine palmitoyl transferase (SPT)— the enzyme that catalyzes the first conserved step in the synthesis of SLs—and we determined that the mutant was unable to synthesize SLs. Here, we characterized the SPT enzyme encoded by PG1780, analyzed the impact of SPT deletion on *P. gingivalis* gene expression (RNA-Seq analysis), and began to define the impact of SL synthesis on its interactions with host cells. Enzymatic analysis verified that the protein encoded by PG1780 is indeed an SPT. RNA-Seq analysis determined that a lack of SL synthesis results in differential expression of extracytoplasmic function sigma factors, components of the type IX secretion system (T9SS), and CRISPR and *cas* genes. Our data demonstrate that when human THP1 macrophage-like cells were challenged with the wild type (W83) and the SL-null mutant (W83 ⊗ SPT), the SL-null strain elicited a robust inflammatory response (elevated IL-1β, IL-6, IL-10, IL-8, RANTES, and TNFα) while the response to the parent strain W83 was negligible. Interestingly, we also discovered that SLs produced by *P. gingivalis* can be delivered to host cells independent of cell-to-cell contact. Overall, our results support our working hypothesis that synthesis of SLs by *P. gingivalis* is central to its ability to manipulate the host inflammatory response, and they demonstrate the integral importance of SLs in the physiology of *P. gingivalis*.

Keywords: homeostasis, Bacteroidetes, inflammation, dihydroceramides, membrane microdomains, sigma factors

Introduction

Sphingolipids (SLs) are a class of amphipathic lipids containing a long-chain amino alcohol backbone (also called a sphingoid base) attached via an amide linkage to a fatty acyl chain. The first committed step in the generation of SLs is the condensation of an amino acid, often serine, and palmitoyl CoA to form sphinganine by the enzyme serine palmitoyl transferase (SPT; Merrill and Carman 2015; Harrison et al. 2018). SLs play a prominent role in numerous eukaryotic cellular processes, including inflammation, cell migration, adhesion, growth, and apoptosis (Hannun and Obeid 2008, 2018; Maceyka and Spiegel 2014; Merrill and Carman 2015), and they have been linked to a growing number of inborn genetic diseases (Dunn et al. 2019).

While SL synthesis is ubiquitous in eukaryotes, it is rare in prokaryotes. Intriguingly, a variety of bacteria belonging to the phylum Bacteroidetes that persist in the oral microbiome, including *Porphyromonas gingivalis, Tannerella forsythia*, and *Prevotella intermedia*, are proficient in SL synthesis (Olsen and Jantzen 2001). Although SLs produced by these bacteria are highly similar to the host SLs, these lipids are distinct in their head groups and an isomethyl branch in the long chain base and ceramide component (Harrison et al. 2018.). Practically, these chemical distinctions are highly significant since they have been used to detect and distinguish bacterially derived SLs (Nichols et al. 2004; Brown et al. 2019). In particular, the SLs produced by oral anaerobes, including *P. gingivalis*, have been shown to permeate host tissues (Nichols 1998; Nichols and Rojanasomsith 2006; Nichols et al. 2011), and the types of SLs were found to be distinct in healthy versus diseased tissues (Nichols and Rojanasomsith 2006; Nichols

[1]Department of Oral Biology, College of Dentistry, University of Florida, Gainesville, FL, USA
[2]School of Chemistry, University of Edinburgh, Edinburgh, Scotland, UK
*Authors contributing equally to this article.
†Authors contributing equally to this article.

A supplemental appendix to this article is available online.

Corresponding Authors:
M.E. Davey, Department of Oral Biology, College of Dentistry, University of Florida, PO Box 100424, Gainesville, FL 32610, USA.
Email: mdavey@dental.ufl.edu
F.C. Gibson III, Department of Oral Biology, College of Dentistry, University of Florida, PO Box 100424, Gainesville, FL 32610, USA.
Email: fgibson@dental.ufl.edu

et al. 2011). Given that *P. gingivalis* is strongly implicated in the etiology of periodontal disease (Lamont and Jenkinson 1998; Socransky et al. 1998; Byrne et al. 2009; Darveau 2010), understanding the impact of SLs on the physiology of this bacterium as well as defining their impact on the host as purified lipids has been investigated (Moye et al. 2016; Olsen and Nichols 2018). Purified SLs derived from *P. gingivalis* induce a number of changes in the physiology of eukaryotic cells in vitro (Olsen and Nichols 2018), and often these effects are observed only for SLs bearing a particular headgroup. For example, phosphoglycerol dihydroceramides induce the RANKL-dependent pathway of osteoclastogenesis in osteoclasts (Kanzaki et al. 2017), initiate apoptosis in endothelial cells (Zahlten et al. 2007), and increase the generation of prostaglandin E2 by gingival fibroblasts (Nichols et al. 2004). In model systems of disease, phosphoethanolamine dihydroceramides induced inflammation in a murine model of experimental autoimmune encephalomyelitis (Nichols et al. 2009). Thus, SLs synthesized by *P. gingivalis* profoundly affect a variety of eukaryotic signaling pathways in a highly cell- and lipid-specific manner and may form a link to systemic conditions.

While there are few reports describing the role of bacterially derived SLs in bacterial physiology or membrane structure and function, the data indicate that they may function in similar ways as in eukaryotic cells (Heaver et al. 2018). Studies with *Bacteroides fragilis* have demonstrated the formation of SL-dependent membrane microdomains, similar to eukaryotic lipid rafts, and that SLs are essential for mounting a stress response and long-term survival, suggesting that SLs play a role in regulating gene expression (An et al. 2011). We recently demonstrated that SLs are essential for *P. gingivalis* survival under oxidative stress. Also, we determined that select SLs are present in outer membrane vesicles, thereby identifying a potential mechanism of SL secretion (Moye et al. 2016). Here, we define the enzyme kinetics of the SPT produced by *P. gingivalis* and describe a working model where SLs regulate gene expression via ECF sigma factors. Furthermore, we show a hyperinflammatory response of macrophage-like cells when cultured with the SL null mutant. Interestingly, we also discovered that *P. gingivalis* can deliver its SLs to host cells in a contact-independent manner. Overall, our studies exemplify the integral importance of SLs in the physiology of *P. gingivalis* and provide new evidence supporting the concept that, like other members of the Bacteroidetes, synthesis of SLs by *P. gingivalis* is likely central to its ability to manipulate the host inflammatory response.

Methods

See Appendix for details.

Purification and Characterization of SPT Enzyme

The PG1780 gene (strain W83) was cloned into expression plasmids that contained a C-terminal stop codon in lieu of a tag (PgSPT), a C-terminal 10-histidine tag (pEBSRCTE-VC_{10}HIS), or an N-terminal 6-histidine tag (pEHISTEV). Constructs were transformed into *Escherichia coli* BL21 (DE3)–competent cells. PgSPT was purified either by nickel affinity column chromatography (His-tagged) or by HiTrap anion exchange chromatography (nontagged), followed by gel filtration chromatography. Purification was monitored by SDS-PAGE and size characterized by LC-ESI-MS (liquid chromatography electrospray ionization mass spectrometry). Dissociation constants (K_d) were determined by ultraviolet-visible absorbance spectrophotometry. Kinetic experiments were performed with a 5,5′-dithiobis-2-nitrobenzoic acid (DTNB) assay, and resultant products were measured with MALDI-TOF-MS (matrix assisted laser desorption ionization-time of flight mass spectrometry).

RNA-Seq Analysis

P. gingivalis strain W83 was used in this study with the matching SPT mutant (W83 ⊗ PG1780), which was generated and characterized previously (Moye et al. 2016). RNA was extracted from cells grown anaerobically in TSBHK to OD_{600} of 1.0; then, the quality was assessed, and sequencing was performed and analyzed as previously described (Moradali et al. 2019; Moye et al. 2019).

Host Cell Cytokine/Chemokine Profiling

The human cell line THP-1 was maintained in RPMI-1640 + 10% FBS and differentiated for 48 h into macrophage-like cells with 100nM phorbol 12-myristate 13-acetate (PMA), and 5×10^5 cells were seeded into 24-well tissue culture plates. Parent or ⊗ SPT mutant *P. gingivalis* (cultured as stated earlier) was added to THP-1 cells (multiplicity of infection, 100). Following 2 h, 6 h, and 24 h of incubation, cell culture supernatant fluids were collected, and cytokine and chemokine levels were deter- mined by Milliplex Multiplex Assays with a Luminex 200 sys- tem. THP-1 cell viability was assessed by MTT assay.

P. gingivalis *SL Labeling and Tracking*

SL labeling was performed as previously described for *Bacteroides thetaiotaomicron* (Johnson et al. 2019) with slight modifications. Briefly, *P. gingivalis* strains were cultured for 24 h in rich medium and transferred into chemically defined medium (Vermilyea et al. 2019) supplemented with chemically modified palmitic acid containing an alkyne (PAA). PMA-differentiated THP-1 cells were placed in the bottom wells of 24-well plates containing sterile glass coverslips. Sterile 0.4-μm-pore Transwell inserts were placed into the wells of the cell culture dishes, and 1×10^9 bacteria were then placed in the upper chamber. After 24 h of culture at 37 °C + 5% CO_2, coverslips were removed, washed, and then click labeled with an azide 488 fluorophore per manufacturer specifications. Coverslips were mounted onto slides with a DAPI-containing medium and imaged by fluorescence microscopy. W83 parent and SPT mutant + PAA were click labeled directly to validate PAA incorporation and labeling only in the parent.

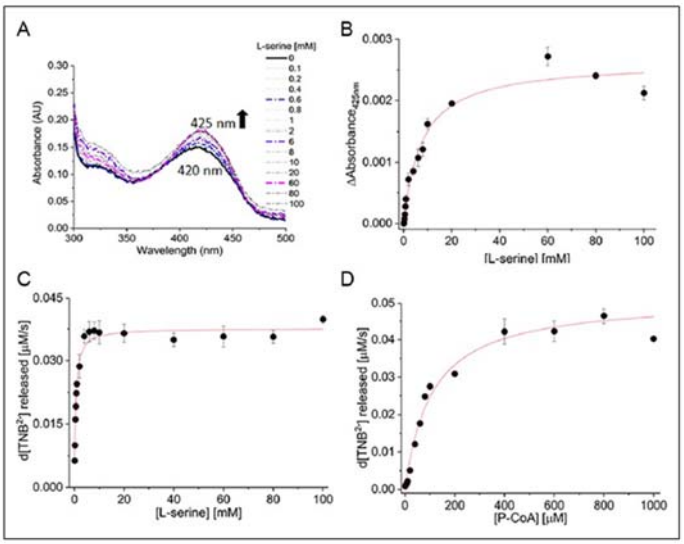

Figure 1. Characterization of recombinant *Porphyromonas gingivalis* serine palmitoyl transferase (SPT). (**A**) Absorption ultraviolet-visible spectrum of PLP-dependent (pyridoxal-5′phosphate) *P. gingivalis* SPT. Upon addition of L-serine, the enzyme (20 μM) converts from the internal aldimine to the external aldimine form, performed in 20mM potassium phosphate, 250mM NaCl, pH 7.5, at 25 °C. Solid line (0mM L-serine) or dashed lines in the presence of 0.1mM to 100mM L-serine. (**B**) Analysis of L-serine binding to C-terminal PgSPT by monitoring the change in absorbance at 425 nm. (**C**) Michaelis-Menten kinetic analysis of SPT with substrates L-serine (0.1 to 100 mM) and palmitoyl-CoA (250 μM) with 1 μM enzyme, 100mM HEPES, pH 7.0, 250mM NaCl, and 0.2mM DTNB and measured spectrophotometrically at 412 nm. (**D**) The concentration of L-serine (20 mM) with different palmitoyl-CoA concentrations (1 to 1000 μM). All data are plotted as mean readings ± 2-SD error bars.

Results

SPT Sequence Comparisons

All bacterial SPTs are members of the pyridoxal-5′phosphate (PLP)–dependent α-oxoamine synthase family, catalyzing Claisen-like condensation reactions between acyl-CoA substrates and amino acid to form different α-oxoamine products (Harrison et al. 2018). In the case of SPT, this would be ketodihydrosphingosine (KDS). The average amino acid sequence similarity across the α-oxoamine synthase enzymes is ~30% to 35%, depending on different functions (see Appendix Table 1 and Appendix Fig. 1A). The amino acid sequence alignment among *Sphingomonas paucimobilis* SPT (SpSPT, Q93UV0; Yard et al. 2007), *B. fragilis* SPT (BfSPT, Q5LCK4), and *P. gingivalis* SPT (PgSPT, W1R7E5) shows high sequence homology, with conservation of key residues involved in PLP binding and catalysis. Moreover, gut human microbial BfSPT shares the highest amino acid sequence identity (76%) with PgSPT.

Expression and Purification of Recombinant PgSPT

Recombinant PgSPT was prepared in a manner similar to that described for SpSPT (Yard et al. 2007; Raman et al. 2009). Briefly, the PgSPT gene (PG1780 from strain W83) was cloned and expressed in *E. coli* from plasmid pET-28a/PgSPT with a 6His-affinity tag at the C-terminus. A combined HisTrap column and size-exclusive chromatography (Sephadex HR S200; GE Healthcare) approach was used to isolate the dimeric PLP-bound holoform of the enzyme, and 10% glycerol was added to avoid PgSPT precipitation. The purity of the protein was assessed by SDS-PAGE (Appendix Fig. 1B).

Spectroscopic Properties of C′ Terminal-Tagged PgSPT

The ultraviolet-visible spectrum of a PLP-dependent enzyme such as SPT usually shows 2 absorption maxima at 335 nm and 425 nm, due to the properties of the 2 forms of the internal aldimine PLP Schiff base: enolimine and ketoenamine. In contrast to the SpSPT enzyme, the ultraviolet-visible spectrum of PgSPT displays an absorbance maximum at 425 nm, suggesting that the PLP cofactor was present predominantly as the ketoenamine form (Fig. 1A). By analyzing the change in the absorbance at 425 nm with varying changes in the concentration of L-serine, the dissociation constant (K_d^{Ser}) was determined to be 5.46 ± .60 mM (Fig. 1B). This value is approximately 5 times weaker than that determined for SpSPT (K_d^{Ser} = 1.1 mM; Raman et al. 2009).

C′ Terminal PgSPT Activity and Kinetics

To find the optimal conditions for PgSPT activity, the enzyme was initially tested in buffers of different pH, and the highest reaction rate was observed in 100mM HEPES at pH 7.0. Here we used a convenient coupled assay that uses DTNB reagent that reacts with the CoASH product. The resulting TNB thiolate anion absorbs strongly at 412 nm (ε_{max} = 14,150 $M^{-1}cm^{-1}$; Raman et al. 2009). The enzyme was analyzed with both substrates, L-serine and palmitoyl-CoA, to obtain the kinetic parameters, and the Michaelis-Menten plot for C′ terminal His-tagged PgSPT (Fig. 1C, D) showed that the enzyme bound L-serine and palmitoyl-CoA, with K_m values of 0.52 ± .06 mM and 84 ± 11.7 μM, respectively. The enzyme turned over with a k_{cat} of 43.5 ± 0.4 × 10^{-3} s^{-1} and an efficiency (k_{cat}/K_m) of 84.6 $M^{-1}s^{-1}$ for L-serine and 524 M^{-1} s^{-1} for pimeloyl-CoA. This compares to similar values determined for SpSPT with respect to substrate binding but with the PgSPT turning over much slower.

Identification of KDS Formation by PgSPT

Since the kinetic assay is indirect and measures only CoASH release, we confirmed that PgSPT catalyzed conversion of

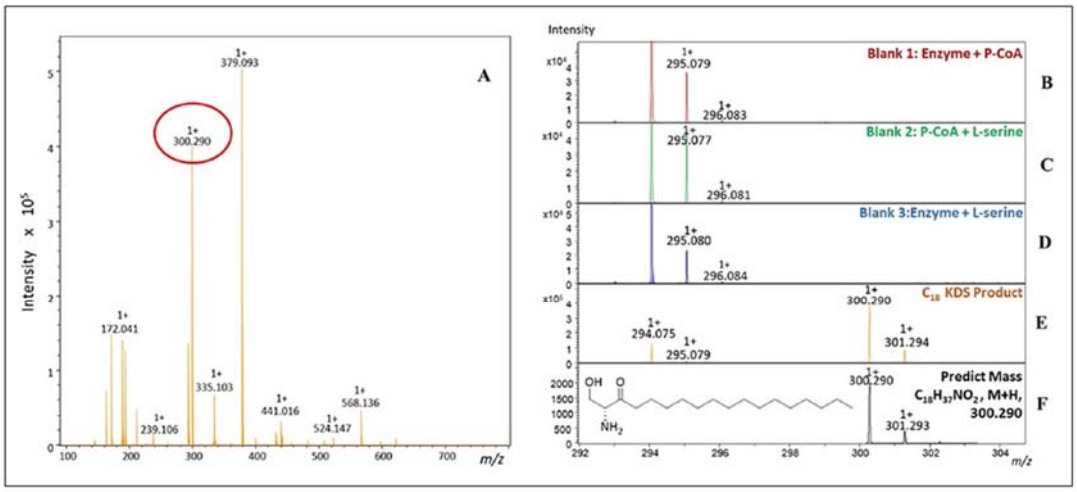

Figure 2. MALDI-ToF (matrix assisted laser desorption ionization-time of flight) mass spectra analysis of the PgSPT (*Porphyromonas gingivalis* serine palmitoyl transferase) reaction between L-serine and palmitoyl-CoA. Each assay, which contained 1 μM enzyme, 100mM HEPES, pH 7.0, 250mM NaCl, 0.2mM 5,5′-dithiobis-2-nitrobenzoic acid, and 20mM L-serine or 250μM palmitoyl-CoA, was added dependent on samples. All reaction samples were eluted with 100% acetonitrile (ACN) by C4 zip-tip and mixed with α-Cyano-4-hydroxycinnamic acid matrix dissolved in 50% ACN within 0.25% trifluoroacetic acid. The spectrum was analyzed on positive ion mode in triplicates. (**A**) Observation of the product ketodihydrosphingosine (KDS) with m/z = 300.290 during a sweep of masses (m/z = 100 to 800 amu). (**B–D**) Negative controls. (**E**) Full assay with PgSPT, L-serine, and P-CoA with a mass range of m/z = 292 to 304. (**F**) Theoretical mass spectrum based on the KDS formula (M+H)+.

L-serine and palmitoyl-CoA to the product KDS. For this, we used MALDI-TOF MS analysis of the PgSPT assay to detect the formation of the molecular ion related to the product C18:0 KDS $[C_{18}H_{37}NO_2,\ M+H]^+$ (m/z 300.290; Fig. 2A). A series of controls (Fig. 2B–D) confirmed that the KDS was formed only in the presence of the enzyme and both substrates.

RNA-Seq Analysis

The rigid structural characteristic of SLs serves an important functional role in eukaryotic cells by condensing around signaling proteins in the cell membrane and forming densely packed regions of the membrane known as lipid rafts. These puncta of closely associated lipids and proteins are thought to increase the efficiency of cellular signaling pathways by bringing signaling proteins into close proximity. This information led us to hypothesize that a SL-null mutant may possess a defect in gene expression. Transcriptomic analysis of the SL-null strain in comparison with the parent strain identified 120 genes that were differentially expressed (≥2-fold, q value <0.01). Of the 120 genes, the expression of 61 genes was lower while expression of 59 genes was higher. Most notably, 3 extracytoplasmic function (ECF) sigma factors were found to be differentially expressed: 1 gene (PG0985) was 3.2-fold lower while the other 2 (PG0162 and PG0214) were expressed 2.2- and 6.1-fold higher, respectively. In addition, the data show that all of the genes harbored in 2 distinct loci encoding CRISPR-associated genes (PG1981-PG1989 and PG2013-PG2020) were lower, while genes encoding type IX secretion structural and cargo proteins were among the most overexpressed. As expected, numerous genes encoding hypothetical proteins were differentially expressed (23 reduced and 21 overexpressed; Tables 1 and 2).

Synthesis of SLs by P. gingivalis Limits the Host Capacity to Mount a Robust Proinflammatory Response

To examine the contribution of SL synthesis to the host inflammatory response, we cultured macrophage-like THP-1 cells with *P. gingivalis* wild type (WT) and the corresponding SPT mutant for up to 24 h and measured cytokine and chemokine levels. THP-1 is a transformed cell line of human origin. It is a frequently used model cell for investigating macrophage function, a cell that is central to periodontal disease. Our data show that THP-1 cells cultured with the SPT mutant produced a robust immune response that was not observed from cells cultured with the WT (Fig. 3). Even as rapidly as 2 h after initiation of coculture, significant increases in the levels of TNF-α, IL-1β, and IL-10 were measured from the cultures infected with the SL-null mutant as compared with those elicited by parent W83 ($P < 0.05$ for all by t test). By 6 h, the signature of elevated inflammation initiated by the SPT mutant accelerated, with the addition of a significant increase in IL-6 and RANTES also observed (Fig. 3). The trend of lower cytokine and chemokine production in response to the WT remained evident at 24 h of

Table 1. Genes Expressed at Lower Levels in the SPT Mutant versus the Parent Strain W83.

Name	Gene ID	Product	Q Value	Fold Change
SPT	PG1780	Serine palmitoyltransferase	0	0.01
Proteolysis and amino acid metabolism				
pepD-2	PG0537	Aminoacyl-histidine dipeptidase	1.30E-216	0.17
pruA	PG1269	Delta-1-pyrroline-5-carboxylate dehydrogenase	2.01E-35	0.38
—	PG1270	PLP-dependent aminotransferase	3.38E-35	0.37
—	PG1271	Acetylornithine aminotransferase	2.92E-13	0.38
Transposon				
—	PG0549	ISPg1, transposase	4.72E-19	0.45
—	PG0872	Mobilizable transposon, Xis protein	1.20E-09	0.50
—	PG1480	Conjugative transposon protein TraI	1.68E-07	0.50
—	PG1482	Conjugative transposon protein TraF	1.62E-13	0.33
—	PG1483	Conjugative transposon protein TraE	6.11E-11	0.50
Hypothetical				
—	PG0354	Hypothetical protein	1.26E-07	0.50
—	PG0554	Hypothetical protein	7.25E-13	0.46
—	PG0609	Hypothetical protein	6.13E-15	0.50
—	PG0617	Hypothetical protein	7.14E-14	0.41
—	PG0727	Hypothetical protein	7.89E-57	0.28
—	PG0835	Hypothetical protein	2.58E-26	0.33
—	PG0914	Hypothetical protein	1.54E-29	0.40
—	PG0986	Hypothetical protein	4.38E-24	0.37
—	PG0987	Hypothetical protein	1.42E-125	0.21
—	PG1229	Hypothetical protein	1.68E-09	0.50
—	PG1268	Hypothetical protein	1.54E-53	0.32
—	PG1494	Hypothetical protein	5.30E-05	0.50
—	PG1508	Hypothetical protein	0.003359	0.35
—	PG1510	Hypothetical protein	1.57E-21	0.40
—	PG1511	Hypothetical protein	2.39E-21	0.37
—	PG1512	Hypothetical protein	2.21E-18	0.36
—	PG1516	Hypothetical protein	2.53E-06	0.48
—	PG1547	Hypothetical protein	7.02E-06	0.50
—	PG1549	Hypothetical protein	4.25E-17	0.33
—	PG1795	Hypothetical protein	0.005	0.38
—	PG1798	Hypothetical protein	1.79E-12	0.44
—	PG1871	Hypothetical protein	7.38E-05	0.33
—	PG1908	Hypothetical protein	2.23E-04	0.44
CRISPR loci				
cas2-1	PG1981	CRISPR-associated Cas2 family protein	2.67E-11	0.42
—	PG1982	CRISPR-associated Cas1 family protein	2.27E-12	0.44
—	PG1983	CRISPR-associated Cmr5 family protein	2.25E-06	0.50
—	PG1984	Hypothetical protein	1.27E-19	0.33
—	PG1985	CRISPR-associated Cmr4 family protein	1.13E-20	0.42
—	PG1986	CRISPR-associated Cmr3 family protein	2.10E-32	0.35
—	PG1987	CRISPR-associated Csm1 family protein	4.80E-30	0.29
—	PG1988	Hypothetical protein	2.31E-40	0.24
—	PG1989	Hypothetical protein	6.29E-65	0.27
cas2-2	PG2013	CRISPR-associated Cas2 family protein	2.73E-12	0.47
cas1	PG2014	CRISPR-associated Cas1 family protein	5.31E-31	0.39
cas4	PG2015	CRISPR-associated Cas4 family protein	1.92E-26	0.40
cas3	PG2016	CRISPR-associated helicase Cas3	5.50E-09	0.33
—	PG2017	Hypothetical protein	4.44E-14	0.33
—	PG2018	Hypothetical protein	3.10E-11	0.33
—	PG2019	Hypothetical protein	6.56E-22	0.31
	PG2020	CRISPR-associated Cas5e family protein	?	0.39
Redox homeostasis				
—	PG0616	Thioredoxin	0.003	0.38
Cell wall				
—	PG0726	Putative lipoprotein, s-layer	8.42E-08	0.25
Transcription				
—	PG0985	ECF subfamily RNA polymerase sigma factor	3.41E-68	0.29
—	PG1535	Transcriptional regulator	1.88E-10	0.50
Metabolism				
hprA	PG1190	Glycerate dehydrogenase	8.69E-12	0.49
—	PG1504	NAD dependent protein	0.009	0.33
—	PG1509	HAD superfamily hydrolase	3.63E-24	0.34
Biosynthesis of cofactors	PG1514	Glycerol dehydrogenase	3.16E-11	0.44
—	PG1505	Ribulose-5-phosphate-4-epimerase protein	3.08E-15	0.32

SPT, serine palmitoyl transferase.

Table 2. Genes Expressed at Higher Levels in the SPT Mutant versus the Parent Strain W83.

Name	Gene ID	Product	Q Value	Fold Change
Type IX secretion system	PG0027	Hypothetical protein	1.81E-28	2.83
—				
porP	PG0287	Hypothetical protein porP	3.33E-56	2.58
porK	PG0288	Putative lipoprotein porK	1.24E-32	2.65
porL	PG0289	Hypothetical protein porL	1.14E-40	2.56
porM	PG0290	Hypothetical protein porM	8.78E-20	2.21
porN	PG0291	Hypothetical protein porN	2.53E-29	2.58
porT	PG0751	porT protein	8.54E-30	2.00
sov	PG0809	Hypothetical protein	3.61E-10	2.10
	PG0810	Hypothetical protein	4.20E-55	2.60
tpr	PG1055	Thiol protease	0	8.00
—	PG1947	Hypothetical protein	1.48E-17	2.00
TapA	PG2100	TapA	0	10.88
TapB	PG2101	TapB	0	20.33
TapC	PG2102	TapC	0	20.33
Hypothetical and other				
ispF	PG0028	2-C-methyl-D-erythritol 2,4-cyclodiphosphate synthase	1.19E-28	2.20
—	PG0161	Hypothetical protein	1.58E-134	3.34
—	PG0216	Hypothetical protein	1.49E-182	4.80
—	PG0217	Hypothetical protein	1.57E-298	4.69
—	PG0218	Hypothetical protein	0	5.00
—	PG0241	Putative lipoprotein	2.60E-05	2.07
—	PG0297	Hypothetical protein	1.52E-18	2.00
—	PG0323	Hypothetical protein	2.96E-36	2.31
—	PG0419	Hypothetical protein	7.47E-20	2.27
—	PG0606	Hypothetical protein	2.13E-29	2.25
—	PG0607	Hypothetical protein	3.11E-13	2.44
clpB	PG1118	clpB protein	9.12E-23	2.28
—	PG1374	Hypothetical protein	6.87E-16	2.51
—	PG1527	Hypothetical protein	1.39E-19	2.00
—	PG1571	Metallo-beta-lactamase superfamily protein	5.44E-10	2.00
—	PG1625	Hypothetical protein	1.62E-11	2.17
—	PG1626	Hypothetical protein	3.75E-17	2.32
—	PG1634	Hypothetical protein	3.84E-20	2.16
—	PG1662	Hypothetical protein	7.73E-27	2.12
—	PG1682	Glycosyl transferase	8.04E-54	2.44
—	PG1683	Hypothetical protein	2.03E-26	2.10
—	PG1684	Hypothetical protein	5.65E-42	3.20
udk	PG1781	Uridine kinase	2.11E-30	2.30
—	PG1835	Putative lipoprotein	3.05E-10	2.12
aroA	PG1944	3-phosphoshikimate 1-carboxyvinyltransferase	1.40E-20	2.04
—	PG1945	Hypothetical protein	3.76E-34	2.31
—	PG1967	Hypothetical protein	2.07E-34	2.33
—	PG2103	Hypothetical protein	1.68E-37	2.30
Transport				
—	PG0064	CzcA family heavy metal efflux protein	3.76E-42	2.29
—	PG0280	ABC transporter permease	1.97E-11	2.00
—	PG0281	ABC transporter permease	2.05E-14	2.00
—	PG0282	ABC transporter ATP-binding protein	4.46E-13	3.00
—	PG0680	RND family efflux transporter MFP subunit	3.77E-07	2.00
—	PG1010	ABC transporter ATP-binding protein	5.74E-33	2.00
—	PG1117	MATE efflux family protein	1.10E-07	2.00
—	PG1176	ABC transporter ATP-binding protein	0.001661967	2.00
—	PG1663	ABC transporter ATP-binding protein	6.34E-34	2.05
—	PG1664	ABC transporter permease	2.07E-33	2.11
—	PG1665	ABC transporter permease	3.06E-24	2.00
—	PG1946	ABC transporter	1.56E-25	2.25
Transcription				
—	PG0162	ECF subfamily RNA polymerase sigma factor	4.84E-10	2.10
—	PG0214	ECF subfamily RNA polymerase sigma factor	0	5.87
—	PG0215	Putative anti-sigma factor	1.25E-199	4.46
—	PG1007	GntR family transcriptional regulator	9.11E-24	2.10

SPT, serine palmitoyl transferase.

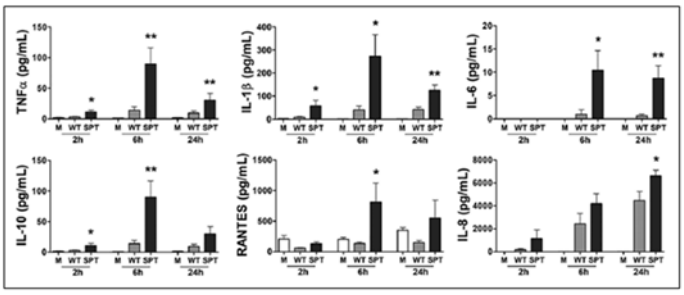

Figure 3. The inability of *Porphyromonas gingivalis* to synthesize sphingolipids (SLs) leads to an enhanced cytokine and chemokine response. PMA-treated human macrophage–like THP-1 cells were directly cultured with *P. gingivalis* W83 (wild type [WT]; gray bars) or the *P. gingivalis* W83 SL-null mutant (serine palmitoyl transferase [SPT]; black bars) at a multiplicity of infection of 100. Cell culture supernatant fluids were collected at 2, 6, and 24 h of coculture, and the levels of TNFα, IL-1β, IL-6, IL-10, RANTES, and IL-8 were measured by multiplex immunoassay. Medium alone (M; white bars) served as unchallenged control. Data are presented as mean ± SEM ($n = 8$ independent experiments). *$P < 0.05$ and **$P < 0.01$ versus wild type (WT) *P. gingivalis* with unpaired *t* tests. PMA, phorbol 12-myristate 13-acetate.

coculture but trended lower than observed at 6 h. No significant differences in THP-1 cell viability was observed between cells cultured with SPT mutant and WT per the MTT assay ($P > 0.05$ by analysis of variance; Appendix Table 2). These findings support our hypothesis that in the context of live bacteria, synthesis of SLs limits and/or suppresses the host capacity to mount a robust proinflammatory response to this organism.

Transfer of SLs from P. gingivalis *to THP-1 Cells in a Transwell System*

Last, we assessed whether SLs could be transferred from *P. gingivalis* to THP-1 macrophages. By employing a 0.4-µm-pore Transwell system, metabolically labeled *P. gingivalis* (grown in the presence of PAA to allow for specific click labeling of SLs with a fluorophore) were placed in the upper well of the Transwell, with THP-1 cells placed in the lower well. After 24 h of Transwell coculture, click chemistry verified that *P. gingivalis* SLs were transferred to THP-1 cells without physical contact (Fig. 4).

Discussion

P. gingivalis can be present in subgingival plaque even during periodontal health (Griffen et al. 1998), suggesting that the host does not always respond to this bacterium as a pathogen. While other members of the phylum Bacteroidetes, in particular members of the genus *Bacteroides*, are viewed as symbiotic or pathobionts, this framework of a symbiotic relationship with the host is not typically applied to *P. gingivalis*. Our view of *P. gingivalis* as a pathobiont (Cugini et al. 2013) led us to consider its unusual ability to synthesize lipids almost identical to its host as a strategy to evade host immune activation.

To evaluate function, gene PG1780, encoding a predicted SPT, was cloned, and the recombinant protein was isolated, characterized, and confirmed as an SPT (PgSPT) by determining the kinetics of the reaction with the canonical substrates L-serine and palmitoyl-CoA. Formation of the KDS product was confirmed by MALDI-TOF-MS analysis. This allowed a comparison with another well-characterized bacterial SpSPT from *S. paucimobilis* (Harrison et al. 2019). The PgSPT bound both substrates with a similar affinity to SpSPT, but in contrast to this isoform, PgSPT displayed much slower kinetics. The molecular details of these differences may be revealed by a comparative x-ray structural analysis, and to that end, crystal trials of PgSPT enzyme are underway. Once the protein structure is known, a comparative evolutionary study of the microbial SPTs will be carried out to explore the species-specific features of the bacterial and eukaryotic SPTs (Harrison et al. 2018; Heaver et al. 2018).

Lipid microdomains are known to position proteins associated with signal transduction, membrane trafficking (protein secretion systems), and regulation of metabolism (protease complexes) in close proximity (Bramkamp and Lopez 2015; Lopez 2015). It is tempting to speculate that a subset of the SLs may support T9SS machinery, given their known function in protein secretion systems. Furthermore, our RNA-Seq analysis indicates that SLs may indeed stabilize certain proteins involved in signal transduction, in particular sequestration of antisigma factors. Antisigma factors are known to be localized to the inner membrane, where they bind their target ECF sigma factors, preventing transcription. Our working model is that, when SLs are not produced, the targets are overexpressed because the ECF sigma factors are free to interact with target promoters. Some T9SS genes have been shown to be regulated via ECF sigma factors, and we identified 14 T9SS genes that are expressed at higher levels in the SPT mutant, some as much as 20-fold. Importantly, the genes encoding gingipains were not differentially expressed in the mutant. Our prior studies showed that the SL-null mutant actually demonstrated elevated secreted gingipain activity, not less, suggesting that the higher levels of cytokines are not due to a lack of gingipain activity. That being said, since these proteases are proficient at degrading cytokines, studies are ongoing to further evaluate a link between SL synthesis and secreted gingipain activity.

Our cell infection modeling shows that SL synthesis leads to a reduced inflammatory response, suggesting that synthesis supports homeostasis. This discovery in some ways contradicts published results. Prior studies with purified *P. gingivalis* SLs point to TLR-2-inducing activity (Nichols et al. 2009), stimulation of cellular inflammatory responses (Nichols et al. 2001), and driving of apoptosis (Zahlten et al. 2007). Yet, our findings

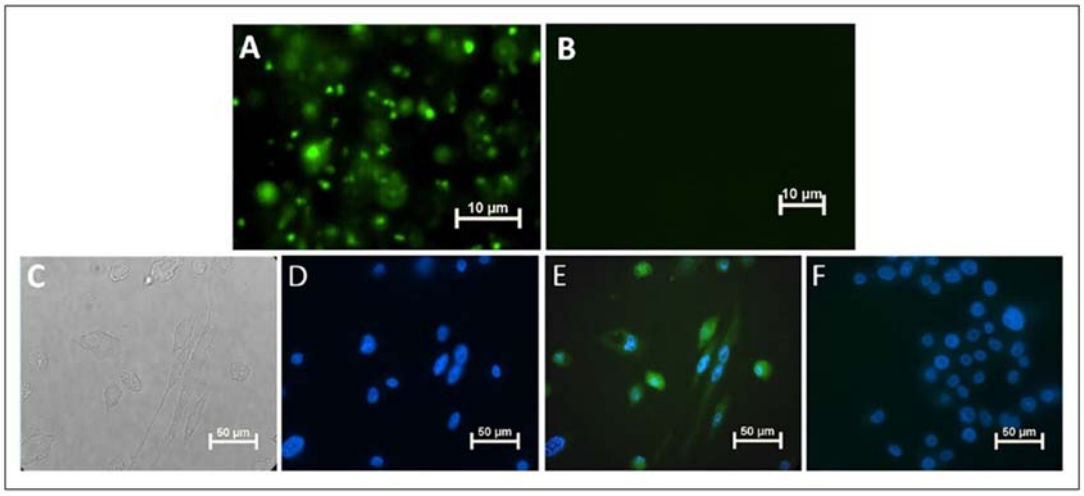

Figure 4. Sphingolipids transfer from *Porphyromonas gingivalis* to THP-1 cells in a Transwell system. (**A**) Epifluorescent image of wild-type W83 bacterial cells shows detection of palmitic acid alkyne (PAA) when bacteria were grown with addition of PAA (green–azide Fluor 488) by click chemistry. (**B**) As expected, the serine palmitoyl transferase–null mutant did not incorporate PAA. (**C**) Bright field image of THP-1 cells on cover slip in the lower well of a Transwell system after 24-h coculture with strain W83. (**D**) Epifluorescent image of the same THP-1 cells shows DAPI (blue) staining of nucleus, and (**E**) THP-1 cells incorporated the *P. gingivalis* alkyne-tagged sphingolipids (green) that were transferred from W83 constrained to the upper well of the Transwell system. (**F**) Click labeling of THP-1 cells cocultured with W83 grown in medium without PAA via the Transwell system; no green–azide Fluor 488 was detected.

parallel studies on SL function in other members of the Bacteroidetes phylum that strongly support a role for SLs in immune suppression (An et al. 2011; An et al. 2014; Heaver et al. 2018; Brown et al. 2019). Specifically, one study reported an inverse relationship between SL synthesis by *Bacteroides* and inflammatory bowel disease, indicating that bacterial SLs can serve as key factors that mechanistically promote intestinal homeostasis (Brown et al. 2019). As gingival tissues from periodontally healthy and diseased individuals contain SLs and yet the SL types are distinct, our working model has been that, not only does SL synthesis play a central role in membrane trafficking in *P. gingivalis*, but the secreted SLs may also directly influence host cell function. Our in vitro findings agree with clinical findings that *P. gingivalis* releases and/or secretes its SLs; moreover, our findings support that *P. gingivalis* SLs are transferred to host cells. This later discovery is particularly compelling, as transfer of SLs from bacteria to host suggests an intriguing interplay, which may serve an important role by which host and microbe interact and which in turn may control oral inflammation, as shown for *B. thetaiotaomicron* in the gut (Johnson et al. 2019). Last, our results show that the absence of SLs elicited high levels of proinflammatory cytokines, as well as IL-10, a highly expressed anti-inflammatory cytokine. Our findings of the presence of pro- and anti-inflammatory cytokines occurring concurrently is not fully understood; however, these results are consistent with clinical profiles observed in inflamed periodontal tissues. The ultimate outcome of this unusual inflammatory pattern requires further evaluation.

In summary, *P. gingivalis* is often described as a master manipulator of the immune response (Hajishengallis and Lamont 2014), primarily due to its ability to degrade immunoglobulins, complement, and cytokines via its repertoire of secreted proteases (Hajishengallis and Lambris 2012). We posit that SL synthesis is another mechanism of control. Future studies testing these findings in the context of periodontal disease may identify novel approaches to control SL production by *P. gingivalis* and thus shift the balance of inflammation elicited by the subgingival biofilm to a more homeostatic state.

Author Contributions

F.G. Rocha, Z.D. Moye, F.C. Gibson III, M.E. Davey, contributed to conception, design, data acquisition, analysis, and interpretation, drafted and critically revised the manuscript; G. Ottenberg, contributed to data acquisition, analysis, and interpretation, drafted and critically revised the manuscript; P. Tang, D.J. Campopiano, contributed to data acquisition, analysis, and interpretation, critically revised the manuscript. All authors gave final approval and agree to be accountable for all aspects of the work.

Acknowledgments

The authors thank the School of Chemistry, University of Edinburgh, and the Edinburgh Global Research Scholarship for PhD studentship funding (P.T.). The authors also thank Dr. Peter Harrison, Dr. Bohdan Mykhaylyk, Dr. Jo Simpson, and Dr. Van Kelly for helpful discussion on SPT, as well as all members of the Davey laboratory for many helpful discussions on SLs. The

research was supported by the National Institute of Craniofacial Research (R01DE019117 and R01DE24580 to M.E.D.; T90 DE021990 to Z.D.M. and F.G.R.; R90 DE22530 to F.G.R.) as well as start-up funds (to F.C.G. and M.E.D.). The authors declare no potential conflicts of interest with respect to the authorship and/or publication of this article.

References

An D, Na C, Bielawski J, Hannun YA, Kasper DL. 2011. Membrane sphingolipids as essential molecular signals for *Bacteroides* survival in the intes- tine. Proc Natl Acad Sci U S A. 108 Suppl 1:4666–4671.

An D, Oh SF, Olszak T, Neves JF, Avci FY, Erturk-Hasdemir D, Lu X, Zeissig S, Blumberg RS, Kasper DL. 2014. Sphingolipids from a symbiotic microbe regulate homeostasis of host intestinal natural killer T cells. Cell. 156(1–2):123–133.

Bramkamp M, Lopez D. 2015. Exploring the existence of lipid rafts in bacteria. Microbiol Mol Biol Rev. 79(1):81–100.

Brown EM, Ke X, Hitchcock D, Jeanfavre S, Avila-Pacheco J, Nakata T, Arthur TD, Fornelos N, Heim C, Franzosa EA, et al. 2019. *Bacteroides*-derived sphingolipids are critical for maintaining intestinal homeostasis and symbiosis. Cell Host Microbe. 25(5):668–680.e7.

Byrne SJ, Dashper SG, Darby IB, Adams GG, Hoffmann B, Reynolds EC. 2009. Progression of chronic periodontitis can be predicted by the levels of *Porphyromonas gingivalis* and *Treponema denticola* in subgingival plaque. Oral Microbiol Immunol. 24(6):469–477.

Cugini C, Klepac-Ceraj V, Rackaityte E, Riggs JE, Davey ME. 2013. *Porphyromonas gingivalis*: keeping the pathos out of the biont. J Oral Microbiol. 5:19804.

Darveau RP. 2010. Periodontitis: a polymicrobial disruption of host homeosta- sis. Nat Rev Microbiol. 8(7):481–490.

Dunn TM, Tifft CJ, Proia RL. 2019. A perilous path: the inborn errors of sphingolipid metabolism. J Lipid Res. 60(3):475–483.

Griffen AL, Becker MR, Lyons SR, Moeschberger ML, Leys EJ. 1998. Prevalence of *Porphyromonas gingivalis* and periodontal health status. J Clin Microbiol. 36(11):3239–3242.

Hajishengallis G, Lambris JD. 2012. Complement and dysbiosis in periodontal disease. Immunobiology. 217(11):1111–1116.

Hajishengallis G, Lamont RJ. 2014. Breaking bad: manipulation of the host response by *Porphyromonas gingivalis*. Eur J Immunol. 44(2):328–338.

Hannun YA, Obeid LM. 2008. Principles of bioactive lipid signalling: lessons from sphingolipids. Nat Rev Mol Cell Biol. 9(2):139–150.

Hannun YA, Obeid LM. 2018. Sphingolipids and their metabolism in physiology and disease. Nat Rev Mol Cell Biol. 19(3):175–191.

Harrison PJ, Dunn TM, Campopiano DJ. 2018. Sphingolipid biosynthesis in man and microbes. Nat Prod Rep. 35(9):921–954.

Harrison PJ, Gable K, Somashekarappa N, Kelly V, Clarke DJ, Naismith JH, Dunn TM, Campopiano DJ. 2019. Use of isotopically labeled substrates reveals kinetic differences between human and bacterial serine palmi- toyltransferase. J Lipid Res. 60(5):953–962. Erratum in: J Lipid Res. 2019;60(8):1489.

Heaver SL, Johnson EL, Ley RE. 2018. Sphingolipids in host-microbial interactions. Curr Opin Microbiol. 43:92–99.

Johnson EL, Heaver SL, Waters JL, Kim BI, Bretin A, Goodman AL, Gewirtz AT, Worgall TS, Ley RE. 2019. Sphingolipid production by gut Bacteroidetes regulates glucose homeostasis. bioRxiv. doi:10.1101/632877

Kanzaki H, Movila A, Kayal R, Napimoga MH, Egashira K, Dewhirst F, Sasaki H, Howait M, Al-Dharrab A, Mira A, et al. 2017. Phosphoglycerol dihydroceramide, a distinctive ceramide produced by *Porphyromonas gingivalis*, promotes RANKL-induced osteoclastogenesis by acting on non-muscle myosin II-A (Myh9), an osteoclast cell fusion regulatory factor. Biochim Biophys Acta Mol Cell Biol Lipids. 1862(5):452–462.

Lamont RJ, Jenkinson HF. 1998. Life below the gum line: pathogenic mechanisms of *Porphyromonas gingivalis*. Microbiol Mol Biol Rev. 62(4):1244–1263.

Lopez D. 2015. Molecular composition of functional microdomains in bacterial membranes. Chem Phys Lipids. 192:3–11.

Maceyka M, Spiegel S. 2014. Sphingolipid metabolites in inflammatory dis- ease. Nature. 510(7503):58–67.

Merrill AH Jr, Carman GM. 2015. Introduction to thematic minireview series: novel bioactive sphingolipids. J Biol Chem. 290(25):15362–15364.

Moradali MF, Ghods S, Angelini TE, Davey ME. 2019. Amino acids as wetting agents: surface translocation by *Porphyromonas gingivalis*. ISME J. 13(6):1560–1574.

Moye ZD, Gormley CM, Davey ME. 2019. Galactose impacts the size and intracellular composition of the asaccharolytic oral pathobiont *Porphyromonas gingivalis*. Appl Environ Microbiol. 85(4):e02268-18.

Moye ZD, Valiuskyte K, Dewhirst FE, Nichols FC, Davey ME. 2016. Synthesis of sphingolipids impacts survival of *Porphyromonas gingivalis* and the presentation of surface polysaccharides. Front Microbiol. 7:1919.

Nichols FC. 1998. Novel ceramides recovered from *Porphyromonas gingivalis*: relationship to adult periodontitis. J Lipid Res. 39(12):2360–2372.

Nichols FC, Housley WJ, O'Conor CA, Manning T, Wu S, Clark RB. 2009. Unique lipids from a common human bacterium represent a new class of toll-like receptor 2 ligands capable of enhancing autoimmunity. Am J Pathol. 175(6):2430–2438.

Nichols FC, Levinbook H, Shnaydman M, Goldschmidt J. 2001. Prostaglandin e2 secretion from gingival fibroblasts treated with interleukin-1beta: effects of lipid extracts from *Porphyromonas gingivalis* or calculus. J Periodontal Res. 36(3):142–152.

Nichols FC, Riep B, Mun J, Morton MD, Bojarski MT, Dewhirst FE, Smith MB. 2004. Structures and biological activity of phosphorylated dihydro- ceramides of *Porphyromonas gingivalis*. J Lipid Res. 45(12):2317–2330.

Nichols FC, Rojanasomsith K. 2006. *Porphyromonas gingivalis* lipids and diseased dental tissues. Oral Microbiol Immunol. 21(2):84–92.

Nichols FC, Yao X, Bajrami B, Downes J, Finegold SM, Knee E, Gallagher JJ, Housley WJ, Clark RB. 2011. Phosphorylated dihydroceramides from common human bacteria are recovered in human tissues. PLoS One. 6(2):e16771.

Olsen I, Jantzen E. 2001. Sphingolipids in bacteria and fungi. Anaerobe. 7(2):103–112.

Olsen I, Nichols FC. 2018. Are sphingolipids and serine dipeptide lipids underestimated virulence factors of *Porphyromonas gingivalis*? Infect Immun. 86(7):e00035-18.

Raman MC, Johnson KA, Yard BA, Lowther J, Carter LG, Naismith JH, Campopiano DJ. 2009. The external aldimine form of serine palmitoyl- transferase: structural, kinetic, and spectroscopic analysis of the wild-type enzyme and HSAN1 mutant mimics. J Biol Chem. 284(25):17328–17339.

Socransky SS, Haffajee AD, Cugini MA, Smith C, Kent RL Jr. 1998. Microbial complexes in subgingival plaque. J Clin Periodontol. 25(2):134–144.

Vermilyea DM, Ottenberg GK, Davey ME. 2019. Citrullination mediated by PPAD constrains biofilm formation in *P. gingivalis* strain 381. NPJ Biofilms Microbiomes. 5:7.

Yard BA, Carter LG, Johnson KA, Overton IM, Dorward M, Liu H, McMahon SA, Oke M, Puech D, Barton GJ, et al. 2007. The structure of serine palmitoyltransferase; gateway to sphingolipid biosynthesis. J Mol Biol. 370(5):870–886.

Zahlten J, Riep B, Nichols FC, Walter C, Schmeck B, Bernimoulin JP, Hippenstiel S. 2007. *Porphyromonas gingivalis* dihydroceramides induce apoptosis in endothelial cells. J Dent Res. 86(7):635–640.

***Porphyromonas gingivalis* Sphingolipid Synthesis Limits the Host Inflammatory Response**

F.G. Rocha, Z.D. Moye, G. Ottenberg, P. Tang, D.J. Campopiano, F.C. Gibson, and M.E. Davey

APPENDIX

MATERIALS AND METHODS

Bacterial strains and growth conditions.

Wild type strain *P. gingivalis* W83 (Dr. Christian Mouton, Laval University, Quebec City, Quebec, Canada) was used in this study along with the matching SPT mutants (W83 ΔPG1780), which was generated and characterized previously (Moye et al. 2016). Strains were stored at -80°C and sub-cultured to blood agar plates (BAPHK) comprised of Trypticase Soy Broth (Becton, Dickinson and Company, Franklin Lakes, NJ, USA) supplemented with 5 µg/ml hemin, 1 µg/ml menadione, and 5% defibrinated sheep blood (Northeast Laboratory Services, Winslow, ME, USA) and incubated at 37°C in an anaerobic chamber (Coy Lab Products, Grass Lake, MI, USA) with an atmosphere containing 5% hydrogen, 10% carbon dioxide, and 85% nitrogen. These primary cultures were used to verify purity and were sub-cultured to fresh BAPHK plates only once during these studies (minimal passaging). Broth cultures of *P. gingivalis* were grown in Trypticase Soy Broth supplemented with 5 µg/ml hemin, 1 µg/ml menadione (TSBHK) and incubated at 37°C in a COY anaerobic chamber, as described above. The *P. gingivalis* SPT deletion mutant was maintained on blood agar plates by supplementing the medium with 10 µg/ml erythromycin; however, TSBHK without antibiotics was used for all broth cultures.

Cloning and Expression of C-terminal, N-terminal and No-tag PG1780 (PgSPT).

The PG1780 gene was cloned into an expression plasmid (pEBSRCTEVC$_{10}$HIS), which contained a ten-histidine tag at the C-terminus or expression plasmid (pEHISTEV), a six-histidine tag at the N-terminus. For no-tag PgSPT, a stop codon was put in the end of protein sequence in C-terminal his-tag plasmid. The constructs were transformed into *E. coli* BL21 (DE3) competent cells on LB agar plates selected with ampicillin (100 µg/ml) for C-terminal and No-tag SPT or kanamycin (30 µg/ml) for N-terminal SPT. A single colony was grown overnight in LB/ampicillin or LB/kanamycin broth at 37°C with shaking. The inoculant was diluted to

LB/ampicillin or LB/kanamycin broth starting with OD_{600} of 0.1. Until the OD_{600} reached to 0.6-0.8, expression was induced with the addition of 0.1 mM isopropyl-β-D-1-thiogalactopyranoside (IPTG) and grown at 30°C for 5 hrs for his-tag protein, and 16°C for overnight for untagged protein. Cells were harvested by centrifugation at 5000 xg for 7 min.

Purification of C'terminal and N'terminal PgSPT

The harvested cells were resuspended in wash buffer, 20 mM potassium phosphate buffer, pH 7.5, 250 mM NaCl, 10 mM imidazole and 25 µM pyridoxal phosphate (PLP). Cells were lysed by sonication on ice (Soniprep, 150, 10 cycles of 30 seconds on by 30 seconds off). The cell lysates were separated by centrifugation at 24,000 xg for 40 min. and filtered through a 0.45 µm filter. Cell-free extracts were loaded onto a 1 mL HisTrap nickel affinity columns (GE Healthcare). The protein was eluted with an imidazole gradient (10 mM to 500 mM) over 30 column volumes, then further purified by gel filtration (GF) chromatography (S200 HR, GE Healthcare) with buffer (20 mM potassium phosphate buffer, pH 7.5, 250 mM NaCl, 10% w/v glycerol and 25 µM PLP). Purification was monitored by 12% SDS-PAGE.

Purification of No-tag PgSPT

The harvested cells were resuspended in wash buffer, 50 mM Tris-HCl buffer, pH 8.5. Cells were lysed by sonication on ice (Soniprep, 150, 10 cycles of 30 seconds on the followed by 30 seconds off). The cell lysate was separated by centrifugation at 24,000 g for 40 minutes and filtered through a 0.45 µm filter. The cell-free extract was loaded onto a 1 mL HiTrap Q HP anion exchange column (GE Healthcare). The protein was eluted with a NaCl gradient (0 mM to 1M) over 30 column volumes, then further purified by GF chromatography (S200 HR) with buffer (50 mM HEPES, pH 7.5, 250 mM NaCl, 10% w/v glycerol and 25 µM PLP). Purification was monitored by 12% SDS-PAGE.

Liquid Chromatography Electrospray Ionization Mass Spectrometry of PgSPT

Samples were analyzed in positive ion mode using HPLC coupled to a Waters Synapt G2 QTOF with an electrospray ionization source (ESI). A 5-10 µl volume of 10 µM protein was injected into a Phenomenex C4 3.6u column. The conditions for the qTOF are as follows: source temperature 120°C, backing pressure 2 mbar, and sampling cone voltage 54V. The protein was eluted with a 12 minute gradient, starting at 5% acetonitrile with 0.1% formic acid to 95% acetonitrile. The resulting spectra were processed and the charge distributions deconvoluted using MassLynx V4.1 software (Waters Corporation, Milford, MA).

Spectroscopic Measurements and Determination of Dissociation Constants (K_d) of PgSPT.

All UV-visible spectra were recorded on Cary 50 UV-visible spectrophotometer (Varian) and analysed using Cary WinUV software (Varian). Prior to all enzymatic assays, the protein was dialysed in the GF buffer for 1 hour in order to convert into its internal aldimine (holo-) form. A

PD-10 (Sephadex G-25M; GE Healthcare) desalting column was used to remove excess PLP. A typical experiment for determination of K_d was performed in 20 mM potassium phosphate buffer, pH 7.5, 250 mM NaCl, and had the initial concentration of protein at 20 µM by monitoring the changes at 425 nm upon incubation with various amounts of L-serine (0-100 mM) for 15 min at room temperature. The K_d values were calculated from plots of Δ425 versus L-serine concentrations by using Origin 2016 Software (OriginLab Corporation, Northampton, MA) by rearranging the equation:

$$\Delta A_{obs} = \frac{\Delta A_{MAX}\,[serine]}{Kd + [serine]},$$

where ΔA_{obs} and ΔA_{MAX} represents the observed and maximum changes of absorbance at 425 nm respectively, [serine] is L-serine concentration, and the K_d is the dissociation constant.

Enzyme kinetics of PgSPT using 5,5'-dithiobis-2-nitrobenzoic acid (DTNB) assay

The enzyme was incubated with first substrate in a buffered solution containing DTNB, and started by the addition of second substrate to product CoASH thiol product, which was monitored by observation of the TNB^- anion at 412nm (ε_{max} = 14,150 M/cm). The experiment to determine the K_m value for L-serine contained 1 µM PgSPT, 0.1-100 mM L-serine, 250 µM palmitoyl-CoA, and 0.2 mM DTNB in 100 mM HEPES buffer, pH 7.0, 250 mM NaCl, pH 7.0, and for palmitoyl-CoA contained 1 µM PgSPT, 20 mM L-serine, 1-1000 µM palmitoyl-CoA, and 0.2 mM DTNB. The assays were carried out over 1 hour on a BioTek Synergy HT plate reader by using 96 well plates. Kinetic parameters were calculated from Michaelis-Menten equation from plotting the initial rate versus concentration by using Origin 2016.

$$\mathrm{v} = \frac{V_{MAX}\,[S]}{K_M + [S]}$$

Measuring KDS Product using MALDI-TOF-MS

The sample was obtained from the DTNB assay and desalted using OMIX C4 pipette tips. Samples were eluted in 100% acetonitrile containing 0.2% formic acid. 1 µl of matrix seed [20 mg/mL apha-cyano-4-hydroxycinnamic acid (CHCA) in methanol/acetone (2:3)] was spotted onto an MTP 384 ground steel plate and left to air dry. The sample was then mixed with matrix (20 mg/mL CHCA in 50% acetonitrile within 0.25% trifluoroacetic acid (TFA)) in a 1:1 ratio, and 1 µl of this mixture was spotted on top of CHCA-acetone layer and left to air-dry. The sample was analyzed in reflector mode using a calibrated Bruker UltrafleXtreme MALDI TOF mass spectrometer. The analysis was carried out in positive ion mode. The laser power was adjusted to provide optimum signal. 500 laser shots were used per sample and each spectrum was a sum of over 5000 shots. Spectra were acquired over a range of 200-1500 *m/z*. The data acquisition software used was Flex Control version 3.4. The data were analyzed using Data Analysis version 4.4 software.

RNA extraction and sequencing

Colonies of *P. gingivalis* strain W83 and W83 ΔPG1780 were inoculated into pre-reduced TSBHK and grown overnight to stationary phase. Cultures were sub-cultured into pre-reduced TSBHK and grown to an OD_{600} of 1.0. To avoid aerobic stress, the RNA extraction was performed in the anaerobic chamber using the Direct-zol™ RNA MiniPrep Kit (Zymo Research, Tustin, CA), as previously (Moradali et al. 2019; Moye et al. 2019). In brief, cells were lysed, samples were centrifuged to remove cell debris, followed by mixing with an equal volume of 100% ethanol. Mixtures were then transferred to a Zymo-Spin™ IIC column (Zymo Research),

centrifuged and washed with RNA wash buffer. Samples were incubated on the column with DNase I for 1 hr, washed with RNA wash buffer, and incubated with DNase I a second time using the same conditions to completely remove genomic DNA. Finally, the columns were washed with Direct-zol™ RNA PreWash buffer followed by RNA wash buffer. The RNA samples were eluted by briefly incubating the column with nuclease free water and centrifuging into a RNAse free sterile microcentrifuge tube. RNA samples were then delivered to the Gene Expression and Genotyping core of the Interdisciplinary Center for Biotechnology Research

(ICBR) at University of Florida to determine sample quality and perform sequencing, as previously described (Moradali et al. 2019; Moye et al. 2019). The quality of the RNA was assessed with an Agilent 2100 Bioanalyzer (Agilent Technologies, Inc) only samples with an RNA integrity number (RIN) of 7.0 or greater were retained for further analysis. For library construction, 600 ng of each sample was treated with the Illumina Ribo-Zero™ magnetic kit for bacterial RNA according to the manufacturer's instructions. Samples (5ul) were fragmented and used to perform first strand cDNA synthesis with random primers, treated to create the second strand, and ligated with NEBNext adaptors after repairing the ends of DNA strands using the NEBNext® Ultra™ RNA library prep kit for Illumina® (New England Biolabs). Enrichment of the libraries was accomplished by PCR amplification with subsequent purification of the samples performed using the Agencourt AMPure XP system (Beckman Coulter). For quality control of the library and pooling, barcoded libraries were sized on the bioanalyzer and then quantitated by Qubit assay kits (Invitrogen). Typically, a 200-1000 broad library peak was observed. Quantitative PCR was used to validate the library's functionality, using the KAPA Library Quantification Kits for Illumina platforms (Kapa Biosystems, Wilmington, MA). All samples were equimolar-pooled for one lane of HiSeq 3000 with 2X 100 cycles run. Sequencing was

performed on the Illumina® HiSeq® 3000 system instrument using the clustering and sequencing reagents provided by Illumina®. Paired-end, 2X 100 cycles runs required the adding together of reagents from the 150 cycles and the 50 cycles. Sequencing reactions were set up using 5 µl of the library (2.5 nM).

RNA sequencing data analysis

The cleaned data files were downloaded from the Illumina® website and analyzed using the bioinformatics tool Rockhopper (McClure et al. 2013; Tjaden 2015), which was run using the default settings. The sequences annotated as tRNA and rRNA messages were eliminated, and of the remaining transcripts, we eliminated any with a $P > 0.01$ and a fold change of less than 1.5. Raw sequencing data is available on the NCBI Sequence Read Archive (SRA) under accession number PRJNA607525.

Cell culture

The human monocyte cell line THP-1 (ATCC®, TIB-202) was cultured in RPMI-1640 (Corning) supplemented with 10% heat-inactivated fetal bovine serum, L-glutamine (2 mM), penicillin/streptomycin (100 U/100 µg/ml), HEPES (10 mM), sodium pyruvate (1 mM), glucose (4.5 mg/ml), sodium bicarbonate (1.5 mg/ml) and 2-mercaptoethanol (0.05 mM; Sigma-Aldrich, St. Louis, MO). Cells were cultured at 37°C in a 5% CO_2 incubator. To induce differentiation into a macrophage-like state, THP-1 cells were placed into fresh medium containing 100 ng/ml phorbol 12-myristate 13-acetate (PMA; Sigma-Aldrich, St. Louis, MO), and after differentiation, adherent cells were harvested, adjusted to $5x10^5$ viable cells/ml, and 1 ml or 100 µl of THP-1

cells were added to each well of 24-well or 96-well cell culture plates, respectively. After 48 hrs incubation, cells were used in challenge studies.

Cytokine and chemokine detection assay

PMA-differentiated THP-1 cells in 24-well tissue culture plates were cultured in medium alone, or in medium with *P. gingivalis* W83 parent strain, or SPT mutant strain at a multiplicity of infection of 100. After 2, 6 and 24 hrs of co-culture, the cell culture supernatant fluids were collected and the levels of TNFα, IL-1β, IL-6, IL-8, IL-10 and RANTES were determined by Milliplex Multiplex Assays (EMD, Millipore, Billerica, MA). Data was acquired on a Luminex 200® system running xPONENT® 3.1 software (Luminex, Austin, TX) and analyzed using a 5-paramater logistic spline-curve fitting method using Milliplex®Analyst V5.1 software (Vigene Tech, Carlisle, MA).

Cell viability assay

PMA-differentiated THP-1 cells were seeded into wells of 96-well culture plates, and cultured in medium alone, or infected with *P. gingivalis* W83 or SPT mutant at multiplicity of infection of 100. After incubation at 37°C in a 5% CO_2 for 2, 6 and 24 hrs, cell viability was determined using 3-(4,5-dimethylthiazol-2-yl)-2,5-diphenyltetrazolium bromide MTT assay (Vybrant® MTT Cell Proliferation Assay Kit, Thermo Fisher) according to the instructions of the manufacturer using DMSO (Sigma-Aldric, St. Louis, MO, USA) as a formazan solubilizing agent. A microplate reader (Synergy H1, BioTek Instruments, Inc., VT) was used to record absorbance at 540 nm.

chamber. After 24 hr of incubation at 37°C + 5% CO_2, transwells were removed and wells containing coverslips were washed with PBS + 3% BSA prior to click labeling. Coverslips were treated with 150 µl of Click reaction mixture and labeling was performed as described above then washed with PBS + 3%BSA. Coverslips were mounted with mounting medium containing DAPI (DAPI Fluoromount G, Fisher), allowed to dry, and were imaged with a Nikon Eclipse-TiE inverted fluorescence microscope.

Statistical analysis

Results are presented as the mean and error bars represented by either ± 2 standard deviations (2SD) or standard error of the mean (SEM) as indicated. The significance of differences between values of groups was evaluated by unpaired t-test, using GraphPad Prism 5.0 (GraphPad Software, Inc; La Jolla, CA) statistical analysis software, and differences were considered significant at $P<0.05$.

References for Appendix Material

Johnson EL, Heaver SL, Waters JL, Kim BI, Bretin A, Goodman AL, Gewirtz AT, Worgall TS, Ley RE. 2019. Sphingolipid production by gut bacteroidetes regulates glucose homeostasis. bioRxiv.

McClure R, Balasubramanian D, Sun Y, Bobrovskyy M, Sumby P, Genco CA, Vanderpool CK, Tjaden B. 2013. Computational analysis of bacterial rna-seq data. Nucleic Acids Res. 41(14):e140.

Moradali MF, Ghods S, Angelini TE, Davey ME. 2019. Amino acids as wetting agents: Surface translocation by *Porphyromonas gingivalis*. The ISME journal.

Moye ZD, Gormley CM, Davey ME. 2019. Galactose impacts the size and intracellular composition of the asaccharolytic oral pathobiont *Porphyromonas gingivalis*. Appl Environ Microbiol. 85(4).

Moye ZD, Valiuskyte K, Dewhirst FE, Nichols FC, Davey ME. 2016. Synthesis of sphingolipids impacts survival of *Porphyromonas gingivalis* and the presentation of surface polysaccharides. Front Microbiol. 7:1919.

Tjaden B. 2015. De novo assembly of bacterial transcriptomes from rna-seq data. Genome Biol. 16:1.

Supplemental Table 1. Amino acid percentage of identity and similarity of bacterial SPT isoforms.

SPT	*S. paucimobilis*	*S. wittichii*	*S. multivorum*	*B. fragilis*	*P. gingvalis*
S. paucimobilis	100/100*	75/86	38/60	35/58	34/56
S. wittichii		100/100	36/59	39/61	37/58
S. multivorum			100/100	58/79	59/77
B. fragilis				100/100	76/89
P. gingvalis					100/100

* = Numbers presented are percent identity/percent similarity of the compared SPTs.

Supplemental Table 2: Viability of THP-1 cells in co-culture with *P. gingivalis* assessed by MTT assay.

	Time in Co-Culture (h)		
Treatment *	2h	6h	24h
Medium	100 ± 0	100 ± 0	100 ± 0
P. gingivalis W83	108.3 ± 13.7	103.1 ± 17.8	70.3 ± 11.5
P. gingivalis ΔPG1780	126.8 ± 29.4	109.6 ± 23.9	110 ± 27.3

* THP-1 cells were cultured with medium alone, or medium with *P. gingivalis* W83 wild type strain or the *P. gingivalis* sphingolipid null mutant ΔPG1780 at multiplicity of infection of 100. THP-1 cell viability was determined following 2, 6, and 24h of co-culture using the MTT assay. For each experiment the Medium only treatment values were set at 100% viability, and percent viability was calculated. No significant differences in THP-1 cell viability were observed between groups at any time point using ANOVA with Tukey multiple comparisons (Prism 8); data are presented as mean ± SEM (n=4 biologic replicates).

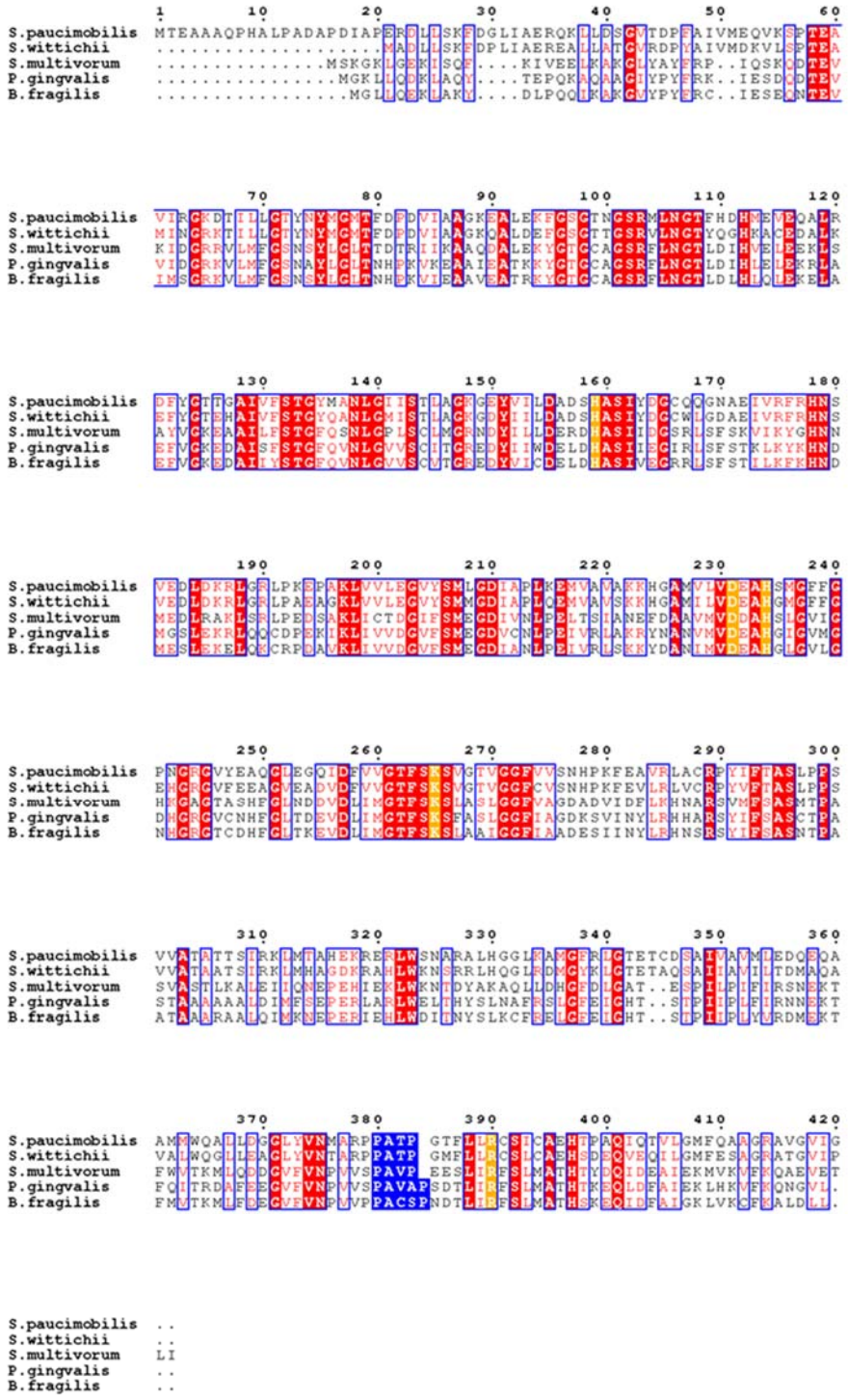

Supplemental Figure 1A: Alignment of the five microbial SPT amino acid sequences from Supplemental Table 1. Red boxes = conserved residues, yellow boxes = active sites, pink box = conserved properties, blue box = sequence motif denoting a structural loop.

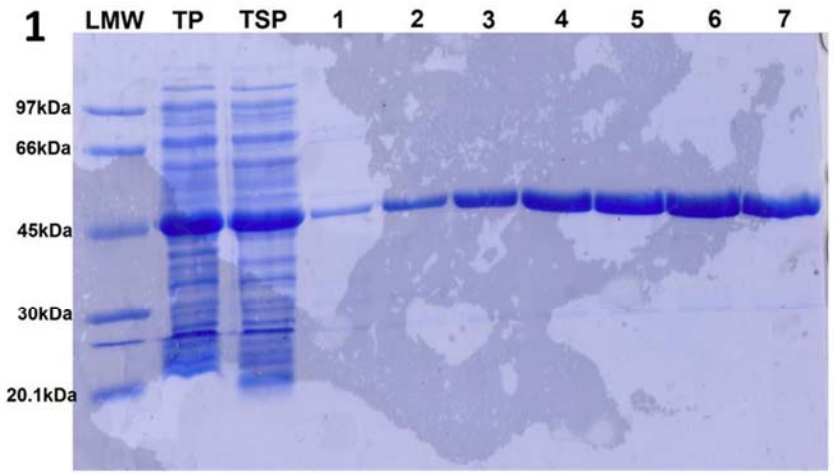

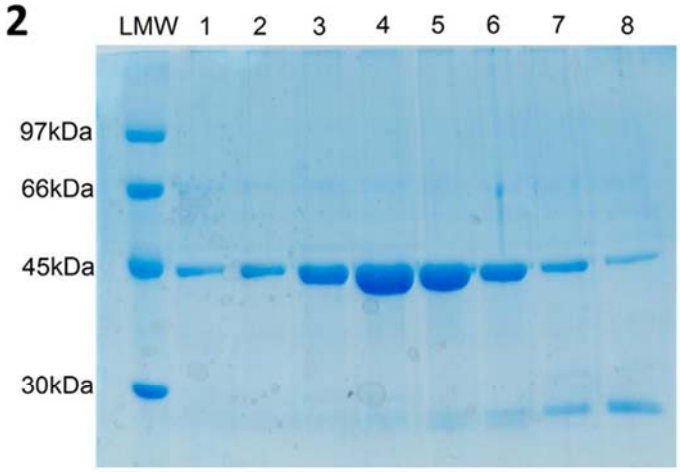

Supplementary Figure 1B. (**1**) Expression and purification of His-tagged PgSPT; LMW = marker, TP = pellet extract, TSP = soluble extract, lanes 1-7 = elution of PgSPT from column. (**2**) Purification of PgSPT from S200 size exclusion column; LMW = marker, lanes 1-8 = fraction eluting from the column.